

Advances in DOA Estimation and Source Localization

Lead Guest Editor: Elias Aboutanios

Guest Editors: Aboulhasr Hassanien, Amr El-Keyi, Youssef Nasser,
and Sergiy A. Vorobyov





Advances in DOA Estimation and Source Localization

International Journal of Antennas and Propagation

Advances in DOA Estimation and Source Localization

Lead Guest Editor: Elias Aboutanios

Guest Editors: Aboulnasr Hassanien, Amr El-Keyi,
Youssef Nasser, and Sergiy A. Vorobyov



Copyright © 2017 Hindawi. All rights reserved.

This is a special issue published in “International Journal of Antennas and Propagation.” All articles are open access articles distributed under the Creative Commons Attribution License, which permits unrestricted use, distribution, and reproduction in any medium, provided the original work is properly cited.

Editorial Board

Ana Alejos, Spain
Mohammad Ali, USA
Jaume Anguera, Spain
Rodolfo Araneo, Italy
Alexei Ashikhmin, USA
Herve Aubert, France
Paolo Baccarelli, Italy
Xiulong Bao, Ireland
T. Björninen, Finland
Stefania Bonafoni, Italy
Paolo Burghignoli, Italy
S. Nawaz Burokur, France
Giuseppe Castaldi, Italy
Luca Catarinucci, Italy
F. Catedra, Spain
Marta Cavagnaro, Italy
Shih Yuan Chen, Taiwan
Yu Jian Cheng, China
Renato Cicchetti, Italy
Riccardo Colella, Italy
Laura Corchia, Italy
Lorenzo Crocco, Italy
Claudio Curcio, Italy
Francesco D'Agostino, Italy
M. E. de Cos Gómez, Spain
T. A. Denidni, Canada

Giuseppe Di Massa, Italy
Michele D'Urso, Italy
Francisco Falcone, Spain
M. F. Bataller, Spain
Flaminio Ferrara, Italy
Vincenzo Galdi, Italy
C. Gennarelli, Italy
Farid Ghanem, Algeria
Sotirios K. Goudos, Greece
Rocco Guerriero, Italy
Kerim Guney, Turkey
Song Guo, Japan
Tamer S. Ibrahim, USA
M. R. Kamarudin, UK
Slawomir Koziel, Iceland
Luis Landesa, Spain
Ding-Bing Lin, Taiwan
Angelo Liseno, Italy
P. Lombardo, Italy
Lorenzo Luini, Italy
Atsushi Mase, Japan
Diego Masotti, Italy
C. F. Mecklenbräuker, Austria
A. T. Mobashsher, Australia
Ananda S. Mohan, Australia
J.-M. Molina-Garcia-Pardo, Spain

Giuseppina Monti, Italy
Giorgio Montisci, Italy
N. Nasimuddin, Singapore
Mourad Nedil, Canada
Symeon Nikolaou, Cyprus
Giacomo Oliveri, Italy
Ikmo Park, Republic of Korea
Josep Parrón, Spain
Matteo Pastorino, Italy
Xianming Qing, Singapore
Ahmad Safaai-Jazi, USA
S. Safavi-Naeini, Canada
M. Salazar-Palma, Spain
Stefano Selleri, Italy
Raffaele Solimene, Italy
Gino Sorbello, Italy
Seong-Youp Suh, USA
Sheng Sun, Hong Kong
Larbi Talbi, Canada
L. Tarricone, Italy
Parveen Wahid, USA
Wen-Qin Wang, China
Shiwen Yang, China
Yuan Yao, China

Contents

Advances in DOA Estimation and Source Localization

Elias Aboutanios, Aboulnasr Hassanién, Amr El-Keyi, Youssef Nasser, and Sergiy A. Vorobyov
Volume 2017, Article ID 1352598, 3 pages

Experimental Results of Novel DoA Estimation Algorithms for Compact Reconfigurable Antennas

Henna Paaso, Aki Hakkarainen, Nikhil Gulati, Damiano Patron, Kapil R. Dandekar, Mikko Valkama, and Aarne Mämmelä
Volume 2017, Article ID 1613638, 13 pages

Robust Cyclic MUSIC Algorithm for Finding Directions in Impulsive Noise Environment

Sen Li, Xiaojing Chen, and Rongxi He
Volume 2017, Article ID 9038341, 9 pages

Direction-of-Arrival Estimation for Coprime Array Using Compressive Sensing Based Array Interpolation

Aihua Liu, Qiang Yang, Xin Zhang, and Weibo Deng
Volume 2017, Article ID 6425067, 10 pages

Tensor-Based Methods for Blind Spatial Signature Estimation in Multidimensional Sensor Arrays

Paulo R. B. Gomes, André L. F. de Almeida, João Paulo C. L. da Costa, João C. M. Mota, Daniel Valle de Lima, and Giovanni Del Galdo
Volume 2017, Article ID 1615962, 11 pages

Performance Analysis of Two-Dimensional Maximum Likelihood Direction-of-Arrival Estimation Algorithm Using the UCA

Yun-Seong Cho, Jeong-Min Seo, and Joon-Ho Lee
Volume 2017, Article ID 6926825, 28 pages

Azimuth/Elevation Directional Finding with Automatic Pair Matching

Nizar Tayem
Volume 2016, Article ID 5063450, 9 pages

Application Research of the Sparse Representation of Eigenvector on the PD Positioning in the Transformer Oil

Qing Xie, Dan Liu, Ying Zhang, Shuguo Gao, Tong Li, Xinjie Wang, and Fangcheng Lü
Volume 2016, Article ID 1343194, 13 pages

DOA Estimation of Cylindrical Conformal Array Based on Geometric Algebra

Minjie Wu, Xiaofa Zhang, Jingjian Huang, and Naichang Yuan
Volume 2016, Article ID 7832475, 9 pages

Efficient AM Algorithms for Stochastic ML Estimation of DOA

Haihua Chen, Shibao Li, Jianhang Liu, Yiqing Zhou, and Masakiyo Suzuki
Volume 2016, Article ID 4926496, 10 pages

Editorial

Advances in DOA Estimation and Source Localization

**Elias Aboutanios,¹ Aboulnasr Hassanien,² Amr El-Keyi,³
Youssef Nasser,⁴ and Sergiy A. Vorobyov⁵**

¹*School of Electrical Engineering and Telecommunications, University of New South Wales, Sydney, NSW 2052, Australia*

²*Department of Electrical Engineering, Wright State University, Dayton, OH 45435, USA*

³*Department of Systems and Computer Engineering, Carleton University, Ottawa, ON, Canada*

⁴*Department of Electrical and Computer Engineering, American University of Beirut, Beirut, Lebanon*

⁵*Department of Signal Processing and Acoustics, Aalto University, 00076 Aalto, Finland*

Correspondence should be addressed to Elias Aboutanios; elias@ieee.org

Received 1 August 2017; Accepted 1 August 2017; Published 27 August 2017

Copyright © 2017 Elias Aboutanios et al. This is an open access article distributed under the Creative Commons Attribution License, which permits unrestricted use, distribution, and reproduction in any medium, provided the original work is properly cited.

Since the emergence of radars in the middle of the last century, the determination of the direction of arrival (DOA) has been an active research topic with applications in various areas including, in addition to the radar itself, sonar and communications. DOA estimation has come a long way from its early days when mechanically steered narrow-beam antennas were employed to determine the direction of incidence of the incoming signal [1, 2]. The introduction of digital signal processors has made a wide range of mathematical techniques available for DOA estimation. Approaches such as subspace decomposition, eigenanalysis, sparsity, and compressed sensing based methods, as well as the advanced Fourier based processing techniques, are playing a fundamental role in achieving performance enhancements in speed, accuracy, and robustness.

Presently, the range of applications of DOA estimation continues to expand and the devices that rely upon it continue to proliferate. Automotive radars are currently being deployed for situational awareness, thus assisting in emergency braking, steering, and cruise control [3]. In communications, the quality of the wireless services is greatly enhanced if the user information is known. DOA estimation is, for instance, essential for the delivery of context-based and targeted information to the user [4]. In navigation, interference localization permits interferers to be disabled [5–7], which is essential to ensure safety in critical applications such as air travel.

DOA estimation is often implemented using either sensor arrays or multiple antennas working cooperatively. There

exist a wide variety of approaches in the literature for obtaining the DOA of single and multiple sources. High-resolution (HR) methods and subspace-based techniques can achieve very good resolution and accuracy at the expense of high computational cost. Perhaps the best known methods are the MUSIC [8] and ESPRIT [9] algorithms, although other well-known methods include the Capon estimator [10] and matrix pencil [11]. HR approaches, however, incur a high computational cost and cannot resolve correlated sources. They also cannot be applied in the single snapshot case unless spatial smoothing is employed, which compromises both the resolution and the accuracy. In contrast, discrete Fourier transform (DFT) methods (e.g., [12, 13]) are computationally much simpler and suitable for the single snapshot case.

Owing to the widening range of applications for DOA estimation, the increased variety of sensor configurations, and the spread of constraints imposed by the hardware (e.g., low power devices), the research into novel DOA estimation strategies has continued unabated. This special issue presents a collection of papers detailing recent advances in technologies and techniques for enhanced DOA estimation and its applications in radar, sonar, wireless communications, and other fields.

The classical maximum likelihood (ML) DOA estimation of a number of sources using an array of antennas is studied by H. Chen et al. in the paper titled “Efficient AM Algorithms for Stochastic ML Estimation of DOA.” The paper adopts an alternating minimization strategy where each source is estimated sequentially and the process is then repeated until

all source estimates have converged. This allows the authors to reduce the computational complexity of the stochastic ML (SML) algorithm. In the paper “Robust Cyclic MUSIC Algorithm for Finding Directions in Impulsive Noise Environment,” the DOA estimation problem of cyclostationary signals in impulsive noise environments is addressed. The impulsive noise is modeled using the family of alpha stable distributions that has a heavy tail. Such distributions do not have finite second-order statistics, which limits the applicability of subspace-based methods. The authors circumvent this problem by defining robust cyclic correlation functions and then employ the MUSIC algorithm to obtain the DOAs.

Reconfigurable, sparse, coprime, and conformal arrays are playing an important role in enhancing the DOA estimation performance as well. Indeed, these allow the array configuration to be used as an extra degree of freedom. In the paper titled “Experimental Results of Novel DoA Estimation Algorithms for Compact Reconfigurable Antennas,” H. Paaso et al. study the problem of estimating the DOA when the antenna is reconfigurable. The authors consider a reconfigurable composite right/left handed (CRLH) leaky-wave antenna. They then evaluate and compare the adjacent pattern power ratio (APPR) and MUSIC algorithms for estimating the DOA. The APPR is a lookup table based approach that requires the prior characterization of the antenna.

Reduction in the number of sensors is desirable and is achieved using coprime arrays, which allow the estimation of the DOAs of more sources than sensors. A. Liu et al. deal with this problem in the paper “Direction-of-Arrival Estimation for Coprime Array Using Compressive Sensing Based Array Interpolation” by employing compressive sensing in tandem with array interpolation in order to achieve improved DOA estimation performance. Another variation in the array configuration allows the array geometry to conform to a nonflat surface, which complicates the estimation process. The paper “DOA Estimation of Cylindrical Conformal Array Based on Geometric Algebra” by M. Wu et al. addresses the DOA estimation for conformal arrays by combining a geometric algebra approach with MUSIC. The authors propose the GA-MUSIC algorithm which simplifies the calculations.

Antenna arrays provide multiple multidimensional data, permitting the estimation of multiple spatial parameters such as azimuth and elevation as well as temporal parameters, such as range and Doppler. Therefore, two- and multidimensional data processing techniques play an enabling role in source parameter estimation. In the paper “Azimuth/Elevation Directional Finding with Automatic Pair Matching,” N. Tayem deals with the problem of two-dimensional (2D) DOA estimation for multiple far-field sources. The azimuth and elevation angles are obtained via constructing three cross-correlation matrices and applying parallel factor analysis. Automatic pair matching is achieved via using trilinear least squares based solutions. In the paper “Performance Analysis of Two-Dimensional Maximum Likelihood Direction-of-Arrival Estimation Algorithm,” on the other hand, Y.-S. Cho et al. consider the 2D problem of estimating the azimuth and elevation using a uniform circular array (UCA). More specifically, the authors study the ML estimator and derive explicit expressions for the mean squared error.

Higher dimensional data comprising, for instance, space, time, frequency, and polarization is studied in the paper “Tensor-Based Methods for Blind Spatial Signature Estimation in Multidimensional Sensor Arrays.” The work presents two tensor-based techniques that employ the covariance tensor to obtain the DOAs. The first method assumes that the sources are correlated and hence the covariance matrix is not diagonal. In the second case, the sources are assumed to be uncorrelated and the method is shown to be equivalent to parallel factor analysis (PARAFAC). The DOA estimation is obtained using an alternating least squares (ALS) approach.

DOA estimation finds an interesting application in the paper “Application Research of the Sparse Representation of Eigenvector on the PD Positioning in the Transformer Oil.” In this work, the authors consider the problem of detecting partial discharge in high voltage transformer oil where the ultrasonic signal is wideband. Using a circular array, the signal is spatially sampled and then DOA estimation is implemented using sparse decomposition and the matching pursuit algorithm.

The works presented in this special issue showcase the depth of the DOA estimation problem as well as the range of challenges and breadth of applications. We hope that the contributions made by the published papers will advance the state of the art and contribute to this fertile field.

Acknowledgments

We would like to thank the authors for their novel and insightful contributions and the anonymous reviewers for their positive and helpful feedback.

*Elias Aboutanios
Aboulnasr Hassani
Amr El-Keyi
Youssef Nasser
Sergiy A. Vorobyov*

References

- [1] H. Krim and M. Viberg, “Two decades of array signal processing research,” *IEEE Signal Processing Magazine*, vol. 13, no. 4, pp. 67–94, 1996.
- [2] T. E. Tuncer and B. Friedlander, Eds., *Classical and Modern Direction-of-Arrival Estimation*, Academic Press, 2009.
- [3] F. Engels, P. Heidenreich, A. M. Zoubir, F. K. Jondral, and M. Wintermantel, “Advances in automotive radar: a framework on computationally efficient high-resolution frequency estimation,” *IEEE Signal Processing Magazine*, vol. 34, no. 2, pp. 36–46, 2017.
- [4] A. Yassin, Y. Nasser, M. Awad et al., “Recent advances in indoor localization: a survey on theoretical approaches and applications,” *IEEE Communications Surveys & Tutorials*, vol. 19, no. 2, pp. 1327–1346, 2017.
- [5] X. Wang, M. Amin, F. Ahmad, and E. Aboutanios, “Interference DOA estimation and suppression for GNSS receivers using fully augmentable arrays,” *IET Radar, Sonar & Navigation*, vol. 11, no. 3, pp. 474–480, 2017.
- [6] M. G. Amin, X. Wang, Y. D. Zhang, F. Ahmad, and E. Aboutanios, “Sparse arrays and sampling for interference mitigation and

- DOA estimation in GNSS,” *Proceedings of the IEEE*, vol. 104, no. 6, pp. 1302–1317, 2016.
- [7] W. Abdessamad, Y. Nasser, H. Artail, S. Chazbek, G. Fakher, and O. Bazzi, “An SDR platform using direction finding and statistical analysis for the detection of interferers,” in *Proceedings of the 8th International Congress on Ultra Modern Telecommunications and Control Systems and Workshops (ICUMT '16)*, pp. 43–48, Lisbon, Portugal, October 2016.
- [8] R. O. Schmidt, “Multiple emitter location and signal parameter estimation,” *IEEE Transactions on Antennas and Propagation*, vol. 34, no. 3, pp. 276–280, 1986.
- [9] R. Roy, A. Paulraj, and T. Kailath, “ESPRIT—a subspace rotation approach to estimation of parameters of cisoids in noise,” *IEEE Transactions on Acoustics, Speech, and Signal Processing*, vol. 34, no. 5, pp. 1340–1342, 1986.
- [10] J. Capon, “High-resolution frequency-wavenumber spectrum analysis,” *Proceedings of the IEEE*, vol. 57, no. 8, pp. 1408–1418, 1969.
- [11] Y. Hua and T. K. Sarkar, “Matrix pencil method for estimating parameters of exponentially damped/undamped sinusoids in noise,” *IEEE Transactions on Acoustics, Speech, and Signal Processing*, vol. 38, no. 5, pp. 814–824, 1990.
- [12] J. Li and P. Stoica, “Efficient mixed-spectrum estimation with applications to target feature extraction,” *IEEE Transactions on Signal Processing*, vol. 44, no. 2, pp. 281–295, 1996.
- [13] E. Aboutanios, A. Hassanien, M. G. Amin, and A. M. Zoubir, “Fast iterative interpolated beamforming for accurate single-snapshot DOA estimation,” *IEEE Geoscience and Remote Sensing Letters*, vol. 14, no. 4, pp. 574–578, 2017.

Research Article

Experimental Results of Novel DoA Estimation Algorithms for Compact Reconfigurable Antennas

Henna Paaso,¹ Aki Hakkarainen,² Nikhil Gulati,³ Damiano Patron,³ Kapil R. Dandekar,³ Mikko Valkama,² and Aarne Mämmelä¹

¹VTT Technical Research Centre of Finland, Kaitoväylä 1, P.O. Box 1100, 90571 Oulu, Finland

²Department of Electronics and Communications Engineering, Tampere University of Technology, P.O. Box 553, 33101 Tampere, Finland

³Department of Electrical and Computer Engineering, Drexel University, 3141 Chestnut Street, Philadelphia, PA 19104, USA

Correspondence should be addressed to Henna Paaso; henna.paaso@vtt.fi

Received 9 September 2016; Revised 18 December 2016; Accepted 13 April 2017; Published 24 July 2017

Academic Editor: Sergiy A. Vorobyov

Copyright © 2017 Henna Paaso et al. This is an open access article distributed under the Creative Commons Attribution License, which permits unrestricted use, distribution, and reproduction in any medium, provided the original work is properly cited.

Reconfigurable antenna systems have gained much attention for potential use in the next generation wireless systems. However, conventional direction-of-arrival (DoA) estimation algorithms for antenna arrays cannot be used directly in reconfigurable antennas due to different design of the antennas. In this paper, we present an adjacent pattern power ratio (APPR) algorithm for two-port composite right/left-handed (CRLH) reconfigurable leaky-wave antennas (LWAs). Additionally, we compare the performances of the APPR algorithm and LWA-based MUSIC algorithms. We study how the computational complexity and the performance of the algorithms depend on number of selected radiation patterns. In addition, we evaluate the performance of the APPR and MUSIC algorithms with numerical simulations as well as with real world indoor measurements having both line-of-sight and non-line-of-sight components. Our performance evaluations show that the DoA estimates are in a considerably good agreement with the real DoAs, especially with the APPR algorithm. In summary, the APPR and MUSIC algorithms for DoA estimation along with the planar and compact LWA layout can be a valuable solution to enhance the performance of the wireless communication in the next generation systems.

1. Introduction

Direction-of-arrival (DoA) estimation algorithms using compact antenna sizes are of significant importance to next generation wireless systems. Directive adaptive antennas can estimate the DoA, steer the beam to the desired direction, and suppress the power in undesired directions to avoid interference. Thus, they can greatly improve the spectrum reuse, interference avoidance, and device localization.

Adaptive antennas can be divided into two categories: phased arrays and reconfigurable antennas. Conventionally, phased arrays use many antenna array elements to adapt the radiation pattern shape and beam direction [1, 2]. Antenna arrays usually require one receiver chain per antenna branch. The cost usually increases with the number of antenna elements because the array needs the same number of radio frequency (RF) high-power or low-noise amplifiers as the elements in traditional antenna arrays [3].

Particularly for digital beamforming antennas, the same number of frequency converters, RF amplifiers, and digital-to-analog (D/A) or analog-to-digital (A/D) converters are needed. This leads to high-power consumption and high fabrication cost. In contrast to multielement antenna arrays, reconfigurable antennas do not need the multiple antenna elements or feeding networks [4]. In this paper, we present a certain type of compact reconfigurable antennas, namely, the composite right/left-handed (CRLH) leaky-wave antenna (LWA) [5]. The reconfigurable LWAs have many advantages: low manufacturing cost, low DC power consumption, full-space beam scanning using significantly less printed circuit board space, and absence of extra RF circuitry. By considering these advantages, especially compactness and beamsteering, CRLH-LWAs have a significant potential to be used in DoA systems.

In the context of conventional antenna arrays, DoA estimation algorithms have been extensively researched in

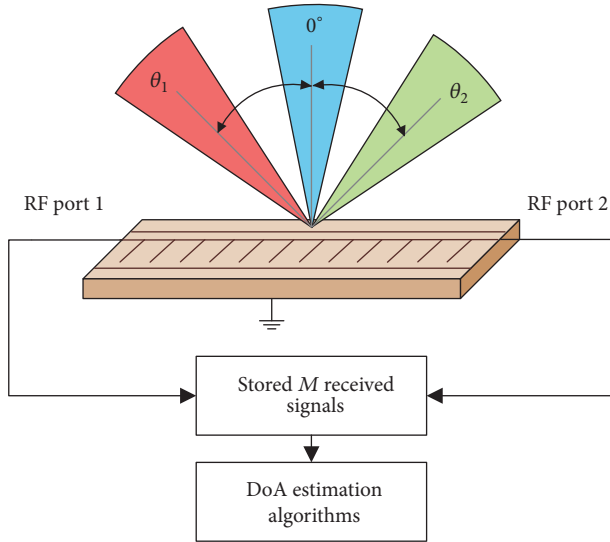


FIGURE 1: System model.

the literature [6–10]. However, these algorithms cannot be used directly in CRLH-LWAs because of the inherent design and operation of the LWAs versus multielement antenna arrays. An LWA has only one port and thus it has a single observation available at each sampling incident unlike in multielement antenna arrays where signals can be detected from different elements of the antenna array [11]. For this reason, DoA estimation algorithms for LWAs require that the LWA receives the transmitted signal M times through M different radiation patterns, as illustrated in Figure 1.

There are only a limited number of papers where DoA estimation algorithms are introduced for LWAs. In [12, 13], we preliminarily introduced a modified multiple signal classification (MUSIC) algorithm for LWAs. The CRLH-LWA has the inherent difference in the design. Our modified MUSIC algorithm uses M received signals, each obtained with a different radiation pattern and measured from two antenna ports. Then, a correlation matrix can be formed by using these M received signals. We presented experimental results of a LWA-based MUSIC algorithms in [14] where we introduced the performance of the MUSIC and power pattern cross-correlation (PPCC) algorithms in real wireless multipath environment. However, the paper presents only results for one radiation pattern configuration and does not study how different configurations affect the performance of the algorithms. Additionally, an adjacent pattern power ratio (APPR) algorithm and the complexity analysis of the algorithms are not presented in [14]. Similar work for DoA estimation has also been presented independently in [15, 16] that use the MUSIC algorithm for CRLH-LWA. In [15], only experimental results are introduced and the authors do not present how the MUSIC algorithm can be built up using LWAs. Additionally, [15, 16] present only experimental results of the MUSIC algorithm in an anechoic chamber. In addition, [17, 18] introduce reactance domain MUSIC [17] and unitary MUSIC [18] algorithms for electronically steerable parasitic array radiator (ESPAR) antennas. In [19], APPR algorithm is introduced

for the ESPAR antenna. The APPR algorithm is a simple DoA estimation algorithm which measures signal powers from M different directions and chooses the radiation pattern with the maximum signal power. Then, the adjacent pattern power ratios with respect to the maximum signal power pattern are calculated and the DoA is estimated by comparing these ratios with the predefined ratios from a look-up table (LUT). The performance of the algorithm is presented by using computer simulations and experiments in an anechoic chamber.

In this paper, we apply the APPR DoA estimation algorithm for CRLH-LWA. Additionally, we compare the performance of the APPR algorithm with the performance of the LWA-based MUSIC algorithm. The computational complexity of the APPR algorithm is much smaller than that of the MUSIC algorithm without much degradation in estimation accuracy. Unlike in our previous studies [12–14] and other DoA estimation techniques in the literature [19], we now study how the computational complexity and the performance of the algorithms depend on the number of selected radiation patterns in different kinds of environments: theoretical additive white Gaussian noise (AWGN) channel and a real world indoor multipath wireless environment with both line-of-sight (LoS) and non-line-of-sight (NLoS) components.

This paper is organized as follows: Section 2 introduces a detailed description of the DoA estimation algorithms for a compact CRLH-LWA. Section 3 presents shortly the CRLH-LWA design. Numerical and complexity analysis and experimental results of the DoA estimation algorithms are presented in Section 4. Finally, conclusions are drawn in Section 5.

2. CRLH-LWA-Based DoA Estimation Algorithms

In this section, we introduce an APPR DoA estimation algorithm for LWAs. Additionally, we present briefly a modified single/two-port MUSIC algorithms [12] whose performance we compare with the APPR algorithm. The first algorithm is based on evaluating the received powers for different voltage sets and the second algorithm is variant of the popular MUSIC algorithm [6] that we have modified to work with LWA. In the following sections, θ denotes the DoA and $\hat{\theta}$ an estimate thereof.

2.1. Single/Two-Port MUSIC Algorithm. Traditionally, the MUSIC algorithm [6] defines the spatial correlation matrix using the signals received by multiple antenna elements. In this subsection, we present how the spatial capabilities of the traditional antenna array can be virtually formulated with the CRLH-LWA and how the correlation matrix can be defined when using the two-port LWA.

Firstly, we have to collect the same transmitted signal $u(k)$, M times, while the LWA switches between M different radiation patterns. Thus, we can recreate spatial diversity due to M observations of the same signal but with different

beams. With the LWA, the $M \times 1$ received signal vector $\mathbf{y}(k)$ can be expressed as

$$\mathbf{y}(k) = \mathbf{a}(\theta) u(k) + \mathbf{z}(k), \quad (1)$$

where k denotes the received symbol index, $\mathbf{z}(k)$ is an $M \times 1$ AWGN vector, where the elements have variance equal to σ^2 , and $\mathbf{a}(\theta)$ is the $M \times 1$ steering vector. The m th element of the steering vector can be defined as

$$a_m(\theta) = \sqrt{G'_m} \sum_{n=1}^N I_n \exp[j(n-1)k_0 d (\sin(\theta) - \sin(\theta_m))], \quad (2)$$

where $m = 1, \dots, M$, N is the number of cascaded unit cells, and

$$G'_m = \frac{G_m}{\left(\sum_{n=1}^N I_n\right)^2}, \quad (3)$$

where θ is the angular direction of the received signal, θ_m is the main beam direction of the LWA with control voltage set m , $I_n = I_0 \exp[-\alpha(n-1)d]$ is an exponential function with a leakage factor α , and G_m is the measured antenna gain (in linear scale) of set m . The initial value of the exponential function $I_0 = 1$, with structure period d [5].

The MUSIC algorithm makes eigenvalue decomposition of the signal covariance matrix and uses a subspace algorithm to estimate DoA. Firstly, we have to estimate the covariance matrix from the received signals. The estimated covariance matrix can be expressed as

$$\widehat{\mathbf{R}}_{yy} = \frac{1}{N_s} \sum_{k=1}^{N_s} \mathbf{y}(k) \mathbf{y}^\dagger(k), \quad (4)$$

where N_s denotes the number of samples and the Hermitian transpose of \mathbf{y} is denoted as \mathbf{y}^\dagger . Then, the eigenvalue decomposition (EVD) of $\widehat{\mathbf{R}}_{yy}$ can be represented as

$$\widehat{\mathbf{R}}_{yy} = \widehat{\mathbf{E}}_s \widehat{\Lambda}_s \widehat{\mathbf{E}}_s^\dagger + \widehat{\mathbf{E}}_n \widehat{\Lambda}_n \widehat{\mathbf{E}}_n^\dagger, \quad (5)$$

where $\widehat{\mathbf{E}}_s = [\widehat{\mathbf{e}}_1, \widehat{\mathbf{e}}_2, \dots, \widehat{\mathbf{e}}_L]$ includes the estimated eigenvectors for the signal subspace, $\widehat{\Lambda}_s = \text{diag}[\widehat{\lambda}_1, \widehat{\lambda}_2, \dots, \widehat{\lambda}_L]$ denotes a diagonal matrix of the largest estimated eigenvalues, and L is the number of incident sources. Additionally, $\widehat{\mathbf{E}}_n = [\widehat{\mathbf{e}}_{L+1}, \widehat{\mathbf{e}}_{L+2}, \dots, \widehat{\mathbf{e}}_M]$ is the noise subspace matrix and $\widehat{\Lambda}_n = \text{diag}[\widehat{\lambda}_{L+1}, \widehat{\lambda}_{L+2}, \dots, \widehat{\lambda}_M]$ denotes the diagonal matrix of $M - L$ noise eigenvalues. Finally, the MUSIC pseudospectrum can be generated as

$$P_{\text{MUSIC}}(\theta) = \frac{\mathbf{a}^\dagger(\theta) \mathbf{a}(\theta)}{\mathbf{a}^\dagger(\theta) \widehat{\mathbf{E}}_n \widehat{\mathbf{E}}_n^\dagger \mathbf{a}(\theta)}. \quad (6)$$

The estimated direction-of-arrival (DoA) is the angle where the pseudospectrum $P_{\text{MUSIC}}(\theta)$ attains its maximum; that is,

$$\widehat{\theta}_{\text{MUSIC}} = \arg \max_{\theta} P_{\text{MUSIC}}(\theta). \quad (7)$$

The MUSIC algorithm is limited to uncorrelated signals. The estimated covariance matrix $\widehat{\mathbf{R}}_{yy}$ is nonsingular as long as the incident signals are not highly correlated [20]. When the incident signals are highly correlated signals or signals with a low SNR, the performance of the MUSIC algorithms reduces or the algorithm fails even completely [21]. Thus, the MUSIC algorithm has problems when determining the number of impinging source; that is, it cannot divide the signal subspace and noise subspace correctly, and thus it is not able to estimate the spatial spectrum correctly. This problem can be solved by using spatial smoothing techniques, signal feature vector technique, and frequency smoothing techniques, among others. However, these techniques are out of the scope of this paper.

2.2. Adjacent Pattern Power Ratio. Adjacent pattern power ratio is introduced for ESPAR antennas in [19]. The APPR algorithm calculates the adjacent power pattern ratio between the maximum received power pattern and the adjacent patterns. In this paper, we show how to apply the APPR algorithm to LWAs and show how configuring the antenna radiation patterns for signal observations can impact the performance of the algorithm, which has not been further evaluated in [19]. We first calculate the received power P_m from M different directions and normalize each power yielding the gain-normalized powers $P_m^{\text{norm}} = P_m/G_m$. Then, the radiation pattern that gives the maximum received power is selected. Thereafter, the adjacent pattern power ratio between the adjacent pattern to the selected pattern is calculated. Firstly, the APPR ratio is calculated from the measured radiation patterns in an anechoic chamber. The APPR can be presented as

$$\Gamma_{m+}(\theta) = \frac{P_m^{\text{norm}}(\theta)}{P_{m+1}^{\text{norm}}(\theta)}, \quad (8)$$

$$\Gamma_{m-}(\theta) = \frac{P_m^{\text{norm}}(\theta)}{P_{m-1}^{\text{norm}}(\theta)}. \quad (9)$$

Equation (8) tells that when the DoA falls into the right side of the m th pattern, $P_{m+1}^{\text{norm}}(\theta) > P_m^{\text{norm}}(\theta)$, as illustrated in Figure 2. Additionally, (9) tells that when the DoA falls into the left side of the m th pattern, $P_{m-1}^{\text{norm}}(\theta) > P_m^{\text{norm}}(\theta)$. These ratios for the selected θ range are calculated and stored into an LUT beforehand to reduce run-time computations. Hence, the DoA is to be estimated over the θ range. The length of θ range, J , depends on how radiation pattern configuration is selected. These searching areas are illustrated as a dotted line in Figure 2. Secondly, the APPR is measured for the received power and it can be presented as

$$\widehat{\Gamma}_{m+}(\theta) = \frac{\widehat{P}_m^{\text{norm}}(\theta)}{\widehat{P}_{m+1}^{\text{norm}}(\theta)}, \quad (10)$$

$$\widehat{\Gamma}_{m-}(\theta) = \frac{\widehat{P}_m^{\text{norm}}(\theta)}{\widehat{P}_{m-1}^{\text{norm}}(\theta)}.$$

Finally, we compare these adjacent pattern power ratios. The selection of $\Gamma_{m+/m-}$ is defined in the following way: if

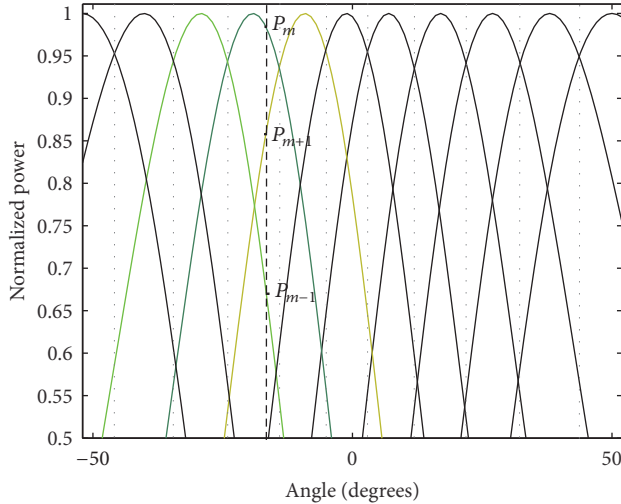


FIGURE 2: Theoretical radiation patterns.

$\hat{P}_{m+1}^{\text{norm}}(\theta) > \hat{P}_{m-1}^{\text{norm}}(\theta)$, we compare $\Gamma_{m+}(\theta)$ and $\hat{\Gamma}_{m+}(\theta)$. If $\hat{P}_{m+1}^{\text{norm}}(\theta) < \hat{P}_{m-1}^{\text{norm}}(\theta)$, we compare $\Gamma_{m-}(\theta)$ and $\hat{\Gamma}_{m-}(\theta)$. Hence, the estimated DoA can be defined as

$$\hat{\theta} = \begin{cases} \arg \min |\Gamma_{m-}(\theta) - \hat{\Gamma}_{m-}(\theta)| & \text{if } \hat{P}_{m+1}^{\text{norm}}(\theta) < \hat{P}_{m-1}^{\text{norm}}(\theta), \\ \arg \min |\Gamma_{m+}(\theta) - \hat{\Gamma}_{m+}(\theta)| & \text{if } \hat{P}_{m+1}^{\text{norm}}(\theta) > \hat{P}_{m-1}^{\text{norm}}(\theta). \end{cases} \quad (11)$$

The computational complexity and the performance of the algorithm depend on the number of received directions. These options are researched in Section 4.

3. Antenna Design

The APPR and MUSIC algorithms were designed to perform the DoA estimation using reconfigurable CRLH-LWA. The leaky-wave antenna is a traveling-wave antenna [5]. As opposed to conventional resonating-wave antennas, LWAs leak out energy progressively as the wave travels along the waveguide structure. The main radiation beam of the LWA is normal to the plane of the antenna and can be in general directed by changing the electrical properties of the radiating elements.

The introduced LWA consists of 12 cascaded metamaterial CRLH unit cells which are populated with two varactor diodes in series and one in shunt configuration. The physical size of the antenna is 156 mm–38 mm. By changing the two DC bias voltages across the varactors, the antenna is able to steer the main beam from broadside to backward and forward directions. Due to the practically symmetric antenna structure, the ports of the antenna have symmetric radiation properties with respect to the broadside direction. The beam symmetry is illustrated in Figure 1 where $\theta_1 = -\theta_2$. The used LWAs are able to steer their main beam orientation approximately from -50° to $+50^\circ$. The CRLH-LWAs were adjusted to operate within the entire 2.4 GHz WiFi band. The measurements of the radiation patterns were measured at the

TABLE 1: Measured LWA main beam directions and gains.

Sector	1	2	3	4	5	6
Main beam direction θ_m ($^\circ$)	± 0	± 8	± 18	± 28	± 39	± 47
Gain G_m (dB)	5.0	5.1	5.6	5.8	4.9	3.5

TABLE 2: Selection of radiation patterns in DoA estimation cases.

Case	Main beam directions ($^\circ$)										
	-47	-39	-28	-18	-8	0	8	18	28	39	47
Case 1	x	x	x	x	x	x	x	x	x	x	x
Case 2	x		x		x		x		x		x
Case 3		x		x		x		x		x	
Case 4	x			x			x			x	
Case 5		x				x					x

frequency of 2.46 GHz in the anechoic chamber facility. The measured main beam directions and the corresponding gains are presented in Table 1.

4. Numerical and Complexity Analysis and Experimental Results of DoA Estimation Algorithms

To verify and validate the performance of the proposed DoA estimation algorithms for the LWA, we perform several simulations to numerically evaluate the performances and conduct experimental measurements, which are performed in an indoor multipath environment. We research the effect of the number of radiation patterns on the accuracy of the estimated DoAs. We particularly consider different choices of the radiation patterns for estimating the DoA. In Table 2, different radiation pattern choices are shown. The first column in this table shows cases 1 to 5 that correspond to different choices for the number of radiation patterns and their main beam directions. For each case, we estimate the DoA using only the radiation patterns which are identified by cross-marks.

4.1. Simulation Setup and Numerical Analysis. Firstly, we have studied how the selection of the radiation pattern impacts on the performance of the DoA estimation algorithms. In the simulations, we formulate the received signal according to the signal model (1). We generate orthogonal frequency-division multiplexing (OFDM) with 48 active subcarriers as the physical signal waveform. We use the same radiation patterns as in our experimental measurements. The LWA is chosen to have 6 radiation patterns with the 12 main beam directions, as shown in Table 1. In all estimation cases, 100 complex in-phase/quadrature (I/Q) samples are used to estimate the DoA. The estimations are done prior to fast Fourier transform (FFT) processing. The direction of the incoming signal is steered from -54° to 54° with a resolution of 1° . The estimation results are averaged over 1000 signal realizations for each estimated DoA.

In Figure 3, the root-mean-squared error (RMSE) of the MUSIC and APPR algorithms as a function of the SNR is

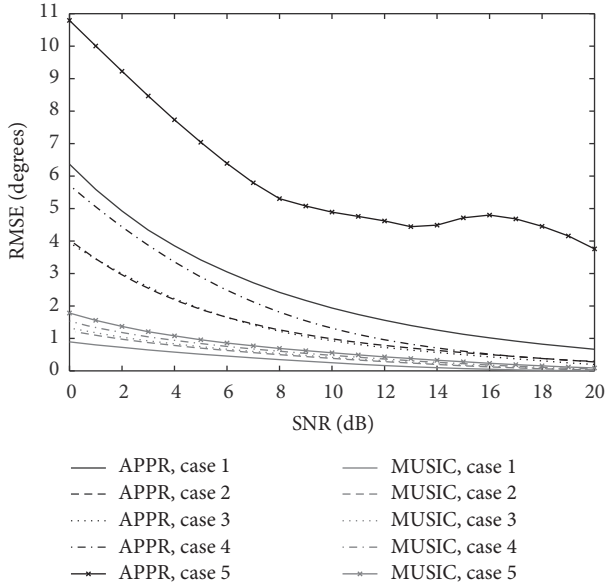


FIGURE 3: RMSE of the APPR and MUSIC algorithms as a function of the SNR.

presented. The plot shows results for cases 1–5. From Figure 3, it can be noted that the MUSIC algorithm works better than the APPR algorithm. However, if the SNR is higher than 10 dB, the RMSE difference between the algorithms in case 3 is lower than 0.5° . It can be observed that case 1 gives clearly the best result for the MUSIC algorithm. Furthermore, the MUSIC algorithm has less performance difference between different cases than the APPR algorithm. For example, if the SNR is higher than 10 dB, the differences between the different cases are less than 0.3° for the MUSIC algorithm. It can be also seen that the APPR algorithm works reasonably well in all cases, except in case 5. Cases 2-3, in turn, give the best performances in all SNR values and their RMSEs are almost the same. Moreover, we can see that the RMSE is significantly large for case 5. Additionally, case 1 works worse than cases 2–4. The reason for these observations is that the radiation patterns cover very well the estimation area in cases 2–4, especially in case 3, as seen in Figure 4. The radiation patterns are not too near to or too far from each other. However, in case 1, the radiation patterns are too near, whereas they are too far in case 5 (as also visible in Figure 5), causing higher DoA estimation errors for the APPR algorithm.

Figures 6 and 7 depict the simulated performance of the APPR and MUSIC algorithm as a function of the DoA when the SNR is fixed to 10 dB. It is visible in Figure 6 that the RMSE is the smoothest in cases 2-3. We can also notice that the configuration of the radiation pattern should be selected carefully for the APPR algorithm. If we selected five radiation patterns, as in case 3, instead of the 11 radiation patterns, as in case 1, the overall signal storing time would be halved. However, the estimation DoA range increases when using fewer radiation patterns because of the increased gap between the adjacent radiation patterns. However, we do not need to calculate the power of the signal so many times if fewer radiation patterns are selected. Furthermore, the amount of

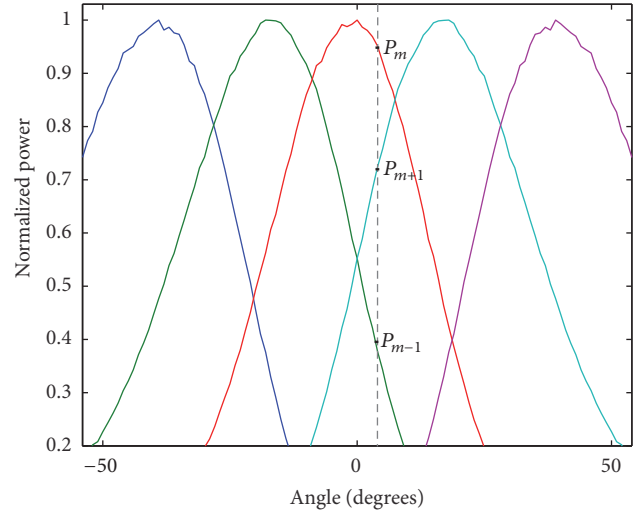


FIGURE 4: Measured radiation patterns for case 3.

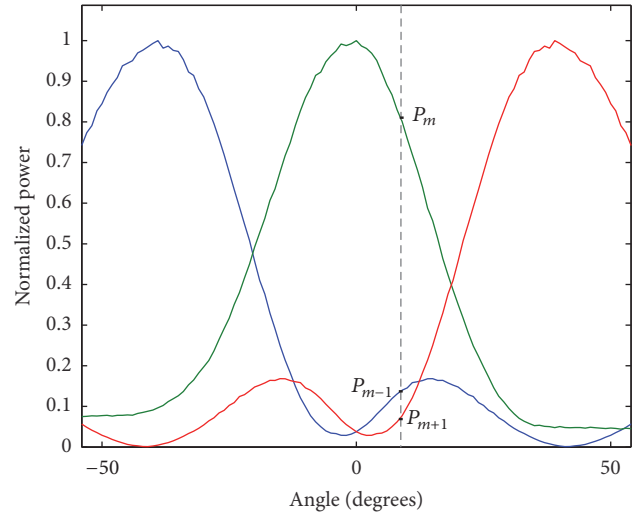


FIGURE 5: Measured radiation patterns for case 5.

data to be processed offline and online will be decreased if fewer radiation patterns are selected. Based on the results in Figure 7 for the MUSIC algorithm, we notice that the RMSE behaves similarly in all cases, and only the absolute level of the RMSE is varying in different cases. The highest number of radiation patterns provides again the best performance, as expected. From the results, we can say that the selection of the number of radiation patterns is a trade-off between the desired performance and computational complexity. In Section 4.2, computational complexity is analyzed in more detail.

4.2. Computational Complexity Analysis. In this section, we analyze the computational complexity of the single/two-port MUSIC and APPR algorithms. We define the complexity of these DoA estimation algorithms in terms of basic operations [22], that is, additions and subtractions, multiplications, and

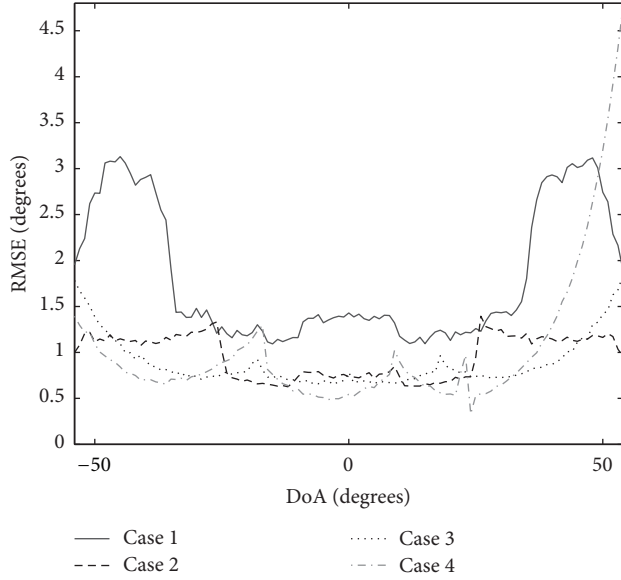


FIGURE 6: RMSE of the APPR algorithm as a function of the DoA.

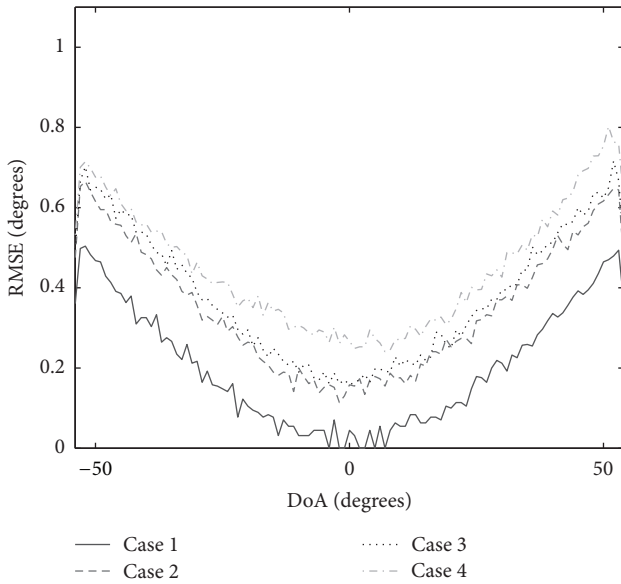


FIGURE 7: RMSE of the MUSIC algorithm as a function of the DoA.

divisions, and refer to them as ADD, MUL, and DIV, respectively. In the APPR algorithm case, part of the calculations can be calculated offline and stored into the LUT, in which case they do not need to be calculated in real time. The analysis is presented in Table 3. There, J_0 is the number of the DoA estimation points and is here equal to 109° (-54° to 54° with 1° resolution). In addition, J is the length of the specific range of θ for the APPR algorithm which depends on how the radiation pattern configuration is selected, as explained in Section 2.2. Selecting $M = 11$ results in $J = 15^\circ$, whereas for $M = 5$ we get $J = 31^\circ$. Regarding the computational complexities, the covariance matrix of the MUSIC algorithm has $N_s M^2$ multiplications and $(N_s - 1)M^2$ additions and subtractions. Additionally, the EVD has the complexity of

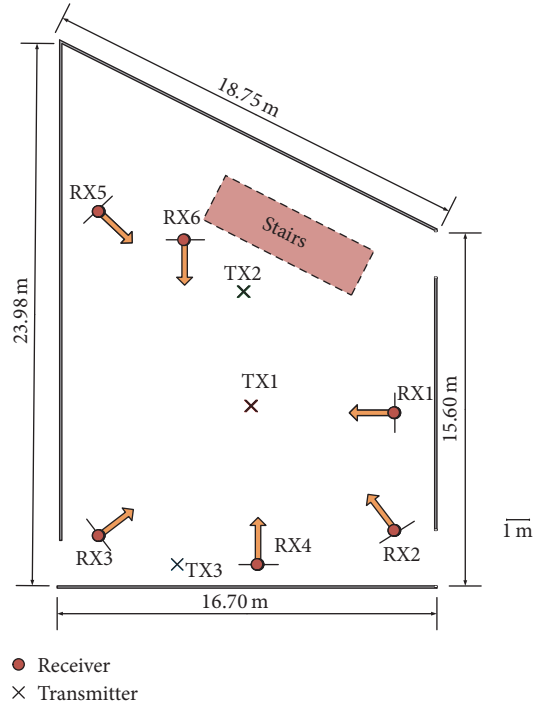


FIGURE 8: Layout of the measurement lobby area and the locations of the TXs and RXs.

TABLE 3: The computational complexity analysis.

Algorithm	MUSIC	APPR
MUL	$M^3 + M^2(N_s + 2J_0)$	$2MN_s$
DIV	J_0	2
ADD	$M^2(N_s - 1 + 2J_0) - 2J_0M$	$J + M(N_s - 1)$
LUT	—	$(MJ_0)\text{MUL}$ $(2MJ + MJ_0)\text{DIV}$

M^3 and the calculations of the MUSIC spectra need $J_0 2M^2$ multiplications, J_0 divisions, and $J_0(2M^2 - 2M)$ additions and subtractions. The APPR algorithm, in turn, needs $2MN_s$ multiplications, 2 divisions, and $J + M(N_s - 1)$ additions and subtractions. In addition, we need MJ_0 multiplications and $2MJ + MJ_0$ divisions that are calculated offline and stored into a LUT. It is clear that the APPR algorithm has much lower computational complexity than the MUSIC algorithm.

4.3. Measurement Setup. The performance of the LWA-based APPR and MUSIC DoA estimation algorithms is evaluated using experimental measurements performed in a multipath indoor environment. The experiments are done in the premises of the Drexel University. The indoor setup is a closed large lobby with stairs and glass walls. In this lobby setting, the measured signals experience both LoS and NLoS components due to severe multipath between the transmitters (TXs) and the receivers (RXs). The layout, illustrated in Figure 8, shows the arrangement of TXs and RXs in the described indoor environment. In our measurements, we used three TX nodes and six RX nodes.

In the RX nodes, the reconfigurable two-port CRLH-LWAs were used and the three TX nodes were equipped with two standard omnidirectional antennas. The lobby dimensions and the locations of the transceiver antennas are carefully measured with a measuring tape. In Figure 8, the orange arrows show the broadside direction $\theta = 0^\circ$ of the RX LWAs. We made measurements in such a way that only one TX-RX pair was active at a time. Thus, we needed to ensure a justness between different transmission links by transmitting the same data over all links. We measured all the TX-RX pairs but the data with TX3 were studied only for RX1–RX3 and RX5–RX6 because the TX3–RX4 pair was out of the spatial scanning directions.

In our measurement campaign, each transceiver uses a field-programmable gate array (FPGA) based software defined radio platform which is called wireless open-access research platform (WARP) v3 [23]. Each WARP board was connected to its own antenna and to a centralized controlling system which centrally synchronize all the nodes, control antenna beam directions, and collect all the measurement data. We used OFDM signals with the total of 64 subcarriers where 48 subcarriers were used for loading data symbols, 4 for carrier frequency offset (CFO) correction, and 12 empty subcarriers. After each transmission, all the RXs stored 300 packets, each containing 5420 binary phase shift keying (BPSK) complex symbols and then the antenna beam direction was steered for the next reception. The TX power of the TX nodes was set to 15 dBm. Additionally, we used $d = 1.3$ cm and $\alpha = 1$ in the measurement processing for the MUSIC algorithm. Furthermore, we assume that only one signal is received in the RX, and thus we set $L = 1$.

All the measured data were saved for offline postprocessing with the DoA estimation algorithms introduced in Section 2. The DoA estimation was done before the FFT. Furthermore, the measurements were carried out in the WiFi frequency range of 2.452 GHz–2.472 GHz as the leaky-wave antennas (LWAs) were calibrated for this range. Since the measurements were carried out at open WiFi frequencies with various WiFi access points in the close vicinity, all WiFi traffic acts directly as cochannel interference making the measurement environment very challenging. Additionally, this WiFi traffic and passersby are not stationary during the measurements.

4.4. Experimental Results Based on Measurements. The aim of our experiment measurement is to demonstrate the DoA estimation capabilities for LWAs using the algorithms which were introduced in Section 2. Based on the simulation results with the AWGN channel, cases 2–3 give the best RMSE results for the APPR algorithm and case 1 gives the best results for the MUSIC algorithm, and thus we analyzed these three cases also in a real multipath environment. Here, we present also the results of the power detector (PD) algorithm, as a reference because the APPR algorithm is based on these PD results. The summary of the results for the APPR, MUSIC algorithms, and PD is presented in Tables 4–12. DoA estimation results for TX1–RX6, TX3–RX6, and TX2–RX6 pairs are

TABLE 4: DoA estimation results for TX1 with PD, APPR, and MUSIC algorithms in case 1.

$\theta_{\text{real}} (^{\circ})$	PD		APPR		MUSIC	
	$\hat{\theta} (^{\circ})$	$\epsilon (^{\circ})$	$\hat{\theta} (^{\circ})$	$\epsilon (^{\circ})$	$\hat{\theta} (^{\circ})$	$\epsilon (^{\circ})$
RX1: -3	8	11	12	15	25	28
RX2: 12	-18	-30	-21	-33	-16	-28
RX3: 3	8	5	8	5	0	-3
RX4: 2	-8	10	-13	-15	0	-4
RX5: -9	-28	-19	-33	-24	1	10
RX6: 22	28	6	22	0	28	6
RMSE		16.0		18.9		16.8

TABLE 5: DoA estimation results for TX2 with PD, APPR, and MUSIC algorithms in case 1.

$\theta_{\text{real}} (^{\circ})$	PD		APPR		MUSIC	
	$\hat{\theta} (^{\circ})$	$\epsilon (^{\circ})$	$\hat{\theta} (^{\circ})$	$\epsilon (^{\circ})$	$\hat{\theta} (^{\circ})$	$\epsilon (^{\circ})$
RX1: -39	-47	-8	-41	-2	-54	-15
RX2: -5	-28	-23	-24	-19	-1	-4
RX3: 22	0	-22	4	-18	18	-4
RX4: 3	8	5	6	3	0	-3
RX5: 14	8	-6	8	-6	1	-13
RX6: 49	39	-10	39	-10	54	5
RMSE		14.4		11.8		8.7

TABLE 6: DoA estimation results for TX3 with PD, APPR, and MUSIC algorithms in case 1.

$\theta_{\text{real}} (^{\circ})$	PD		APPR		MUSIC	
	$\hat{\theta} (^{\circ})$	$\epsilon (^{\circ})$	$\hat{\theta} (^{\circ})$	$\epsilon (^{\circ})$	$\hat{\theta} (^{\circ})$	$\epsilon (^{\circ})$
RX1: 35	47	12	42	7	48	13
RX2: 62	47	-15	41	-21	54	-8
RX3: -57	-47	10	-47	10	-54	3
RX5: -34	-47	-13	-44	-10	-54	-20
RX6: -1	-28	-27	-32	-31	-17	-16
RMSE		16.5		18.1		13.4

also illustrated in Figures 9–11 for three considered cases. In the figures, the first column (a) illustrates a measurement case when all methods estimate very well the DoA of the received signal. The second column (b) presents a measurement when the APPR algorithm and PD fail to estimate the DoA. The last column (c) illustrates the measurement case when the APPR algorithm estimates very well the DoA while the MUSIC algorithm fails the DoA estimation.

4.4.1. Case 1. Based on the results of Tables 4–6, the total RMSE, calculated over all TX cases, is 13.9° for the PD, 9.8° for the APPR algorithm, and 13.6° for the MUSIC algorithm in case 1. If the DoA estimation error is large in the PD case, the APPR algorithm cannot estimate the DoA accurately, as illustrated in Figure 9(b). It can be noticed that the APPR has the best performance if we compare overall results. As we explained earlier in Section 2.1, the MUSIC algorithm works well only for uncorrelated signals. In our experimental

TABLE 7: DoA estimation results for TX1 with PD, APPR, and MUSIC algorithms in case 2.

$\theta_{\text{real}} (^{\circ})$	PD		APPR		MUSIC	
	$\hat{\theta} (^{\circ})$	$\epsilon (^{\circ})$	$\hat{\theta} (^{\circ})$	$\epsilon (^{\circ})$	$\hat{\theta} (^{\circ})$	$\epsilon (^{\circ})$
RX1: -3	8	11	1	4	19	22
RX2: 12	-28	-40	-18	-30	-4	-16
RX3: 3	8	5	1	-2	0	-3
RX4: 2	-8	10	-17	-19	-1	-3
RX5: -9	-28	-19	-19	10	1	10
RX6: 22	28	6	22	0	38	16
RMSE		19.3		15.2		13.6

TABLE 8: DoA estimation results for TX2 with PD, APPR, and MUSIC algorithms in case 2.

$\theta_{\text{real}} (^{\circ})$	PD		APPR		MUSIC	
	$\hat{\theta} (^{\circ})$	$\epsilon (^{\circ})$	$\hat{\theta} (^{\circ})$	$\epsilon (^{\circ})$	$\hat{\theta} (^{\circ})$	$\epsilon (^{\circ})$
RX1: -39	-47	-8	-39	0	-54	-15
RX2: -5	-28	-23	-21	-16	13	18
RX3: 22	28	6	35	13	36	14
RX4: 3	8	5	3	0	0	-3
RX5: 14	8	-6	17	3	1	-13
RX6: 49	47	-2	37	-12	37	-12
RMSE		10.8		9.8		13.3

TABLE 9: DoA estimation results for TX3 with PD, APPR, and MUSIC algorithms in case 2.

$\theta_{\text{real}} (^{\circ})$	PD		APPR		MUSIC	
	$\hat{\theta} (^{\circ})$	$\epsilon (^{\circ})$	$\hat{\theta} (^{\circ})$	$\epsilon (^{\circ})$	$\hat{\theta} (^{\circ})$	$\epsilon (^{\circ})$
RX1: 35	47	12	40	5	54	19
RX2: 62	47	-15	38	-24	54	-8
RX3: -57	-47	10	-46	11	-54	3
RX5: -34	-47	-13	-42	-8	-54	-20
RX6: -1	-28	-27	-33	-32	-23	-22
RMSE		16.5		19.0		16.2

TABLE 10: DoA estimation results for TX1 with PD, APPR, and MUSIC algorithms in case 3.

$\theta_{\text{real}} (^{\circ})$	PD		APPR		MUSIC	
	$\hat{\theta} (^{\circ})$	$\epsilon (^{\circ})$	$\hat{\theta} (^{\circ})$	$\epsilon (^{\circ})$	$\hat{\theta} (^{\circ})$	$\epsilon (^{\circ})$
RX1: -3	-18	-15	-8	-5	-4	1
RX2: 12	-18	-30	-26	38	-13	-25
RX3: 3	0	-3	8	5	32	29
RX4: 2	-18	10	-9	-11	-2	-4
RX5: -9	-39	-30	-28	-19	-19	-10
RX6: 22	18	-4	26	4	17	-5
RMSE		20.2		18.2		16.4

measurements, the measured signals experience both LoS and NLoS components due to severe multipath between the TX and the RX in the indoor environment. Multipath signals are mutually correlated, and the signal covariance becomes rank-deficient [21]. Consequently, the eigenvalue

TABLE 11: DoA estimation results for TX2 with PD, APPR, and MUSIC algorithms in case 3.

$\theta_{\text{real}} (^{\circ})$	PD		APPR		MUSIC	
	$\hat{\theta} (^{\circ})$	$\epsilon (^{\circ})$	$\hat{\theta} (^{\circ})$	$\epsilon (^{\circ})$	$\hat{\theta} (^{\circ})$	$\epsilon (^{\circ})$
RX1: -39	-39	0	-32	7	-54	-15
RX2: -5	-18	-13	-26	-21	-3	2
RX3: 22	0	-22	6	16	-15	-37
RX4: 3	-18	21	-11	-14	-1	-4
RX5: 14	0	-14	9	-5	6	-8
RX6: 49	39	-10	32	-17	54	5
RMSE		15.2		14.5		16.8

TABLE 12: DoA estimation results for TX3 with PD, APPR, and MUSIC algorithms in case 3.

$\theta_{\text{real}} (^{\circ})$	PD		APPR		MUSIC	
	$\hat{\theta} (^{\circ})$	$\epsilon (^{\circ})$	$\hat{\theta} (^{\circ})$	$\epsilon (^{\circ})$	$\hat{\theta} (^{\circ})$	$\epsilon (^{\circ})$
RX1: 35	39	4	35	0	54	19
RX2: 62	39	-23	29	33	54	-8
RX3: -57	-39	18	-42	15	54	111
RX5: -34	-39	-5	-34	-34	-54	-20
RX6: -1	-39	-38	-29	-28	-6	-5
RMSE		21.6		20.5		51.3

decomposition of the signal covariance fails to split the signal and noise subspaces. That is the reason why the results of the MUSIC algorithms are so much poorer in indoor environments than in the AWGN channel environment. What is also interesting is that we can notice multiple peaks in the PD plots in Figures 9(b) and 9(c) and the power of the signal is noticeably lower than in Figure 9(a). The peaks are most likely affected by the multipath effects like reflections from the walls and stairs, passersby, or WiFi traffic acting directly as cochannel interference in these measurements. For the PD, it is clear that multipath or other signals result in additional peaks in the figures. In cases where the PD estimator has no high peaks in the results or there are two or more low peaks or the received signal power level is low, the MUSIC algorithm has difficulties in estimating the DoA. This somewhat flat response is, again, most probably affected by a weak LoS component as well as rich scattering environment causing multiple impinging NLoS signal paths.

There are large differences in the DoA estimation accuracy in different receiver locations. The estimated DoAs are in good agreement with the real DoAs in the several APPR algorithm cases, particularly in TX1-RX3, TX1-RX6, TX2-RX1, and TX2-RX4 cases. The MUSIC algorithm has also good accuracy in these TX-RX pairs, except the TX2-RX1 case. This is clearly the worst result for the MUSIC algorithm, as seen in Figure 9(c), and is most probably affected by harmful reflections from the stairs which are made of metal, concrete, and glass.

4.4.2. *Case 2.* Based on the results of Tables 7–9, the total RMSE, calculated over all TX cases, is 15.0° for the PD, 10.2° for the APPR algorithm, and 14.8° for the MUSIC algorithm

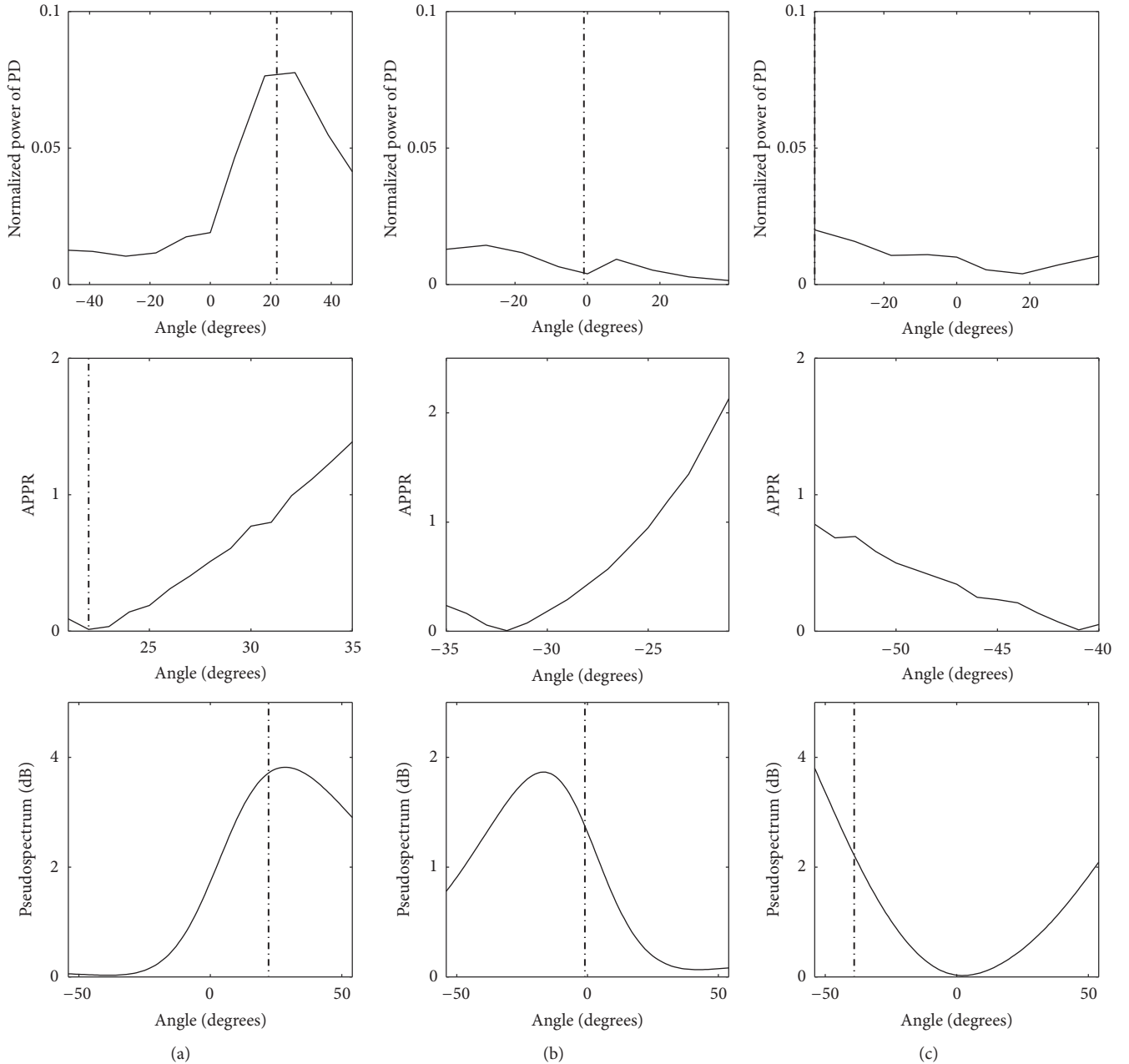


FIGURE 9: DoA estimation results with PD, APPR, and MUSIC algorithms in case 2 with different TX-RX pairs: (a) TX1-RX6 $\theta_{\text{real}} = 22^\circ$, (b) TX3-RX6 $\theta_{\text{real}} = -1^\circ$, and (c) TX2-RX1 $\theta_{text{real}} = -39^\circ$.

in case 2. It can be seen that there is not a significant performance difference between case 1 and case 2. From the tables, we can notice again that the estimation error is rather small, smaller than 11° in many TX-RX pairs in several cases. However, there are also many larger DoA estimation errors which are most likely caused by severe reflections and other multipath effects, as explained earlier and illustrated in Figure 10(b).

4.4.3. Case 3. Based on the results of Tables 10–12, the total RMSE, calculated over all TX cases, is 14.1° for the PD, 11.2° for the APPR algorithm, and 32.1° for the MUSIC

algorithm in case 3. It can be noticed that the difference of the performance is not big between cases 1–3 for the APPR algorithm. In particular, the difference of the RMSE is only 1.4° between case 1 and case 3. The results show that we can achieve almost the same performance using fewer radiation patterns; thus the overall signal storing time will be decreased. However, the adjacent radiation patterns cannot be too far away from each other, as seen in Section 4.1. Regarding the MUSIC algorithm, the RMSEs are significantly higher in case 3 when compared with cases 1–2. We can conclude that the MUSIC algorithm does not work very well if the number of radiation patterns is only five in our

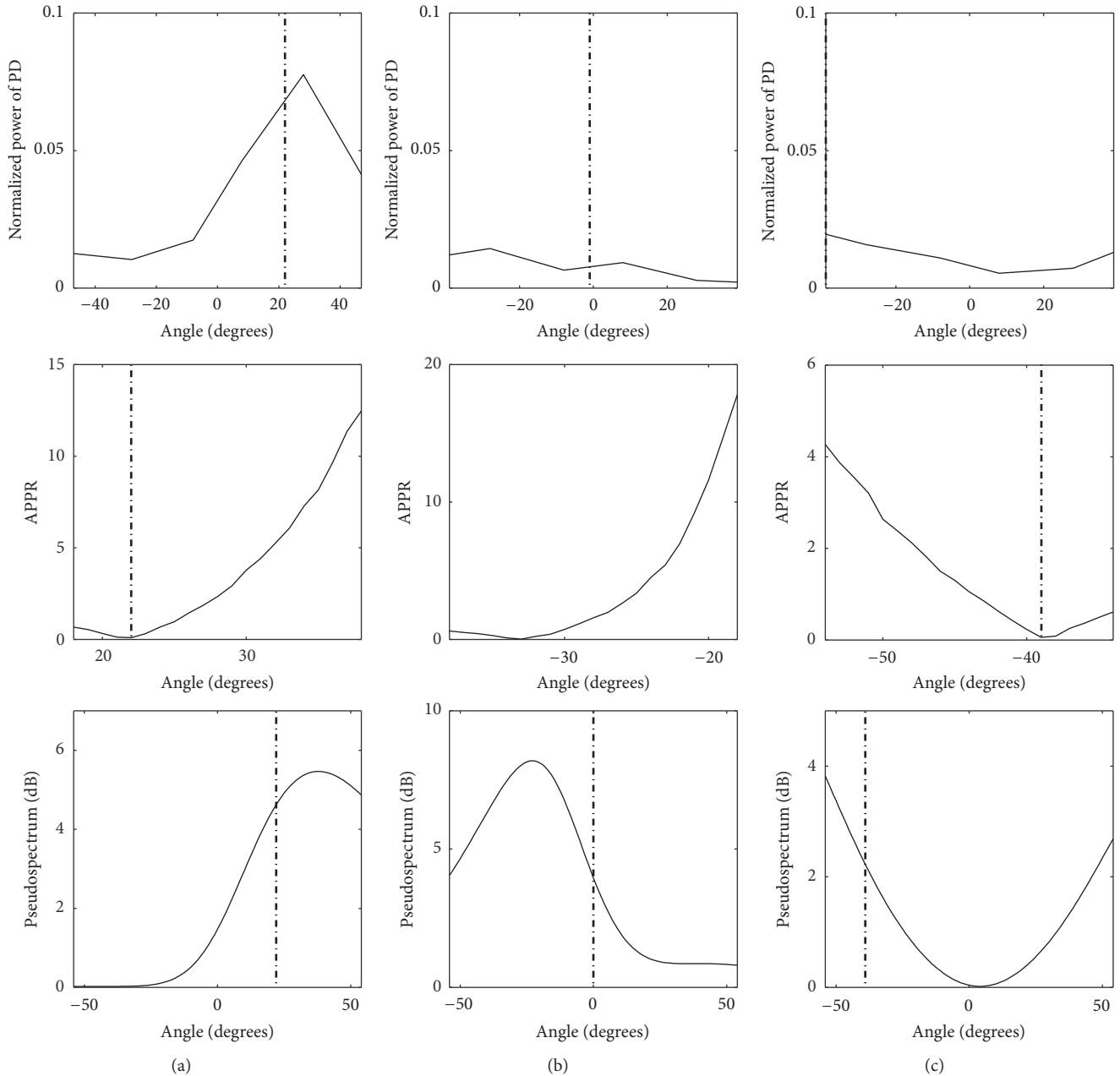


FIGURE 10: DoA estimation results with PD, APPR, and MUSIC algorithms in case 2 with different TX-RX pairs: (a) TX1-RX6 $\theta_{\text{real}} = 22^\circ$, (b) TX3-RX6 $\theta_{\text{real}} = -1^\circ$, and (c) TX2-RX1 $\theta_{\text{real}} = -39^\circ$.

real world measurements. We can also notice that the total RMSE difference between case 1 and case 2 is only 1.2° for the MUSIC algorithm. If fewer radiation patterns are selected, the complexity of the MUSIC algorithm will be reduced significantly, as explained in Section 4.2. To conclude, the selection of the number of radiation patterns is a trade-off between the desired performance and computational complexity.

4.4.4. Discussion of the Experimental Results. Based on our observations from the experimental results, it seems

that the APPR algorithm works better in a real multipath environment than the MUSIC algorithm. In our measurements, the measured signals experience both LoS and NLoS components due to severe multipath between the TX and the RX in the indoor environment. Due to the correlated multipath signals, the eigenvalue decomposition of the signal covariance cannot split the signal and noise subspaces; thus the RMSE increases significantly when compared with the AWGN channel simulations. In case 1, the total RMSE is 3.8° less with the APPR algorithm than with the MUSIC algorithm. It can be concluded that the performance gap

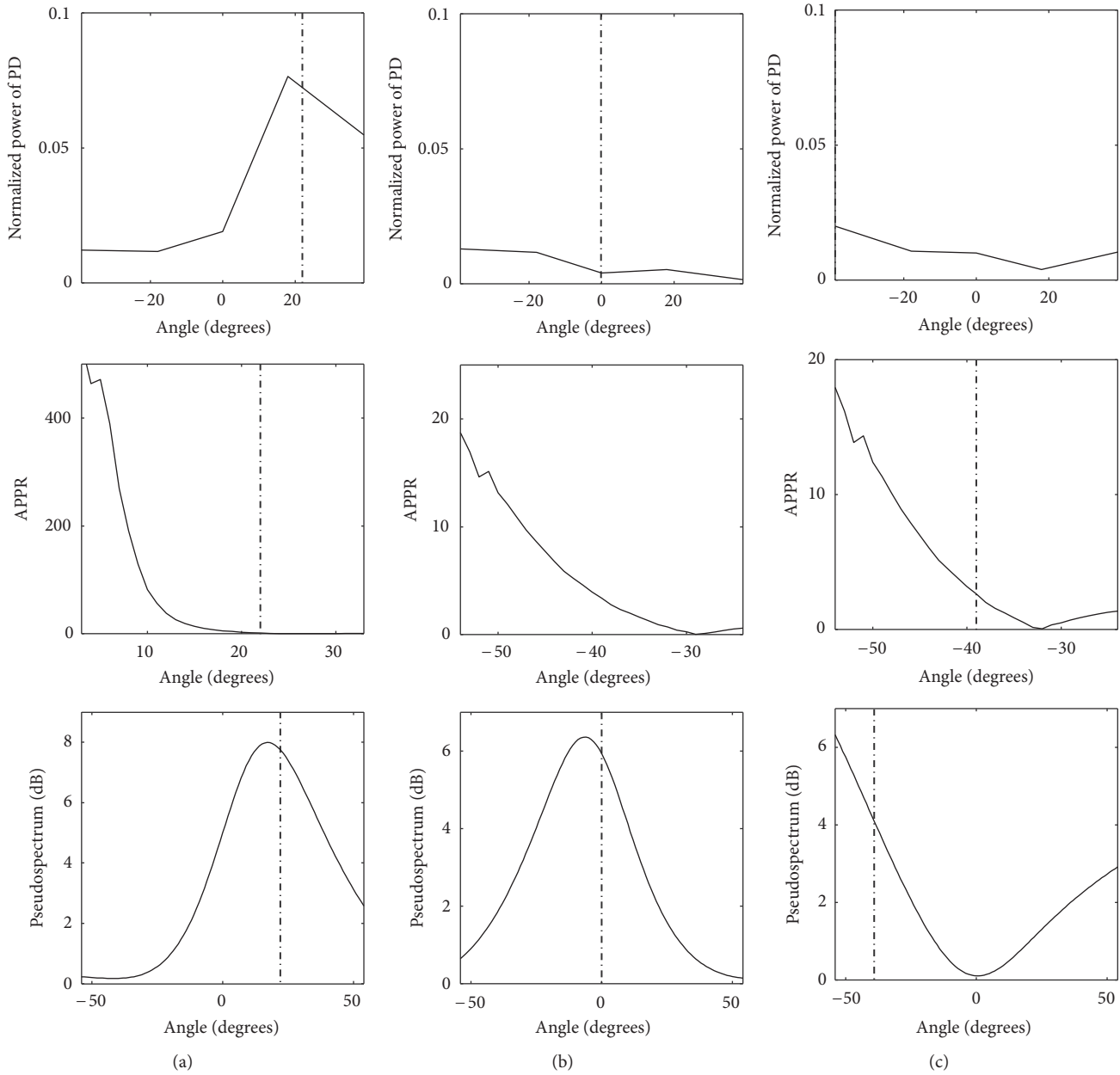


FIGURE 11: DoA estimation results with PD, APPR, and MUSIC algorithms in case 3 with different TX-RX pairs: (a) TX1-RX6 $\theta_{\text{real}} = 22^\circ$, (b) TX3-RX6 $\theta_{\text{real}} = -1^\circ$, and (c) TX2-RX1 $\theta_{\text{real}} = -39^\circ$.

between these two algorithms increases when the number of radiation patterns is decreased.

The resolution of both the algorithms is the same, that is, 1° . However, the computational complexity of the algorithms is significantly different, as explained in Section 4.2. The APPR algorithm has clearly lower computational complexity than MUSIC algorithm because the algorithm does not use eigenvalue decomposition. We can conclude that both algorithms, especially the APPR algorithm, and the considered LWA structure enable reliable DoA estimation, despite very challenging demonstration and measurement environment.

In our measurement, we have assumed, particularly in the MUSIC algorithm case, that only one signal is received in each receiver. We have noticed that there are multiple peaks in the PD plots. It is clear that multipath or other signals result in additional peaks in the figures. These interference signals are one reason why the performance of the MUSIC algorithm is much poorer than in AWGN simulations. In general, signals are better resolvable if the bandwidth is increased (e.g., using impulse radio [24]) and if the beamwidth of the antenna is decreased. In literature, Akaike information criterion (AIC) [25] is presented and the minimum description length (MDL) [26] algorithms estimate the number of the incident signals.

However, it is shown that these algorithms can estimate a wrong number of components for a small sample size and a low SNR [27]. In future work, we will study how we could resolve the received signals, that is, multipath and interference signals, and estimate the number of the received signals reliably so that the DoA estimation algorithms can work in a more robust way.

5. Conclusion

In this paper, we considered DoA estimation with a certain type of reconfigurable antennas, namely, CRLH-LWAs. We started by presenting the APPR algorithm for two-port LWAs. Thereafter, we evaluated the performance of the APPR solution by numerical simulations in an AWGN channel and with varying numbers of selected radiation patterns. The results were also compared with those of the LWA-based MUSIC algorithm. We continued by evaluating the DoA estimation performance of both methods in an indoor environment based on real world measurements involving typical multipath propagation with both line-of-sight and non-line-of-sight components. Not only the results of numerical simulations but also the measurement-based results showed that the DoA estimates were in a good agreement with the real DoAs, especially with the APPR method, indicating that CRLH-LWAs are capable of successful DoA estimation while having often a smaller form factor than conventional antenna arrays with multiple antenna elements. To conclude, the combination of the proposed DoA estimation algorithms and the CRLH-LWA implementation can provide a valuable solution for future generation wireless communications systems where spectrum reuse, interference avoidance, and device localization are of special interest.

Conflicts of Interest

The authors declare that they have no conflicts of interest.

Acknowledgments

This work has been performed in the framework of the Reconfigurable Antenna Based Enhancement of Dynamic Spectrum Access Algorithms (READS) and Future Small-Cell Networks using Reconfigurable Antennas (FUNERA) projects which were funded by VTT Technical Research Center of Finland and the Finnish Funding Agency for Technology and Innovation (Tekes). The authors would like to thank Adant S.r.l. for the antenna prototypes. The measurements have been carried out at the Drexel University. This work was also supported by CNS-1147838 from the U.S. National Science Foundation as part of the Wireless Innovation between Finland and United States (WiFiUS) partnership.

References

- [1] J. D. Kraus and R. J. Marhefka, *Antennas for All Applications*, McGraw-Hill, Boston, MA, USA, 3rd edition, 2001.
- [2] C. A. Balanis, *Antenna Theory: Analysis and Design*, John Wiley Sons, Hoboken, NJ, 3rd edition, 2005.
- [3] T. Ohira and K. Gyoda, "Electronically steerable passive array radiator antennas for low-cost analog adaptive beamforming," in *Proceedings of the 2000 IEEE International Conference on Phased Array Systems and Technology*, pp. 101–104, May 2011.
- [4] J. R. De Luis and F. De Flaviis, "A reconfigurable dual frequency switched beam antenna array and phase shifter using PIN diodes," in *Proceedings of the 2009 IEEE International Symposium on Antennas and Propagation and USNC/URSI National Radio Science Meeting, APSURSI 2009*, June 2009.
- [5] C. Caloz and T. Itoh, *Electromagnetic Metamaterials Transmission Line Theory and Microwave Applications*, John Wiley Sons, Hoboken, NJ, 2006.
- [6] R. Schmidt, "Multiple emitter location and signal parameter estimation," in *Proceedings of the RADAR Spectrum Estimation Workshop*, pp. 243–258, 1979.
- [7] K.-C. Huarng and C.-C. Yeh, "A Unitary Transformation Method for Angle-of-Arrival Estimation," *IEEE Transactions on Signal Processing*, vol. 39, no. 4, pp. 975–977, 1991.
- [8] M. D. Zoltowski, G. M. Kautz, and S. D. Silverstein, "Beamspace root-MUSIC," *IEEE Transactions on Signal Processing*, vol. 41, no. 1, pp. 344–364, 1993.
- [9] M. Haardt and J. A. Nosssek, "Unitary ESPRIT: how to obtain increased estimation accuracy with a reduced computational burden," *IEEE Transactions on Signal Processing*, vol. 43, no. 5, pp. 1232–1242, 1995.
- [10] R. Roy, *ESPRIT: Estimation of Signal Parameters via Rotational Invariance Techniques [Phd. Dissertation]*, Stanford University, Stanford, CA, USA.
- [11] S. Sugiura, "A review of recent patents on reactance-loaded reconfigurable antennas," *Recent Patents on Electrical Engineering*, vol. 2, no. 3, pp. 200–206, 2009.
- [12] H. Paaso, A. Mammela, D. Patron, and K. R. Dandekar, "Modified MUSIC algorithm for doa estimation using CRLH leaky-wave antennas," in *Proceedings of the 2013 8th International Conference on Cognitive Radio Oriented Wireless Networks and Communications, CROWNCOM 2013*, pp. 166–171, usa, July 2013.
- [13] D. Patron, H. Paaso, A. Mammela, D. Piazza, and K. R. Dandekar, "Improved design of a CRLH leaky-wave antenna and its application for DoA estimation," in *Proceedings of the 2013 3rd IEEE-APS Topical Conference on Antennas and Propagation in Wireless Communications, IEEE APWC 2013*, pp. 1343–1346, September 2013.
- [14] H. Paaso, N. Gulati, D. Patron et al., "DoA estimation using compact CRLH leaky-wave antennas: novel algorithms and measured performance," *IEEE Transactions on Antennas*, In press.
- [15] V. Vakilian, J.-F. Frigon, and S. Roy, "Direction-of-arrival estimation in a clustered channel model," in *Proceedings of the 2012 IEEE 10th International New Circuits and Systems Conference, NEWCAS 2012*, pp. 313–316, can, June 2012.
- [16] V. Vakilian, H. V. Nguyen, S. Abielmona, S. Roy, and J.-F. Frigon, "Experimental study of direction-of-arrival estimation using reconfigurable antennas," in *Proceedings of the 2014 IEEE 27th Canadian Conference on Electrical and Computer Engineering, CCECE 2014*, can, May 2014.
- [17] C. Plapous, J. Cheng, E. Taillefer, A. Hirata, and T. Ohira, "Reactance domain MUSIC algorithm for ESPAR antennas," in *Proceedings of the 33rd European Microwave Conference, EuMC 2003*, pp. 793–796, deu, October 2003.

- [18] S. Akkar and A. Gharsallah, "Reactance domains unitary MUSIC algorithms based on real-valued orthogonal decomposition for electronically steerable parasitic array radiator antennas," *IET Microwaves, Antennas and Propagation*, vol. 6, no. 2, pp. 223–230, 2012.
- [19] Y. Ozaki, J. Ozawa, E. Taillefer, J. Cheng, and Y. Watanabe, "A simple DoA estimator using adjacent pattern power ratio with switched beam antenna," *Progress In Electromagnetics Research C*, vol. 22, pp. 55–71, 2011.
- [20] M. Wax, *Detection and estimation superimposed signals [Ph.D. thesis]*, Stanford University, Stanford, 1985.
- [21] Z. Chen, *Introduction to Direction-of-Arrival Estimation*, Artech House Books, Norwood, MA, USA, 2010.
- [22] P. Pirsch, *Architectures for Digital Signal Processing*, Artech House Books, John Wiley & Sons, Chichester, UK, 1996.
- [23] "Mango communications WARP v3 kit," <http://mangocomm.com/products/kits/warp-v3-kit>.
- [24] S. Gezici, Z. Tian, G. B. Giannakis et al., "Localization via ultra-wideband radios: a look at positioning aspects of future sensor networks," *IEEE Signal Processing Magazine*, vol. 22, no. 4, pp. 70–84, 2005.
- [25] H. Akaike, "A new look at the statistical model identification," *IEEE Transactions on Automatic Control*, vol. 19, no. 6, pp. 716–723, 1974.
- [26] M. Wax and T. Kailath, "Detection of signals by information theoretic criteria," *Institute of Electrical and Electronics Engineers. Transactions on Acoustics, Speech, and Signal Processing*, vol. 33, no. 2, pp. 387–392, 1985.
- [27] P. M. Djuric, "A model selection rule for sinusoids in white gaussian noise," *IEEE Transactions on Signal Processing*, vol. 44, no. 7, pp. 1744–1751, 1996.

Research Article

Robust Cyclic MUSIC Algorithm for Finding Directions in Impulsive Noise Environment

Sen Li, Xiaojing Chen, and Rongxi He

College of Information and Science Technology, Dalian Maritime University, Dalian 116026, China

Correspondence should be addressed to Rongxi He; hxr@dmlu.edu.cn

Received 5 November 2016; Revised 2 March 2017; Accepted 5 March 2017; Published 13 April 2017

Academic Editor: Youssef Nasser

Copyright © 2017 Sen Li et al. This is an open access article distributed under the Creative Commons Attribution License, which permits unrestricted use, distribution, and reproduction in any medium, provided the original work is properly cited.

This paper addresses the issue of direction finding of a cyclostationary signal under impulsive noise environments modeled by α -stable distribution. Since α -stable distribution does not have finite second-order statistics, the conventional cyclic correlation-based signal-selective direction finding algorithms do not work effectively. To resolve this problem, we define two robust cyclic correlation functions which are derived from robust statistics property of the correntropy and the nonlinear transformation, respectively. The MUSIC algorithm with the robust cyclic correlation matrix of the received signals of arrays is then used to estimate the direction of cyclostationary signal in the presence of impulsive noise. The computer simulation results demonstrate that the two proposed robust cyclic correlation-based algorithms outperform the conventional cyclic correlation and the fractional lower order cyclic correlation based methods.

1. Introduction

Arrays of sensors such as radio antennas can be used to detect the presence of propagating signals and estimate their directions of arrival (DOA) and other parameters. Their applications have been found in many areas, for example, radar, sonar, biomedical signal processing, and communication systems [1, 2]. Conventional array processing methods generally exploit spatial properties of the signals impinging on an array of sensors. In applications for radar, sonar, or telecommunications there are many man-made signals whose cyclostationary properties can be used to cancel interference and background noise [3]. The earliest approach was proposed by Gardner [4] who introduced the concept of cyclostationarity into array signal processing to suppress interference and noise. Including this property in signal processing algorithm design can improve the performance of existing algorithms, especially the DOA estimation algorithms. Several algorithms have been proposed in the literature along this line [5–7]. Instead of using the correlation matrix as being done in conventional methods, these cyclostationarity-based algorithms require estimating the cyclic correlation (CCO) matrix to reflect the cyclostationarity of incoming signals which can be one of the following

three cases: (1) having baud rates or (2) being modulated by a carrier signal in the way that they are used in radar and radio communication applications or (3) both.

One common assumption made by conventional methods and cyclostationarity methods is that the ambient noise is assumed to be Gaussian distributed and can be characterized by only second-order statistics (SOS). However, in many real world applications the noise often exhibits non-Gaussian properties and sometimes is accompanied by strong impulsiveness [8]. For example, natural sources such as atmospheric noise resulting from thunder storms, car ignitions, microwave ovens, and other types of man-made signal sources generally result in aggregating noises that may produce high amplitudes during small time intervals. To address this type of noise the α -stable distribution was proposed as a better and suitable noise model [9]. It has been also shown to have potential in characterizing various impulsive noises via selecting different values of the parameter α .

Since α -stable distribution has no finite SOS, the SOS-based estimation of signal parameters, such as DOA, is generally not applicable. Therefore, to address this issue the fractional lower order statistics (FLOS) was recently proposed [10, 11] such as the fractional lower order moments (FLOM) [11] and the phased fractional lower order moments

(PFLOM) [10, 11]. However, FLOS requires a priori knowledge of α -stable distribution, which is difficult to estimate in some practical applications. In order to measure similarity between two random variables, correntropy has been proposed and successfully applied in α -stable signal processing [12]. By virtue of correntropy, [13, 14] defined a robust correlation criterion, the correntropy-based correlation (CECO) to estimate DOA by MUSIC, which can be called CECO-MUSIC algorithm. Recently, [15] also defined a robust correlation, called nonlinear transform correlation (NTCO), by introducing a nonlinear compression function into correlation. This paper developed a novel algorithm for DOA estimation in impulsive noise, to be called NTCO-MUSIC which uses the NTCO matrix to replace the correlation matrix of the common used by MUSIC algorithm.

To further handle the cyclostationary signals under α -stable impulsive noise environment, You et al. defined the fractional lower order cyclic correlation (FLOCC) [16, 17] and the phased fractional lower order cyclic correlation (PFLOCC) [18] for the DOA estimation. Liu et al. also defined the fractional lower order cyclic cross-ambiguity function [19] for joint estimation of time difference of arrival and frequency difference of arrival for cyclostationary signals under α -stable impulsive noise.

In this paper, we introduce two robust cyclic statistics based on CECO and NTCO for cyclostationary signal, called the correntropy-based cyclic correlation (CECCO) and nonlinear transform based cyclic correlation (NTCCO), both of which can be implemented in conjunction with the MUSIC algorithm for DOA estimation of cyclostationary signals under α -stable impulsive noise environment. Specifically, the MUSIC algorithm uses CECCO or NTCCO matrix of signals received from the array which are called CECCO-MUSIC and NTCCO-MUSIC algorithms. To demonstrate the performance of the proposed two methods to the FLOCC-based MUSIC algorithm (FLOCC-MUSIC) and cyclic correlation-based MUSIC algorithm (CCO-MUSIC), computer simulation experiments are conducted for comparative study and analysis.

2. α -Stable Distribution Specified Noise Model

This section describes a noise model specified by α -stable distribution with its characteristic function specified by

$$\phi(t) = e^{\{jat - \gamma|t|^\alpha [1 + j\beta \operatorname{sgn}(t)\omega(t, \alpha)]\}}, \quad (1)$$

where γ and a are the dispersion and location parameters, respectively, and $\omega(t, \alpha)$ is defined by

$$\omega(t, a) = \begin{cases} \tan \frac{\pi\alpha}{2}, & \text{if } \alpha \neq 1 \\ \frac{2}{\pi} \log |t|, & \text{if } \alpha = 1 \end{cases} \quad (2)$$

and the sign function, $\operatorname{sgn}(t)$, is given as

$$\operatorname{sgn}(t) = \begin{cases} \frac{t}{|t|}, & \text{if } t \neq 0 \\ 0, & \text{if } t = 0. \end{cases} \quad (3)$$

In particular, α ($0 < \alpha \leq 2$) is the characteristic exponent that measures the thickness of the tails of the distribution where the smaller α is, the thicker its tails are. Also, β is the symmetry parameter, if $\beta = 0$, the distribution in which case the observation is referred to as the symmetry α -stable (S α S) distribution. When $\alpha = 2$ and $\beta = 0$, the α -stable distribution becomes a Gaussian distribution. An important difference between the Gaussian and the α -stable distribution is that the former has only first two moments while the latter does not have any statistics when the moments of order are greater than or equal to α .

3. Problem Formulation and CCO-Based Method

3.1. Problem Definition. Suppose that there is a uniform linear array (ULA) of L antennas and K electromagnetic waves impinging on the array from angular directions θ_k , $k = 1, \dots, K$ where the incident waves are also assumed to be far-field narrowband point sources. In this paper, K_e signals of interest (SOIs) are further assumed to be cyclostationary signals with cycle frequency ε (with $K_e \leq K$), and all of the remaining $L - K_e$ signals are referred to as signals of no interest (SONIs), which either have different cycle frequencies or are not cyclically correlated with SOIs. Furthermore, the noise is also assumed to be i.i.d and is not correlated with signals. Based on the above assumptions, the signal received from the l th sensor in the array with the complex envelope representation is given by

$$x_l(t) = \sum_{k=1}^{K_e} A_{lk} s_k(t) + n_l(t), \quad l = 1, 2, \dots, L, \quad (4)$$

where A_{lk} is the response of the l th sensor with respect to $s_k(t)$ which is the signal emitted by the k th source with the cycle frequency ε and $n_l(t)$ represents all SONIs plus noise received by the l th sensor.

Now we assume that an observation vector $X(t)$ received from the array is denoted by $X(t) = [x_1(t), \dots, x_L(t)]^T$ and expressed as

$$X(t) = A(\theta) S(t) + N(t), \quad (5)$$

where $S(t) = [s_1(t), \dots, s_{K_e}(t)]^T$ contains the SOIs and $N(t)$ represents SONIs plus noise. Let $A(\theta) = \{A_{lk}\}_{L \times K_e} = [\mathbf{a}(\theta_1), \dots, \mathbf{a}(\theta_{K_e})]$ be the matrix made up of steering vectors of the arriving SOIs with their steering vector $\mathbf{a}(\theta_k)$, $k = 1, \dots, K_e$ given by

$$\mathbf{a}(\theta_k) = [1, e^{-j(2\pi/\lambda)d \sin \theta_k}, \dots, e^{-j(2\pi/\lambda)(L-1)d \sin \theta_k}]^T, \quad (6)$$

where λ is the carrier wavelength of all SOIs and d is the interspacing.

3.2. CCO-Based Method. Under the Gaussian noise assumption, for the cyclic frequency ε and some lag parameter τ , the CCO matrix of the received data vector $X(t)$ is defined by

$$R_{XX}(\varepsilon, \tau) = \langle X(t) X^H(t + \tau) e^{-j2\pi\varepsilon t} \rangle_t. \quad (7)$$

Instead of using the eigenvalue decomposition (EVD) to decompose (7), the DOA estimation algorithm uses the singular value decomposition (SVD) to decompose (7) as into

$$R_{XX}(\varepsilon, \tau) = [E_s \ E_n] \begin{bmatrix} \Sigma_s & 0 \\ 0 & \Sigma_n \end{bmatrix} [V_s \ V_n]^H, \quad (8)$$

where the subscripts s and n stand for signal and noise subspaces, respectively, $[E_s \ E_n]$ and $[V_s \ V_n]$ are unitary matrices, and the diagonal elements of the diagonal matrices Σ_s and Σ_n are arranged in the decreasing order. Specifically, the diagonal elements of Σ_n tend to approach to zero as the number of samples increases to infinity. Thus, the CCO-based MUSIC algorithm, defined as CCO-MUSIC, can estimate DOA by searching for the peaks of the following spatial spectrum:

$$P(\theta) = \frac{1}{\mathbf{a}^H(\theta) E_n E_n^H \mathbf{a}(\theta)}. \quad (9)$$

4. FLOCC-Based Method

Despite the fact that the CCO_MUSIC algorithm has been shown to be effective in high-resolution direction finding under the Gaussian noise assumption, it cannot be applied to α -stable distributed random processes because CCO does not have finite variance in these processes. To deal with this issue, the FLOCC statistics was proposed to be implemented with MUSIC algorithm to obtain the DOA estimations of SOIs [16, 17]. The resulting algorithm is called the FLOCC-MUSIC algorithm.

In the FLOCC-MUSIC algorithm, the CCO matrix defined in (7) was replaced by the FLOCC matrix $R_{XX}^p(\varepsilon, \tau)$, defined by

$$R_{XX}^p(\varepsilon, \tau) = \left\langle X(t) [X^T(t + \tau)]^{(p-1)} e^{-j2\pi\tau t} \right\rangle_t, \quad (10)$$

where p is the order of the fractional lower order moment and $1 < p < \alpha \leq 2$. For a complex process x , $x^{(p)} = |x|^{p-1} x^*$. If x is expressed in the form of polar coordinates as $x = r e^{j\theta}$, it is easy to derive $x^{(p)} = |r|^{p-1} e^{-j\theta}$ which can be used to suppress the amplitude of the impulsive noise rather than the phase θ . So, the cyclic frequency defined by the second-order cyclic statistics is also suitable for the FLOCC.

5. Robust Cyclic Correlation

Although FLOCC can effectively suppress the α -stable impulsive noise contained in the cyclostationary signal, it needs to know the characteristic exponent of the α -stable distribution in advance which is difficult to estimate in practical applications. So, in this paper we introduce two new robust cyclic correlation functions which can be used under α -stable impulsive noise environment without knowing the characteristic exponent of α -stable distribution.

5.1. Correntropy-Based Cyclic Correlation. By taking advantage of CECO and Gaussian kernel, a new cyclic statistics for two random variables x and y can be defined as an effective alternative to the conventional cyclic correlation which can be used in α -stable impulsive noise environment, to be called correntropy-based cyclic correlation (CECCO) as follows:

$$r_{\text{CECCO}}(\varepsilon, \tau) = \left\langle \exp\left(-\frac{|x(t) - \mu y^*(t + \tau)|^2}{2\sigma^2}\right) x(t) \cdot y^*(t + \tau) e^{-j2\pi\tau t} \right\rangle_t, \quad \mu \neq 1, \quad (11)$$

where μ is a given positive constant and σ is the scale parameter. It was shown in [13] that the CECO behaved like a correlation in Gaussian noise as well as a robust M -estimation correlation in impulsive noise environment. Similarly, the CECCO also behaves like a cyclic correlation in Gaussian noise and a robust M -estimation cyclic correlation in impulsive noise environment.

5.2. Nonlinear Transform Based Cyclic Correlation. By applying a nonlinear transform to cyclic correlation, we can define a nonlinear transform based cyclic correlation (NTCCO) as follows:

$$r_{\text{NTCCO}}(\varepsilon, \tau) = \left\langle \frac{x(t) y^*(t + \tau)}{|x(t) y(t + \tau)| + \delta^2} e^{-j2\pi\tau t} \right\rangle_t, \quad (12)$$

$$\delta \geq 1,$$

where δ is called scale factor.

Equations (11) and (12) can be further combined as

$$\left\langle \varphi(x(t) y^*(t + \tau)) e^{-j2\pi\tau t} \right\rangle_t, \quad (13)$$

where $\varphi(x(t) y^*(t + \tau)) = \gamma x(t) y^*(t + \tau)$ and γ is a scalar quantity where $\varphi(\cdot)$ is used to suppress the amplitude of the correlation between random variables x and y and does not affect their periodicity. So, the robust cyclic correlation function defined by (13) has the same cyclic frequency as CCO. In the meantime it also has a good inhibition effect on the amplitude of the impulsive noise.

5.3. Simulation of the Robust Cyclic Correlation. For α -stable impulsive noise the commonly used the signal-to-noise ratio (SNR) is not applicable because the noise variance σ^2 is not finite. Since the dispersion of α -stable distribution is characterized by the parameter γ , we use the generalized signal-to-noise ratio (GSNR) [11] here, which is expressed as

$$\text{GSNR} = 10 \lg \frac{\sigma_s^2}{\gamma}, \quad (14)$$

where σ_s^2 is the variance of the signal.

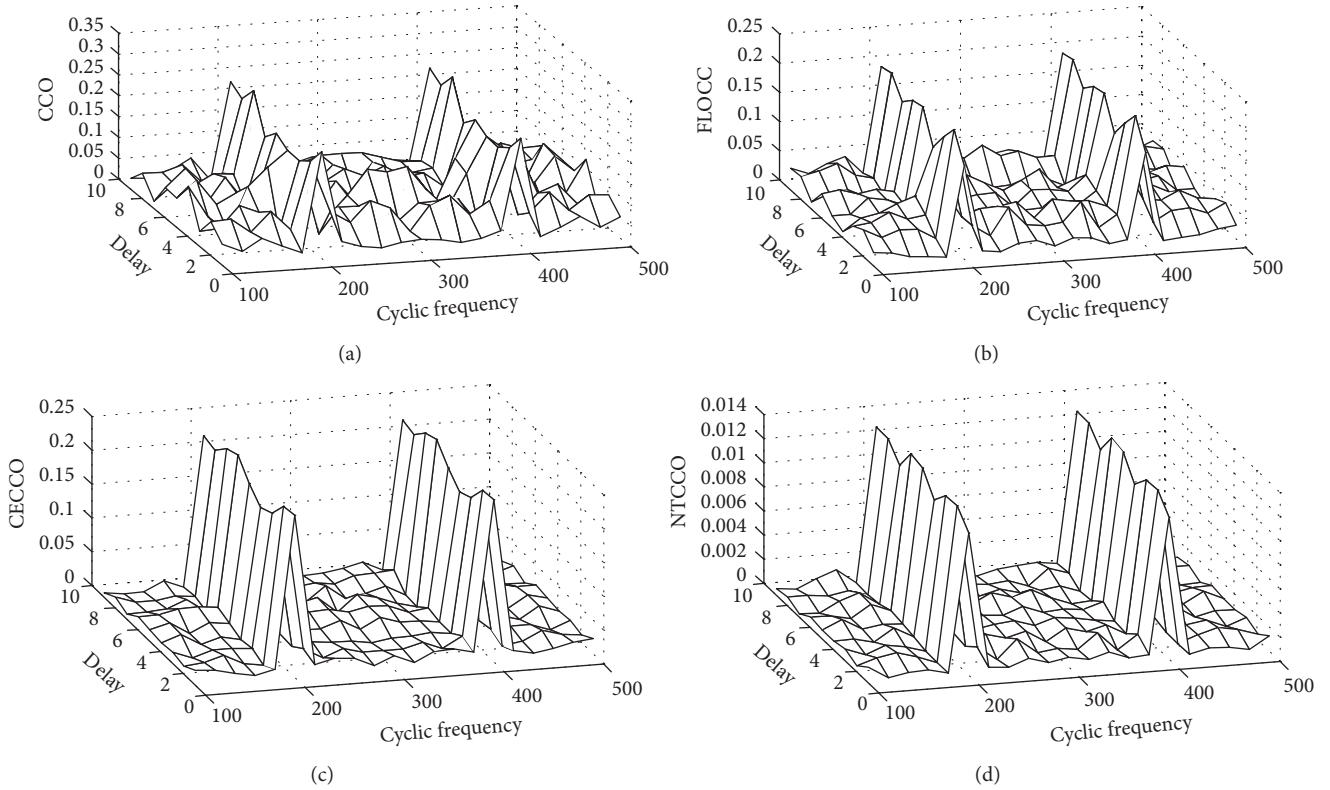


FIGURE 1: The CCO (a), FLOCC (b), CECCO (c), and NTCCO (d) of the two time varying AM signals under α -stable impulsive noise environment.

There are two time varying AM signals of interest with the α -stable impulsive noise $n_i(t)$ for $i = 1, 2$ defined by

$$x_i(t) = A [1 + B \cos(2\pi f_{bi}t)] \cos(2\pi f_{ai}t + \theta) + n_i(t) \quad (15)$$

$i = 1, 2,$

where A is the same amplitude for both carriers, B is the amplitude modulation factor, θ is the initial phase, f_{bi} is the modulating frequency, and f_{ai} is the carrier frequency. Set $A = 1$, $B = 1$, $\theta = 0$, $f_{b1} = 7$ Hz, $f_{b2} = 17$ Hz, $f_{a1} = f_{a2} = 100$ Hz, and sample frequency $f_s = 600$ Hz. Figure 1 shows the CCO, FLOCC, CECCO, and NTCCO of the two time varying AM signals defined by (15) with the characteristic exponent of the impulsive noise $\alpha = 1.5$ and the GSNR = 2 dB.

It can be seen from Figure 1 that CCO cannot represent the cyclic statistics characteristics of the two signals accurately at the cyclic frequency $\varepsilon = 200$ Hz and 400 Hz, and in the meantime it has nonzero values at noncyclic frequency because of the infinite second-order moments of the α -stable noise. Although FLOCC can demonstrate the cyclic statistics characteristics at the cyclic frequency, it also has some nonzero values at noncyclic frequency. Unlike CCO and FLOCC, CECCO and NTCCO not only can demonstrate the sharply cyclic statistics characteristics at the cyclic frequency, but also have very close to zero values at noncyclic frequency. Accordingly, it is expected that a DOA estimation algorithm based on CECCO and NTCCO will be superior to algorithms

designed based on CCO and FLOCC, a fact that will be verified by the simulations in Section 8.

6. DOA Estimation Based on Robust Cyclic Correlation

Using CECCO, we can define a CECCO matrix $R_{XX}^{ce}(\varepsilon, \tau)$ of a signal received by an array described by (4) where its (i, l) th element is defined as

$$[R_{XX}^{ce}(\varepsilon, \tau)]_{il} = \left\langle \exp\left(-\frac{|x_i(t) - \mu x_l^*(t + \tau)|^2}{2\sigma^2}\right) \cdot x_i(t) x_l^*(t + \tau) e^{-j2\pi\varepsilon t} \right\rangle_t, \quad \mu \neq 1. \quad (16)$$

Applying SVD to the matrix $R_{XX}^{ce}(\varepsilon, \tau)$ and formulating the corresponding spatial spectrum to obtain the DOA estimates of SOIs yields the CECCO-MUSIC algorithm.

In analogy with the CECCO-MUSIC algorithm we can also derive the NTCCO-MUSIC algorithm using the NTCCO matrix $R_{XX}^{nt}(\varepsilon, \tau)$ defined as

$$[R_{XX}^{nt}(\varepsilon, \tau)]_{il} = \left\langle \frac{x_i(t) x_l^*(t + \tau)}{|x_i(t) x_l(t + \tau)| + \delta^2} e^{-j2\pi\varepsilon t} \right\rangle_t, \quad (17)$$

$\delta \geq 1.$

TABLE 1: The summarization of the different algorithms.

Method	CR	CS	RN	S/C	Correlation matrix
CCO [4]	√	×	×	×	$R_{XX}(\epsilon, \tau) = \langle X(t)X^H(t+\tau)e^{-j2\pi\epsilon t} \rangle_t$
CECO [13]	√	×	√	SMSC	$[R_{XX}(t)]_{il} = \left\langle \exp\left(-\frac{ x_i(t) - \mu x_i^*(t) ^2}{2\sigma^2}\right) x_i(t) x_i^*(t) \right\rangle_t, \mu \neq 1;$
CCE [20]	×	√	√	SMSC	$V_x^\epsilon(\tau) = \left\langle \exp\left(-\frac{ x(t) - x(t+\tau) ^2}{2\sigma^2}\right) e^{-j2\pi\epsilon t} \right\rangle_t;$
DA_ZM [21]	√	×	√	SQSC	$Y(t) = w(t)X(t) \quad R_{YY}(t) = E(Y(t)Y^H(t));$
EM INIT [22]	√	×	√	SQSC	$Y(t) = H_t'(X(t)) \quad R_{YY}(t) = E(Y(t)Y^H(t));$
FLOCC [16–18]	√	√	√	SQSC	$X'(t+\tau) = [X^T(t+\tau)]^{(p-1)} \quad R_{XX}^p(\epsilon, \tau) = \langle X(t)X'(t+\tau)e^{-j2\pi\epsilon t} \rangle_t$
CECCO	√	√	√	SMSC	$[R_{XX}^{ce}(\epsilon, \tau)]_{il} = \left\langle \exp\left(-\frac{ x_i(t) - \mu x_i^*(t+\tau) ^2}{2\sigma^2}\right) x_i(t) x_i^*(t+\tau) e^{-j2\pi\epsilon t} \right\rangle_t, \mu \neq 1;$
NTCCO	√	√	√	SMSC	$[R_{XX}^{nt}(\epsilon, \tau)]_{il} = \left\langle \frac{x_i(t) x_i^*(t+\tau)}{ x_i(t) x_i(t+\tau) + \delta^2} e^{-j2\pi\epsilon t} \right\rangle_t, \delta \geq 1$

CR: correlation of received signals; CS: Cyclostationarity of the source signal; RN: robust for impulsive α -stable noise; S/C: suppression/correlation; SMSC: simultaneous suppression and correlation process; SQSC: sequential suppression and correlation process.

7. Discussions

The correntropy [12] is a local similarity measure between two arbitrary random variables based on the Gaussian kernel function. The cyclic correntropy (CCE) which was proposed in [20] was a generalized correntropy for cyclostationary signals. The correntropy-based correlation (CECO) defined in [13] is an effective substitute for conventional correlation functions that were used for DOA estimation in an α -stable impulsive noise. This paper generalizes the CECO concept for cyclostationary signals, to be called the correntropy-based cyclic correlation (CECO) which can be used for DOA estimation of the cyclostationary signals in an α -stable impulsive noise. In addition to CECCO another new concept of a robust cyclic correlation called nonlinear transform cyclic correlation (NTCCO) is also introduced in this paper for the DOA estimation of the cyclostationary signals by incorporating a nonlinear compression function into cyclic correlation. According to our experiments it turns out that the NTCCO-based method performs better than the CECCO-based method.

There are also other methods to estimate the DOA in the impulsive noise environment, such as the data-adaptive zero-memory (DA-ZM) algorithm in [22], the expectation-maximization (EM) algorithm in [21], and the FLOS based methods in [16–18]. These three methods along with our proposed CECCO and NTCCO-based DOA estimation method are all subspace-based algorithms in the sense that the subspace can be obtained by the SVD of the robust correlation matrix calculated by signals received by the array. However, there is also a significant difference between the three DOA estimation methods, DA-ZM, EM, and FLOS, and our proposed methods, which is how the robust correlation matrix of the array received signals is calculated. In the three previously mentioned DOA estimation methods, the data vectors received by the array are first preprocessed by a zero-memory

nonlinearity process to suppress the impulsive noise. It then uses the correlation matrix of the preprocessed received data vectors as the robust correlation matrix estimation of the array received signals. It is a two-stage sequence process with the first stage process of impulsive noise suppression followed by the second stage process of correlation matrix estimation. Such resulting process is called sequential suppression and correlation (SQSC) process. In our two proposed CECCO- and NTCCO-based methods both the suppression of the impulsive noise and the correlation matrix estimation are carried out simultaneously. The resulting process is referred to as simultaneous suppression and correlation (SMSC) process. The simulation results demonstrate that the performance of SMSC is better than SQSC.

When a source signal is cyclostationary, the methods in [21, 22] do not utilize the cyclostationarity of the source signal. In other words, the methods in [21, 22] do not have signal selectivity. By contrast, our proposed two methods utilize the cyclostationarity of source signals. Accordingly, our proposed methods not only can suppress the impulsive noise in the array received signal but also have signal selectivity.

Finally, Table 1 summarizes the above discussions by comparing various signals and different functions used to process the array received signals vector and the correlation matrix of the array received signals.

8. Simulation Results

This section conducts computer simulation experiments to compare the relative performance of our proposed CECCO-MUSIC and NTCCO-MUSIC algorithms to CCO-MUSIC and FLOCC-MUSIC algorithms under the S α S impulsive noise environment. Two criteria are used to evaluate their performances. One is the probability of resolution. In doing

so, a popular resolution criterion is used and defined by the following threshold equation [11]:

$$P(\theta_m) - \frac{1}{2} \{P(\theta_1) + P(\theta_2)\} > 0, \quad (18)$$

where θ_1 and θ_2 are the angles of arrival of the two SOIs and $\theta_m = (\theta_1 + \theta_2)/2$ is the mid-point between θ_1 and θ_2 . The two SOIs are said to be resolvable if (18) holds. Two hundred independent Monte Carlo experiments were simulated. Let N_{ok} be the number of pairs of two incident angles that can be resolved. The probability of resolution is then defined as $N_{ok}/200$. In case two SOIs can be resolved by the n th Monte Carlo experiment, $\bar{\theta}_i(n)$, $i = 1, 2$ is then set to the estimation of θ_i . With this definition, the average mean square error (MSE) of the DOA estimation is then defined as

$$\begin{aligned} \text{MSE} = & \frac{1}{2N_{ok}} \sum_{n=1}^{N_{ok}} (\bar{\theta}_1(n) - \theta_1)^2 \\ & + \frac{1}{2N_{ok}} \sum_{n=1}^{N_{ok}} (\bar{\theta}_2(n) - \theta_2)^2. \end{aligned} \quad (19)$$

Suppose that a ULA consists of ten sensors with an interspacing of half a wavelength and the incoming signals are uncorrelated binary phase-shift keying- (BPSK-) modulated sources. We further assume that sample frequency is $f_s = 900$ KHz, and the carrier frequency of the BPSK SOIs is $f_1 = 100$ KHz. Other signals are considered as interference with a carrier frequency of $f_2 = 70$ KHz. In what follows, the cycle frequency was simulated by $\varepsilon = 2f_1$ which was usually twice the carrier frequency f_1 . The four algorithms, CCO-MUSIC, FLOCC-MUSIC, CECCO-MUSIC, and NTCCO-MUSIC algorithms, were evaluated for performance comparison.

Simulation 1. Suppose that there are one SONI arriving from 50° and two BPSK SOIs coming from 30° and 35° , respectively. The noise was S α S distributed with $\alpha = 1.8$. The GSNR is set to GSNR = 20 dB, and the number of snapshots is 600. Figure 2 plots the spatial spectrum of the four versions of the MUSIC algorithm, CCO-MUSIC, FLOCC-MUSIC, CECCO-MUSIC, and NTCCO-MUSIC algorithms, where the CCO-MUSIC algorithm failed to separate the two DOAs of the SOIs, while the FLOCC-MUSIC algorithm could separate the two DOAs of the SOIs, but its estimate was not very accurate. By contrast, our proposed algorithms, the CECCO-MUSIC and NTCCO-MUSIC algorithms, not only successfully separated the two DOAs of the SOIs and but also correctly estimated DOA with very high accuracy. In particular, the NTCCO-MUSIC algorithm has a much sharper spatial spectrum than that generated by the CECCO-MUSIC algorithm.

Simulation 2. Figure 3 plots probabilities of resolution and MSEs produced by the four test MUSIC algorithms with various GSNRs. The SOIs' angles of arrival were 30° and 40° , and the SONI's angle of arrival was set to 50° . The characteristic exponent of the α -stable impulsive noise was

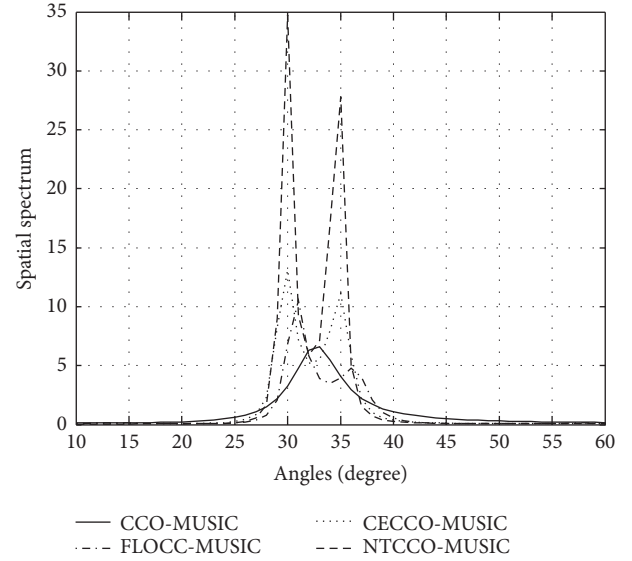


FIGURE 2: Spatial spectrum of the algorithms.

$\alpha = 1.4$. The snapshots number used by the simulation was 600. As we can see from Figure 3 the performance of NTCCO-MUSIC and CECCO-MUSIC algorithms was much better than that produced by FLOCC-MUSIC and CCO-MUSIC algorithms. Especially, the best one was NTCCO-MUSIC algorithm which produced the highest probabilities of resolution with more than 90% of success and the least MSE in all GSNRs. The worst one was the CCO-MUSIC algorithm which nearly failed and produced largest MSE when GSNR < 14 dB.

Simulation 3. Figure 4 plots probabilities of resolution and MSEs produced by the four algorithms varying with different values of the characteristic exponent of the α -stable impulsive noise. The SOIs' angles of arrival were 30° and 40° , and the SONI's angle of arrival was set to 50° , the number of snapshots used by the simulation was 600, and GSNR = 14 dB. As shown in Figure 4 NTCCO-MUSIC and CECCO-MUSIC algorithms demonstrated their performance enhancement over FLOCC-MUSIC and CCO-MUSIC algorithms in the sense of both probability of resolution and MSE. Moreover, the performance of NTCCO-MUSIC algorithm is slightly superior to CECCO-MUSIC algorithm.

Simulation 4. Figure 5 plots probabilities of resolution and MSEs produced by the four algorithms by changing the number of snapshots. The SOIs' angles of arrival were 30° and 40° , and the SONI's angle of arrival was 50° . The characteristic exponent of impulsive noise was set to $\alpha = 1.4$ and GSNR = 14 dB. As demonstrated in Figure 5 the performance of all four methods was improved as the number of snapshots increased. Nevertheless, our proposed NTCCO-MUSIC algorithm and CECCO-MUSIC algorithm produced lower MSEs and higher probabilities of resolution compared to the other two MUSIC algorithms, CCO-MUSIC algorithm and FLOCC-MUSIC algorithm, when the same number of snapshots was used.

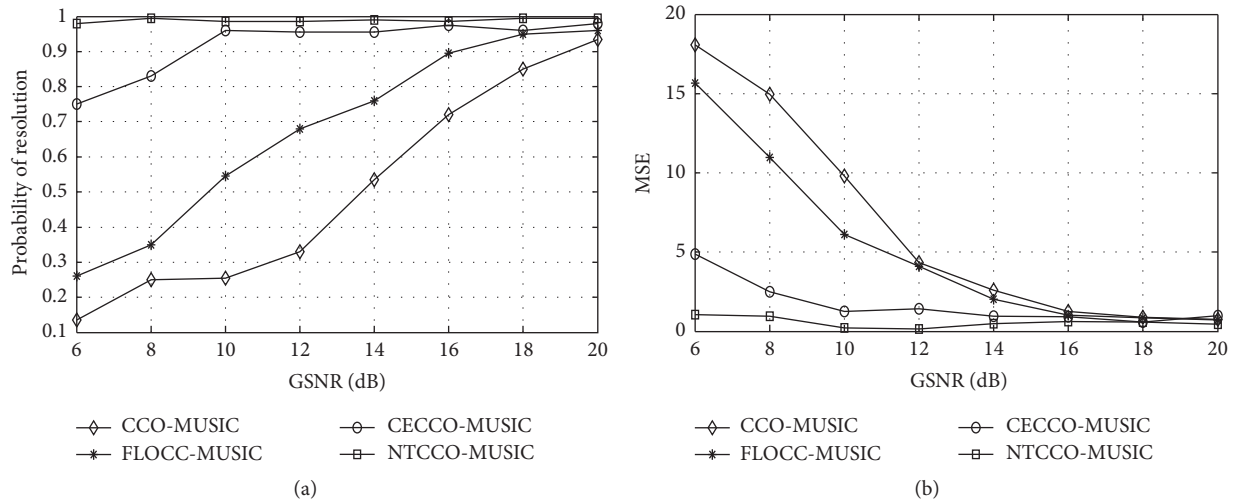


FIGURE 3: Probability of resolution (a) and MSE (b) versus GSNR.

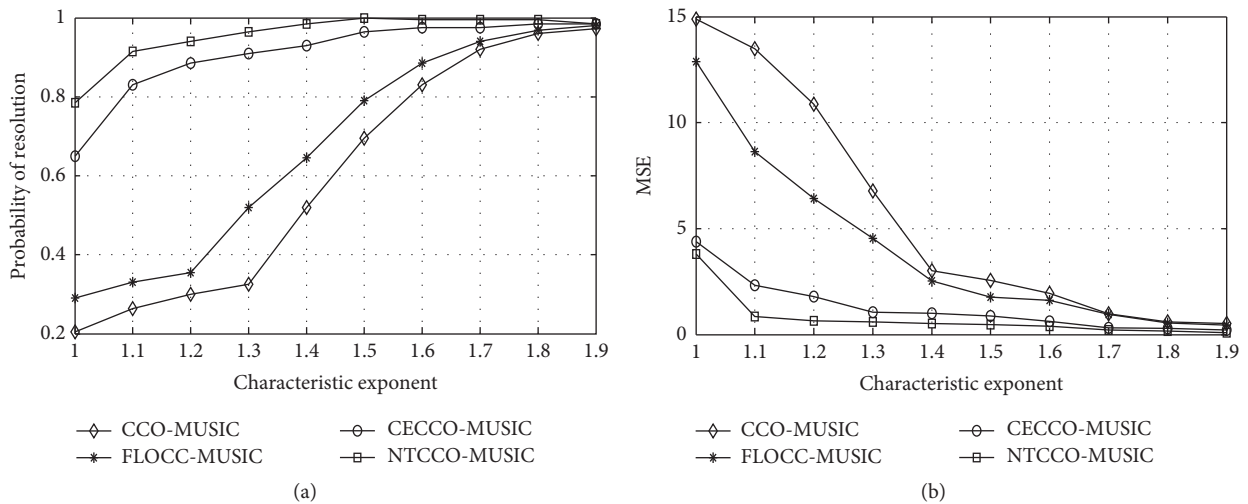


FIGURE 4: Probability of resolution (a) and MSE (b) versus characteristic exponent.

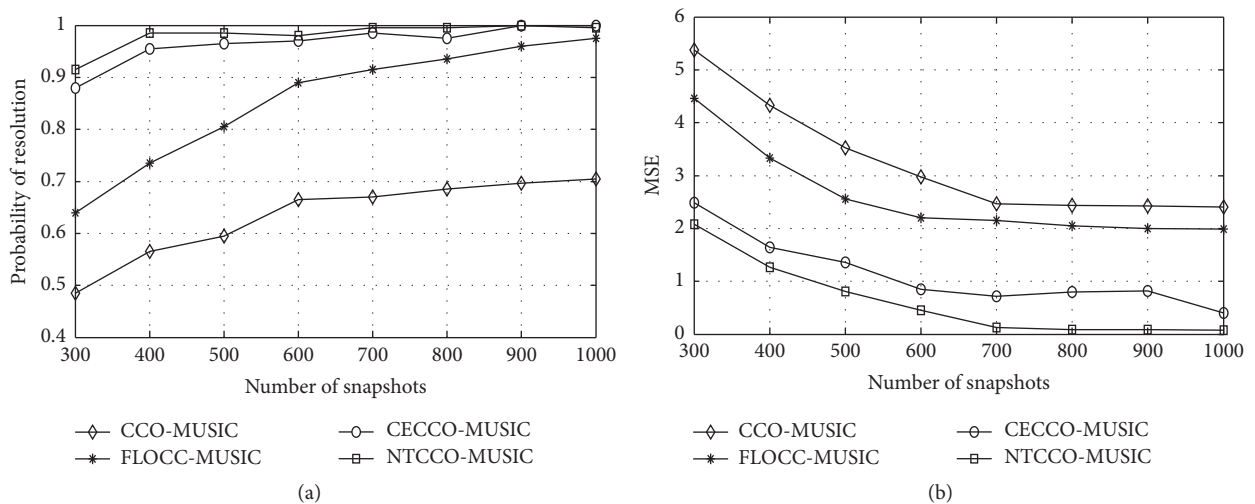


FIGURE 5: Probability of resolution (a) and MSE (b) versus number of snapshots.

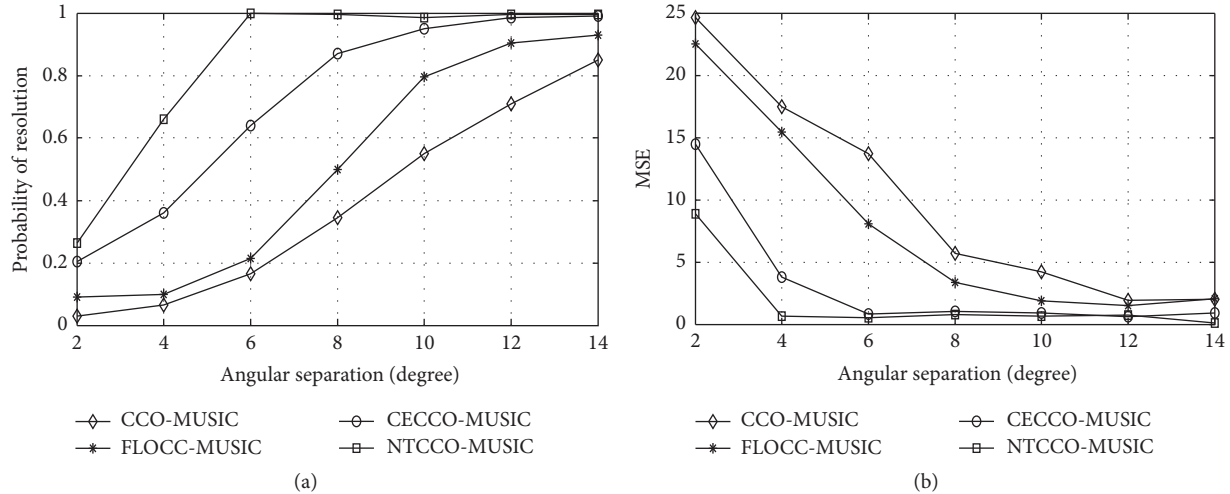


FIGURE 6: Probability of resolution (a) and MSE (b) versus angular separation.

Simulation 5. Figure 6 plots probabilities of resolution and MSEs produced by the four algorithms changing with various degrees of the angular separation. The angles of arrival of the SOIs were 30° and $30^\circ + \delta$, where δ is the angular separation of the two SOIs and varied from 2° to 14° in a step size of 2° . The DOA of SONI was 50° . The characteristic exponent of impulsive noise was set to $\alpha = 1.4$ and $\text{GSNR} = 14$ dB. From Figure 6 the proposed NTCCO-MUSIC algorithm and CECCO-MUSIC algorithm were superior to CCO-MUSIC and FLOCC-MUSIC algorithm in the sense that the probability of resolution of the NTCCO-MUSIC algorithm almost reached 100%, while the probabilities of resolution of CCO-MUSIC and FLOCC-MUSIC algorithms were lower than 20% when the angular separation was 6° .

9. Conclusion

This paper proposes two robust cyclic correlation functions, correntropy-based cyclic correlation (CECCO) and the non-linear transform based cyclic correlation (NTCCO). By virtue of CECCO and NTCCO we can implement the CECCO-based and NTCCO-based array received signals matrix in conjunction with the MUSIC algorithm to obtain DOA estimates of SOIs. Computer simulation results demonstrate that CECCO-MUSIC and NTCCO-MUSIC algorithms indeed outperform FLOCC-MUSIC and CCO-MUSIC algorithms in α -stable impulsive noise environments. In addition, experiments also show that NTCCO-MUSIC algorithm performs slightly better than CECCO-MUSIC algorithm.

Conflicts of Interest

The authors declare no conflicts of interest regarding the publication of this paper.

Acknowledgments

This work was supported in part by the National Natural Science Foundation of China under Grants 61301228 and

61371091 and the Fundamental Research Funds for the Central Universities under Grant 3132016331.

References

- [1] L. Li, F. Chen, and J. Dai, "Separate DOD and DOA estimation for bistatic MIMO radar," *International Journal of Antennas and Propagation*, vol. 2016, Article ID 9170403, 11 pages, 2016.
- [2] I. Pasya, N. Iwakiri, and T. Kobayashi, "Joint direction-of-departure and direction-of-arrival estimation in a UWB MIMO radar detecting targets with fluctuating radar cross sections," *International Journal of Antennas and Propagation*, vol. 2014, Article ID 847815, 15 pages, 2014.
- [3] W. A. Gardner, A. Napolitano, and L. Paura, "Cyclostationarity: half a century of research," *Signal Processing*, vol. 86, no. 4, pp. 639–697, 2006.
- [4] W. A. Gardner, "Simplification of MUSIC and ESPRIT by exploitation of cyclostationarity," *Proceedings of the IEEE*, vol. 76, no. 7, pp. 845–847, 1988.
- [5] J.-H. Lee, C.-C. Chao, C.-C. Huang, and W.-C. Lo, "Adaptive cyclostationary array beamforming with robust capabilities," *Journal of the Franklin Institute*, vol. 352, no. 6, pp. 2486–2503, 2015.
- [6] C. Du, H. Zeng, W. Lou, and Y. T. Hou, "On cyclostationary analysis of WiFi signals for direction estimation," in *Proceedings of the IEEE International Conference on Communications (ICC '15)*, pp. 3557–3561, London, UK, June 2015.
- [7] H. Yan and H. H. Fan, "Signal-selective DOA tracking for wideband cyclostationary sources," *IEEE Transactions on Signal Processing*, vol. 55, no. 5, pp. 2007–2015, 2007.
- [8] M. D. Button, J. G. Gardiner, and I. A. Glover, "Measurement of the impulsive noise environment for satellite-mobile radio systems at 1.5 GHz," *IEEE Transactions on Vehicular Technology*, vol. 51, no. 3, pp. 551–560, 2002.
- [9] C. L. Nikias and M. Shao, *Signal Processing with Alpha-Stable Distributions and Applications*, John Wiley & Sons, New York, NY, USA, 1995.
- [10] H. Belkacemi and S. Marcos, "Robust subspace-based algorithms for joint angle/Doppler estimation in non-Gaussian clutter," *Signal Processing*, vol. 87, no. 7, pp. 1547–1558, 2007.

- [11] S. Li and Z. Liang, "DOA estimation of the coherent sources based on SVD and the fractional lower order statistics," in *Proceedings of the 6th International Conference on Wireless Communications and Signal Processing (WCSP '14)*, pp. 1–4, Hefei, China, October 2014.
- [12] W. F. Liu, P. P. Pokharel, and J. C. Principe, "Correntropy: properties and applications in non-Gaussian signal processing," *IEEE Transactions on Signal Processing*, vol. 55, no. 11, pp. 5286–5298, 2007.
- [13] J. F. Zhang, T. S. Qiu, A. M. Song, and H. Tang, "A novel correntropy based DOA estimation algorithm in impulsive noise environments," *Signal Processing*, vol. 104, pp. 346–357, 2014.
- [14] T. S. Qiu, J. F. Zhang, A. M. Song, and H. Tang, "The generalized correntropy-analogous statistics based direction of arrival estimation in impulsive noise environments," *Journal of Signal Processing*, vol. 28, pp. 463–466, 2012.
- [15] J. Q. Ma, L. D. Ge, and L. Tong, "A new DOA algorithm based on nonlinear compress core function in symmetric α -stable distribution noise environment," *Telecommunication Engineering*, vol. 54, pp. 34–39, 2014.
- [16] G.-H. You, T.-S. Qiu, and J. Yang, "A novel DOA estimation algorithm of cyclostationary signal based on UCA in impulsive noise," *AEU—International Journal of Electronics and Communications*, vol. 67, no. 6, pp. 491–499, 2013.
- [17] G. H. You, T. S. Qiu, and Y. Zhu, "A novel extended fractional order cyclic MUSIC algorithm in impulsive noise," *ICIC Express Letters*, vol. 6, no. 9, pp. 2371–2376, 2012.
- [18] G.-H. You, T.-S. Qiu, and A.-M. Song, "Novel direction findings for cyclostationary signals in impulsive noise environments," *Circuits, Systems, and Signal Processing*, vol. 32, no. 6, pp. 2939–2956, 2013.
- [19] Y. Liu, T. Qiu, and J. Li, "Joint estimation of time difference of arrival and frequency difference of arrival for cyclostationary signals under impulsive noise," *Digital Signal Processing*, vol. 46, pp. 68–80, 2015.
- [20] S. Luan, T. Qiu, Y. Zhu, and L. Yu, "Cyclic correntropy and its spectrum in frequency estimation in the presence of impulsive noise," *Signal Processing*, vol. 120, pp. 503–508, 2016.
- [21] J. He, Z. Liu, and K. T. Wong, "Snapshot-instantaneous $\| \cdot \|_{\infty}$ normalization against heavy-tail noise," *IEEE Transactions on Aerospace and Electronic Systems*, vol. 44, no. 3, pp. 1221–1227, 2008.
- [22] R. J. Kozick and B. M. Sadler, "Maximum-likelihood array processing in non-GAUssian noise with GAUssian mixtures," *IEEE Transactions on Signal Processing*, vol. 48, no. 12, pp. 3520–3535, 2000.

Research Article

Direction-of-Arrival Estimation for Coprime Array Using Compressive Sensing Based Array Interpolation

Aihua Liu, Qiang Yang, Xin Zhang, and Weibo Deng

Department of Electronic and Information Engineering, Harbin Institute of Technology, Harbin 150001, China

Correspondence should be addressed to Qiang Yang; yq@hit.edu.cn

Received 16 October 2016; Revised 6 January 2017; Accepted 12 January 2017; Published 16 February 2017

Academic Editor: Aboulnasr Hassanien

Copyright © 2017 Aihua Liu et al. This is an open access article distributed under the Creative Commons Attribution License, which permits unrestricted use, distribution, and reproduction in any medium, provided the original work is properly cited.

A method of direction-of-arrival (DOA) estimation using array interpolation is proposed in this paper to increase the number of resolvable sources and improve the DOA estimation performance for coprime array configuration with holes in its virtual array. The virtual symmetric nonuniform linear array (VSNLA) of coprime array signal model is introduced, with the conventional MUSIC with spatial smoothing algorithm (SS-MUSIC) applied on the continuous lags in the VSNLA; the degrees of freedom (DoFs) for DOA estimation are obviously not fully exploited. To effectively utilize the extent of DoFs offered by the coarray configuration, a compressing sensing based array interpolation algorithm is proposed. The compressing sensing technique is used to obtain the coarse initial DOA estimation, and a modified iterative initial DOA estimation based interpolation algorithm (IMCA-AI) is then utilized to obtain the final DOA estimation, which maps the sample covariance matrix of the VSNLA to the covariance matrix of a filled virtual symmetric uniform linear array (VSULA) with the same aperture size. The proposed DOA estimation method can efficiently improve the DOA estimation performance. The numerical simulations are provided to demonstrate the effectiveness of the proposed method.

1. Introduction

Antenna arrays are usually used to perform spatial sampling of impinging electromagnetic waves for improving detection performance of the source signal, and direction-of-arrival (DOA) estimation is a major application area of antenna arrays. It is well-known that the number of sources that can be resolved with an N element uniform linear array (ULA) using conventional subspace-based DOA estimation method like MUSIC [1] is $N - 1$. In order to get more degrees of freedom (DoFs) and hence resolve more sources than the actual number of physical sensors, minimum redundancy array (MRA) is proposed to maximize the number of continuous virtual sensors in the resulting difference coarray with given number of physical sensors. However, there are no closed form expressions for the array geometry or achievable DoFs for the MRA. To overcome this problem, the nested array [2] and the coprime array [3] are proposed with the exact expressions of the virtual sensor locations and the achievable DoFs. The nested array can resolve $O(N^2)$ sources with N sensors. And coprime array [3] and the extended coprime

array [4] can resolve $O(MN)$ sources with $M + N - 1$ and $2M + N - 1$ physical sensors, respectively. There are also two kinds of generalized coprime array configurations proposed in [5]. The virtual array of a coprime array is actually a symmetric linear array. And there are usually holes in the virtual array [6]. Therefore, the virtual array of a coprime array is a virtual symmetric nonuniform linear array (VSNLA) rather than a filled uniform linear array (ULA) when holes exist in the virtual array.

The increased DoFs provided by the coprime structure can be utilized to improve DOA estimation performance, and there are two major categories of representative DOA estimation techniques that have been proposed recently to utilize these increased DoFs for coprime arrays: one is compressive sensing (CS) technique, such as orthogonal matching pursuit (OMP) [7] and the least absolute shrinkage and selection operator (LASSO) [8]. The LASSO algorithm is considered in [9–11] for sparse signal recovery using coprime array. The main drawback of CS technique is that every source must fall on the predefined grid, off-grid sources can highly jeopardize the reconstruction performance. To

overcome dictionary mismatch problem for CS technique, joint-OMP and joint LASSO algorithms are proposed in [12], and a classic off-grid DOA estimation method using sparse Bayesian inference is proposed in [13], which also explores the underlying structure between the sparse signal and the grid mismatch.

The other representative DOA estimation technique for coprime array is based on the well-known MUSIC algorithm called MUSIC algorithm with spatial smoothing (SS-MUSIC) [2], which uses spatial smoothing technique [14, 15] to build a suitable covariance matrix from the virtual sensor output before applying MUSIC spectrum estimation [2, 4]. However, spatial smoothing cannot be used directly when the virtual array is not a filled ULA, which means that only the continuous lags in the VSNLA can be utilized for the application of spatial smoothing [5]. When the number of continuous lags in the VSNLA is lower than that of the unique lags in the VSNLA, the DoFs offered by coprime array are only partly explored, which significantly reduces the DOA estimation precision and the number of resolvable sources. To fully explore the virtual array aperture of the VSNLA using SS-MUSIC, on the one hand, multiple frequencies are utilized to fill the missing elements in the VSNLA [16]. However, it requires that the reflections of sources have large bandwidth to cover all specific frequencies used for filling the holes, and the sources spectrums at all operational frequencies should be proportional, which may be difficult to meet in the practical application. On the other hand, array interpolation techniques are proposed to fill the holes in the VSNLA and the sparsity-based extrapolation technique [6] uses sparse reconstruction to extrapolate observations at the holes of the VSNLA, but the basis mismatch problem at the sparse reconstruction stage is not considered. The coprime coarray interpolation technique is proposed in [17] to fill the holes by using nuclear norm minimization, while it needs to solve a complex semidefinite programming problem.

In this paper, we consider single frequency operation to utilize all of the DoFs for DOA estimation in coprime array using preprocessing method like interpolation [18] as mentioned in [2]. However, conventional interpolation techniques [18–21] cause big interpolation errors over the entire field of view due to the holes in the VSNLA of coprime array. To reduce interpolation errors, the idea of initial DOA estimation based array interpolation is used in [22, 23] by specifying a union of small subsectors that cover only the source directions inside. To obtain the initial DOA estimation, two different special nonuniform linear array (NLA) structures, partially augmentable nonredundant array [24] and partly filled NLA, are considered in [22], and the iterative initial DOA estimate based array interpolation approach (IMCI-AI) is proposed to solve multipath problem for the partly filled NLA. Like [22], the IMCI-AI method is used in this paper to build up the rank of the observation matrix of the VSNLA of coprime array. However, the initial DOA estimation of signals is the prerequisite of this method; although the SS-MUSIC can be used to obtain the initial DOA estimation with the continuous lags in the VSNLA, it has the limitation that the number of sources resolvable should be less than half that of the continuous lags in the VSNLA.

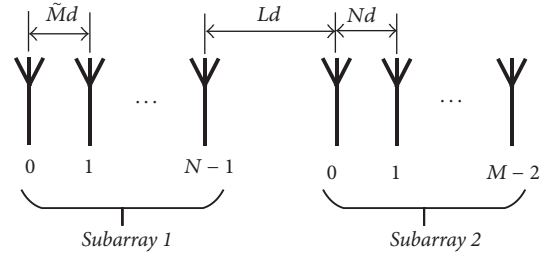


FIGURE 1: The coprime array with displaced subarrays (CADiS) [5].

To detect more sources and improve the DOA estimation accuracy for coprime array with VSNLA, a compressive sensing based array interpolation approach for DOA estimation is proposed in this paper. Firstly, the coarse initial DOA estimation of sources is obtained using the LASSO compressive sensing technique. Then, a modified IMCI-AI approach is used to interpolate the data of a symmetric uniform linear array (VSULA) using the received data of the VSNLA; after the interpolation, the holes in the VSNLA are filled, leading to a filled VSULA with the same array aperture as the VSNLA. Then, the ESPRIT-Like algorithm [25] is applied to the filled VSULA for the improved DOA estimation of sources using the symmetric structure of the VSULA. Compared with the VSNLA, the filled VSULA after interpolation has more continuous elements and it can be used to detect more sources. Like the traditional IMCI-AI method, the proposed interpolation approach can make full use of the array aperture offered by coprime array. However, the proposed method can resolve more sources. Compared with general CS algorithms, the proposed algorithm does not suffer from basis mismatch effects.

The remainder of this paper is organized as follows. In Section 2, the signal model of the VSNLA of coprime array is reviewed. In Section 3, DOA estimation using SS-MUSIC and the proposed array interpolation methods are compared. Simulation results are provided in Section 4. Finally, Section 5 concludes the study.

2. Signal Model

We consider generalized coprime arrays [5]; the coprime array with displaced subarrays (CADiS) in this paper is an example of coprime array with holes in its virtual array. The CADiS is illustrated in Figure 1. This kind of coprime array configuration consists of two collinearly located uniform linear subarrays: one has N antennas with distance $\tilde{M}d$ between two continuous antennas and the other has $M - 1$ antennas with distance Nd between two continuous antennas, where d is the unit spacing set to $\lambda/2$, and λ denotes the wavelength. M and N are coprime integers and M can be expressed as a product of two positive integers p and \tilde{M} ($M = p\tilde{M}$). The two subarrays are placed collinearly with the closest spacing between the two subarrays set to Ld . The total number of the sensors in each coprime array is kept to $M + N - 1$.

Denote $\mathbf{p} = [p_1, \dots, p_{M+N-1}]^T$ as the sensor position vector of the coprime array, where $(\bullet)^T$ denotes transpose

operator, and the first sensor is assumed as the reference, that is, $p_1 = 0$. Assume that K far-field uncorrelated narrowband sources imping on the array from directions θ_k , $k = 1, 2, \dots, K$, and their discretized baseband waveforms are expressed as $s_k(t)$, $k = 1, 2, \dots, K$. Then, the received data vector at time t is expressed as

$$\mathbf{x}(t) = \sum_{k=1}^K \mathbf{a}(\theta_k) s_k(t) + \mathbf{n}(t) = \mathbf{A}\mathbf{s}(t) + \mathbf{n}(t), \quad (1)$$

for $t = 1, \dots, T$, and $\mathbf{A} = [\mathbf{a}(\theta_1), \dots, \mathbf{a}(\theta_K)]$, where

$$\begin{aligned} \mathbf{a}(\theta_k) &= [e^{j2\pi p_1 \sin(\theta_k)/\lambda}, e^{j2\pi p_2 \sin(\theta_k)/\lambda}, \dots, e^{j2\pi p_{M+N-1} \sin(\theta_k)/\lambda}]^T \end{aligned} \quad (2)$$

is the manifold vector of the coarray corresponding to θ_k , and $\mathbf{s}(t) = [s_1(t), \dots, s_K(t)]^T$ is the signal vector, and $\mathbf{n}(t)$ is the noise vector supposed to be temporally and spatially white Gaussian which is uncorrelated with the sources. The covariance matrix of data vector $\mathbf{x}(t)$ is obtained as

$$\begin{aligned} \mathbf{R}_{\mathbf{xx}} &= E[\mathbf{x}(t)\mathbf{x}^H(t)] = \mathbf{A}\mathbf{R}_s\mathbf{A}^H + \sigma_n^2\mathbf{I}_{M+N-1} \\ &= \sum_{k=1}^K \sigma_k^2 \mathbf{a}(\theta_k) \mathbf{a}^H(\theta_k) + \sigma_n^2 \mathbf{I}_{M+N-1}, \end{aligned} \quad (3)$$

where $E(\bullet)$ is the statistical expectation operator and \mathbf{I}_{M+N-1} is an $(M+N-1) \times (M+N-1)$ identity matrix. $\mathbf{R}_s = E[\mathbf{s}(t)\mathbf{s}^H(t)] = \text{diag}([\sigma_1^2, \dots, \sigma_K^2])$ is the signal covariance matrix, where $(\bullet)^H$ denotes Hermitian transposition operator, $\text{diag}(\bullet)$ denotes a diagonal matrix that uses the elements of a vector as its diagonal elements, σ_k^2 denotes the input signal power of the k th signal, and σ_n^2 denotes the noise variance.

By vectorizing $\mathbf{R}_{\mathbf{x}}$, a new vector is obtained as

$$\mathbf{z} = \text{vec}(\mathbf{R}_{\mathbf{x}}) = \bar{\mathbf{A}}\mathbf{b} + \sigma_n^2\bar{\mathbf{I}}, \quad (4)$$

where $\text{vec}(\bullet)$ denotes the vectorization operator that turns a matrix into a vector by stacking all columns on top of the other, and $\bar{\mathbf{A}} = [\bar{\mathbf{a}}(\theta_1), \dots, \bar{\mathbf{a}}(\theta_K)]$, $\mathbf{b} = [\sigma_1^2, \dots, \sigma_K^2]^T$ and $\bar{\mathbf{I}} = \text{vec}(\mathbf{I}_{M+N-1})$, where $\bar{\mathbf{a}}(\theta_k) = \mathbf{a}^*(\theta_k) \otimes \mathbf{a}(\theta_k)$, $(\bullet)^*$ is the complex conjugation operator and \otimes denotes the Kronecker product. Vector \mathbf{z} amounts to the received data from a coherent source vector \mathbf{b} . The matrix $\bar{\mathbf{A}}$ behaves as the array manifold matrix of a virtual array with an extended aperture whose sensors are located at $p_i - p_j$ with $1 \leq i, j \leq M+N-1$. It has been shown in [5] that the choice of $L = \bar{M} + N$ yields the largest number of continuous lags for CADiS, and there are $M_1 = 2MN + 2\bar{M} - 1$ unique lags in the virtual array, among which the range $[(\bar{M}-1)(N-1), MN + \bar{M} - 1]$ and its corresponding negative range are, respectively, continuous. In this paper, $\bar{M} > 1$ is considered, and the virtual arrays of both coprime configurations are VSNLAs.

After removing repeated rows of (4) and sorting the remaining rows according to the unique lags set, the received source of the VSNLA is expressed as

$$\tilde{\mathbf{z}} = \tilde{\mathbf{A}}\mathbf{b} + \sigma_n^2\mathbf{I}_{M_1}, \quad (5)$$

where $\tilde{\mathbf{A}} = [\tilde{\mathbf{a}}(\theta_1), \dots, \tilde{\mathbf{a}}(\theta_K)]$, and $\tilde{\mathbf{a}}(\theta_k) = [e^{j2\pi\tilde{p}_1 \sin(\theta_k)/\lambda}, \dots, e^{j2\pi\tilde{p}_{M_1} \sin(\theta_k)/\lambda}]^T$ is $M_1 \times 1$ steering vector, and $\tilde{\mathbf{p}} = [\tilde{p}_1, \dots, \tilde{p}_{M_1}]^T$ is the positions of the array sensors in the VSNLA. It is easy to verify that \mathbf{I}_{M_1} is a vector whose elements are obtained by removing repeated elements of $\bar{\mathbf{I}}$ and sorting the remaining elements according to the unique lags set. Since the virtual signal in (5) becomes a single snapshot of \mathbf{b} , MUSIC algorithm fails to yield reliable DOA estimation when multiple sources imping to the array because that the rank of the noise-free covariance matrix $\mathbf{R}_{\tilde{\mathbf{z}}} = \tilde{\mathbf{z}}\tilde{\mathbf{z}}^H$ of the VSNLA is one. The problem is similar to handling fully coherent sources. To solve this problem, spatial smoothing technique is applied to restore the rank of the covariance matrix [2]. Since spatial smoothing technique requires a filled ULA, data of continuous lag in the VSNLA is extracted [5], which means that only part of unique lags in the VSNLA can be used to implement the SS-MUSIC. Therefore, the maximum number of the sources that can be detected with this method is $\lfloor M_c/2 \rfloor$, where M_c is the number of continuous lags and $\lfloor \bullet \rfloor$ denotes the largest integer not exceeding the argument. The CADiS has $M_c = MN + \bar{M} - (\bar{M} - 1)(N - 1)$ continuous lags. Obviously, the virtual aperture offered by coprime array is not fully explored and the maximum number of detectable sources is lower than half that of the unique lags $\lfloor M_1/2 \rfloor$. It is noted that other kinds of coprime arrays with holes in their virtual array have the same problem.

3. DOA Estimation with Array Interpolation Based on Compressing Sensing

The usage of SS-MUSIC for the coprime array only exploits the continuous lag set in the VSNLA of a coprime array, resulting in relatively poor DOA estimation precision and low number of resolvable sources. To explore the whole aperture of the VSNLA for DOA estimation, CS-based methods such as OMP and LASSO can be used, while such methods suffer from basis mismatch effects. The sparsity-based extrapolation technique [6] uses sparse reconstruction to extrapolate observations at the holes in the VSNLA and then utilizes SS-MUSIC to obtain the final DOA estimation. However, some of the measurements may not be accurately reconstructed due to basis mismatch effects. The coarray interpolation using nuclear norm minimization in [17] has no basis mismatch problem, while it requires a complex semidefinite programming solver. To overcome basis mismatch problem and obtain a relatively low computational complexity, a compressing sensing based array interpolation approach is proposed in this section, like the sparsity-based extrapolation technique, CS reconstruction is also used in our proposed method, while it is used to obtain the initial DOA estimation. We first review the conventional iterative initial DOA estimation based array interpolation and the LASSO compressing sensing technique. Then, in Section 3.2, we introduce the compressing sensing based array interpolation approach, which uses the LASSO compressing sensing technique to obtain the coarse initial DOA estimation. Finally, we outline the proposed method by joining the main procedures together.

3.1. Conventional Iterative Initial DOA Estimation Based Array Interpolation for Coprime Array. The key idea of the initial DOA estimation based array interpolation approach in [22] is to design an appropriate mapping matrix \mathbf{B} . The mapping matrix is then used to map the data of the VSNLA of the coprime to that of a virtual filled ULA with the same aperture over a union of particular interpolation sectors $\{\theta_k\}$ that covers all the sources inside. Suppose that $\tilde{\mathbf{a}}(\theta)$ and $\tilde{\mathbf{a}}'(\theta)$ are array steering vectors for the VSNLA of coprime array and the virtual filled ULA (i.e., a filled VSNLA with the same aperture size as the VSNLA), respectively. The interpolation matrix \mathbf{B} should obey

$$\tilde{\mathbf{a}}'(\theta) = \mathbf{B}\tilde{\mathbf{a}}(\theta), \quad \theta \in \theta_k. \quad (6)$$

It is noted that there is no guarantee that a signal outside interpolation sectors will be identified correctly, because signal outside of the interpolation sector will cause large interpolation errors. Therefore, initial DOA estimation $\hat{\boldsymbol{\theta}} = [\hat{\theta}_1, \dots, \hat{\theta}_K]^T$ is required to locate these particular interpolation sectors. After that, the initial DOA estimation is obtained, each small interpolation sector $\theta_k = [\hat{\theta}_k - \theta_\varepsilon, \hat{\theta}_k + \theta_\varepsilon]$ that contains the k th signal inside is uniformly divided with $\delta\theta$ intervals, and array manifolds $\tilde{\mathbf{A}}(\bar{\theta})$ and $\tilde{\mathbf{A}}'(\bar{\theta})$ for the VSNLA and the virtual filled ULA are generated by considering $\bar{\theta}_i = i\delta\theta$ ($i = 1, \dots, 2\theta_\varepsilon/\delta\theta + 1$), respectively. To improve the DOA performance for noisy observations, the mapping matrix of the Wiener solution is then given as [22]

$$\mathbf{B} = \sigma_s^2 \tilde{\mathbf{A}}'(\bar{\theta}) \tilde{\mathbf{A}}(\bar{\theta})^H (\tilde{\mathbf{A}}(\bar{\theta}) \tilde{\mathbf{A}}(\bar{\theta}) + \sigma_n^2 \mathbf{I})^{-1}, \quad (7)$$

where σ_s^2 is the average power of sources.

As discussed in [23], if the width of the interpolation sector, $2\theta_\varepsilon$ is too wide, the interpolation error may be unacceptable. To overcome this problem, we set the width of the interpolation sector to be equal to half of the main beam width of the VSNLA. The interval size $\delta\theta$ is chosen experimentally as described in [21].

The conventional iterative initial DOA estimation based array interpolation method, IMCA-AI [22], is applied to the VSNLA of coprime array for DOA estimation of sources as follows.

Step 1. Obtain the estimation of the covariance matrix of the real array \mathbf{R}_x :

$$\hat{\mathbf{R}}_x = \frac{1}{T} \sum_{t=1}^T \mathbf{x}(t) \mathbf{x}^H(t). \quad (8)$$

Step 2. Get vector $\tilde{\mathbf{z}}$ of the VSNLA from (4) and (5), and find the estimation of the covariance matrix of the VSNLA $\hat{\mathbf{R}}_{\tilde{\mathbf{z}}}$:

$$\hat{\mathbf{R}}_{\tilde{\mathbf{z}}} = \tilde{\mathbf{z}}\tilde{\mathbf{z}}^H. \quad (9)$$

Step 3. Extract the output samples of one continuous lags set of the VSNLA $\tilde{\mathbf{z}}_1$ from $\tilde{\mathbf{z}}$ to find the covariance matrix estimation $\hat{\mathbf{R}}_{\tilde{\mathbf{z}}_1}$ for spatial smoothing:

$$\hat{\mathbf{R}}_{\tilde{\mathbf{z}}_1} = \tilde{\mathbf{z}}_1 \tilde{\mathbf{z}}_1^H. \quad (10)$$

Step 4. Then apply the SS-MUSIC algorithm to $\hat{\mathbf{R}}_{\tilde{\mathbf{z}}_1}$ for the coarse initial DOA estimate $\hat{\boldsymbol{\theta}}$.

Step 5. Given $\hat{\boldsymbol{\theta}}$, construct \mathbf{B} from (7).

Step 6. Find the covariance matrix estimate of the virtual filled VSULA $\tilde{\mathbf{R}}_{\tilde{\mathbf{z}}} = \mathbf{B}\hat{\mathbf{R}}_{\tilde{\mathbf{z}}}\mathbf{B}^H$, and use the forward-backward spatial smoothing to find the DOA by the MUSIC algorithm.

Step 7. Use the estimated DOA in Step 4 and repeat Steps from 3 to 6 until the preset maximal number of iterations K_{\max} ($K_{\max} \geq 3$) is reached.

According to the above steps, the whole aperture of the VSNLA of the coprime array is used to get the DOA estimates after using array interpolation, which will significantly improve the DOA estimation precision. However, the key part of the IMCA-AI lies on the assumption that the reliable initial DOA estimates $\hat{\boldsymbol{\theta}}$ will be obtained in Step 4 with continuous lags in the VSNLA. When the number of sources is higher than $\lfloor M_c/2 \rfloor$, the SS-MUSIC algorithm fails to get the roughly initial DOA estimates of sources, thus causing unacceptable interpolation error and big DOA estimation bias. Therefore, the maximum number of resolvable sources using IMCA-AI is equal to half the number of continuous lags in the VSNLA.

3.2. Compressing Sensing for Coprime Array. Alternatively, (5) can be solved using the CS algorithm [5, 7, 9]. By discretizing the entire angular space from -90° to 90° as a grid $\boldsymbol{\Theta} = [\theta_1, \dots, \theta_D]^T$ with $\theta_{l+1} - \theta_l = 180^\circ/(D-1)$, for $l = 1, \dots, D$, where $D \gg K$, the model in (5) can be transformed into

$$\tilde{\mathbf{z}} = \tilde{\mathbf{A}}^\circ \mathbf{b}^\circ + \sigma_n^2 \mathbf{I}_{M_1} \mathbf{b}^\circ, \quad (11)$$

where $\tilde{\mathbf{A}}^\circ = [\tilde{\mathbf{a}}(\theta_1), \dots, \tilde{\mathbf{a}}(\theta_D)]$ is the overcomplete basis matrix for $\tilde{\mathbf{A}}$ parameterized by all the directions in set $\boldsymbol{\Theta}$ and \mathbf{b}° is the sparse representation of the source power vector in which only the positions of entries corresponding to the actual DOAs are occupied by nonzero entries. In addition, $\mathbf{B}^\circ = [\tilde{\mathbf{A}}^\circ, \mathbf{I}_{M_1}]$, and $\tilde{\mathbf{b}}^\circ = [\mathbf{b}^\circ, \sigma_n^2]^T$. Therefore, signal $\tilde{\mathbf{b}}^\circ$ is $K+1$ sparse in this setting. If $\tilde{\mathbf{b}}^\circ$ can be recovered from (11), the DOAs and σ_n^2 can be identified from the nonzero entries of $\tilde{\mathbf{b}}^\circ$.

Given the model in (11), DOA estimation proceeds in terms of sparse signal reconstruction by solving the following constrained minimization problem:

$$\begin{aligned} \hat{\tilde{\mathbf{b}}^\circ} &= \arg \underset{\tilde{\mathbf{b}}^\circ}{\text{minimize}} \quad \|\tilde{\mathbf{b}}^\circ\|_1 \\ &\text{subject to} \quad \|\tilde{\mathbf{z}} - \mathbf{B}^\circ \tilde{\mathbf{b}}^\circ\|_2 < \varepsilon, \end{aligned} \quad (12)$$

where ε is a user-specified bound which depends on the noise variance. This type of problem has been the objective of intensive studies in the area of CS, and various techniques can be used to solve the constrained minimization problem in (12), such as LASSO, BP, and OMP [7, 8, 26, 27]. In

[9, 28, 29], the LASSO algorithm was used to solve an equivalent problem to (12):

$$\hat{\mathbf{b}}^\circ = \arg \underset{\tilde{\mathbf{b}}^\circ}{\text{minimize}} \left[\frac{1}{2} \|\tilde{\mathbf{z}} - \mathbf{B}^\circ \tilde{\mathbf{b}}^\circ\|_2 + \lambda_t \|\tilde{\mathbf{b}}^\circ\|_1 \right], \quad (13)$$

where λ_t is a penalty parameter used to control the weight of the sparsity constraint in the overall cost function. According to [28], the maximum number of resolvable sources using LASSO equals the number of unique positive lags in the VSNLA of coprime array, that is, $\lfloor M_1/2 \rfloor$. However, it should be noted that the sparse model (11) is exact only when all the sources are located exactly on points in the grid set Θ ; otherwise, the compressed sensing suffers from dictionary mismatches and the performance is deteriorated [30].

3.3. Proposed Array Interpolation Based on Compressed Sensing for Coprime. From above analysis, we see that IMCI-AI has better DOA estimation accuracy than the SS-MUSIC algorithm. However, the maximum number of resolvable sources of these two methods is relatively smaller when compared with compressed sensing algorithm like LASSO. Since the true DOAs are unlikely to lie on the prespecified grid, no matter how finely it is chosen, the LASSO algorithm suffers from basis mismatch effects. A simple but effective way to improve the estimation accuracy and increase the maximum number of resolvable sources is to combine both advantages of IMCI-AI and the LASSO algorithm. Here, we propose a modified array interpolation based on compressed sensing for coprime array with holes in its virtual array. The proposed method uses LASSO to obtain the initial DOA estimate for iterative initial DOA estimation based array interpolation. Though basis mismatch may deteriorate the reconstruction performance of LASSO, the result of LASSO with bias can still be used as initial DOA estimate for the proposed method. The approach proposed for the VSNLA of coprime array is given as follows.

Step 1. Obtain the estimation of the covariance matrix of the real array \mathbf{R}_x .

Step 2. Use vector $\tilde{\mathbf{z}}$ of the VSNLA from (4) and (5), and find the estimation of the covariance matrix of the VSNLA $\hat{\mathbf{R}}_{\tilde{\mathbf{z}}}$.

Step 3. Apply the LASSO algorithm to $\tilde{\mathbf{z}}$ for the coarse initial DOA estimate $\hat{\boldsymbol{\theta}}$.

Step 4. Given $\hat{\boldsymbol{\theta}}$, construct \mathbf{B} from (7).

Step 5. Find the covariance matrix estimate of the virtual filled ULA $\hat{\mathbf{R}}_{\tilde{\mathbf{z}}}^l = \mathbf{B}\hat{\mathbf{R}}_{\tilde{\mathbf{z}}}\mathbf{B}^H$, and use the ESPRIT-Like algorithm proposed in [25] for coherent DOA estimation.

Step 6. Use estimated DOA in Step 5 and repeat Steps 3 and 4 until the preset maximal number of iterations K_{\max} ($K_{\max} \geq 3$) is reached.

Remark 1. Since the estimation of σ_n^2 for the VSNLA and the estimation of the average power of sources σ_s^2 in $\tilde{\mathbf{z}}$ are required in (7) for the construction of the map matrix \mathbf{B} .

TABLE 1: Comparison of the four methods for coprime array.

	SS-MUSIC	IMCA-AI	LASSO	The proposed method
Maximum number of resolvable sources	$\lfloor M_c/2 \rfloor$	$\lfloor M_c/2 \rfloor$	$\lfloor M_1/2 \rfloor$	$\lfloor M_1/2 \rfloor$
Accuracy	Low	High	Low (off-grid source)	High

The eigenvalue decomposition of the covariance matrix of the VSNLA $\hat{\mathbf{R}}_{\tilde{\mathbf{z}}}$ is used to yield

$$\hat{\mathbf{R}}_{\tilde{\mathbf{z}}} = \sum_m^{M_1} \lambda_m \mathbf{e}_m \mathbf{e}_m^H, \quad (14)$$

where $\lambda_1 \geq \lambda_2 \geq \dots \geq \lambda_K \geq \dots \geq \lambda_{M_1}$ are the eigenvalues of $\hat{\mathbf{R}}_{\tilde{\mathbf{z}}}$ and \mathbf{e}_m ($m = 1, \dots, M_1$) are corresponding eigenvectors. According to [31], the estimate of noise variance σ_n^2 can be obtained by averaging the $M_1 - K$ smallest eigenvalues. Similarly, the estimation of the average power of sources σ_s^2 can also be obtained by averaging the K largest eigenvalues.

Remark 2. The filled virtual ULA after interpolation using data of VSNLA is actually a virtual filled VSULA. The VSULA of CADiS has a total number of $M_\alpha = 2(MN + \widetilde{M}N - \widetilde{M} - 2N + L) + 1$ lags. The ESPRIT-Like algorithm [25] is used instead of MUSIC with forward-backward spatial smoothing for its simple computation and robust DOA estimation performance. Compared with LASSO, the proposed method can detect up to $\lfloor M_1/2 \rfloor$ sources with the filled VSULA, while it has no problem of basis mismatch problem. Table 1 summarizes the number of resolvable sources and angle accuracy using four methods.

Remark 3. The reliable coarse initial DOA estimate obtained using Step 3 is essential for the success of the subsequent DOA estimation. And it is noted that the source number K is assumed to be known a priori in this paper. The K largest peaks in the spectrum of LASSO are taken as detected sources. If the initial estimate has missed detections, the obtained small interpolation sectors fail to cover the missed sources inside, which leads to big interpolation errors in the directions of the missed sources, thus causing big DOA estimate bias for the missed sources, while these detected sources that are covered in the obtained small interpolation sectors can still be detected with increased DOA estimation bias. If the initial estimate using LASSO has spurious peaks with larger amplitude than that of true sources, the spurious peaks may be wrongly taken as sources while true sources with smaller amplitude will be lost. As a result, redundant interpolation sectors that cover the spurious peaks inside are used in the designed interpolation sectors, and the missed sources are not covered, which also leads to big interpolation errors.

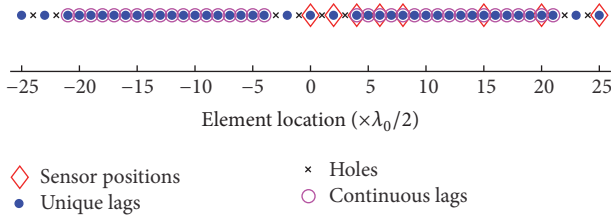


FIGURE 2: The VSOLA of a CADiS coarray with $M = 4$, $N = 5$, $p = 2$, $\bar{M} = 2$, and $L = 7$.

4. Simulation Results

In this section, computer simulations are performed to evaluate the proposed approach. Since the CADiS and other coprime array with holes in their VSOLA structures have the same problem. For simplicity, we only use the CADiS coprime array in the following simulations to demonstrate the advantages of the proposed method. A CADiS configuration with $M = 4$, $N = 5$ and $p = 2$ is considered and the displacement between the two subarrays is set as $L = \bar{M} + N = 7$. This configuration has $M + N - 1 = 8$ physical antenna sensors and the VSOLA corresponding to the CADiS is shown in Figure 2. The VSOLA has $M_1 = 43$ unique lags, among which, lags within $[-21, -4]$ and $[4, 21]$ are, respectively, continuous. After interpolation, the filled VSOLA has $M_\alpha = 51$ lags. Other existing methods are also listed for comparison, including SS-MUSIC [2], LASSO [5], IMCA-AI [22], sparsity-based extrapolation method (Sparse MUSIC) [6], coprime coarray interpolation technique using nuclear norm minimization (nuclear norm) [17], the off-grid DOA estimation method using sparse Bayesian inference (OGSBI) [13], and joint LASSO (JLASSO) [12]. The number of achievable DoFs is 9 for SS-MUSIC and IMCA-AI, while the number of achievable DoFs is 21 for LASSO, Sparse MUSIC, JLASSO, OGSBI, and the proposed approach. We take the grid from -90° to 90° with step size 1° to perform the proposed array interpolation method with off-grid sources. We perform both IMCA-AI and the proposed method with the maximum number of iterations $K_{\max} = 4$, and $\theta_e = [1^\circ, 0.5^\circ, 0.25^\circ, 0.125^\circ]$ is used at each iteration. The parameter λ_t used in LASSO is normally chosen by cross-validation [32]. These simulations are performed on a Windows 10 workstation with Intel Core i7-2600 3.4 GHz processor and 14 GB RAM.

4.1. Resolution Tests. In the first simulation, we test the resolution ability by detecting two closely located sources. The two off-grid uncorrelated narrowband sources are located at -31.45° and -28.65° , respectively. To compare the performance among the aforementioned eight methods, $T = 500$ snapshots are used. We perform the experiment with signal-to-noise ratio (SNR) that is equal to 0 dB and -10 dB for both sources with $\lambda_t = 0.25$ and $\lambda_t = 0.035$ for LASSO, respectively. The underlying DOAs are denoted in the figures by red dashed lines. We use black circle without amplitude to denote the DOA estimations of the proposed method for convenience in the following figures including Figures 3, 4, 6, and 8.

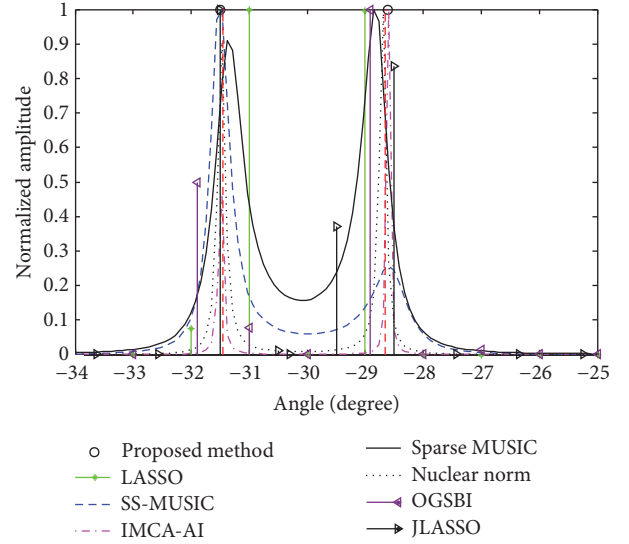


FIGURE 3: Resolution performance (SNR = 0 dB, $\lambda_t = 0.25$).

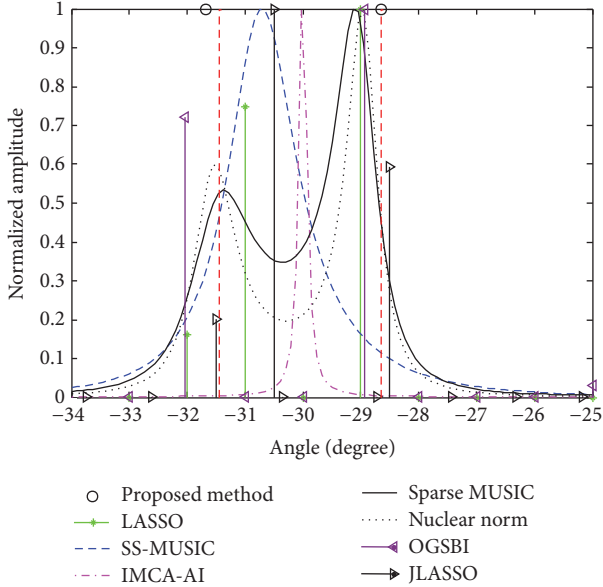
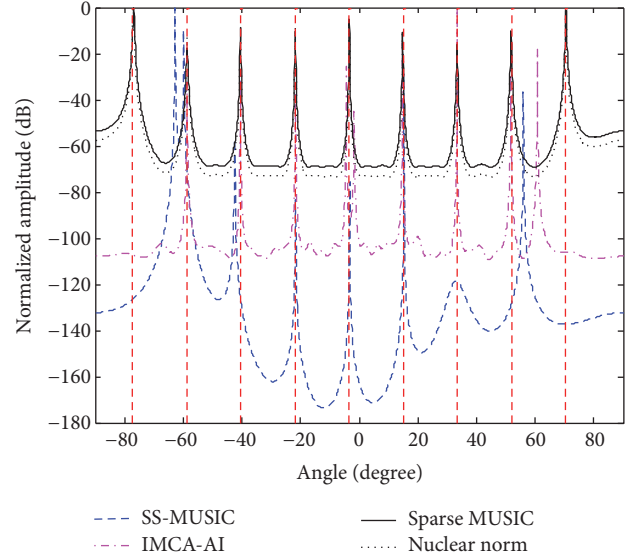
We can see from Figure 3 that both sources can be separated using all eight methods when SNR = 0 dB, while the proposed method, IMCA-AI, Sparse MUSIC, and nuclear norm have better resolution performance than SS-MUSIC because the whole aperture of VSOLA is used after using array interpolation. For the LASSO algorithm, relatively big DOA bias is caused by the dictionary mismatch effects; however, it can be used for the coarse initial DOA for the proposed method. Though the DOA estimations of OGSBI and JLASSO are closer to the true source DOA than that of LASSO, the proposed method has better estimation than OGSBI and JLASSO. Figure 4 shows that SS-MUSIC fails to separate two sources when SNR equals -10 dB, which also leads to the failure of IMCA-AI because the coarse initial DOAs of two sources are not obtained, only one source is detected with big bias, the obtained interpolation sector fails to cover both sources inside. However, other six algorithms succeed in separating both sources.

We compute the CPU time to run the eight algorithms on the same data for a quantitative comparison. The results are tabulated in Table 2. LASSO takes the shortest time while JLASSO takes the longest time because the time-consuming convex optimization is required. Nuclear norm also has the same problem with JLASSO in solving the reconstruction problem. The proposed method takes the second shortest time because ESPRIT-Like algorithm that avoids the spatial search is used in the last stage for the final DOA estimation. SS-MUSIC takes longer time than the proposed method because it uses spatial search. Sparse MUSIC takes longer time than LASSO and SS-MUSIC because it uses both LASSO and SS-MUSIC in the first and second stage, respectively. IMCA-AI and OGSBI take comparable time.

4.2. Detect Performance. In the second numerical experiment, we demonstrate that the proposed array interpolation method can detect more targets than SS-MUSIC and IMCA-AI. We consider $K = 9$ off-grid narrowband sources, which

TABLE 2: CPU times of the eight methods.

Algorithm	LASSO	Proposed method	SS-MUSIC	Sparse MUSIC	IMCA-AI	OGSBI	Nuclear norm	JLASSO
CPU time (s)	0.0118	0.0724	0.0940	0.0971	0.5049	0.5386	2.2018	3.6824

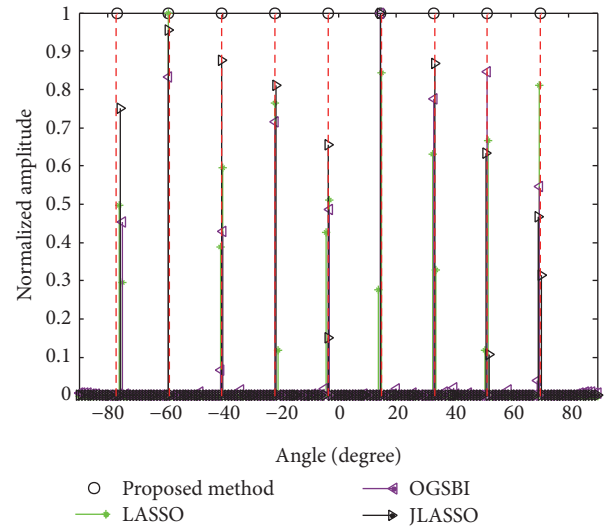
FIGURE 4: Resolution performance (SNR = -10 dB, $\lambda_t = 0.035$).FIGURE 5: Spatial spectra of MUSIC, IMCA-AI, Sparse MUSIC, and nuclear norm ($K = 9$).

is the maximum number that SS-MUSIC and IMCA-AI can detect theoretically. The 9 sources are uniformly distributed between -73.2° and 70.3° . The number of snapshots is $T = 500$, and the SNR is set to be 0 dB.

We can see from Figure 5 that one source is lost using both SS-MUSIC and IMCA-AI, while Sparse MUSIC and nuclear norm succeed in detecting all 9 sources. The proposed method, LASSO, OGSBI, and JLASSO can detect all 9 sources as shown in Figure 6, which is more than the number of physical sensors.

To further demonstrate that the proposed method can detect more targets, we consider $K = 14$ off-grid uncorrelated narrowband sources, which are uniformly distributed between -73.2° and 70.3° , and other simulation parameters are set as above. In this setting, SS-MUSIC is unable to produce a spectrum because the number of sources exceeds its limit. Therefore, IMCA-AI also fails because the initial DOA estimations are not obtained using SS-MUSIC. Figure 7 only shows the spatial spectra of Sparse MUSIC and nuclear norm, which shows that both methods succeed in detecting all sources. Figure 8 shows that JLASSO misses several sources, while the proposed method, LASSO, and OGSBI can also detect all 14 sources.

4.3. Estimation Accuracy. In the next experiment, we further compare the DOA estimation accuracy of all eight methods through 500 Mont Carlo trials by estimation $K = 2$ uncorrelated narrowband sources with an angle separation of 10° , and their directions are $-5^\circ + \varphi$ and $5^\circ + \varphi$, respectively,

FIGURE 6: Spatial spectra of LASSO, OGSBI, and the DOA results of the proposed method ($K = 9, \lambda_t = 0.25$).

with φ chosen uniformly and randomly in the range from -0.5° to 0.5° in each trial. The average root mean square error (RMSE) of the DOA estimate is used as the performance metric, which is index written by

$$\text{RMSE} = \sqrt{\frac{1}{500K} \sum_{m=1}^{500} \sum_{i=1}^K [\vartheta_i(m) - \theta_i]^2}, \quad (15)$$

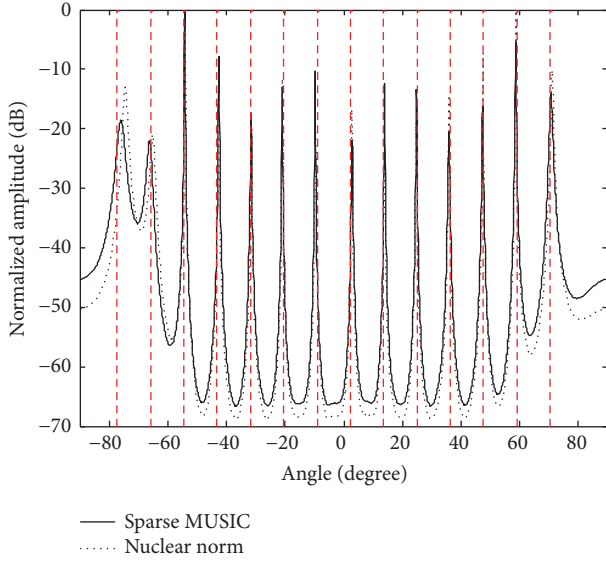


FIGURE 7: Spatial spectrums of Sparse MUSIC and nuclear norm ($K = 14$).

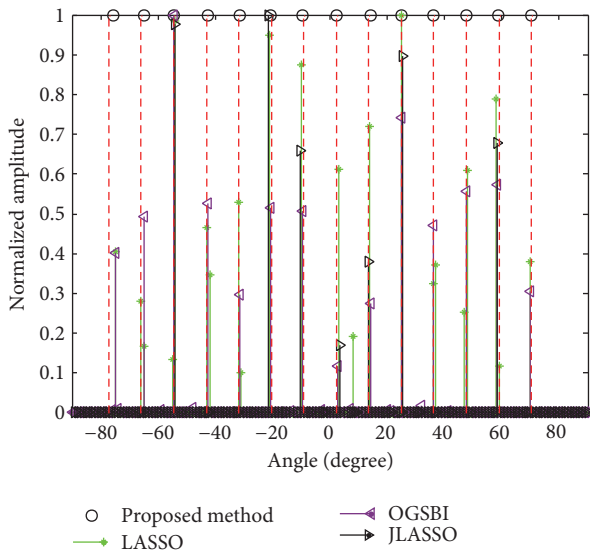


FIGURE 8: Spatial spectrums of LASSO, OGSBI, and the DOA results of the proposed method ($K = 14$, $\lambda_t = 0.25$).

where $\vartheta_i(m)$ denotes the estimate of θ_i for the m th Monte Carlo trial. The number of snapshots is $T = 300$. Figure 9 compares the RMSE performance as a function of the input SNR. We can see that the performance of LASSO does not improve with the increase of SNR due to basis mismatch effects. OGSBI has better performance than LASSO when SNR is above 1 dB, but it has bigger RMSE than other six methods when SNR is below 1 dB. Because IMCA-AI, Sparse MUSIC, nuclear norm, and the proposed method have made the most of the array aperture of the VSNLA after interpolation, they all have better performance than SS-MUSIC. The proposed method and IMCA-AI have better performance than two interpolation methods, while the proposed method

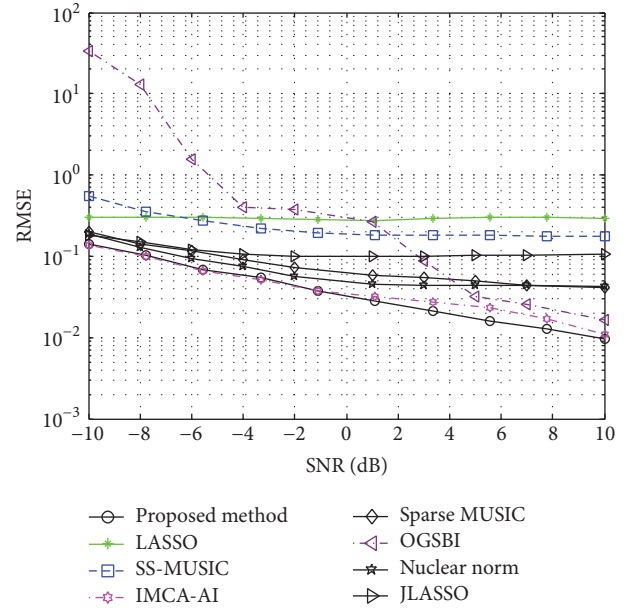


FIGURE 9: RMSE versus SNR ($T = 300$, $K = 2$).

achieves higher precision than IMCA-AI when SNR is above 0 dB.

In the last experiment, we fix the angle separation of the two sources at 10° and their SNR at 0 dB. When the snapshot number increases from 50 to 5000, the averaged DOA estimation RMSE curves of the all eight methods are shown in Figure 10. The proposed method and IMCA-AI have almost the same better performance than other six methods when the snapshots are more than about 550, while the proposed method has the lowest RMSE when the snapshot is low. LASSO has better performance than IMCA-AI and SS-MUSIC when the number of snapshot is low, while the performance of LASSO method does not improve with the increase of snapshots due to the basis mismatch effects. The OGSBI has slightly better performance than LASSO, while JLASSO has better performance than OGSBI. As the snapshot number increases, the DOA estimation precision of SS-MUSIC, Sparse MUSIC, and nuclear norm improves slowly, and these three methods have almost the same precision. However, both IMCA-AI and the proposed method surpass the other six methods.

5. Conclusion

A compressed sensing based array interpolation approach that uses the DOA estimation from compressing sensing method as initial DOA estimation is proposed to fill the holes in the VSNLA of coprime array, which can obtain a filled VSULA with more DoFs when the ESPRIT-Like algorithm is used. The proposed method can also be used to overcome the off-grid problem of CS. In addition, the proposed method can solve more sources compared with conventional initial DOA estimation based array interpolation method. Simulation results show the validity and efficiency of our proposed method.

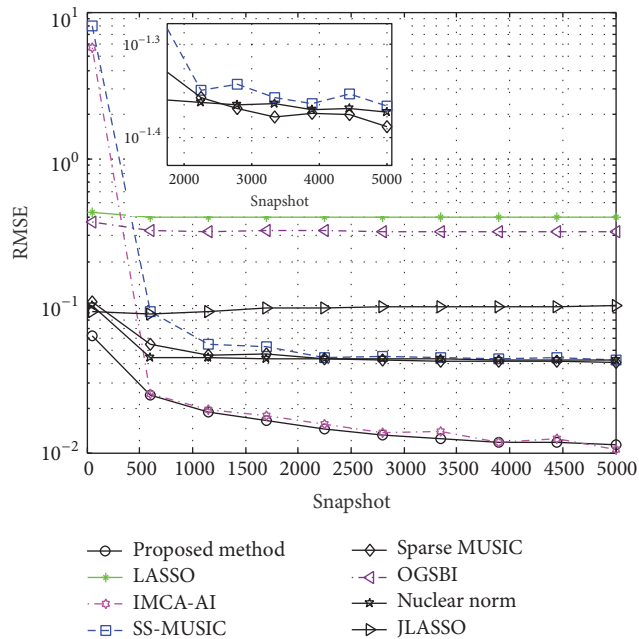


FIGURE 10: RMSE versus snapshot (SNR = 0, $K = 2$).

Competing Interests

The authors declare that there is no conflict of interests regarding the publication of this paper.

Acknowledgments

This work was supported by the National Natural Science Foundation of China under Grant no. 611711802 and no. 61032011.

References

- [1] R. O. Schmidt, "Multiple emitter location and signal parameter estimation," *IEEE Transactions on Antennas and Propagation*, vol. 34, no. 3, pp. 276–280, 1986.
- [2] P. Pal and P. P. Vaidyanathan, "Nested arrays: a novel approach to array processing with enhanced degrees of freedom," *IEEE Transactions on Signal Processing*, vol. 58, no. 8, pp. 4167–4181, 2010.
- [3] P. P. Vaidyanathan and P. Pal, "Sparse sensing with co-prime samplers and arrays," *IEEE Transactions on Signal Processing*, vol. 59, no. 2, pp. 573–586, 2011.
- [4] P. Pal and P. P. Vaidyanathan, "Coprime sampling and the music algorithm," in *Proceedings of the IEEE Digital Signal Processing Workshop and IEEE Signal Processing Education Workshop (DSP/SPE '11)*, pp. 289–294, Napa, Calif, USA, 2011.
- [5] S. Qin, Y. D. Zhang, and M. G. Amin, "Generalized coprime array configurations for direction-of-arrival estimation," *IEEE Transactions on Signal Processing*, vol. 63, no. 6, pp. 1377–1390, 2015.
- [6] E. BouDaher, F. Ahmad, and M. G. Amin, "Sparsity-based extrapolation for direction-of-arrival estimation using co-prime arrays," in *Compressive Sensing V: From Diverse Modalities to Big Data Analytics*, F. Ahmad, Ed., vol. 9857 of *Proceedings of SPIE*, Baltimore, Md, USA, April 2016.
- [7] J. A. Tropp and A. C. Gilbert, "Signal recovery from random measurements via orthogonal matching pursuit," *Transactions on Information Theory*, vol. 53, no. 12, pp. 4655–4666, 2007.
- [8] R. Tibshirani, "Regression shrinkage and selection via the lasso," *Journal of the Royal Statistical Society. Series B. Methodological*, vol. 58, no. 1, pp. 267–288, 1996.
- [9] Y. D. Zhang, M. G. Amin, and B. Himed, "Sparsity-based DOA estimation using co-prime arrays," in *Proceedings of the IEEE International Conference on Acoustics, Speech and Signal Processing (ICASSP '13)*, pp. 3967–3971, IEEE, Vancouver, Canada, May 2013.
- [10] P. Pal and P. P. Vaidyanathan, "On application of LASSO for sparse support recovery with imperfect correlation awareness," in *Proceedings of the 46th Asilomar Conference on Signals, Systems and Computers (ASILOMAR '12)*, pp. 958–962, Pacific Grove, Calif, USA, November 2012.
- [11] S. Qin, Y. D. Zhang, and M. G. Amin, "Generalized coprime array configurations," in *Proceedings of the IEEE 8th Sensor Array and Multichannel Signal Processing Workshop (SAM '14)*, pp. 529–532, A Coruna, Spain, June 2014.
- [12] Z. Tan and A. Nehorai, "Sparse direction of arrival estimation using co-prime arrays with off-grid targets," *IEEE Signal Processing Letters*, vol. 21, no. 1, pp. 26–29, 2014.
- [13] Z. Yang, L. Xie, and C. Zhang, "Off-grid direction of arrival estimation using sparse Bayesian inference," *IEEE Transactions on Signal Processing*, vol. 61, no. 1, pp. 38–43, 2013.
- [14] A. J. Weiss and B. Friedlander, "Performance analysis of spatial smoothing with interpolated arrays," in *Proceedings of the International Conference on Acoustics, Speech, and Signal Processing (ICASSP '91)*, vol. 2, pp. 1377–1380, San Francisco, Calif, USA, May 1991.
- [15] A. J. Weiss and B. Friedlander, "Performance analysis of spatial smoothing with interpolated arrays," *IEEE Transactions on Signal Processing*, vol. 41, no. 5, pp. 1881–1892, 1993.
- [16] E. BouDaher, Y. Jia, F. Ahmad, and M. G. Amin, "Multi-frequency co-prime arrays for high-resolution direction-of-arrival estimation," *IEEE Transactions on Signal Processing*, vol. 63, no. 14, pp. 3797–3808, 2015.
- [17] C.-L. Liu, P. P. Vaidyanathan, and P. Pal, "Coprime coarray interpolation for DOA estimation via nuclear norm minimization," in *Proceedings of the IEEE International Symposium on Circuits and Systems (ISCAS '16)*, pp. 2639–2642, May 2016.
- [18] B. Friedlander and A. J. Weiss, "Direction finding using spatial smoothing with interpolated arrays," *IEEE Transactions on Aerospace and Electronic Systems*, vol. 28, no. 2, pp. 574–587, 1992.
- [19] B. Friedlander and A. J. Weiss, "Direction finding for wideband signals using an interpolated array," in *Proceedings of the Conference Record of the 25th Asilomar Conference on Signals, Systems and Computers*, vol. 1, pp. 583–587, Pacific Grove, Calif, USA, November 1991.
- [20] B. Friedlander and A. J. Weiss, "Performance analysis of wide-band direction finding using interpolated arrays," in *Proceedings of the IEEE International Conference on Acoustics, Speech, and Signal Processing (ICASSP '92)*, vol. 4, pp. 457–460, 1992.
- [21] B. Friedlander, "The root-MUSIC algorithm for direction finding with interpolated arrays," *Signal Processing*, vol. 30, no. 1, pp. 15–29, 1993.
- [22] T. E. Tuncer, T. K. Yasar, and B. Friedlander, "Direction of arrival estimation for nonuniform linear arrays by using array interpolation," *Radio Science*, vol. 42, no. 4, Article ID RS4002, 2007.

- [23] B. Li, B. Xu, and Y. Yuan, "Preestimation-based array interpolation approach to coherent source localization using multiple sparse subarrays," *IEEE Signal Processing Letters*, vol. 16, no. 2, pp. 81–84, 2009.
- [24] Y. I. Abramovich, N. K. Spencer, and A. Y. Gorokhov, "Positive-definite Toeplitz completion in DOA estimation for nonuniform linear antenna arrays. II. Partially augmentable arrays," *IEEE Transactions on Signal Processing*, vol. 47, no. 6, pp. 1502–1521, 1999.
- [25] F.-M. Han and X.-D. Zhang, "An ESPRIT-like algorithm for coherent DOA estimation," *IEEE Antennas and Wireless Propagation Letters*, vol. 4, no. 1, pp. 443–446, 2005.
- [26] J. Wang, S. Kwon, P. Li, and B. Shim, "Recovery of sparse signals via generalized orthogonal matching pursuit: a new analysis," *IEEE Transactions on Signal Processing*, vol. 64, no. 4, pp. 1076–1089, 2016.
- [27] S. K. Sahoo and A. Makur, "Signal recovery from random measurements via extended orthogonal matching pursuit," *IEEE Transactions on Signal Processing*, vol. 63, no. 10, pp. 2572–2581, 2015.
- [28] E. BouDaher, F. Ahmad, and M. G. Amin, "Sparse reconstruction for direction-of-arrival estimation using multi-frequency co-prime arrays," *EURASIP Journal on Advances in Signal Processing*, vol. 2014, article no. 168, 2014.
- [29] Q. Shen, W. Liu, W. Cui, S. Wu, Y. D. Zhang, and M. G. Amin, "Low-complexity direction-of-arrival estimation based on wideband co-prime arrays," *IEEE Transactions on Audio, Speech and Language Processing*, vol. 23, no. 9, pp. 1445–1456, 2015.
- [30] Y. Chi, L. L. Scharf, A. Pezeshki, and A. R. Calderbank, "Sensitivity to basis mismatch in compressed sensing," *IEEE Transactions on Signal Processing*, vol. 59, no. 5, pp. 2182–2195, 2011.
- [31] C. El Kassis, J. Picheral, G. Fleury, and C. Mokbel, "Direction of arrival estimation using EM-ESPRIT with nonuniform arrays," *Circuits, Systems, and Signal Processing*, vol. 31, no. 5, pp. 1787–1807, 2012.
- [32] D. Malioutov, M. Cetin, and A. S. Willsky, "A sparse signal reconstruction perspective for source localization with sensor arrays," *IEEE Transactions on Signal Processing*, vol. 53, no. 8, pp. 3010–3022, 2005.

Research Article

Tensor-Based Methods for Blind Spatial Signature Estimation in Multidimensional Sensor Arrays

Paulo R. B. Gomes,¹ André L. F. de Almeida,¹ João Paulo C. L. da Costa,^{2,3,4}
João C. M. Mota,¹ Daniel Valle de Lima,² and Giovanni Del Galdo^{3,4}

¹Department of Teleinformatics Engineering, Federal University of Ceará, Fortaleza, CE, Brazil

²Department of Electrical Engineering, University of Brasília, DF, Brasília, Brazil

³Institute for Information Technology, Ilmenau University of Technology, Ilmenau, Germany

⁴Fraunhofer Institute for Integrated Circuits IIS, Erlangen, Germany

Correspondence should be addressed to Paulo R. B. Gomes; paulo@gtel.ufc.br

Received 10 September 2016; Accepted 15 January 2017; Published 15 February 2017

Academic Editor: Elias Aboutanios

Copyright © 2017 Paulo R. B. Gomes et al. This is an open access article distributed under the Creative Commons Attribution License, which permits unrestricted use, distribution, and reproduction in any medium, provided the original work is properly cited.

The estimation of spatial signatures and spatial frequencies is crucial for several practical applications such as radar, sonar, and wireless communications. In this paper, we propose two generalized iterative estimation algorithms to the case in which a multidimensional (R - D) sensor array is used at the receiver. The first tensor-based algorithm is an R - D blind spatial signature estimator that operates in scenarios where the source's covariance matrix is nondiagonal and unknown. The second tensor-based algorithm is formulated for the case in which the sources are uncorrelated and exploits the dual-symmetry of the covariance tensor. Additionally, a new tensor-based formulation is proposed for an L -shaped array configuration. Simulation results show that our proposed schemes outperform the state-of-the-art matrix-based and tensor-based techniques.

1. Introduction

High resolution parameter estimation plays a fundamental role in array signal processing and has practical applications in radar, sonar, mobile communications, and seismology. In light of this, several techniques have been developed to increase the accuracy of the estimated parameters, from which we may cite the classical *Multiple Signal Classification* (MUSIC) [1] and *Estimation of Signal Parameters via Rotational Invariance Technique* (ESPRIT) [2]. However, their performance can be further improved by exploiting the multidimensional structure of the data by means of tensor modeling, which can include several signal dimensions such as space, time, frequency, and polarization. Tensor decompositions have been successfully employed in array signal processing for parameters estimation since they provide better identifiability conditions when compared to conventional matrix-based methods. Another advantage of tensor-based methods is the so-called “tensor gain” which manifests itself with more precise parameter estimates due to the good

noise rejection capability of tensor-based signal processing, as shown in [3–6].

In regards to tensor-based methods for blind spatial signatures estimation, the *Parallel Factor* (PARAFAC) analysis decomposition [7] is widely applied due to its well-defined conditions for uniqueness [8]. As seen in [9], an iterative technique for PARAFAC decomposition such as *Trilinear Alternating Least Squares* (TALS) can be applied to estimate the directions of arrival of the sources. Closed-form solutions such as the Standard Tensor ESPRIT (STE) [10] and Closed-Form PARAFAC [11] are also appealing, since these exploit the multidimensional structure in a noniterative fashion. Recently in [12], an iterative algorithm was proposed in a manner similar to Independent Component Analysis (ICA) based on the Orthogonal Procrustes Problem (OPP) and Khatri-Rao factorization [13] for a PARAFAC decomposition with dual-symmetry. This solution exploits the dual-symmetry property of the data tensor and can be applied in covariance-based array signal processing techniques. The method proposed in [14] is based on the Tucker

decomposition [15] of a fourth-order covariance tensor and was elaborated for arrays with arbitrary structures, where a priori knowledge about the geometry of the sensor array is not required. However, a limitation of the method in [14] is the necessity of transmitting the same sequence of symbols in different time blocks, which results in a loss of spectral efficiency. The proposed solution is an algorithm for a multidimensional (R -D) sensor array in which the different dimensions of the array are exploited, thus dismissing the need to transmit a repeated sequence as in [14], as will be detailed later.

In this paper, two tensor-based approaches to the estimation of spatial signatures are presented. By using the signals received on a R -D sensor array, covariance tensors are calculated and solutions for correlated and uncorrelated sources are presented, respectively. For the former scenario, in which the source's covariance structure is nondiagonal and unknown, the covariance tensor of the received data is formulated as a Tucker decomposition of order $2R$. Such a formulation yields a generalized Tucker model based R -D sensor array processing that deals with arbitrary source covariance structures. By assuming uncorrelated sources, we then show that the problem boils down to a PARAFAC decomposition, from which a method that exploits the dual-symmetry property of the covariance tensor is derived by considering the ideas rooted in [12]. For both Tucker and PARAFAC based models, the blind estimation of the spatial signatures is achieved by means of an alternating least squares (ALS) algorithm. The contributions of this paper are twofold: (i) we propose a covariance-based generalization of the Tucker decomposition for the blind spatial signature estimation problem with R -D sensor arrays and (ii) we establish a link between dual-symmetry decompositions and techniques based on covariance-based array signal processing for parameter estimation. The performance of the proposed algorithms is evaluated by Monte Carlo simulations, corroborating their gains over competing state-of-the-art matrix-based and tensor-based techniques.

The rest of this paper is organized as follows: Section 2 briefly introduces tensor operations and decompositions. The signal model for an R -D sensor array is then presented in Section 3. In Section 4 a novel covariance-based tensor model for the received data is formulated and our blind spatial signature estimation algorithms are formulated. In Section 5 an approach for L -shaped sensor arrays is proposed. The computational complexity of the proposed methods is analyzed in Section 6. In Section 7, the advantages and disadvantages of the proposed methods are discussed. Simulation results are provided in Section 8, and the conclusions are drawn in Section 9.

Notation. Scalar values are represented by lowercase letters a , vectors by bold lowercase letters \mathbf{a} , matrices by bold uppercase letters \mathbf{A} , and tensors by calligraphic letters \mathcal{A} . The symbols T , H , \dagger , and $*$ represent the transpose, conjugate transpose, pseudoinverse, and complex conjugate operations, respectively. $\text{diag}(\mathbf{a})$ operator generates a diagonal matrix from a vector \mathbf{a} . The i th row of $\mathbf{A} \in \mathbb{C}^{I \times R}$ is represented by $\mathbf{A}(i, :)$ $\in \mathbb{C}^{1 \times R}$, while its r th column is represented by

$\mathbf{A}(:, r) \in \mathbb{C}^{I \times 1}$. $\text{vec}(\mathbf{A})$ operator converts \mathbf{A} into a vector $\mathbf{a} \in \mathbb{C}^{IR \times 1}$, while $\text{unvec}_{I \times R}(\mathbf{a})$ converts \mathbf{a} into a $I \times R$ matrix. $\mathbf{D}_i(\mathbf{A})$ stands for a diagonal matrix constructed from the i th row of \mathbf{A} . $\|\cdot\|_F$ stands for the Frobenius norm of a matrix or tensor. “ \circ ” operator stands for the vector outer product. The Kronecker product is represented by \otimes . The Khatri-Rao product between the matrices $\mathbf{A} \in \mathbb{C}^{I \times R}$ and $\mathbf{B} \in \mathbb{C}^{J \times R}$, represented by \diamond , is defined as

$$\mathbf{A} \diamond \mathbf{B} = [\mathbf{A}(:, 1) \otimes \mathbf{B}(:, 1), \dots, \mathbf{A}(:, R) \otimes \mathbf{B}(:, R)]. \quad (1)$$

2. Tensor Preliminaries

In the following, we briefly introduce for convenience the basics on operations involving tensors and tensor decompositions, which refer to [16, 17]. Firstly, we present the Tucker decomposition. Then, the PARAFAC decomposition is introduced and issues involving uniqueness are briefly discussed for both cases, which will be useful later. Then, we introduce the dual-symmetry property for these decompositions. The basic material presented in this section is exploited in later sections in the context of our blind spatial signature estimation problem.

2.1. Basic Tensor Operations. Let $\mathcal{X} \in \mathbb{C}^{I_1 \times \dots \times I_N}$ denote an N th order tensor, (i_1, \dots, i_N) th entry of which is denoted by x_{i_1, \dots, i_N} . The fibers are the higher-order analogues of matrix rows and columns. The n -mode fibers of \mathcal{X} are vectors of size I_n defined by fixing every index but i_n . The n -mode unfolding operation, denoted by $[\mathcal{X}]_{(n)}$, stands for the process of reordering the elements of \mathcal{X} into a matrix by arranging its n -mode fibers to be the columns of the resulting matrix. The n -mode product between \mathcal{X} and a matrix $\mathbf{A} \in \mathbb{C}^{J \times I_n}$ along of the n th mode, denoted by $\mathcal{X} \times_n \mathbf{A}$, is a tensor of size $I_1 \times \dots \times I_{n-1} \times J \times I_{n+1} \times \dots \times I_N$, obtained by taking the inner product between each n -mode fiber and the rows of the matrix \mathbf{A} ; that is, [16, 17]

$$\begin{aligned} \mathcal{Y} &= \mathcal{X} \times_n \mathbf{A} \iff \\ [\mathcal{Y}]_{(n)} &= \mathbf{A} [\mathcal{X}]_{(n)}. \end{aligned} \quad (2)$$

2.2. Tucker Decomposition. The Tucker decomposition [15] represents a tensor $\mathcal{X} \in \mathbb{C}^{I_1 \times \dots \times I_N}$ of order N as a multilinear transformation of a core tensor $\mathcal{G} \in \mathbb{C}^{R_1 \times \dots \times R_N}$ by factor matrices $\mathbf{A}^{(n)} = [\mathbf{a}_1^{(n)}, \mathbf{a}_2^{(n)}, \dots, \mathbf{a}_{R_n}^{(n)}] \in \mathbb{C}^{I_n \times R_n}$ along each mode $n = 1, 2, \dots, N$. In scalar form, the N th order Tucker decomposition is given by

$$x_{i_1, i_2, \dots, i_N} = \sum_{r_1=1}^{R_1} \sum_{r_2=1}^{R_2} \dots \sum_{r_N=1}^{R_N} g_{r_1, r_2, \dots, r_N} a_{i_1, r_1}^{(1)} a_{i_2, r_2}^{(2)} \dots a_{i_N, r_N}^{(N)}, \quad (3)$$

where $a_{i_n, r_n}^{(n)}$ is (i_n, r_n) th entry of the n th mode factor matrix $\mathbf{A}^{(n)} \in \mathbb{C}^{I_n \times R_n}$ and g_{r_1, r_2, \dots, r_N} is (r_1, \dots, r_N) th entry of the core tensor $\mathcal{G} \in \mathbb{C}^{R_1 \times \dots \times R_N}$. Using n -mode product notation, the Tucker decomposition can be written as

$$\mathcal{X} = \mathcal{G} \times_1 \mathbf{A}^{(1)} \times_2 \mathbf{A}^{(2)} \dots \times_N \mathbf{A}^{(N)}, \quad (4)$$

which admits the following factorization in terms of the factor matrices and core tensor:

$$[\mathcal{X}]_{(n)} = \mathbf{A}^{(n)} [\mathcal{G}]_{(n)} \left(\mathbf{A}^{(N)} \otimes \dots \otimes \mathbf{A}^{(n+1)} \otimes \mathbf{A}^{(n-1)} \otimes \dots \otimes \mathbf{A}^{(1)} \right)^T. \quad (5)$$

In general, the Tucker decomposition is not unique; that is, there are infinite solutions for $\mathbf{A}^{(n)}$, $n = 1, \dots, N$, and \mathcal{G} that yield the same reconstructed version of the data tensor \mathcal{X} . However, in special cases where several elements of the core tensor are constrained to be equal to zero, that is, if the core tensor has some sparsity, the number of solutions may be finite, and the associated factor matrices and core tensor become unique up to trivial permutations and scaling ambiguities [18]. The Tucker based methods presented in Sections 4.2 and 5.1 belong to a special category where unique solutions exist.

2.3. PARAFAC Decomposition. The PARAFAC decomposition [7] expresses a tensor $\mathcal{X} \in \mathbb{C}^{I_1 \times \dots \times I_N}$ as a sum of R rank-one tensors; that is,

$$\mathcal{X} = \sum_{r=1}^R \mathbf{a}_r^{(1)} \circ \mathbf{a}_r^{(2)} \circ \dots \circ \mathbf{a}_r^{(N)}, \quad (6)$$

where R is the number of factors, also known as the *rank* of the decomposition, and is defined as the minimum number of rank-one tensors that yield \mathcal{X} exactly.

The N th order PARAFAC decomposition (6) can be seen as a special case of the Tucker decomposition (4) with a core tensor $\mathcal{G} = \mathcal{I}_{N,R}$ and $R_n = R$ for $n = 1, \dots, N$. The elements of the N th order identity tensor $\mathcal{I}_{N,R}$ are equal to one when all indices are equal and zero elsewhere. Using the n -mode product notation, the PARAFAC decomposition can be written as

$$\mathcal{X} = \mathcal{I}_{N,R \times 1} \times_1 \mathbf{A}^{(1)} \times_2 \mathbf{A}^{(2)} \dots \times_N \mathbf{A}^{(N)}, \quad (7)$$

while the n -mode unfolding of \mathcal{X} can be expressed as

$$[\mathcal{X}]_{(n)} = \mathbf{A}^{(n)} \left(\mathbf{A}^{(N)} \diamond \dots \diamond \mathbf{A}^{(n+1)} \diamond \mathbf{A}^{(n-1)} \diamond \dots \diamond \mathbf{A}^{(1)} \right)^T. \quad (8)$$

The N th order PARAFAC decomposition is unique up to permutation and scaling ambiguities affecting the columns of factors matrices $\mathbf{A}^{(n)} \in \mathbb{C}^{I_n \times R}$, $n = 1, \dots, N$, if the following sufficient condition is satisfied [19]:

$$\sum_{n=1}^N \kappa_{\mathbf{A}^{(n)}} \geq 2R + N - 1, \quad (9)$$

where $\kappa_{\mathbf{A}^{(n)}}$ denotes the Kruskal-rank of $\mathbf{A}^{(n)}$, defined as the maximum value κ such that any subset of κ columns is linearly independent [20].

Throughout this work, special attention is given to dual-symmetric tensors. The PARAFAC decomposition of a given tensor $\mathcal{X} \in \mathbb{C}^{I_1 \times \dots \times I_{2N}}$ of order $2N$ is said to have dual-symmetry if defined as follows:

$$\mathcal{X} = \mathcal{I}_{2N,R \times 1} \times_1 \mathbf{A}^{(1)} \times_2 \mathbf{A}^{(2)} \dots \times_N \mathbf{A}^{(N)} \times_{N+1} \mathbf{A}^{(1)*} \times_{N+2} \mathbf{A}^{(2)*} \dots \times_{2N} \mathbf{A}^{(N)*}. \quad (10)$$

Note that this definition also applies to Tucker decomposition by simply replacing the identity tensor $\mathcal{I}_{2N,R}$ by an arbitrary core tensor \mathcal{G} of order $2N$.

3. Signal Model

We consider K snapshots originating from the superposition of M far-field narrowband signal sources sampled by a R -dimensional sensor array of size $N_1 \times N_2 \times \dots \times N_R$, where N_r is the size of the r th array dimension, $r = 1, \dots, R$. The matrix $\mathbf{X} \in \mathbb{C}^{N \times K}$ collects the samples received by the sensor array, which can be factored as [10]

$$\mathbf{X} = \left(\mathbf{A}^{(1)} \diamond \mathbf{A}^{(2)} \dots \diamond \mathbf{A}^{(R)} \right) \mathbf{S} + \mathbf{V}, \quad (11)$$

where

- (i) $\mathbf{A} = \mathbf{A}^{(1)} \diamond \mathbf{A}^{(2)} \dots \diamond \mathbf{A}^{(R)} \in \mathbb{C}^{N \times M}$ is the spatial signature matrix of the R -D array for $r = 1, \dots, R$ and $N = \prod_{r=1}^R N_r$;
- (ii) $\mathbf{A}^{(r)} = [\mathbf{a}_1^{(r)}, \dots, \mathbf{a}_M^{(r)}] \in \mathbb{C}^{N_r \times M}$ is the spatial signature matrix of the r th dimension;
- (iii) $\mathbf{a}_m^{(r)} = [1 \ e^{j\mu_m^{(r)}} \ e^{j2\mu_m^{(r)}} \ \dots \ e^{j(N_r-1)\mu_m^{(r)}}]^T \in \mathbb{C}^{N_r \times 1}$ is the array response in the r th dimension to the m th planar wavefront ($m = 1, \dots, M$) which is function of the spatial frequency $\mu_m^{(r)}$;
- (iv) $\mathbf{S} = [\mathbf{s}(1), \dots, \mathbf{s}(K)] \in \mathbb{C}^{M \times K}$ is the matrix containing the signal transmitted by the sources;
- (v) $\mathbf{V} = [\mathbf{v}(1), \dots, \mathbf{v}(K)] \in \mathbb{C}^{N \times K}$ is the additive white Gaussian noise (assumed uncorrelated to the source signals).

From (11), the sample covariance matrix $\widehat{\mathbf{R}} \in \mathbb{C}^{N \times N}$ of the signals received at the sensor array is given by

$$\begin{aligned} \widehat{\mathbf{R}} &\triangleq \frac{1}{K} \mathbf{X} \mathbf{X}^H \approx \mathbf{A} \mathbf{R}_s \mathbf{A}^H + \sigma_v^2 \mathbf{I} \\ &\approx \left(\mathbf{A}^{(1)} \diamond \dots \diamond \mathbf{A}^{(R)} \right) \mathbf{R}_s \left(\mathbf{A}^{(1)} \diamond \dots \diamond \mathbf{A}^{(R)} \right)^H \\ &\quad + \sigma_v^2 \mathbf{I}, \end{aligned} \quad (12)$$

where $\mathbf{R}_s = (1/K) \mathbf{S} \mathbf{S}^H$ is the sample covariance matrix of the source signals and σ_v^2 is the noise variance.

4. Tensor-Based Methods for Blind Spatial Signature Estimation

In this section, we propose two iterative algorithms to solve the blind spatial signature estimation problem in R -D sensor arrays. Initially, a novel multidimensional structure is formulated from the covariance matrix of the received data. Then, an alternating least squares- (ALS-) based algorithm for a Tucker decomposition of order $2N$ is proposed. Finally, we derive a link between the method in [12] and a covariance-based blind spatial signature estimation problem.

4.1. Novel Covariance Tensor. With the intention of exploiting the multidimensional structure of the received signal, the noiseless sample covariance matrix (12), given by $\mathbf{R}_o = \widehat{\mathbf{R}} - \sigma_v^2 \mathbf{I} \in \mathbb{C}^{N \times N}$, is interpreted as a multimode unfolding of the noiseless covariance tensor $\mathcal{R}_o \in \mathbb{C}^{N_1 \times N_2 \times \dots \times N_R \times N_1 \times N_2 \times \dots \times N_R}$ of order $2N$, defined as

$$\mathcal{R}_o = \mathcal{R}_s \times_1 \mathbf{A}^{(1)} \times_2 \mathbf{A}^{(2)} \cdots \times_R \mathbf{A}^{(R)} \times_{R+1} \mathbf{A}^{(1)*} \times_{R+2} \mathbf{A}^{(2)*} \cdots \times_{2R} \mathbf{A}^{(R)*}, \quad (13)$$

where \mathcal{R}_s is the source covariance tensor, which has $2R$ dimensions, each of size M . Note that this tensor is dual-symmetric; that is, the factor matrix related to $(R+r)$ th dimension is equal to $\mathbf{A}^{(r)*}$, and $N_r = N_{R+r}$ ($r = 1, \dots, R$). The m th frontal slice of \mathcal{R}_s is a diagonal matrix whose main diagonal is given by the m th column of the covariance matrix \mathbf{R}_s . For instance, considering $R = 2$ for the sake of notation, the following expression satisfies the relationship previously cited:

$$\mathcal{R}_s(:, :, m, m) = \text{diag}(\mathbf{R}_s(:, m)) \quad m = 1, \dots, M, \quad (14)$$

where the matrix $\mathcal{R}_s(:, :, m, m) \in \mathbb{C}^{M \times M}$ denotes the m th frontal slice of the covariance tensor \mathcal{R}_s obtained by fixing its last two modes. The tensor \mathcal{R}_o follows a dual-symmetric Tucker decomposition of order $2R$ with factor matrices $\mathbf{A}^{(r)}$ and $\mathbf{A}^{(r)*}$, $r = 1, \dots, R$, and core tensor \mathcal{R}_s .

Considering the case in which the sources are uncorrelated and have unitary variance, we can rewrite (13) as

$$\mathcal{R}_o = \mathcal{I}_{2R, M} \times_1 \mathbf{A}^{(1)} \times_2 \mathbf{A}^{(2)} \cdots \times_R \mathbf{A}^{(R)} \times_{R+1} \mathbf{A}^{(1)*} \times_{R+2} \mathbf{A}^{(2)*} \cdots \times_{2R} \mathbf{A}^{(R)*}, \quad (15)$$

where $\mathcal{I}_{2R, M}$ is the identity tensor of order $2R$ in which each dimension has size M . In this case, the covariance tensor \mathcal{R}_o follows a dual-symmetric PARAFAC decomposition of order $2R$.

In general, the Tucker decomposition does not impose restrictions on the core tensor structure, which makes this model more flexible. In the context of this paper, this characteristic reflects an arbitrary and unknown structure for the source's covariance \mathbf{R}_s which can also be estimated from (13). In contrast, the PARAFAC decomposition (15) denotes a particular case of the Tucker decomposition when the sources' signals are uncorrelated and the source covariance matrix is perfectly known (i.e., diagonal). In practice, this may not hold.

4.2. ALS-Tucker Algorithm. Our goal is to blindly estimate the spatial signature matrices $\mathbf{A}^{(r)}$ and $\mathbf{A}^{(r)*}$, ($r = 1, \dots, R$) which refer to the different dimensions of the sensor array from the covariance tensor \mathcal{R}_o . For the sake of simplicity, from this point on, we consider $\mathbf{A}^{(R+r)} = \mathbf{A}^{(r)*}$. In matrix-based notation, the Tucker decomposition (13) allows the following factorization in terms of its factor matrices and core tensor in accordance with (5):

$$[\mathcal{R}_o]_{(r)} = \mathbf{A}^{(r)} \Delta^{(r)}, \quad (16)$$

where

$$\Delta^{(r)} = [\mathcal{R}_s]_{(r)} \cdot (\mathbf{A}^{(2R)} \otimes \dots \otimes \mathbf{A}^{(r+1)} \otimes \mathbf{A}^{(r-1)} \otimes \dots \otimes \mathbf{A}^{(1)})^T, \quad (17)$$

while $[\mathcal{R}_o]_{(r)}$ and $[\mathcal{R}_s]_{(r)}$, $r = 1, \dots, 2R$, denote the n -mode unfolding of the covariance tensor \mathcal{R}_o and the core tensor \mathcal{R}_s , respectively.

From the matrix unfoldings of \mathcal{R}_o , an ALS based algorithm is formulated to estimate the desired factor matrices. An estimate of the spatial signature matrix $\widehat{\mathbf{A}}^{(r)}$ ($r = 1, \dots, 2R$), associated with the r th dimension of the covariance tensor, is obtained by solving the following least squares (LS) problem:

$$\widehat{\mathbf{A}}^{(r)} = \arg \min_{\mathbf{A}^{(r)}} \left\| [\mathcal{R}_o]_{(r)} - \mathbf{A}^{(r)} \Delta^{(r)} \right\|_F^2, \quad (18)$$

whose analytic solution is given by

$$\widehat{\mathbf{A}}^{(r)} = [\mathcal{R}_o]_{(r)} (\Delta^{(r)})^\dagger. \quad (19)$$

As discussed in Section 4.1, the Tucker decomposition does not impose restrictions on the structure of the core tensor and its estimation becomes necessary. Let $\widehat{\mathbf{R}}_s$ be an unknown matrix of arbitrary structure. The following LS problem is formulated from the vectorization of the sample covariance matrix $\widehat{\mathbf{R}}$:

$$\text{vec}(\widehat{\mathbf{R}}_s) = \arg \min_{\mathbf{R}_s} \left\| \text{vec}(\widehat{\mathbf{R}}) - (\mathbf{A}^* \otimes \mathbf{A}) \text{vec}(\mathbf{R}_s) \right\|_F^2, \quad (20)$$

from which an estimate of $\widehat{\mathbf{R}}_s$ can be obtained as

$$\text{vec}(\widehat{\mathbf{R}}_s) = (\mathbf{A}^* \otimes \mathbf{A})^\dagger \text{vec}(\widehat{\mathbf{R}}), \quad (21)$$

where $\mathbf{A} = \mathbf{A}^{(1)} \diamond \mathbf{A}^{(2)} \cdots \diamond \mathbf{A}^{(R)} \in \mathbb{C}^{N \times M}$.

Since (19) and (21) are nonlinear functions of the parameters to be estimated, the blind spatial signature estimation problem can be solved using a classical ALS iterative solution [21, 22]. The basic idea of the algorithm is to estimate one factor matrix at each step while the others remain fixed at the values obtained in previous steps. This procedure is repeated until convergence. The proposed generalized ALS-Tucker algorithm for R -D sensor arrays is summarized in Algorithm 1.

In this approach the factor matrices are treated as independent variables; that is, the dual-symmetry property of the covariance tensor is not exploited. In this case, a final estimate of the spatial signature matrix associated with the r th dimension of the array is given by

$$\widehat{\mathbf{A}}_{\text{final}}^{(r)} = \frac{\widehat{\mathbf{A}}^{(r)} + \widehat{\mathbf{A}}^{(R+r)*}}{2}. \quad (22)$$

4.3. ALS-ProKraft Algorithm. In this section, a link is established between the ALS-ProKraft algorithm proposed initially in [12] and blind spatial signature estimation in

```

(1) Initialize  $\widehat{\mathbf{A}}^{(r)} \in \mathbb{C}^{N_r \times M}$  for  $r = 2, \dots, 2R$  and the core
    tensor  $\widehat{\mathcal{R}}_s$  randomly.
(2) for  $r = 1, \dots, 2R$  do
    According to (19), obtain an estimate for the matrix  $\widehat{\mathbf{A}}^{(r)}$ :
     $\widehat{\mathbf{A}}^{(r)} = [\mathcal{R}]_{(r)}(\Delta^{(r)})^\dagger$ .
    Note. The matrix  $\Delta^{(r)}$ , described in (17), is updated
    by fixing  $\widehat{\mathbf{A}}^{(r)}$  calculated previously.
    end
(3) According to (21), obtain an estimate for  $\widehat{\mathbf{R}}_s$ :
     $\text{vec}(\widehat{\mathbf{R}}_s) = (\mathbf{A}^* \otimes \mathbf{A})^\dagger \text{vec}(\widehat{\mathbf{R}})$ ;
     $\widehat{\mathbf{R}}_s = \text{unvec}_{M \times M}(\text{vec}(\widehat{\mathbf{R}}_s))$ .
(4) Using (14), reconstruct the core tensor  $\widehat{\mathcal{R}}_s$  from  $\widehat{\mathbf{R}}_s$ .
(5) Repeat Steps (2)–(4) until convergence.

```

ALGORITHM 1: Summary of the ALS-Tucker algorithm.

array signal processing. The main idea behind this algorithm is to exploit the dual-symmetry property of the PARAFAC decomposition described in (15). Next, the ALS-ProKRaft algorithm is formulated in the context of this work. A more detailed description of the method can be found in the original reference.

The multimode unfolding of the PARAFAC decomposition in (15) can be rewritten as

$$\mathbf{R}_{\text{mm}} = (\mathbf{A}^{(1)} \diamond \dots \diamond \mathbf{A}^{(R)}) (\mathbf{A}^{(1)} \diamond \dots \diamond \mathbf{A}^{(R)})^H, \quad (23)$$

which assumes the following factorization:

$$\mathbf{R}_{\text{mm}} = \mathbf{R}_{\text{mm}}^{1/2} \cdot (\mathbf{R}_{\text{mm}}^{1/2})^H, \quad (24)$$

where $\mathbf{R}_{\text{mm}}^{1/2} \in \mathbb{C}^{N \times M}$ can be obtained from the singular value decomposition of \mathbf{R}_{mm} given by

$$\mathbf{R}_{\text{mm}} = \mathbf{U} \cdot \mathbf{\Sigma} \cdot \mathbf{V}^H, \quad (25)$$

obeying the following structure:

$$\mathbf{R}_{\text{mm}}^{1/2} = \mathbf{U}^{[M]} \cdot \mathbf{\Sigma}^{[M]} \cdot \mathbf{T}^H = (\mathbf{A}^{(1)} \diamond \dots \diamond \mathbf{A}^{(R)}), \quad (26)$$

where $\mathbf{U}^{[M]} \in \mathbb{C}^{N \times M}$ is formed by the first M columns of \mathbf{U} and $\mathbf{\Sigma}^{[M]} \in \mathbb{C}^{M \times M}$ is a diagonal matrix which contains the M dominant singular values of \mathbf{R}_{mm} . The matrix \mathbf{T} represents a unitary rotation factor.

Equation (26) describes an orthogonal Procrustes problem (OPP) [23], in which \mathbf{T} is a transformation matrix that maps $\mathbf{U}^{[M]} \cdot \mathbf{\Sigma}^{[M]}$ to $(\mathbf{A}^{(1)} \diamond \dots \diamond \mathbf{A}^{(R)})$ such that $\mathbf{U}^{[M]} \cdot \mathbf{\Sigma}^{[M]} \cdot \mathbf{T}^H = (\mathbf{A}^{(1)} \diamond \dots \diamond \mathbf{A}^{(R)})$. An efficient estimate for \mathbf{T} is obtained minimizing the Frobenius norm of the residual error:

$$\arg \min_{\mathbf{T}} \left\| \mathbf{U}^{[M]} \cdot \mathbf{\Sigma}^{[M]} \cdot \mathbf{T}^H - (\mathbf{A}^{(1)} \diamond \dots \diamond \mathbf{A}^{(R)}) \right\|_F. \quad (27)$$

This problem can be solved using a change of basis from the singular value decomposition of the matrix

$$(\mathbf{A}^{(1)} \diamond \dots \diamond \mathbf{A}^{(R)})^H \cdot \mathbf{U}^{[M]} \cdot \mathbf{\Sigma}^{[M]} = \mathbf{U}_P \cdot \mathbf{\Sigma}_P \cdot \mathbf{V}_P^H, \quad (28)$$

which leads to the following solution [23]:

$$\widehat{\mathbf{T}} = \mathbf{U}_P \cdot \mathbf{V}_P^H. \quad (29)$$

From (26) and (29), an ALS-based iterative algorithm is formulated to estimate the spatial signature matrices from the PARAFAC decomposition (15). Firstly, individual estimates for each factor matrix $\widehat{\mathbf{A}}^{(r)}$, $r = 1, \dots, R$, are obtained by applying the multidimensional LS Khatri-Rao factorization (LS-KRF) algorithm on the composite spatial signature matrix $\widehat{\mathbf{A}} = \widehat{\mathbf{A}}^{(1)} \diamond \widehat{\mathbf{A}}^{(2)} \dots \diamond \widehat{\mathbf{A}}^{(R)}$. Then, the matrix $\widehat{\mathbf{T}}$ is obtained from (29). For more details and access to the pseudocode of this algorithm, we refer the interested reader to [12]. The ALS-ProKRaft algorithm for blind spatial signature estimation in R -D sensor arrays is summarized in Algorithm 2.

Note that when compared with conventional ALS-based PARAFAC solutions [21] formulated from the unfolding matrices (8), the ALS-ProKRaft algorithm becomes preferred since only half of the factors matrices needs to be estimated by exploiting the dual-symmetry property of the covariance tensor. This generally leads to a fast convergence rate of the algorithm.

5. Spatial Signature Estimation in L -Shaped Sensor Arrays

In this section, the blind spatial signature estimation problem is formulated for L -shaped array configuration. Considering that the receiver array is divided into smaller subarrays, the Tucker decomposition of a fourth-order tensor is formulated from the sample cross-correlation matrix of the data received by the different subarrays. From this multidimensional structure the proposed generalized ALS-Tucker algorithm previously presented in Section 4.2 can be used to estimate the source's spatial signatures.

5.1. Cross-Correlation Tensor for L -Shaped Sensor Arrays. In this approach, we consider an L -shaped sensor array equipped with $N_1 + N_2 - 1$ sensors positioned in the x - z

$i = 0$; Initialize $\widehat{\mathbf{T}}_{(i=0)} = \mathbf{I}_M$.
 (1) According to (25), obtain $\mathbf{U}^{[M]}$ and $\mathbf{\Sigma}^{[M]}$ from the SVD of the multimode unfolding matrix \mathbf{R}_{mm} .
 (2) $i = i + 1$;
 (3) According to (26), obtain estimates for $\widehat{\mathbf{A}}_{(i)}^{(r)}$ for $r = 1, \dots, R$ by applying the multidimensional LS-KRF algorithm on $\mathbf{U}^{[M]} \cdot \mathbf{\Sigma}^{[M]} \cdot \widehat{\mathbf{T}}_{(i-1)}^H$.
 (4) According to (29), compute the SVD for the matrix $(\widehat{\mathbf{A}}_{(i)}^{(1)} \diamond \dots \diamond \widehat{\mathbf{A}}_{(i)}^{(R)})^H \cdot \mathbf{U}^{[M]} \cdot \mathbf{\Sigma}^{[M]} = \mathbf{U}_p \cdot \mathbf{\Sigma}_p \cdot \mathbf{V}_p^H$ and obtain $\widehat{\mathbf{T}}_{(i)} = \mathbf{U}_p \cdot \mathbf{V}_p^H$.
 (5) Repeat Steps (2)–(4) until convergence.

ALGORITHM 2: Summary of the ALS-ProKRaft algorithm.

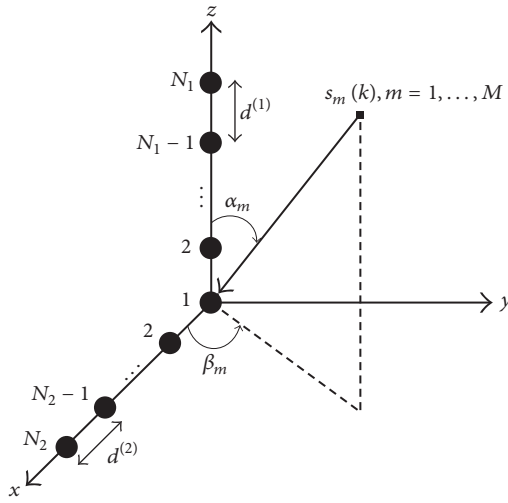


FIGURE 1: L -shaped array configuration with $N_1 + N_2 - 1$ sensors. The distance between the sensors in the z -axis is $d^{(1)}$ while the distance between the sensors in the x -axis is $d^{(2)}$. The m th wavefront has elevation and azimuth angles equal to α_m and β_m , respectively.

plane, as illustrated in Figure 1. Each linear array contains N_1 and N_2 sensors equally spaced at distances $d^{(1)}$ and $d^{(2)}$, respectively. We consider that each linear array is divided into P and W smaller subarrays, respectively. Each subarray contains $N_1^{(\text{sub})} = N_1 - P + 1$ and $N_2^{(\text{sub})} = N_2 - W + 1$ sensors. The signal received at the p th subarray, for $p = 1, \dots, P$, is given by

$$\mathbf{X}_p^{(1)} = \mathbf{A}_s^{(1)} \mathbf{D}_p(\Phi^{(1)}) \mathbf{S} + \mathbf{V}_p^{(1)} \in \mathbb{C}^{N_1^{(\text{sub})} \times K}, \quad (30)$$

and the signal received at the w th subarray, $w = 1, \dots, W$, is given by

$$\mathbf{X}_w^{(2)} = \mathbf{A}_s^{(2)} \mathbf{D}_w(\Phi^{(2)}) \mathbf{S} + \mathbf{V}_w^{(2)} \in \mathbb{C}^{N_2^{(\text{sub})} \times K}, \quad (31)$$

where

- (i) $\mathbf{A}_s^{(r)} \in \mathbb{C}^{N_r^{(\text{sub})} \times M}$ is the spatial signature matrix of the first subarray (or reference subarray) for the r th array dimension, $r = 1, 2$;

- (ii) $\mathbf{D}_p(\Phi^{(1)})$ and $\mathbf{D}_w(\Phi^{(2)})$ are diagonal matrices whose main diagonal is given by the p th and w th row of the matrices $\Phi^{(1)} \in \mathbb{C}^{P \times M}$ and $\Phi^{(2)} \in \mathbb{C}^{W \times M}$, respectively.

The rows of $\Phi^{(1)}$ and $\Phi^{(2)}$ capture the delays suffered by the signals impinging the p th and w th subarrays with respect to the reference subarray, which are defined based on the following spatial frequencies:

$$\begin{aligned} \mu_m^{(1)} &= \frac{2\pi \cdot d^{(1)} \cdot \cos \alpha_m}{\lambda}, \\ \mu_m^{(2)} &= \frac{2\pi \cdot d^{(2)} \cdot \sin \alpha_m \cdot \cos \beta_m}{\lambda}, \end{aligned} \quad (32)$$

where α_m and β_m are the azimuth and elevation angles of the m th source, respectively.

From (30) and (31), let us introduce the following extended data matrices:

$$\begin{aligned} \mathbf{X}^{(1)} &= [\mathbf{X}_1^{(1)}, \dots, \mathbf{X}_P^{(1)}]^T \in \mathbb{C}^{N_1^{(\text{sub})} P \times K}, \\ \mathbf{X}^{(2)} &= [\mathbf{X}_1^{(2)}, \dots, \mathbf{X}_W^{(2)}]^T \in \mathbb{C}^{N_2^{(\text{sub})} W \times K}, \end{aligned} \quad (33)$$

or, more compactly,

$$\mathbf{X}^{(r)} = (\Phi^{(r)} \diamond \mathbf{A}_s^{(r)}) \mathbf{S} + \mathbf{V}^{(r)}, \quad r = 1, 2. \quad (34)$$

In contrast with (12), in this approach we shall work with the following sample cross-correlation matrix:

$$\widehat{\mathbf{R}} = (\Phi^{(1)} \diamond \mathbf{A}_s^{(1)}) \mathbf{R}_s (\Phi^{(2)} \diamond \mathbf{A}_s^{(2)})^H + \sigma_v^2 \mathbf{I}. \quad (35)$$

As mentioned in Section 4.1, we can see that the noiseless term in (35) denotes a multimode unfolding of the following cross-correlation tensor of size $N_1^{(\text{sub})} \times P \times N_2^{(\text{sub})} \times W$:

$$\mathcal{R}_0 = \mathcal{R}_s \times_1 \mathbf{A}_s^{(1)} \times_2 \Phi^{(1)} \times_3 \mathbf{A}_s^{(2)*} \times_4 \Phi^{(2)*}, \quad (36)$$

where $\mathcal{R}_s \in \mathbb{C}^{M \times M \times M \times M}$. In this modeling, the tensor \mathcal{R}_o follows a fourth-order Tucker decomposition. By analogy with (4), we deduce the following correspondences:

$$\begin{aligned} (I_1, I_2, I_3, I_4) &\longleftrightarrow (N_1^{(\text{sub})}, P, N_2^{(\text{sub})}, W) \\ (R_1, R_2, R_3, R_4) &\longleftrightarrow M \\ (\mathcal{G}, \mathbf{A}^{(1)}, \mathbf{A}^{(2)}, \mathbf{A}^{(3)}, \mathbf{A}^{(4)}) & \\ \longleftrightarrow (\mathcal{R}_s, \mathbf{A}_s^{(1)}, \Phi^{(1)}, \mathbf{A}_s^{(2)*}, \Phi^{(2)*}). & \end{aligned} \quad (37)$$

The spatial signatures of the sources can be estimated from (36) by using the proposed generalized ALS-Tucker algorithm. Note that, in this case, the ALS-Tucker algorithm is simplified to a fourth-order tensor input.

For all the previously proposed algorithms, the final estimates for the spatial signature matrices are obtained when the convergence is declared. A usually adopted criterion for convergence is defined as $|e_{(i)} - e_{(i-1)}| \leq 10^{-6}$, where $e_{(i)}$ denotes the residual error of the i th iteration, defined as

$$e_{(i)} = \left\| \mathcal{R} - \widehat{\mathcal{R}}_{(i)} \right\|_F^2, \quad (38)$$

where $\mathcal{R} = \mathcal{R}_o + \mathcal{V}$ is a noisy version of \mathcal{R} , \mathcal{V} is an additive complex-valued white Gaussian noise tensor, and $\widehat{\mathcal{R}}_{(i)}$ is the covariance tensor reconstructed from the estimated factor matrices and core tensor. Since the ALS-ProKRaft algorithm exploits the dual-symmetry property of the data tensor the procedure in (22) is not necessary.

5.2. Estimation of the Spatial Frequencies. After the estimation of the spatial signatures matrices $\widehat{\mathbf{A}}_{\text{final}}^{(r)}$, $r = 1, \dots, R$, the final step is to estimate the spatial frequencies of the sources $\widehat{\mu}_m^{(r)}$, $m = 1, \dots, M$. The final estimates can be computed from the average over the values obtained in each row of $\widehat{\mathbf{A}}_{\text{final}}^{(r)}$ as follows:

$$\widehat{\mu}_m^{(r)} = \frac{1}{N_r - 1} \sum_{n=2}^{N_r} \frac{\arg \left\{ \widehat{\mathbf{A}}_{\text{final}}^{(r)}(n, m) \right\}}{n - 1}. \quad (39)$$

6. Computational Complexity

In the following, we discuss the computational complexity of the iterative ALS-Tucker and ALS-ProKRaft algorithms. For the sake of simplicity, the computational complexity of the proposed methods is described in terms of the computational cost of the matrix SVD. For a matrix of size $I_1 \times I_2$ the number of floating-point operations associated with the SVD computation is $\mathcal{O}(I_1 \cdot I_2 \cdot \min(I_1, I_2))$ [24]. The computational complexity of one Tucker iteration refers to the cost associated with the SVD used to calculate the matrix pseudoinverses in the least squares problems (18) and (20). The overall computational complexity per iteration of the ALS-Tucker algorithm equals the complexity of $2R$ matrix SVDs associated with each estimated factor matrix according to (19) plus the complexity of one additional matrix SVD associated with the estimated core tensor according to (21).

The overall computational cost per iteration of the ALS-ProKRaft algorithm equals the complexity of $M(R - 1)$ matrix SVDs associated with the application of the multi-dimensional LS-KRF algorithm in (26) plus the complexity of one additional matrix SVD associated with the update of the unknown unitary rotation factor matrix \mathbf{T} according to (29).

7. Advantages and Disadvantages of the Proposed Methods

In this section, we discuss the advantages and disadvantages of the proposed methods to blind spatial signatures estimation in R -D sensor arrays. As previously stated in Section 4.3, the ALS-ProKRaft algorithm works on the assumption that the sample covariance matrix of the sources \mathbf{R}_s is perfectly known and diagonal. However, this is only true in the asymptotic case when a sufficiently large number of snapshots is assumed (i.e., $K \rightarrow \infty$), as well as when the source signals are perfectly uncorrelated. In practice, this assumption is not guaranteed. On the other hand, the ALS-Tucker algorithm previously formulated in Section 4.2 naturally captures any structure for the sources covariance into the core tensor \mathcal{R}_s . Therefore, the assumption of uncorrelated source signals is not necessary for the ALS-Tucker algorithm, making it able to operate in scenarios where the source covariance structure is unknown and arbitrary (nondiagonal). Such scenarios occur, for instance, when the sample covariance is computed from a limited number of snapshots.

In contrast, the ALS-Tucker algorithm does not exploit the dual-symmetry property of the data covariance tensor and all factor matrices need to be estimated as independent variables. However, in the ALS-ProKRaft algorithm, only half of the factor matrices are estimated by exploiting the dual-symmetry property of the covariance tensor. Therefore, the ALS-ProKRaft algorithm is more computationally attractive than the ALS-Tucker algorithm. When compared with the state-of-the-art matrix-based algorithms such as MUSIC, ESPRIT, and Propagator Method, the proposed tensor-based algorithms have the advantage of fully exploiting the multi-dimensional nature of the received signal in less specific scenarios, which leads to more accurate estimates. For instance, the ESPRIT algorithm was formulated for sensor arrays that obey the shift invariance property. On the other hand, the MUSIC algorithm has high computational complexity due to the search of parameters in the spatial spectrum.

8. Simulation Results

In the following, simulation results and performance evaluations of the ALS-Tucker and ALS-ProKRaft algorithms for R -D sensor arrays are presented. This section is divided into two parts. Firstly, the results related to Section 4 are presented and discussed. Then, the same is done for the L -shaped array approach presented in Section 5. Results are obtained from an average of 1000 independent Monte Carlo runs. In the first part of this section, we consider a uniform rectangular array (URA) positioned on the x - z plane. The m th wavefront

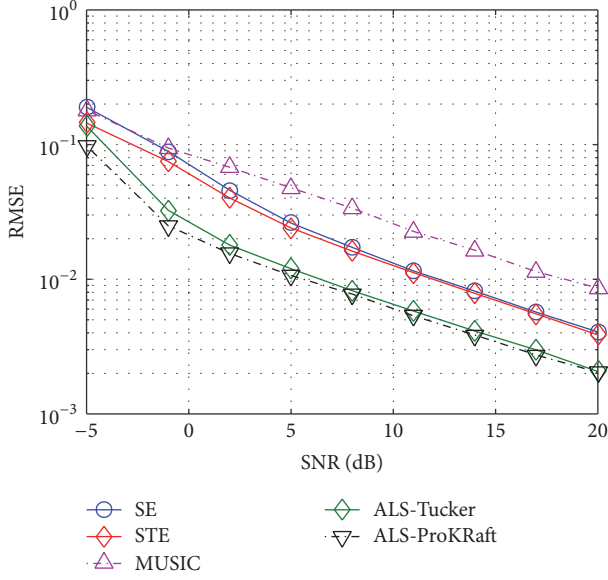


FIGURE 2: Total RMSE versus SNR for $N = 64$ sensors, $K = 10$ samples, and DoAs: $\{30^\circ, 55^\circ\}$ and $\{45^\circ, 60^\circ\}$ for Hadamard sequences.

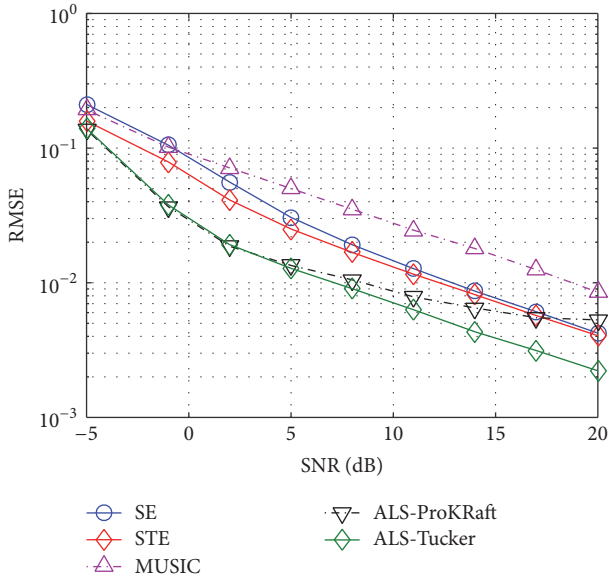


FIGURE 3: Total RMSE versus SNR for $N = 64$ sensors, $K = 10$ samples, and DoAs: $\{30^\circ, 55^\circ\}$ and $\{45^\circ, 60^\circ\}$ for BPSK sequences.

has direction of arrival $\{\alpha_m, \beta_m\}_{m=1}^M$, where α_m and β_m are elevation and azimuth angles, respectively.

In Figures 2 and 3, the performance is measured in terms of the root mean square error (RMSE) of the estimated spatial frequencies $\hat{\mu}_m^{(r)}$ in terms of Signal to Noise Ratio (SNR). The relations between directions of arrival and spatial frequencies are given by (32), where $d^{(r)}$ denotes the distance between sensors in the r th array dimension, which is assumed here equal to $\lambda/2$. In Figure 2, we consider Hadamard sequences for the sources, while in Figure 3 we consider BPSK modulated sources. In both cases, we have $N = 64$ sensors

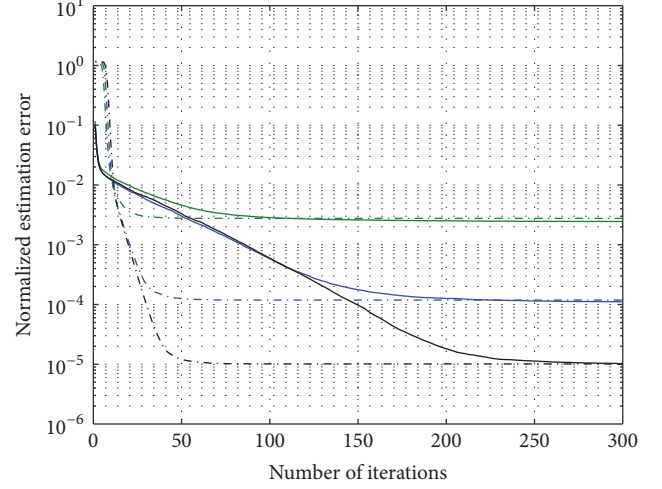


FIGURE 4: Convergence of the ALS-Tucker and ALS-ProKRaft algorithms.

(i.e., N_1 and N_2 equal to 8) and the sample covariance matrix of the received data (12) is calculated from a reduced number $K = 10$ of samples. The total RMSE is defined as

$$\text{RMSE} = \sqrt{E \left\{ \sum_{r=1}^R \sum_{m=1}^M (\mu_m^{(r)} - \hat{\mu}_m^{(r)})^2 \right\}}. \quad (40)$$

From Figure 2, it can be seen that both ALS-Tucker and ALS-ProKRaft algorithms have similar performances in terms of RMSE, when Hadamard sequences are considered. In contrast, in Figure 3, when BPSK symbols are considered, a floor is exhibited by the ALS-ProKraft algorithm for high SNR values. This behavior occurs due to the modeling errors in the core tensor of the PARAFAC decomposition, which in turn arises due to the nonorthogonality of the source signals, resulting in a nondiagonal sample covariance matrix of the sources in this case. Note that in the ALS-Tucker algorithm the covariance matrix of the sources possess an arbitrary and unknown structure which discards possible constraints to the source signals. This difference makes the Tucker decomposition approach more attractive in those practical scenarios in which source uncorrelatedness is not guaranteed. When compared to matrix-based standard ESPRIT (SE) [2], matrix-based MUSIC algorithm to planar array configuration [25], and tensor-based standard ESPRIT (STE) [10], the proposed algorithms have improved accuracy in all the considered scenarios.

Figure 4 shows the convergence performance of the iterative algorithms. In this experiment, the median values of the normalized estimation error $e_{(i)}/N^{(2R)}$ are plotted in terms of the number of iterations for different SNR. It is noteworthy that the ALS-ProKRaft algorithm has a faster convergence compared to the ALS-Tucker algorithm. This

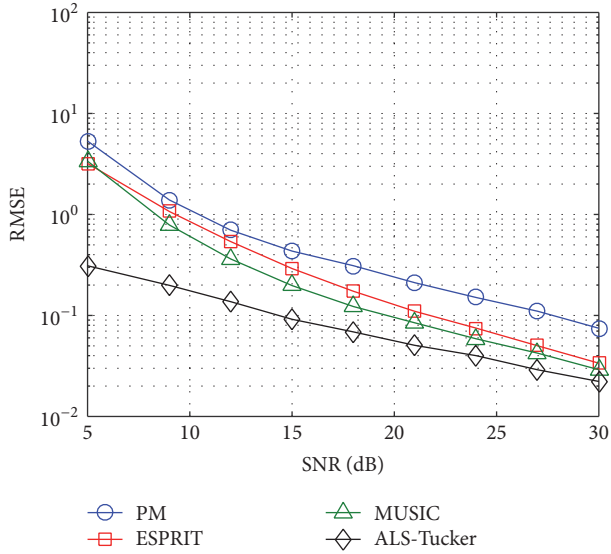


FIGURE 5: Total RMSE versus SNR for $N = 13$ sensors, $K = 500$ samples, and DoAs: $\{30^\circ, 45^\circ\}$ and $\{50^\circ, 55^\circ\}$.

behavior is expected since ALS-ProKraft exploits the dual-symmetry property of the data tensor, which results in estimating half as many factor matrices compared to the ALS-Tucker approach.

In the second part of this section, we consider a L -shaped configuration array. In Figure 5, we set $N = 13$ sensors (i.e., N_1 and N_2 equal to 7) and $K = 500$ samples. Each uniform linear array is divided into $P = 2$ and $W = 2$ subarrays, respectively. In this experiment, the performance of the proposed ALS-Tucker algorithm is compared to the state-of-the-art matrix-based methods, namely, Propagator Method (PM) [26], MUSIC [27], and ESPRIT [28], all of them originally formulated for L -shaped arrays. Note that the ALS-Tucker algorithm presents an improved performance over its competitors, with more evidenced gains in the low-to-medium SNR range. For high SNR values, the performance of the MUSIC method comes close to that of our proposal. However, the ALS-Tucker algorithm dispenses any estimation procedure via bidimensional peak search as occurs with MUSIC, being the former more computationally attractive.

Figure 6 shows the performance of the ALS-Tucker by assuming different number of sensors. In this experiment, we consider $K = 500$ samples. We can observe a better performance in terms of RMSE when the number sensors of the L -shaped array is increased. This is valid for all the simulated SNR values.

In Figure 7, we analyze the influence of the number K of samples on the performance of the ALS-Tucker algorithm. This experiment considers the same parameters as the experiment of Figure 5, except the SNR value that is assumed fixed at 20 dB and the number of samples that varies between 50 and 3000. First, we can see that the performance of the algorithms improves by increasing the number of samples collected by sensor array, as expected. However, similar to Figure 5 the

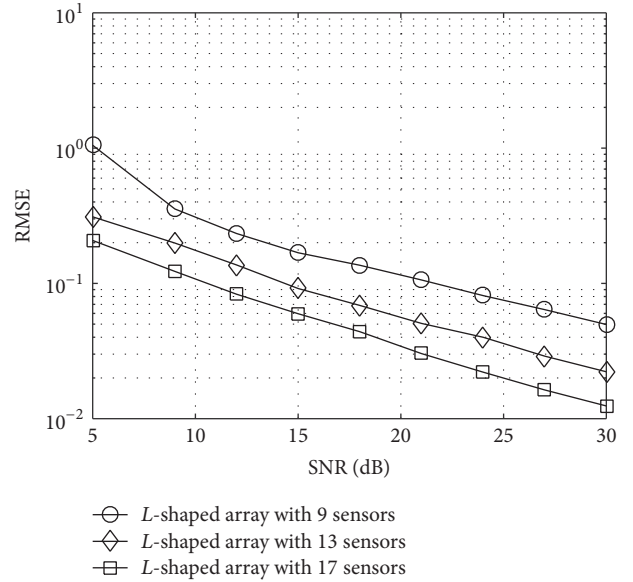


FIGURE 6: Total RMSE versus SNR (performance of the ALS-Tucker algorithm for different number of sensors).

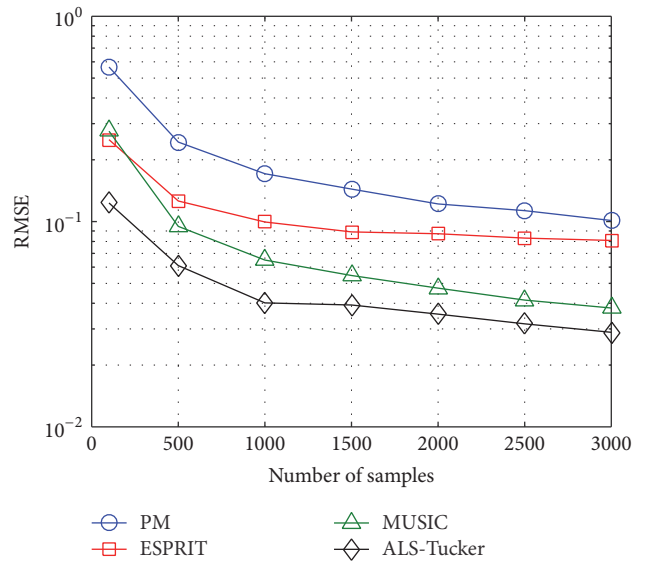


FIGURE 7: Total RMSE versus number of samples.

proposed ALS-Tucker algorithm outperforms the state-of-the-art PM, ESPRIT, and MUSIC methods.

9. Conclusion

In this paper, two tensor-based approaches based on the Tucker and PARAFAC decompositions have been formulated to solve the blind spatial signatures estimation problem in multidimensional sensor arrays. First, we have proposed a covariance-based generalization of the Tucker decomposition for R -D sensor arrays. Then, a link between the ALS-ProKraft algorithm and covariance-based array signal processing for blind spatial signatures estimation has been

established. As another contribution, we have formulated a cross-correlation-based fourth-order Tucker decomposition which makes the proposed ALS-Tucker algorithm applicable in scenarios composed by L -shaped array configurations. The two proposed tensor methods differ in the structure assumed for the source covariance. It is worth pointing out that, in realistic scenarios, when the received covariance matrix is calculated from a reduced number of samples, or snapshots, the ALS-Tucker algorithm becomes preferable since it operates with an arbitrary and unknown structure for the covariance of the source signals. In contrast, when the sources can be assumed to be uncorrelated, we can achieve improved performance by exploiting the dual-symmetry property of the covariance tensor, which makes the ALS-ProKRaft algorithm preferable since it provides good estimation accuracy with a smaller number of ALS iterations. Finally, when compared with other state-of-the-art matrix-based and tensor-based techniques, the proposed tensor-based iterative algorithms have shown their effectiveness with remarkable gains in terms of estimation error.

Competing Interests

The authors declare that there is no conflict of interests regarding the publication of this paper.

Acknowledgments

The authors would like to thank the Fundação Cearense de Apoio ao Desenvolvimento Científico e Tecnológico (FUNCAP), the Coordenação de Aperfeiçoamento de Pessoal de Nível Superior (CAPES) under the PVE Grant no. 88881.030392/2013-01, the productivity Grant no. 303905/2014-0, the postdoctoral scholarship abroad (PDE) no. 207644/2015-2, and the Program Science without Borders, Aerospace Technology supported by CNPq and CAPES for the postdoctoral scholarship abroad (PDE) no. 207644/2015-2.

References

- [1] R. O. Schmidt, "Multiple emitter location and signal parameter estimation," *IEEE Transactions on Antennas and Propagation*, vol. 34, no. 3, pp. 276–280, 1986.
- [2] R. Roy and T. Kailath, "ESPRIT—estimation of signal parameters via rotational invariance techniques," *IEEE Transactions on Acoustics, Speech, and Signal Processing*, vol. 37, no. 7, pp. 984–995, 1989.
- [3] J. P. C. L. da Costa, F. Roemer, M. Haardt, and R. T. de Sousa Jr., "Multi-dimensional model order selection," *EURASIP Journal on Advances in Signal Processing*, vol. 2011, article 26, 2011.
- [4] F. Roemer, *Advanced algebraic concepts for efficient multi-channel signal processing [Ph.D. thesis]*, Ilmenau University of Technology, Ilmenau, Germany, 2013.
- [5] J. P. C. L. Da Costa, K. Liu, H. Cheung So, S. Schwarz, M. Haardt, and F. Römer, "Multidimensional prewhitening for enhanced signal reconstruction and parameter estimation in colored noise with Kronecker correlation structure," *Signal Processing*, vol. 93, no. 11, pp. 3209–3226, 2013.
- [6] J. P. C. L. da Costa, *Parameter Estimation Techniques for Multi-Dimensional Array Signal Processing*, Shaker Publisher, Aachen, Germany, 2010.
- [7] R. Harshman, "Foundations of the PARAFAC procedure: models and conditions for an explanatory multimodal factor analysis," *UCLA Working Papers in Phonetics*, vol. 16, no. 10, pp. 1–84, 1970.
- [8] R. A. Harshman and M. E. Lundy, "Uniqueness proof for a family of models sharing features of Tucker's three-mode factor analysis and PARAFAC/CANDECOMP," *Psychometrika. A Journal of Quantitative Psychology*, vol. 61, no. 1, pp. 133–154, 1996.
- [9] N. D. Sidiropoulos, R. Bro, and G. B. Giannakis, "Parallel factor analysis in sensor array processing," *IEEE Transactions on Signal Processing*, vol. 48, no. 8, pp. 2377–2388, 2000.
- [10] M. Haardt, F. Roemer, and G. Del Galdo, "Higher-order SVD-based subspace estimation to improve the parameter estimation accuracy in multidimensional harmonic retrieval problems," *IEEE Transactions on Signal Processing*, vol. 56, no. 7, pp. 3198–3213, 2008.
- [11] J. P. C. L. Da Costa, F. Roemer, M. Weis, and M. Haardt, "Robust R-D parameter estimation via closed-form PARAFAC," in *Proceedings of the International ITG Workshop on Smart Antennas (WSA '10)*, pp. 99–106, Bremen, Germany, February 2010.
- [12] M. Weis, F. Roemer, M. Haardt, and P. Husar, "Dual-symmetric parallel factor analysis using procrustes estimation and Khatri-Rao factorization," in *Proceedings of the 20th EUSIPCO European Signal Processing Conference*, Bucharest, Romania, August 2012.
- [13] F. Roemer and M. Haardt, "Tensor-based channel estimation (TENICE) for two-way relaying with multiple antennas and spatial reuse," in *Proceedings of the IEEE International Conference on Acoustics, Speech, and Signal Processing (ICASSP '09)*, Taipei, Taiwan, April 2009.
- [14] P. R. B. Gomes, A. L. F. de Almeida, and J. P. C. L. da Costa, "Fourth-order tensor method for blind spatial signature estimation," in *Proceedings of the IEEE International Conference on Acoustics, Speech, and Signal Processing (ICASSP '14)*, pp. 2992–2996, IEEE, Florence, Italy, May 2014.
- [15] L. R. Tucker, "Implications of factor analysis of three-way matrices for measurement of change," in *Problems in Measuring Change*, C. W. Harris, Ed., pp. 122–137, University of Wisconsin Press, 1963.
- [16] T. G. Kolda and B. W. Bader, "Tensor decompositions and applications," *SIAM Review*, vol. 51, no. 3, pp. 455–500, 2009.
- [17] A. Cichocki, D. Mandic, L. De Lathauwer et al., "Tensor decompositions for signal processing applications: from two-way to multiway component analysis," *IEEE Signal Processing Magazine*, vol. 32, no. 2, pp. 145–163, 2015.
- [18] J. M. F. Ten Berge and A. K. Smilde, "Non-triviality and identification of a constrained Tucker3 analysis," *Journal of Chemometrics*, vol. 16, no. 12, pp. 609–612, 2002.
- [19] N. D. Sidiropoulos and R. Bro, "On the uniqueness of multilinear decomposition of N -way arrays," *Journal of Chemometrics*, vol. 14, no. 3, pp. 229–239, 2000.
- [20] J. B. Kruskal, "Three-way arrays: rank and uniqueness of trilinear decompositions, with application to arithmetic complexity and statistics," *Linear Algebra and its Applications*, vol. 18, no. 2, pp. 95–138, 1977.

- [21] R. Bro, *Multi-way analysis in the food industry: models, algorithms and applications [Ph.D. thesis]*, University of Amsterdam, Amsterdam, The Netherlands, 1998.
- [22] A. Smilde, R. Bro, and P. Geladi, *Multi-Way Analysis: Applications in the Chemical Sciences*, John Wiley & Sons, 2004.
- [23] P. H. Schönemann, "A generalized solution of the orthogonal Procrustes problem," *Psychometrika*, vol. 31, no. 1, pp. 1–10, 1966.
- [24] G. H. Golub and C. F. Van Loan, *Matrix Computations*, Johns Hopkins Studies in the Mathematical Sciences, Johns Hopkins University Press, Baltimore, Md, USA, 3rd edition, 1996.
- [25] S. Sekizawa, "Estimation of arrival directions using MUSIC algorithm with a planar array," in *Proceedings of the IEEE International Conference on Universal Personal Communications (ICUPC '98)*, pp. 555–559, Florence, Italy, October 1998.
- [26] N. Tayem and H. M. Kwon, "L-shape 2-dimensional arrival angle estimation with propagator method," *IEEE Transactions on Antennas and Propagation*, vol. 53, no. 5, pp. 1622–1630, 2005.
- [27] H. Changuel, F. Harabi, and A. Gharsallah, "2-L-shape two-dimensional arrival angle estimation with a classical subspace algorithm," in *Proceedings of the International Symposium on Industrial Electronics (ISIE '06)*, pp. 603–607, Montreal, Canada, July 2006.
- [28] X. Zhang, X. Gao, and W. Chen, "Improved blind 2D-direction of arrival estimation with L-shaped array using shift invariance property," *Journal of Electromagnetic Waves and Applications*, vol. 23, no. 5-6, pp. 593–606, 2009.

Research Article

Performance Analysis of Two-Dimensional Maximum Likelihood Direction-of-Arrival Estimation Algorithm Using the UCA

Yun-Seong Cho, Jeong-Min Seo, and Joon-Ho Lee

Department of Information & Communication Engineering, Sejong University, 98 Kunja-dong, Kwangjin-ku, Seoul 143-747, Republic of Korea

Correspondence should be addressed to Joon-Ho Lee; joonhlee@sejong.ac.kr

Received 2 June 2016; Revised 23 August 2016; Accepted 7 September 2016; Published 9 February 2017

Academic Editor: Sergiy A. Vorobyov

Copyright © 2017 Yun-Seong Cho et al. This is an open access article distributed under the Creative Commons Attribution License, which permits unrestricted use, distribution, and reproduction in any medium, provided the original work is properly cited.

We address the performance analysis of the maximum likelihood (ML) direction-of-arrival (DOA) estimation algorithm in the case of azimuth/elevation estimation of two incident signals using the uniform circular array (UCA). Based on the Taylor series expansion and approximation, we get explicit expressions of the root mean square errors (RMSEs) of the azimuths and elevations. The validity of the derived expressions is shown by comparing the analytic results with the simulation results. The derivation in this paper is further verified by illustrating the consistency of the analytic results with the Cramer-Rao lower bound (CRLB).

1. Introduction

There have been many studies on the direction-of-arrival (DOA) estimation [1–5]. Our concern in this paper is the performance analysis of the maximum likelihood- (ML-) based DOA estimation algorithm.

Many studies have been conducted on asymptotic performance analysis of maximum likelihood DOA estimation algorithm [6–8]. The shortcoming of the asymptotic performance analysis is that it is only applicable to high SNR region since it is based on approximation which is valid only for small amount of noise. To circumvent this problem, many studies on nonasymptotic performance analysis have been conducted for performance analysis which is valid for low SNR as well as high SNR.

In [9–12], the authors dealt with threshold performance analysis for single incident signal. On the other hand, our scheme presented in this paper is applicable to multiple incident signal as well as single incident signal.

In this paper, we address the performance analysis of the ML algorithm for the estimation of the DOA of incident signals. Our interest is in the case of multiple incident signals. The ML algorithm exploits the fact that, in the absence of the noise, the incident signal on the array elements can be

expressed as a linear combination of the array steering vectors corresponding to the true incident angles.

Based on this observation, in the ML algorithm, the estimate of the DOA is obtained from the angles whose steering vectors can span the subspace to which the signal on the array elements belongs.

In practical situation, the noise is inevitable. Therefore, the noisy incident signal on the array elements cannot be expressed as a linear combination of the array steering vectors associated with true incident angles, which accounts for why estimation error occurs for noisy array response.

To quantify the bias of the estimate due to the noise on the antenna elements, we adopt the Taylor series approximation around the true incident angle. We derive the closed-form expression of the biases of the estimates, where different estimates are due to some approximations. For one of the many estimates, we derive the closed-form expression of the MSE of the estimate.

In Figure 1, the mathematical and statistical theories used for the performance analysis of the ML algorithm are enumerated.

Novelty of the proposed method over the existing methods is as follows.

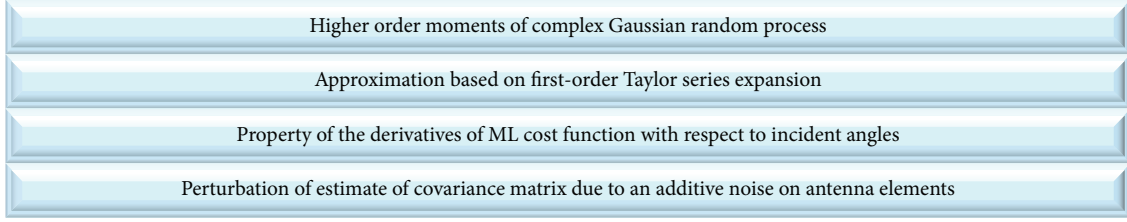


FIGURE 1: Mathematical/statistical foundation of the proposed analytical performance analysis of ML algorithm.

Performance Analysis for Multiple Incident Signals and Simultaneous Estimation of Azimuth/Elevation. In [9–11], the authors made performance analysis of ML DOA algorithm for single incident signals. On the other hand, the scheme presented in this paper handles multiple incident signals as well as single incident signal. In addition, the studies presented in [9–11] consider the estimation of azimuth, not azimuth and elevation. Note that, in this paper, we consider the estimation of azimuth and elevation of multiple incident signals.

Derivation of Explicit Expressions of Bias and MSE, Not the Lower Bound of MSE. In [13], the authors derived the CRLB of the DOA algorithm, which is a lower bound of the variance of the DOA algorithm. Note that the CRLB is the lower bound of the variance, not the variance itself of the DOA algorithm. In this paper, explicit expression of the bias of the estimate and explicit expression of the MSE itself, not the CRLB, have been derived.

Intuition on the Effect of Each Approximation on the Estimation Accuracy. In this paper, we obtain, for $c = 1, 2$, the expressions of $[\hat{\theta}_c, \hat{\phi}_c]$, $[\hat{\theta}_c^{(u=1)}, \hat{\phi}_c^{(u=1)}]$, and $[\hat{\theta}_c^{(u=1,v)}, \hat{\phi}_c^{(u=1,v)}]$. The superscripts u and v denote U approximation and V approximation, respectively. Therefore, $[\hat{\theta}_c, \hat{\phi}_c]$, $[\hat{\theta}_c^{(u=1)}, \hat{\phi}_c^{(u=1)}]$, and $[\hat{\theta}_c^{(u=1,v)}, \hat{\phi}_c^{(u=1,v)}]$ are the estimates with no approximation, U approximation, and U/V approximations, respectively. By comparing these three values, we can intuitively recognize which approximation of U approximation and V approximation results in larger error. The importance of this observation is that the proposed scheme gives us an intuition on which approximation of all the approximations results in large approximation error. The approach presented in [14] does not show any intuition on which approximation results in large approximation error, since in [14] the authors only explicitly consider Taylor series expansion for general problem. Since the approach in [14] is a general approach applicable to many estimation problems, it does not give explicit expressions specific to DOA estimation problem. Since the scheme presented in this paper only considers the estimation of DOA estimation, rather than general estimation problem, the expressions presented in this paper are more explicit than the results presented in [14].

Explicit Expressions of Various Estimates for Each Step of Successive Approximations. To the best of our knowledge,

there has been no study where explicit expressions of successive estimates have been derived [6–13]. Successive estimates imply various estimates obtained as each approximation has been successively applied. In [14], no explicit expression of estimate for each step of successive approximations has been presented. Although the study presented in [14] deals with the estimation of vector parameter as well as scalar parameter, the results in [14] for vector parameter estimation, equations (41) and (42) in [14], are quite implicit, rather than explicit, and it is very difficult to get intuition on how the bias and the covariance matrix are dependent on the amount of an additive noise.

Search-Free Approximate ML DOA Estimation and Derivation of Closed-Form Estimation Error. For getting $\hat{\theta}_c$ and $\hat{\phi}_c$ in (13) for $c = 1, 2$, four-dimensional search with respect to $\theta_1, \theta_2, \phi_1$, and ϕ_2 has to be performed. In general, for estimation of d incident signals, $2d$ dimensional search has to be performed for simultaneous estimation of $[\theta_1, \phi_1], \dots, [\theta_d, \phi_d]$, which is computationally very intensive. In addition, in practical implementation of (13), the estimates are highly dependent on the search range and search step, which implies that the estimates in (13) may be wrong if search step and search range are not properly chosen. In summary, the original ML estimate $[\hat{\theta}_c, \hat{\phi}_c]$ obtained from implementation of (13) has two demerits of computational cost and dependence on search step and search range.

On the other hand, $[\delta\theta_c^{(u=1)}, \delta\phi_c^{(u=1)}]$ and $[\delta\theta_c^{(u=1,v)}, \delta\phi_c^{(u=1,v)}]$ are obtained from (42) and (45), respectively. Note that $[\delta\theta_c^{(u=1)}, \delta\phi_c^{(u=1)}]$ and $[\delta\theta_c^{(u=1,v)}, \delta\phi_c^{(u=1,v)}]$ are obtained in closed-form and that evaluation of $[\delta\theta_c^{(u=1)}, \delta\phi_c^{(u=1)}]$ and $[\delta\theta_c^{(u=1,v)}, \delta\phi_c^{(u=1,v)}]$ is search-free, which implies that evaluation of $[\delta\theta_c^{(u=1)}, \delta\phi_c^{(u=1)}]$ and $[\delta\theta_c^{(u=1,v)}, \delta\phi_c^{(u=1,v)}]$ is much less computationally intensive than evaluation of $[\theta_c^{(u=1)}, \phi_c^{(u=1)}]$. In addition, since evaluation of $[\delta\theta_c^{(u=1)}, \delta\phi_c^{(u=1)}]$ and $[\delta\theta_c^{(u=1,v)}, \delta\phi_c^{(u=1,v)}]$ is search-free, $[\delta\theta_c^{(u=1)}, \delta\phi_c^{(u=1)}]$ and $[\delta\theta_c^{(u=1,v)}, \delta\phi_c^{(u=1,v)}]$ are not dependent on search parameters such as search step and search range.

$[\delta\theta_c^{(u=1)}, \delta\phi_c^{(u=1)}]$ and $[\delta\theta_c^{(u=1,v)}, \delta\phi_c^{(u=1,v)}]$ in (42) and (45) can be regarded as estimation errors for approximate ML DOA algorithm. $[\delta\theta_c^{(u=1)}, \delta\phi_c^{(u=1)}]$ and $[\delta\theta_c^{(u=1,v)}, \delta\phi_c^{(u=1,v)}]$ can be obtained in closed-form, although $[\delta\theta_c^{(u=1)}, \delta\phi_c^{(u=1)}]$ and $[\delta\theta_c^{(u=1,v)}, \delta\phi_c^{(u=1,v)}]$ are less accurate than $[\delta\theta_c, \delta\phi_c]$ in the sense that U approximation is applied in getting

$[\delta\theta_c^{(u=1)}, \delta\phi_c^{(u=1)}]$ and that U/V approximations are applied in getting $[\delta\theta_c^{(u=1,v)}, \delta\phi_c^{(u=1,v)}]$.

Derivation of Analytic Expression of Closed-Form MSE of $[\delta\theta_c^{(u=1,v)}, \delta\phi_c^{(u=1,v)}]$. Many evaluations of (42) and (45) are required for getting empirical performance analysis. Single evaluation of (42) and (45) is not computationally intensive since they are search-free closed-form solutions. Note that main computational cost of evaluating (42) and (45) is inversion of 2×2 matrices, which is not computationally intensive at all. For estimation of d incident signals, $d \times d$ matrices have to be inverted to implement (42) and (45). But for empirical performance analysis based on Monte-Carlo simulation, (42) and (45) have to be evaluated many times. Note that the number of repetitions should be large for getting reliable empirical performance analysis, which implies that the empirical performance analysis based on many evaluations of (42) and (45) is computationally intensive. In this paper, it has been shown that empirical performance of $[\delta\theta_c^{(u=1,v)}, \delta\phi_c^{(u=1,v)}]$ can be obtained from (47), without many evaluations of (45). Note that single evaluation of (47) results in analytic performance analysis, which should be equivalent to empirical performance based on many repetitions of (45). Therefore, although it is not necessary to repeatedly evaluate (45) to get empirical MSE, (45) is evaluated many times for validating the derived expression (47). Also, note that since analytic expression of the MSE of $[\theta_c^{(u=1)}, \phi_c^{(u=1)}]$ is not available, the MSE of $[\theta_c^{(u=1)}, \phi_c^{(u=1)}]$ has to be empirically obtained via many evaluations of (42) with different realizations of additive noise for each evaluation.

In $\hat{\theta}_c^{(u=1)}$ and $\hat{\phi}_c^{(u=1,v)}$, the superscripts u and v denote U approximation and V approximation, respectively. On the other hand, in [14], no explicit expression of MSE is presented, and only the implicit expression of final estimate is presented. Note that, in this paper, explicit expressions of all the estimates associated with each successive approximation have been presented.

2. ML DOA Algorithm

For simplicity, we present performance analysis for two incident signals on the UCA in this paper. But, extension to more incident signals and general planar array structure is straightforward. Let $\Theta, \hat{\Theta}, \Theta^{(0)}$, and $\delta\Theta$ represent

$$\begin{aligned}\Theta &= (\theta_1, \theta_2, \phi_1, \phi_2), \\ \hat{\Theta} &= (\hat{\theta}_1, \hat{\theta}_2, \hat{\phi}_1, \hat{\phi}_2), \\ \Theta^{(0)} &= (\theta_1^{(0)}, \theta_2^{(0)}, \phi_1^{(0)}, \phi_2^{(0)}), \\ \delta\Theta &= (\delta\theta_1, \delta\theta_2, \delta\phi_1, \delta\phi_2).\end{aligned}\tag{1}$$

The number of the antenna elements is denoted by M . When there is no noise, the received signals on the antenna elements are expressed as

$$\mathbf{x}(t_n) = \mathbf{A}(\Theta) \mathbf{s}(t_n),\tag{2}$$

where $\mathbf{s}(t_n)$ is given by

$$\mathbf{s}(t_n) = [s_1(t_n) s_2(t_n)]^T.\tag{3}$$

Array matrix in (2) is written as

$$\mathbf{A}(\Theta) = [\mathbf{a}(\theta_1, \phi_1) \ \mathbf{a}(\theta_2, \phi_2)],\tag{4}$$

where array vector is defined as

$$\mathbf{a}(\theta_n, \phi_n) = [a_1(\theta_n, \phi_n) \ a_2(\theta_n, \phi_n) \ \cdots \ a_M(\theta_n, \phi_n)]^T,\tag{5}$$

$$a_m(\theta_n, \phi_n) = \exp[j\psi_m(\theta_n, \phi_n)],\tag{6}$$

$$\psi_m(\theta_n, \phi_n) = \frac{2\pi r}{\lambda} \cos\left(\theta_n - \frac{2\pi(m-1)}{M}\right) \cos\phi_n.\tag{7}$$

The corresponding expression for the noisy signals is

$$\mathbf{x}'(t_n) = \mathbf{A}(\Theta) \mathbf{s}(t_n) + \mathbf{n}(t_n),\tag{8}$$

where θ and ϕ denote the azimuth and the elevation, respectively.

Expression (7) for a general planar array with $L \times M$ elements can be written as

$$\begin{aligned}\psi_{l,m}(\theta_n, \phi_n) &= \frac{2\pi}{\lambda} ((l-1)\Delta x \sin\theta_n \cos\phi_n \\ &+ (m-1)\Delta y \cos\theta_n \cos\phi_n), \\ l &= 1 \cdots L, \quad m = 1 \cdots M,\end{aligned}\tag{9}$$

where Δx and Δy denote the element spacing in the x -direction and y -direction, respectively, and l and m denote the index in the x -direction and y -direction, respectively.

Also, (8) for general planar array is written as

$$\mathbf{x}'(t_n) = [x'_{l=1,m=1}(t_n) \ \cdots \ x'_{l=1,m=M}(t_n) \ x'_{l=2,m=1}(t_n) \ \cdots \ x'_{l=2,m=M}(t_n) \ \cdots \ x'_{l=L,m=1}(t_n) \ \cdots \ x'_{l=L,m=M}(t_n)]^T$$

$$\begin{aligned}
& \begin{bmatrix} a_{l=1,m=1}(\theta_1, \phi_1) & \cdots & a_{l=1,m=1}(\theta_N, \phi_N) \\ \vdots & & \vdots \\ a_{l=1,m=M}(\theta_1, \phi_1) & \cdots & a_{l=1,m=M}(\theta_N, \phi_N) \\ a_{l=2,m=1}(\theta_1, \phi_1) & \cdots & a_{l=2,m=1}(\theta_N, \phi_N) \\ \vdots & & \vdots \\ a_{l=2,m=M}(\theta_1, \phi_1) & \cdots & a_{l=2,m=M}(\theta_N, \phi_N) \\ \vdots & & \vdots \\ a_{l=L,m=1}(\theta_1, \phi_1) & \cdots & a_{l=L,m=1}(\theta_N, \phi_N) \\ \vdots & & \vdots \\ a_{l=L,m=M}(\theta_1, \phi_1) & \cdots & a_{l=L,m=M}(\theta_N, \phi_N) \end{bmatrix} \begin{bmatrix} s_1(t_n) \\ \vdots \\ s_N(t_n) \end{bmatrix} + \begin{bmatrix} n_{l=1,m=1}(t_n) \\ \vdots \\ n_{l=1,m=M}(t_n) \\ n_{l=2,m=1}(t_n) \\ \vdots \\ n_{l=2,m=M}(t_n) \\ \vdots \\ n_{l=L,m=1}(t_n) \\ \vdots \\ n_{l=L,m=M}(t_n) \end{bmatrix}. \quad (10)
\end{aligned}$$

We have explicitly shown how (7) and (8) should be modified for a two-dimensional planar array. Note that, for an arbitrary array structure, (7) and (8) are modified appropriately to apply the proposed algorithm to the specific array structure. (7) for an arbitrary array structure can be easily obtained from the phase difference between antenna elements, given the azimuth and the elevation of the n th incident signal. Note that the phase difference is both dependent on the array geometry for a specific array structure and the direction of the incident signal.

The projection matrix onto the column space of \mathbf{A} can be expressed as [15]. It is assumed that the entries of the Gaussian vector are independent and identically distributed Gaussian random variables with zero-mean and the same variance. Note that the noise is complex-valued and that the real part and the imaginary part of the noise are independent Gaussian random variables with zero-mean. The variance of the real part is denoted by $\sigma^2/2$, which is equal to the variance of the imaginary part, $\sigma^2/2$:

$$\mathbf{P}_A(\Theta) = \mathbf{A}(\Theta) (\mathbf{A}^H(\Theta) \mathbf{A}(\Theta))^{-1} \mathbf{A}^H(\Theta). \quad (11)$$

Note that, in this paper, the formulation is for the case where there are two incident signals. But, it can be easily extended to the case of more incident signals. Using the maximum likelihood (ML) algorithm, the estimates are given by [16]

$$\widehat{\Theta} = \arg \max_{\Theta} \text{tr}(\mathbf{P}_A(\Theta) \widehat{\mathbf{R}}'). \quad (12)$$

More specifically, (12) for $d = 2$ is written as

$$[\widehat{\theta}_1, \widehat{\theta}_2, \widehat{\phi}_1, \widehat{\phi}_2] = \arg \max_{\theta_1, \theta_2, \phi_1, \phi_2} \text{tr}(\mathbf{P}_A(\theta_1, \theta_2, \phi_1, \phi_2) \mathbf{R}). \quad (13)$$

For notational simplicity, $\mathbf{P}(\Theta)$ is used to denote $\mathbf{P}_A(\Theta)$:

$$\mathbf{P}(\Theta) \equiv \mathbf{P}_A(\Theta). \quad (14)$$

$\widehat{\mathbf{R}}'$ is defined from

$$\widehat{\mathbf{R}}' = \frac{1}{T} \sum_{n=1}^T \mathbf{x}'(t_n) \mathbf{x}'^H(t_n). \quad (15)$$

The explicit expression of the entries of the matrix $(\mathbf{A}^H(\Theta) \mathbf{A}(\Theta))^{-1}$ in (11) is given by

$$\mathbf{A}^H(\Theta) \mathbf{A}(\Theta) = \begin{bmatrix} M & (\mathbf{A}^H \mathbf{A})_{12}(\Theta) \\ ((\mathbf{A}^H \mathbf{A})_{12}(\Theta))^* & M \end{bmatrix}. \quad (16)$$

Using (4) and (5), $(\mathbf{A}^H \mathbf{A})_{12}(\Theta)$ in (16) is given by

$$Q(\Theta) \equiv (\mathbf{A}^H \mathbf{A})_{12}(\Theta) = \sum_{k=1}^M (a_k(\theta_1, \phi_1))^* a_k(\theta_2, \phi_2). \quad (17)$$

Let $a_{m,n}$ represent $a_m(\theta_n, \phi_n)$:

$$a_{m,n} \equiv a_m(\theta_n, \phi_n). \quad (18)$$

Using (16) and (17), $(\mathbf{A}^H(\Theta) \mathbf{A}(\Theta))^{-1}$ can be expressed as

$$(\mathbf{A}^H(\Theta) \mathbf{A}(\Theta))^{-1} = \frac{1}{D(\Theta)} \begin{bmatrix} M & -Q(\Theta) \\ -(Q(\Theta))^* & M \end{bmatrix}, \quad (19)$$

$$\begin{aligned}
D(\Theta) &\equiv \det(\mathbf{A}^H(\Theta) \mathbf{A}(\Theta)) \\
&= M^2 - |Q(\Theta)|^2. \quad (20)
\end{aligned}$$

Using (17), $|Q(\Theta)|^2$ can be written as

$$|Q(\Theta)|^2 = \sum_{k=1}^M \sum_{k'=1}^M (a_{k,1})^* a_{k,2} a_{k,1} (a_{k,2})^*. \quad (21)$$

The explicit expression of the entries of the matrix $\mathbf{P}(\Theta)$ in (11) is given by

$$P_{kl}(\Theta) = \frac{S_{kl}(\Theta)}{D(\Theta)}. \quad (22)$$

Using (16)–(21), $S_{kl}(\Theta)$ in (22) is defined as

$$S_{kl}(\Theta) \equiv (a_{l,1})^* (a_{k,1}M - a_{k,2}Q(\Theta)) + (a_{l,2})^* (a_{k,2}M - a_{k,1}Q(\Theta)). \quad (23)$$

Note that $P_{kl}(\Theta)$ denotes the entry at the k th row and the l th column of $\mathbf{P}(\Theta)$. The explicit expression of the entries of the matrix $\text{tr}(\mathbf{P}(\Theta)\hat{\mathbf{R}}')$ in (12) is given by

$$\begin{aligned} & \text{tr}(\mathbf{P}(\Theta)\hat{\mathbf{R}}') \\ &= \text{tr} \left(\begin{bmatrix} P_{11}(\Theta) & \cdots & P_{1M}(\Theta) \\ \vdots & \ddots & \vdots \\ P_{M1}(\Theta) & \cdots & P_{MM}(\Theta) \end{bmatrix} \begin{bmatrix} \hat{R}'_{11} & \cdots & \hat{R}'_{1M} \\ \vdots & \ddots & \vdots \\ \hat{R}'_{M1} & \cdots & \hat{R}'_{MM} \end{bmatrix} \right) \\ &= \sum_{k=1}^M \sum_{l=1}^M P_{kl}(\Theta) \hat{R}'_{lk}. \end{aligned} \quad (24)$$

Using (24) in (12), we get $\hat{\Theta}$. The biases of the estimates are defined as

$$\begin{aligned} \delta\theta_1 &= \hat{\theta}_1 - \theta_1^{(0)}, \\ \delta\theta_2 &= \hat{\theta}_2 - \theta_2^{(0)}, \\ \delta\phi_1 &= \hat{\phi}_1 - \phi_1^{(0)}, \\ \delta\phi_2 &= \hat{\phi}_2 - \phi_2^{(0)}. \end{aligned} \quad (25)$$

3. Closed-Form Expression of Estimation Error

Since θ_1 , θ_2 , ϕ_1 , and ϕ_2 should be the maximizing arguments of $\text{tr}(\mathbf{P}(\Theta)\hat{\mathbf{R}}')$, the first-order derivative of $\text{tr}(\mathbf{P}(\Theta)\hat{\mathbf{R}}')$ with respect to each argument should be zero at $\Theta = \hat{\Theta}$

$$\begin{aligned} & \frac{\partial}{\partial\theta_1} \text{tr} \left(\mathbf{P}(\Theta)\hat{\mathbf{R}}' \Big|_{\Theta=\hat{\Theta}} \right) \\ &= \sum_{k=1}^M \sum_{l=1}^M \left(\frac{\partial}{\partial\theta_1} P_{kl}(\Theta) \Big|_{\Theta=\hat{\Theta}} \right) \hat{R}'_{lk} \\ &= \sum_{k=1}^M \sum_{l=1}^M (P_{kl,\theta_1}(\Theta) \Big|_{\Theta=\hat{\Theta}}) \hat{R}'_{lk} = 0, \\ & \frac{\partial}{\partial\theta_2} \text{tr} \left(\mathbf{P}(\Theta)\hat{\mathbf{R}}' \Big|_{\Theta=\hat{\Theta}} \right) \\ &= \sum_{k=1}^M \sum_{l=1}^M \left(\frac{\partial}{\partial\theta_2} P_{kl}(\Theta) \Big|_{\Theta=\hat{\Theta}} \right) \hat{R}'_{lk} \\ &= \sum_{k=1}^M \sum_{l=1}^M (P_{kl,\theta_2}(\Theta) \Big|_{\Theta=\hat{\Theta}}) \hat{R}'_{lk} = 0, \end{aligned}$$

$$\begin{aligned} & \frac{\partial}{\partial\phi_1} \text{tr} \left(\mathbf{P}(\Theta)\hat{\mathbf{R}}' \Big|_{\Theta=\hat{\Theta}} \right) \\ &= \sum_{k=1}^M \sum_{l=1}^M \left(\frac{\partial}{\partial\phi_1} P_{kl}(\Theta) \Big|_{\Theta=\hat{\Theta}} \right) \hat{R}'_{lk} \\ &= \sum_{k=1}^M \sum_{l=1}^M (P_{kl,\phi_1}(\Theta) \Big|_{\Theta=\hat{\Theta}}) \hat{R}'_{lk} = 0, \end{aligned}$$

$$\begin{aligned} & \frac{\partial}{\partial\phi_2} \text{tr} \left(\mathbf{P}(\Theta)\hat{\mathbf{R}}' \Big|_{\Theta=\hat{\Theta}} \right) \\ &= \sum_{k=1}^M \sum_{l=1}^M \left(\frac{\partial}{\partial\phi_2} P_{kl}(\Theta) \Big|_{\Theta=\hat{\Theta}} \right) \hat{R}'_{lk} \\ &= \sum_{k=1}^M \sum_{l=1}^M (P_{kl,\phi_2}(\Theta) \Big|_{\Theta=\hat{\Theta}}) \hat{R}'_{lk} = 0, \end{aligned} \quad (26)$$

where the first-order partial derivatives of $P_{kl}(\Theta)$ in (26) with respect to each argument are expressed as, using (22),

$$\begin{aligned} P_{kl,\theta_1}(\Theta) &\equiv \frac{\partial}{\partial\theta_1} P_{kl}(\Theta) \\ &= \frac{((\partial/\partial\theta_1)S_{kl}(\Theta))D(\Theta) - S_{kl}(\Theta)((\partial/\partial\theta_1)D(\Theta))}{(D(\Theta))^2}, \\ P_{kl,\theta_2}(\Theta) &\equiv \frac{\partial}{\partial\theta_2} P_{kl}(\Theta) \\ &= \frac{((\partial/\partial\theta_2)S_{kl}(\Theta))D(\Theta) - S_{kl}(\Theta)((\partial/\partial\theta_2)D(\Theta))}{(D(\Theta))^2}, \end{aligned} \quad (27)$$

$$\begin{aligned} P_{kl,\phi_1}(\Theta) &\equiv \frac{\partial}{\partial\phi_1} P_{kl}(\Theta) \\ &= \frac{((\partial/\partial\phi_1)S_{kl}(\Theta))D(\Theta) - S_{kl}(\Theta)((\partial/\partial\phi_1)D(\Theta))}{(D(\Theta))^2}, \end{aligned}$$

$$\begin{aligned} P_{kl,\phi_2}(\Theta) &\equiv \frac{\partial}{\partial\phi_2} P_{kl}(\Theta) \\ &= \frac{((\partial/\partial\phi_2)S_{kl}(\Theta))D(\Theta) - S_{kl}(\Theta)((\partial/\partial\phi_2)D(\Theta))}{(D(\Theta))^2}. \end{aligned}$$

The first-order partial derivatives of $D(\Theta)$ in (20) and $S_{kl}(\Theta)$ in (23) with respect to each argument in (27) are expressed in the Appendices A and B. Denominator of equation (27) can be written as

$$\begin{aligned} (D(\Theta))^2 &= D(\Theta)D(\Theta) \\ &= M^4 - 2M^2|Q(\Theta)|^2 + |Q(\Theta)|^4. \end{aligned} \quad (28)$$

Using (21), $|Q(\Theta)|^4$ is defined as

$$\begin{aligned} |Q(\Theta)|^4 &= |Q(\Theta)|^2|Q(\Theta)|^2 \\ &= \sum_{k=1}^M \sum_{k'=1}^M \sum_{q=1}^M \sum_{q'=1}^M (a_{k,1})^* a_{k,2} a_{k',1} (a_{k',2})^* (a_{q,1})^* a_{q,2} a_{q',1} (a_{q',2})^*. \end{aligned} \quad (29)$$

We define $\widehat{\mathbf{R}}$ in (26) as

$$\widehat{\mathbf{R}} = \frac{1}{T} \sum_{n=1}^T \mathbf{x}(t_n) \mathbf{x}^H(t_n), \quad (30)$$

where $\mathbf{x}(t_n)$ is given in (2). Let $\delta \mathbf{R}$ represent the difference between $\widehat{\mathbf{R}}'$ and $\widehat{\mathbf{R}}$:

$$\delta \mathbf{R} = \widehat{\mathbf{R}}' - \widehat{\mathbf{R}}, \quad (31)$$

$$\delta R_{lk} = \widehat{R}'_{lk} - \widehat{R}_{lk}. \quad (32)$$

Substituting (32) in (26) and applying the first-order Taylor expansion of $P_{kl,\theta_1}(\Theta)$, $P_{kl,\theta_2}(\Theta)$, $P_{kl,\phi_1}(\Theta)$, and $P_{kl,\phi_2}(\Theta)$ yield

$$\begin{aligned} & \sum_{k=1}^M \sum_{l=1}^M \left(P_{kl,\theta_i}(\Theta) \Big|_{\Theta=\Theta^{(0)}} + \sum_{j=1}^2 (\delta\theta_j P_{kl,\theta_i,\theta_j}(\Theta) \Big|_{\Theta=\Theta^{(0)}}) \right. \\ & \left. + \sum_{j=1}^2 (\delta\phi_j P_{kl,\theta_i,\theta_j}(\Theta) \Big|_{\Theta=\Theta^{(0)}}) \quad i = 1, 2 \right) (\widehat{R}_{lk} \\ & + \delta R_{lk}) = 0, \end{aligned} \quad (33)$$

$$\begin{aligned} & \sum_{k=1}^M \sum_{l=1}^M \left(P_{kl,\phi_i}(\Theta) \Big|_{\Theta=\Theta^{(0)}} + \sum_{j=1}^2 (\delta\theta_j P_{kl,\phi_i,\theta_j}(\Theta) \Big|_{\Theta=\Theta^{(0)}}) \right. \\ & \left. + \sum_{j=1}^2 (\delta\phi_j P_{kl,\phi_i,\theta_j}(\Theta) \Big|_{\Theta=\Theta^{(0)}}) \quad i = 3, 4 \right) (\widehat{R}_{lk} \\ & + \delta R_{lk}) = 0. \end{aligned}$$

Let $\mathbf{w}_1^{(u=1)}$, $\mathbf{w}_2^{(u=1)}$, $\mathbf{w}_3^{(u=1)}$, $\mathbf{w}_4^{(u=1)}$, \mathbf{b} , and $\mathbf{e}^{(u=1)}$ be defined as

$$w_{i,j}^{(u=1)} = \begin{cases} \sum_{k=1}^M \sum_{l=1}^M P_{kl,\theta_j,\theta_i}(\Theta) \Big|_{\Theta=\Theta^{(0)}} (\widehat{R}_{lk} + \delta R_{lk}) & i = 1, 2 \quad j = 1, 2 \\ \sum_{k=1}^M \sum_{l=1}^M P_{kl,\theta_j,\theta_i}(\Theta) \Big|_{\Theta=\Theta^{(0)}} (\widehat{R}_{lk} + \delta R_{lk}) & i = 1, 2 \quad j = 3, 4 \\ \sum_{k=1}^M \sum_{l=1}^M P_{kl,\theta_j,\phi_{i-2}}(\Theta) \Big|_{\Theta=\Theta^{(0)}} (\widehat{R}_{lk} + \delta R_{lk}) & i = 3, 4 \quad j = 1, 2 \\ \sum_{k=1}^M \sum_{l=1}^M P_{kl,\theta_j,\phi_{i-2}}(\Theta) \Big|_{\Theta=\Theta^{(0)}} (\widehat{R}_{lk} + \delta R_{lk}) & i = 3, 4 \quad j = 3, 4, \end{cases} \quad (34)$$

$$b_i = \begin{cases} -\sum_{k=1}^M \sum_{l=1}^M P_{kl,\theta_i}(\Theta) \Big|_{\Theta=\Theta^{(0)}} (\widehat{R}_{lk} + \delta R_{lk}) & i = 1, 2 \\ -\sum_{k=1}^M \sum_{l=1}^M P_{kl,\phi_{i-2}}(\Theta) \Big|_{\Theta=\Theta^{(0)}} (\widehat{R}_{lk} + \delta R_{lk}) & i = 3, 4, \end{cases} \quad (35)$$

$$e_i^{(u=1)} = \begin{cases} \delta\theta_i^{(u=1)} & i = 1, 2 \\ \delta\phi_{i-2}^{(u=1)} & i = 3, 4, \end{cases} \quad (36)$$

where $w_{i,j}^{(u=1)}$ denotes the j th component of \mathbf{w}_i and b_i and e_i denote the i th component of \mathbf{b} and \mathbf{e} , respectively. Using (34)–(36), (33) can be expressed in matrix form

$$\mathbf{W}^{(u=1)} \mathbf{e}^{(u=1)} = \mathbf{b}, \quad (37)$$

where $\mathbf{W}^{(u=1)}$ is defined as

$$\mathbf{W}^{(u=1)} \equiv [\mathbf{w}_1^{(u=1)} \quad \mathbf{w}_2^{(u=1)} \quad \mathbf{w}_3^{(u=1)} \quad \mathbf{w}_4^{(u=1)}]. \quad (38)$$

Note that $w_{i,j}^{(u=1)}$ in (34) denotes the entry at the j th row and the i th column of \mathbf{W} in (38), not at the i th row and the j th column. $\text{tr}(\mathbf{P}(\Theta)\widehat{\mathbf{R}})$ should be maximized at $\Theta = \Theta^{(0)}$, since, with the sample covariance matrix from noiseless response, the ML algorithm estimates the DOA accurately. Therefore, the partial derivatives of $\text{tr}(\mathbf{P}(\Theta)\widehat{\mathbf{R}})$ with respect to the each entry of Θ should be zero at $\Theta = \widehat{\Theta}$

$$\begin{aligned} \frac{\partial}{\partial\theta_i} \text{tr}(\mathbf{P}(\Theta)\widehat{\mathbf{R}}) \Big|_{\Theta=\widehat{\Theta}} &= \sum_{k=1}^M \sum_{l=1}^M \left(\frac{\partial}{\partial\theta_i} P_{kl}(\Theta) \Big|_{\Theta=\widehat{\Theta}} \right) \widehat{R}_{lk} \\ &= \sum_{k=1}^M \sum_{l=1}^M (P_{kl,\theta_i}(\Theta) \Big|_{\Theta=\widehat{\Theta}}) \widehat{R}_{lk} \\ &= 0 \quad i = 1, 2, \end{aligned} \quad (39)$$

$$\begin{aligned} \frac{\partial}{\partial\phi_i} \text{tr}(\mathbf{P}(\Theta)\widehat{\mathbf{R}}) \Big|_{\Theta=\widehat{\Theta}} &= \sum_{k=1}^M \sum_{l=1}^M \left(\frac{\partial}{\partial\phi_i} P_{kl}(\Theta) \Big|_{\Theta=\widehat{\Theta}} \right) \widehat{R}_{lk} \\ &= \sum_{k=1}^M \sum_{l=1}^M (P_{kl,\phi_i}(\Theta) \Big|_{\Theta=\widehat{\Theta}}) \widehat{R}_{lk} \\ &= 0 \quad i = 1, 2. \end{aligned}$$

The last equalities of (39) can be expressed as

$$\begin{aligned} \sum_{k=1}^M \sum_{l=1}^M P_{kl,\theta_i}(\Theta) \Big|_{\Theta=\Theta^{(0)}} \widehat{R}_{lk} &= 0 \quad i = 1, 2, \\ \sum_{k=1}^M \sum_{l=1}^M P_{kl,\phi_i}(\Theta) \Big|_{\Theta=\Theta^{(0)}} \widehat{R}_{lk} &= 0 \quad i = 1, 2. \end{aligned} \quad (40)$$

Substituting (40) in (35), \mathbf{b} is simplified to

$$b_i = \begin{cases} -\sum_{k=1}^M \sum_{l=1}^M P_{kl,\theta_i}(\Theta) \Big|_{\Theta=\Theta^{(0)}} \delta R_{lk} & i = 1, 2 \\ -\sum_{k=1}^M \sum_{l=1}^M P_{kl,\phi_{i-2}}(\Theta) \Big|_{\Theta=\Theta^{(0)}} \delta R_{lk} & i = 3, 4. \end{cases} \quad (41)$$

Using (38) and (35), $\mathbf{e}^{(u=1)}$ in (37) is defined as

$$\mathbf{e}^{(u=1)} = (\mathbf{W}^{(u=1)})^{-1} \mathbf{b}. \quad (42)$$

Since $\widehat{R}_{lk} \gg \delta R_{lk}$ is true in (34), (34) can be approximated as

$$w_{i,j}^{(u=1,v)} = \begin{cases} \sum_{k=1}^M \sum_{l=1}^M P_{kl,\theta_j,\theta_i}(\Theta)|_{\Theta=\Theta^{(0)}} \widehat{R}_{lk} & i=1,2 \ j=1,2 \\ \sum_{k=1}^M \sum_{l=1}^M P_{kl,\phi_{j-2},\theta_i}(\Theta)|_{\Theta=\Theta^{(0)}} \widehat{R}_{lk} & i=1,2 \ j=3,4 \\ \sum_{k=1}^M \sum_{l=1}^M P_{kl,\theta_j,\phi_{i-2}}(\Theta)|_{\Theta=\Theta^{(0)}} \widehat{R}_{lk} & i=3,4 \ j=1,2 \\ \sum_{k=1}^M \sum_{l=1}^M P_{kl,\phi_{j-2},\phi_{i-2}}(\Theta)|_{\Theta=\Theta^{(0)}} \widehat{R}_{lk} & i=3,4 \ j=3,4, \end{cases} \quad (43)$$

where the superscript v denotes that the approximation based on $\widehat{R}_{lk} \gg \delta R_{lk}$ is applied. Accordingly, $\mathbf{W}^{(u=1,v)}$ is defined as

$$\mathbf{W}^{(u=1,v)} = [\mathbf{w}_1^{(u=1,v)} \ \mathbf{w}_2^{(u=1,v)} \ \mathbf{w}_3^{(u=1,v)} \ \mathbf{w}_4^{(u=1,v)}]. \quad (44)$$

The first-order derivatives of $P_{kl,\theta_1}(\Theta)$, $P_{kl,\theta_2}(\Theta)$, $P_{kl,\phi_1}(\Theta)$, and $P_{kl,\phi_2}(\Theta)$ in (34) are derived in Appendix G. Applying V -approximation to (37), $\mathbf{e}^{(u=1,v)}$ is given by

$$\mathbf{e}^{(u=1,v)} = (\mathbf{W}^{(u=1,v)})^{-1} \mathbf{b}, \quad (45)$$

where an explicit expression of the entries of $\mathbf{e}^{(u=1,v)}$ is

$$e_i^{(u=1,v)} = \begin{cases} \delta\theta_i^{(u=1,v)} & i=1,2 \\ \delta\phi_{i-2}^{(u=1,v)} & i=3,4. \end{cases} \quad (46)$$

4. Closed-Form Expression of Mean Square Error

Using (45), an analytic MSE of $\mathbf{e}^{(u=1,v)}$ can be expressed as

$$E[\mathbf{e}^{(u=1,v)} (\mathbf{e}^{(u=1,v)})^H] = (\mathbf{W}^{(u=1,v)})^{-1} E[\mathbf{b}\mathbf{b}^H] ((\mathbf{W}^{(u=1,v)})^{-1})^H. \quad (47)$$

The entry at the i th row and the j th column of $E[\mathbf{b}\mathbf{b}^H]$ can be expressed as

$$(E[\mathbf{b}^H\mathbf{b}])_{i,j} = \begin{cases} \sum_{k=1}^M \sum_{k'=1}^M \sum_{l=1}^M \sum_{l'=1}^M P_{kl,\theta_i,\theta_j} E[\delta R_{lk} \delta R_{l'k'}^*] & i=1,2 \ j=1,2 \\ \sum_{k=1}^M \sum_{k'=1}^M \sum_{l=1}^M \sum_{l'=1}^M P_{kl,\phi_{i-2},\theta_j} E[\delta R_{lk} \delta R_{l'k'}^*] & i=3,4 \ j=1,2 \\ \sum_{k=1}^M \sum_{k'=1}^M \sum_{l=1}^M \sum_{l'=1}^M P_{kl,\theta_i,\phi_{j-2}} E[\delta R_{lk} \delta R_{l'k'}^*] & i=1,2 \ j=3,4 \\ \sum_{k=1}^M \sum_{k'=1}^M \sum_{l=1}^M \sum_{l'=1}^M P_{kl,\phi_{i-2},\phi_{j-2}} E[\delta R_{lk} \delta R_{l'k'}^*] & i=3,4 \ j=3,4. \end{cases} \quad (48)$$

$E[\delta R_{lk} \delta R_{l'k'}^*]$ in (48) is derived in Appendix P. Entries of $E[\mathbf{e}^{(u=1,v)} (\mathbf{e}^{(u=1,v)})^H]$ in (47) are written as

$$(E[\mathbf{e}^{(u=1,v)} (\mathbf{e}^{(u=1,v)})^H])_{i,j} = \begin{cases} E[\delta\theta_i^{(u=1,v)} \delta\theta_j^{*(u=1,v)}] & i=1,2 \ j=1,2 \\ E[\delta\theta_i^{(u=1,v)} \delta\phi_{j-2}^{*(u=1,v)}] & i=1,2 \ j=3,4 \\ E[\delta\phi_{i-2}^{(u=1,v)} \delta\theta_j^{*(u=1,v)}] & i=3,4 \ j=1,2 \\ E[\delta\phi_{i-2}^{(u=1,v)} \delta\phi_{j-2}^{*(u=1,v)}] & i=3,4 \ j=3,4. \end{cases} \quad (49)$$

From (49), it is clear that the MSEs of $\delta\theta_1$, $\delta\theta_2$, $\delta\phi_1$, and $\delta\phi_2$ are given by

$$E[(\delta\theta_i^{(u=1,v)})^2] = E[\delta\theta_i^{(u=1,v)} (\delta\theta_i^{(u=1,v)})^*] = (E[\mathbf{e}^{(u=1,v)} (\mathbf{e}^{(u=1,v)})^H])_{i,i} \quad (50)$$

$$i=1,2,$$

$$E[(\delta\phi_{i-2}^{(u=1,v)})^2] = E[\delta\phi_{i-2}^{(u=1,v)} (\delta\phi_{i-2}^{(u=1,v)})^*] = (E[\mathbf{e}^{(u=1,v)} (\mathbf{e}^{(u=1,v)})^H])_{i,i} \quad (51)$$

$$i=3,4,$$

where $(\delta\theta_i^{(u=1,v)})^2 = \delta\theta_i^{(u=1,v)} (\delta\theta_i^{(u=1,v)})^*$ and $(\delta\phi_{i-2}^{(u=1,v)})^2 = \delta\phi_{i-2}^{(u=1,v)} (\delta\phi_{i-2}^{(u=1,v)})^*$ are true since $\delta\theta_i$ and $\delta\phi_{i-2}$ are real-valued. Mathematical details on the derivation are summarized as follows.

Mathematical Details on the Performance Analysis of ML DOA Estimation. Number of snapshots is L , number of arrays is M , and number of signals is 2.

$$\begin{aligned} \Theta &= (\theta_1, \phi_1, \theta_2, \phi_2), \\ \Theta^{(0)} &= (\theta_1^{(0)}, \phi_1^{(0)}, \theta_2^{(0)}, \phi_2^{(0)}), \\ \widehat{\Theta} &= (\widehat{\theta}_1, \widehat{\phi}_1, \widehat{\theta}_2, \widehat{\phi}_2) \implies \\ \delta\Theta &\equiv \widehat{\Theta} - \Theta^{(0)} = (\delta\theta_1, \delta\phi_1, \delta\theta_2, \delta\phi_2), \\ \mathbf{A}(\theta_1, \phi_1, \theta_2, \phi_2) &= [\mathbf{a}(\theta_1, \phi_1) \ \mathbf{a}(\theta_2, \phi_2)], \\ \mathbf{a}(\theta, \phi) &= [a_1(\theta, \phi) \ \cdots \ a_M(\theta, \phi)]^T \\ &= [\exp(j\psi_1(\theta, \phi)) \ \cdots \ \exp(j\psi_M(\theta, \phi))]^T, \\ \mathbf{s}(t) &= [s_1(t), s_2(t)]^T, \\ \mathbf{x}(t) &\equiv \mathbf{A}(\Theta) \mathbf{s}(t), \\ \mathbf{x}'(t) &\equiv \mathbf{A}(\Theta) \mathbf{s}(t) + \mathbf{n}(t). \end{aligned} \quad (52)$$

Projection matrix of $\mathbf{A}(\Theta)$: $\mathbf{P}(\Theta) = \mathbf{A}(\Theta)(\mathbf{A}^H(\Theta)\mathbf{A}(\Theta))^{-1}\mathbf{A}^H(\Theta)$

$$\begin{aligned}\widehat{\mathbf{R}} &= \frac{1}{L} \sum_{i=1}^L \mathbf{x}(t_i) \mathbf{x}^H(t_i), \\ \widehat{\mathbf{R}}' &= \frac{1}{L} \sum_{i=1}^L \mathbf{x}'(t_i) \mathbf{x}'^H(t_i) \implies \\ \delta \mathbf{R} &\equiv \widehat{\mathbf{R}}' - \widehat{\mathbf{R}}.\end{aligned}\quad (53)$$

The derivatives of the ML cost function, based on the covariance matrix associated with noisy array response, with respect to each incident signal, are not identically zero at true incident angles. From the angles at which the derivative is identically zero, the expression of the estimation error can be derived

$$\begin{aligned}P_{kl,\theta_n}(\Theta) &\equiv \frac{\partial}{\partial \theta_n} \mathbf{P}_{kl}(\Theta), \\ P_{kl,\phi_n}(\Theta) &\equiv \frac{\partial}{\partial \phi_n} \mathbf{P}_{kl}(\Theta), \\ n &= 1, 2,\end{aligned}\quad (54)$$

$$\text{tr}(\mathbf{P}_{kl}(\Theta) \widehat{\mathbf{R}}') = \sum_{k=1}^M \sum_{l=1}^M P_{kl}(\Theta) \widehat{R}'_{lk}.$$

The derivative of the ML cost function, based on the covariance matrix associated with noiseless array response, with respect to each incident signal, is identically zero at true incident angles

$$\begin{aligned}\frac{\partial}{\partial \theta_n} \text{tr}(\mathbf{P}_{kl}(\Theta) \widehat{\mathbf{R}}) \Big|_{\Theta=\Theta^{(0)}} &= \sum_{k=1}^M \sum_{l=1}^M P_{kl,\theta_n}(\Theta) \widehat{R}_{lk} \Big|_{\Theta=\Theta^{(0)}} \\ &= 0, \quad n = 1, 2,\end{aligned}\quad (55)$$

$$\begin{aligned}\frac{\partial}{\partial \phi_n} \text{tr}(\mathbf{P}_{kl}(\Theta) \widehat{\mathbf{R}}) \Big|_{\Theta=\Theta^{(0)}} &= \sum_{k=1}^M \sum_{l=1}^M P_{kl,\phi_n}(\Theta) \widehat{R}_{lk} \Big|_{\Theta=\Theta^{(0)}} \\ &= 0, \quad n = 1, 2,\end{aligned}\quad (56)$$

$$\begin{aligned}\frac{\partial}{\partial \theta_n} \text{tr}(\mathbf{P}_{kl}(\Theta) \Big|_{\Theta=\widehat{\Theta}} \widehat{\mathbf{R}}') &= \text{tr} \left(\frac{\partial}{\partial \theta_n} \mathbf{P}_{kl}(\Theta) \Big|_{\Theta=\widehat{\Theta}} \widehat{\mathbf{R}}' \right) \\ &= \sum_{k=1}^M \sum_{l=1}^M P_{kl,\theta_n}(\Theta) (\widehat{R}_{lk} + \delta R_{lk}) \Big|_{\Theta=\widehat{\Theta}} = 0, \\ n &= 1, 2,\end{aligned}$$

$$\begin{aligned}\frac{\partial}{\partial \phi_n} \text{tr}(\mathbf{P}_{kl}(\Theta) \Big|_{\Theta=\widehat{\Theta}} \widehat{\mathbf{R}}') &= \text{tr} \left(\frac{\partial}{\partial \phi_n} \mathbf{P}_{kl}(\Theta) \Big|_{\Theta=\widehat{\Theta}} \widehat{\mathbf{R}}' \right) \\ &= \sum_{k=1}^M \sum_{l=1}^M P_{kl,\phi_n}(\Theta) (\widehat{R}_{lk} + \delta R_{lk}) \Big|_{\Theta=\widehat{\Theta}} = 0, \\ n &= 1, 2,\end{aligned}\quad (57)$$

$$\begin{aligned}\sum_{k=1}^M \sum_{l=1}^M (f_n)_{kl}(\Theta) (\widehat{R}_{lk} + \delta R_{lk}) \Big|_{\Theta=\Theta^{(0)}+\delta\Theta} & \\ &= \sum_{k=1}^M \sum_{l=1}^M \left((f_n)_{kl}(\Theta) \Big|_{\Theta=\Theta^{(0)}} \right. \\ &+ \delta\theta_1 \frac{\partial}{\partial \theta_1} (f_n)_{kl}(\Theta) \Big|_{\Theta=\Theta^{(0)}} \\ &+ \delta\theta_2 \frac{\partial}{\partial \theta_2} (f_n)_{kl}(\Theta) \Big|_{\Theta=\Theta^{(0)}} \\ &+ \delta\phi_1 \frac{\partial}{\partial \phi_1} (f_n)_{kl}(\Theta) \Big|_{\Theta=\Theta^{(0)}} \\ &+ \left. \delta\phi_2 \frac{\partial}{\partial \phi_2} (f_n)_{kl}(\Theta) \Big|_{\Theta=\Theta^{(0)}} \right) (\widehat{R}_{lk} + \delta R_{lk}) = 0, \\ n &= 1, \dots, N,\end{aligned}\quad (58)$$

$$\begin{aligned}\sum_{k=1}^M \sum_{l=1}^M (g_n)_{kl}(\Theta) (\widehat{R}_{lk} + \delta R_{lk}) \Big|_{\Theta=\Theta^{(0)}+\delta\Theta} & \\ &= \sum_{k=1}^M \sum_{l=1}^M \left((g_n)_{kl}(\Theta) \Big|_{\Theta=\Theta^{(0)}} \right. \\ &+ \delta\theta_1 \frac{\partial}{\partial \theta_1} (g_n)_{kl}(\Theta) \Big|_{\Theta=\Theta^{(0)}} \\ &+ \delta\theta_2 \frac{\partial}{\partial \theta_2} (g_n)_{kl}(\Theta) \Big|_{\Theta=\Theta^{(0)}} \\ &+ \delta\phi_1 \frac{\partial}{\partial \phi_1} (g_n)_{kl}(\Theta) \Big|_{\Theta=\Theta^{(0)}} \\ &+ \left. \delta\phi_2 \frac{\partial}{\partial \phi_2} (g_n)_{kl}(\Theta) \Big|_{\Theta=\Theta^{(0)}} \right) (\widehat{R}_{lk} + \delta R_{lk}) = 0 \\ n &= 1, \dots, N.\end{aligned}$$

Substituting (55) and (56) in (58) results in

$$\begin{bmatrix} \frac{\partial}{\partial \theta_1} (f_1)_{kl}(\Theta) \Big|_{\Theta=\Theta^{(0)}} (\widehat{R}_{lk} + \delta R_{lk}) & \frac{\partial}{\partial \theta_2} (f_1)_{kl}(\Theta) \Big|_{\Theta=\Theta^{(0)}} (\widehat{R}_{lk} + \delta R_{lk}) & \frac{\partial}{\partial \phi_1} (f_1)_{kl}(\Theta) \Big|_{\Theta=\Theta^{(0)}} (\widehat{R}_{lk} + \delta R_{lk}) & \frac{\partial}{\partial \phi_2} (f_1)_{kl}(\Theta) \Big|_{\Theta=\Theta^{(0)}} (\widehat{R}_{lk} + \delta R_{lk}) \\ \frac{\partial}{\partial \theta_1} (f_2)_{kl}(\Theta) \Big|_{\Theta=\Theta^{(0)}} (\widehat{R}_{lk} + \delta R_{lk}) & \frac{\partial}{\partial \theta_2} (f_2)_{kl}(\Theta) \Big|_{\Theta=\Theta^{(0)}} (\widehat{R}_{lk} + \delta R_{lk}) & \frac{\partial}{\partial \phi_1} (f_2)_{kl}(\Theta) \Big|_{\Theta=\Theta^{(0)}} (\widehat{R}_{lk} + \delta R_{lk}) & \frac{\partial}{\partial \phi_2} (f_2)_{kl}(\Theta) \Big|_{\Theta=\Theta^{(0)}} (\widehat{R}_{lk} + \delta R_{lk}) \\ \frac{\partial}{\partial \theta_1} (g_1)_{kl}(\Theta) \Big|_{\Theta=\Theta^{(0)}} (\widehat{R}_{lk} + \delta R_{lk}) & \frac{\partial}{\partial \theta_2} (g_1)_{kl}(\Theta) \Big|_{\Theta=\Theta^{(0)}} (\widehat{R}_{lk} + \delta R_{lk}) & \frac{\partial}{\partial \phi_1} (f_2)_{kl}(\Theta) \Big|_{\Theta=\Theta^{(0)}} (\widehat{R}_{lk} + \delta R_{lk}) & \frac{\partial}{\partial \phi_2} (f_2)_{kl}(\Theta) \Big|_{\Theta=\Theta^{(0)}} (\widehat{R}_{lk} + \delta R_{lk}) \\ \frac{\partial}{\partial \theta_1} (g_2)_{kl}(\Theta) \Big|_{\Theta=\Theta^{(0)}} (\widehat{R}_{lk} + \delta R_{lk}) & \frac{\partial}{\partial \theta_2} (g_2)_{kl}(\Theta) \Big|_{\Theta=\Theta^{(0)}} (\widehat{R}_{lk} + \delta R_{lk}) & \frac{\partial}{\partial \phi_1} (g_2)_{kl}(\Theta) \Big|_{\Theta=\Theta^{(0)}} (\widehat{R}_{lk} + \delta R_{lk}) & \frac{\partial}{\partial \phi_2} (g_2)_{kl}(\Theta) \Big|_{\Theta=\Theta^{(0)}} (\widehat{R}_{lk} + \delta R_{lk}) \end{bmatrix} \begin{bmatrix} \delta\theta_1^{(v=1)} \\ \delta\theta_1^{(v=1)} \\ \delta\phi_1^{(v=1)} \\ \delta\phi_N^{(v=1)} \end{bmatrix}$$

$$= \begin{bmatrix} -\sum_{k=1}^M \sum_{l=1}^M (f_1)_{kl}(\Theta)|_{\Theta=\Theta^{(0)}} \delta R_{lk} \\ -\sum_{k=1}^M \sum_{l=1}^M (f_2)_{kl}(\Theta)|_{\Theta=\Theta^{(0)}} \delta R_{lk} \\ -\sum_{k=1}^M \sum_{l=1}^M (g_1)_{kl}(\Theta)|_{\Theta=\Theta^{(0)}} \delta R_{lk} \\ -\sum_{k=1}^M \sum_{l=1}^M (g_2)_{kl}(\Theta)|_{\Theta=\Theta^{(0)}} \delta R_{lk} \end{bmatrix}. \quad (59)$$

Using $\hat{R}_{lk} + \delta R_{lk} \approx \hat{R}_{lk}$ in (59) results in

$$\begin{bmatrix} \frac{\partial}{\partial \theta_1} (f_1)_{kl}(\Theta)|_{\Theta=\Theta^{(0)}} \hat{R}_{lk} & \frac{\partial}{\partial \theta_2} (f_1)_{kl}(\Theta)|_{\Theta=\Theta^{(0)}} \hat{R}_{lk} & \frac{\partial}{\partial \phi_1} (f_1)_{kl}(\Theta)|_{\Theta=\Theta^{(0)}} \hat{R}_{lk} & \frac{\partial}{\partial \phi_2} (f_1)_{kl}(\Theta)|_{\Theta=\Theta^{(0)}} \hat{R}_{lk} \\ \frac{\partial}{\partial \theta_1} (f_2)_{kl}(\Theta)|_{\Theta=\Theta^{(0)}} \hat{R}_{lk} & \frac{\partial}{\partial \theta_2} (f_2)_{kl}(\Theta)|_{\Theta=\Theta^{(0)}} \hat{R}_{lk} & \frac{\partial}{\partial \phi_1} (f_2)_{kl}(\Theta)|_{\Theta=\Theta^{(0)}} \hat{R}_{lk} & \frac{\partial}{\partial \phi_2} (f_2)_{kl}(\Theta)|_{\Theta=\Theta^{(0)}} \hat{R}_{lk} \\ \frac{\partial}{\partial \theta_1} (g_1)_{kl}(\Theta)|_{\Theta=\Theta^{(0)}} \hat{R}_{lk} & \frac{\partial}{\partial \theta_2} (g_1)_{kl}(\Theta)|_{\Theta=\Theta^{(0)}} \hat{R}_{lk} & \frac{\partial}{\partial \phi_1} (f_2)_{kl}(\Theta)|_{\Theta=\Theta^{(0)}} \hat{R}_{lk} & \frac{\partial}{\partial \phi_2} (f_2)_{kl}(\Theta)|_{\Theta=\Theta^{(0)}} \hat{R}_{lk} \\ \frac{\partial}{\partial \theta_1} (g_2)_{kl}(\Theta)|_{\Theta=\Theta^{(0)}} \hat{R}_{lk} & \frac{\partial}{\partial \theta_2} (g_2)_{kl}(\Theta)|_{\Theta=\Theta^{(0)}} \hat{R}_{lk} & \frac{\partial}{\partial \phi_1} (g_2)_{kl}(\Theta)|_{\Theta=\Theta^{(0)}} \hat{R}_{lk} & \frac{\partial}{\partial \phi_2} (g_2)_{kl}(\Theta)|_{\Theta=\Theta^{(0)}} \hat{R}_{lk} \end{bmatrix} \begin{bmatrix} \delta \theta_1^{(v=1)} \\ \delta \theta_1^{(v=1)} \\ \delta \phi_1^{(v=1)} \\ \delta \phi_N^{(v=1)} \end{bmatrix} \\ = \begin{bmatrix} -\sum_{k=1}^M \sum_{l=1}^M (f_1)_{kl}(\Theta)|_{\Theta=\Theta^{(0)}} \delta R_{lk} \\ -\sum_{k=1}^M \sum_{l=1}^M (f_2)_{kl}(\Theta)|_{\Theta=\Theta^{(0)}} \delta R_{lk} \\ -\sum_{k=1}^M \sum_{l=1}^M (g_1)_{kl}(\Theta)|_{\Theta=\Theta^{(0)}} \delta R_{lk} \\ -\sum_{k=1}^M \sum_{l=1}^M (g_2)_{kl}(\Theta)|_{\Theta=\Theta^{(0)}} \delta R_{lk} \end{bmatrix} \Rightarrow \quad (60)$$

$$\mathbf{W}^{(v=1)} \mathbf{e}^{(v=1)} = \mathbf{b},$$

$$\mathbf{e}^{(v=1)} = (\mathbf{W}^{(v=1)})^{-1} \mathbf{b},$$

$$\begin{aligned} E \left[\mathbf{e}^{(v=1)} (\mathbf{e}^{(v=1)})^H \right] &= E \left[(\mathbf{W}^{(v=1)})^{-1} \mathbf{b} ((\mathbf{W}^{(v=1)})^{-1} \mathbf{b})^H \right] = E \left[(\mathbf{W}^{(v=1)})^{-1} \mathbf{b} \mathbf{b}^H ((\mathbf{W}^{(v=1)})^{-1})^H \right] \\ &= (\mathbf{W}^{(v=1)})^{-1} E \left[\mathbf{b} \mathbf{b}^H \right] ((\mathbf{W}^{(v=1)})^{-1})^H. \end{aligned}$$

An analytic expression of $E[\mathbf{bb}^H]$ can be derived by exploiting statistical distribution of δR_{jk} .

5. Numerical Results

MSEs of $\hat{\theta}_1$, $\hat{\theta}_1^{(u=1)}$, and $\hat{\theta}_1^{(u=1,v)}$ are defined as

$$\begin{aligned} \text{Simulation } E \left[\left(\hat{\theta}_1 - \theta_1^{(0)} \right)^2 \right] &= \frac{1}{T} \sum_{t=1}^T (\delta \theta_{1,(t)})^2, \\ \text{Simulation } E \left[\left(\hat{\theta}_1^{(u=1)} - \theta_1^{(0)} \right)^2 \right] &= \frac{1}{T} \sum_{t=1}^T (\delta \theta_{1,(t)}^{(u=1)})^2, \quad (61) \\ \text{Simulation } E \left[\left(\hat{\theta}_1^{(u=1,v)} - \theta_1^{(0)} \right)^2 \right] &= \frac{1}{T} \sum_{t=1}^T (\delta \theta_{1,(t)}^{(u=1,v)})^2, \end{aligned}$$

where T denotes the number of repetitions. The subscript t denotes the estimate associated with the t th repetition out of T repetitions. $(\delta \theta_{1,(t)})^2$, $(\delta \theta_{1,(t)}^{(u=1)})^2$, and $(\delta \theta_{1,(t)}^{(u=1,v)})^2$ in (61) are given by (42), (45), and (13), respectively.

In Figure 2(a), we illustrate how accurate the MSEs of $\hat{\theta}_1$, $\hat{\theta}_1^{(u=1)}$, and $\hat{\theta}_1^{(u=1,v)}$ are. The results with “Simulation $E[(\hat{\theta}_1 - \theta_1^{(0)})^2]$,” “Simulation $E[(\hat{\theta}_1^{(u=1)} - \theta_1^{(0)})^2]$,” “Simulation $E[(\hat{\theta}_1^{(u=1,v)} - \theta_1^{(0)})^2]$,” and “Analytic $E[(\hat{\theta}_1^{(u=1,v)} - \theta_1^{(0)})^2]$ ” are obtained using (61) and (50), respectively. It has been clearly shown that the results with “Simulation $E[(\hat{\theta}_1^{(u=1,v)} - \theta_1^{(0)})^2]$ ” show good agreement with those with “Analytic $E[(\hat{\theta}_1^{(u=1,v)} - \theta_1^{(0)})^2]$ ”. In addition, the results with “Simulation $E[(\hat{\theta}_1^{(u=1,v)} - \theta_1^{(0)})^2]$ ” get closer to those with “Simulation $E[(\hat{\theta}_1 - \theta_1^{(0)})^2]$ ” as SNR increases. Therefore, at high SNR, the results with “Analytic $E[(\hat{\theta}_1^{(u=1,v)} - \theta_1^{(0)})^2]$ ” can be used for determining how accurate the results with “ $E[(\hat{\theta}_1 - \theta_1^{(0)})^2]$ ” are. The lower bound of the MSE for an unbiased estimator is called the CRLB. The CRLB for θ_1 is also illustrated in Figure 2(a), where it is verified that the CRLB is actually below the analytic MSEs. Generally, the CRLB of each parameter can be obtained from the diagonal entry of \mathbf{B}_{STO} :

$$E \left[\left\{ \hat{\Theta} - \Theta^{(0)} \right\} \left\{ \hat{\Theta} - \Theta^{(0)} \right\}^T \right] \geq \mathbf{B}_{\text{STO}}, \quad (62)$$

$$\left(\mathbf{B}_{\text{STO}}^{-1} \right)_{ij} = \frac{2N}{\sigma^2} \text{Re} \left[\text{tr} \left\{ \mathbf{A}_j^H \mathbf{P}_A^\perp \mathbf{A}_i \mathbf{S} \mathbf{A}^H \mathbf{R}^{-1} \mathbf{A} \mathbf{S} \right\} \right], \quad (63)$$

$$i, j = 1, \dots, 4,$$

where \mathbf{A}_i is defined in [13]. The CRLB of θ_1 is obtained from (1, 1) element of \mathbf{B}_{STO} in (63).

MSEs of $\hat{\theta}_2$, $\hat{\theta}_2^{(u=1)}$, and $\hat{\theta}_2^{(u=1,v)}$ are defined as

$$\begin{aligned} \text{Simulation } E \left[\left(\hat{\theta}_2 - \theta_2^{(0)} \right)^2 \right] &= \frac{1}{T} \sum_{t=1}^T (\delta \theta_{2,(t)}^2)^2, \\ \text{Simulation } E \left[\left(\hat{\theta}_2^{(u=1)} - \theta_2^{(0)} \right)^2 \right] &= \frac{1}{T} \sum_{t=1}^T (\delta \theta_{2,(t)}^{(u=1)})^2, \quad (64) \\ \text{Simulation } E \left[\left(\hat{\theta}_2^{(u=1,v)} - \theta_2^{(0)} \right)^2 \right] &= \frac{1}{T} \sum_{t=1}^T (\delta \theta_{2,(t)}^{(u=1,v)})^2. \end{aligned}$$

$(\delta \theta_{2,(t)})^2$, $(\delta \theta_{2,(t)}^{(u=1)})^2$, and $(\delta \theta_{2,(t)}^{(u=1,v)})^2$ in (64) are given by (13), (42), and (45), respectively. In Figure 2(b), we illustrate how accurate the MSEs of $\hat{\theta}_2$, $\hat{\theta}_2^{(u=1)}$, and $\hat{\theta}_2^{(u=1,v)}$ are. The results with “Simulation $E[(\hat{\theta}_2 - \theta_2^{(0)})^2]$,” “Simulation $E[(\hat{\theta}_2^{(u=1)} - \theta_2^{(0)})^2]$,” “Simulation $E[(\hat{\theta}_2^{(u=1,v)} - \theta_2^{(0)})^2]$,” and “Analytic $E[(\hat{\theta}_2^{(u=1,v)} - \theta_2^{(0)})^2]$ ” are obtained using (64) and (51), respectively. We can easily see that the observation for $\hat{\theta}_1$, $\hat{\theta}_1^{(u=1)}$ and $\hat{\theta}_1^{(u=1,v)}$ in Figure 2(a) is also true for $\hat{\theta}_2$, $\hat{\theta}_2^{(u=1)}$ and $\hat{\theta}_2^{(u=1,v)}$ in Figure 2(b). The CRLB of θ_2 is obtained from the (3, 3) element of the \mathbf{B}_{STO} in (63).

MSEs of the $\hat{\phi}_1$, $\hat{\phi}_1^{(u=1)}$, and $\hat{\phi}_1^{(u=1,v)}$ are defined as

$$\begin{aligned} \text{Simulation } E \left[\left(\hat{\phi}_1 - \phi_1^{(0)} \right)^2 \right] &= \frac{1}{T} \sum_{t=1}^T (\delta \phi_{1,(t)}^2)^2, \\ \text{Simulation } E \left[\left(\hat{\phi}_1^{(u=1)} - \phi_1^{(0)} \right)^2 \right] &= \frac{1}{T} \sum_{t=1}^T (\delta \phi_{1,(t)}^{(u=1)})^2, \quad (65) \\ \text{Simulation } E \left[\left(\hat{\phi}_1^{(u=1,v)} - \phi_1^{(0)} \right)^2 \right] &= \frac{1}{T} \sum_{t=1}^T (\delta \phi_{1,(t)}^{(u=1,v)})^2. \end{aligned}$$

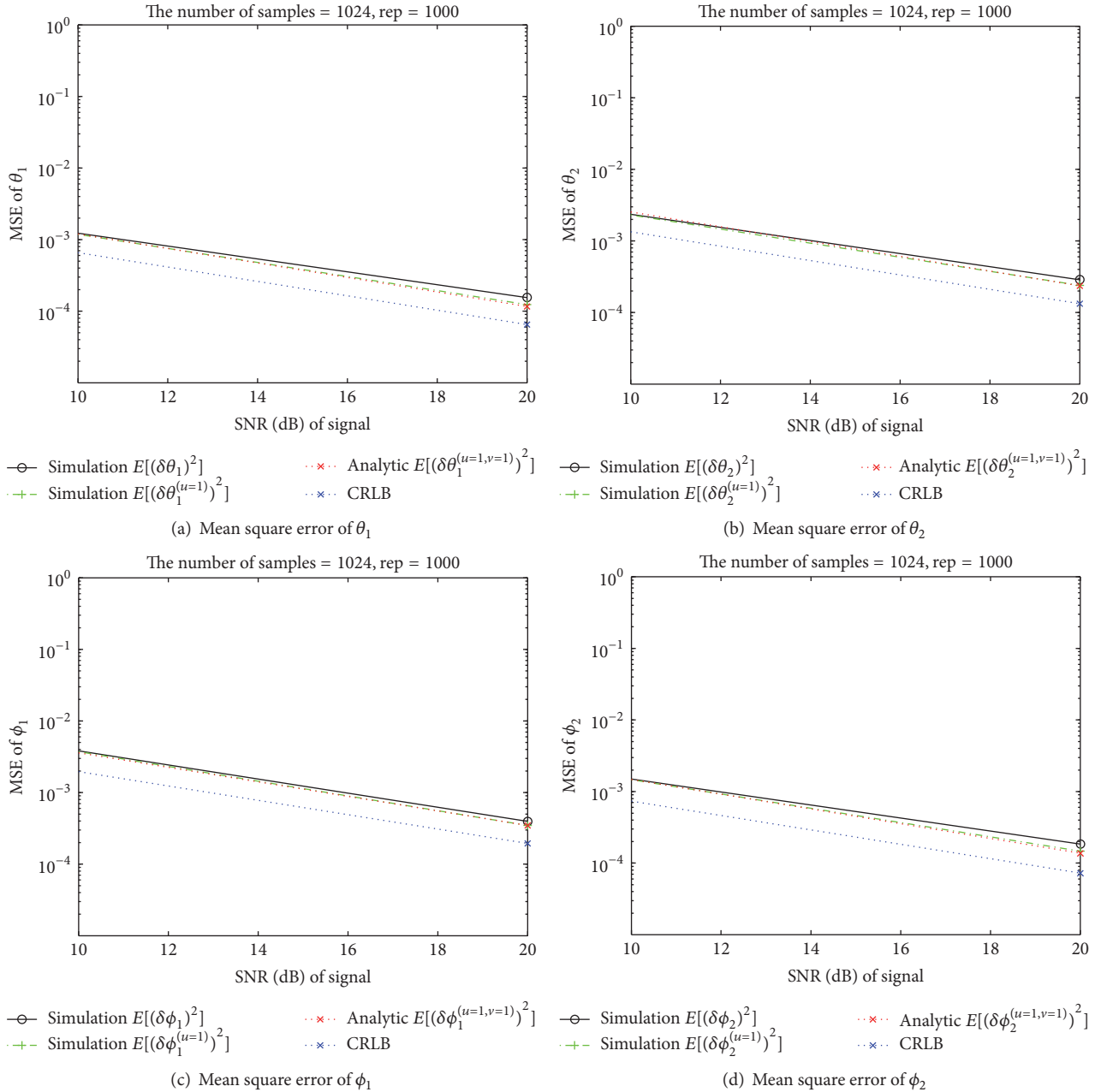
$(\delta \phi_{1,(t)})^2$, $(\delta \phi_{1,(t)}^{(u=1)})^2$, and $(\delta \phi_{1,(t)}^{(u=1,v)})^2$ in (65) are given by (13), (42), and (45), respectively.

In Figure 2(c), we illustrate how accurate the MSEs of $\hat{\phi}_1$, $\hat{\phi}_1^{(u=1)}$, and $\hat{\phi}_1^{(u=1,v)}$ are. The results with “Simulation $E[(\hat{\phi}_1 - \phi_1^{(0)})^2]$,” “Simulation $E[(\hat{\phi}_1^{(u=1)} - \phi_1^{(0)})^2]$,” “Simulation $E[(\hat{\phi}_1^{(u=1,v)} - \phi_1^{(0)})^2]$,” and “Analytic $E[(\hat{\phi}_1^{(u=1,v)} - \phi_1^{(0)})^2]$ ” are obtained using (65) and (51), respectively. It is clear in Figure 2(c) that $\hat{\phi}_1^{(u=1,v)}$ can be used to approximate $\hat{\phi}_1$ and that empirical MSE of $\hat{\phi}_1^{(u=1,v)}$ is equal to an analytic MSE of $\hat{\phi}_1^{(u=1,v)}$ in (51). The CRLB of ϕ_1 is obtained from the (2, 2) element of \mathbf{B}_{STO} in (63).

MSEs of $\hat{\phi}_2$, $\hat{\phi}_2^{(u=1)}$, and $\hat{\phi}_2^{(u=1,v)}$ are defined as

$$\begin{aligned} \text{Simulation } E \left[\left(\hat{\phi}_2 - \phi_2^{(0)} \right)^2 \right] &= \frac{1}{T} \sum_{t=1}^T (\delta \phi_{2,(t)}^2)^2, \\ \text{Simulation } E \left[\left(\hat{\phi}_2^{(u=1)} - \phi_2^{(0)} \right)^2 \right] &= \frac{1}{T} \sum_{t=1}^T (\delta \phi_{2,(t)}^{(u=1)})^2, \quad (66) \\ \text{Simulation } E \left[\left(\hat{\phi}_2^{(u=1,v)} - \phi_2^{(0)} \right)^2 \right] &= \frac{1}{T} \sum_{t=1}^T (\delta \phi_{2,(t)}^{(u=1,v)})^2. \end{aligned}$$

$(\delta \phi_{2,(t)})^2$, $(\delta \phi_{2,(t)}^{(u=1)})^2$, and $(\delta \phi_{2,(t)}^{(u=1,v)})^2$ in (66) are given by (13), (42), and (45), respectively. In Figure 2(d), we illustrate how accurate the MSEs of $\hat{\phi}_2$, $\hat{\phi}_2^{(u=1)}$, and $\hat{\phi}_2^{(u=1,v)}$ are.


 FIGURE 2: Mean square error of θ_1 , θ_2 , ϕ_1 , and ϕ_2 for SNR 10 dB to 20 dB.

The results with “Simulation $E[(\hat{\phi}_2 - \phi_2^{(0)})^2]$,” “Simulation $E[(\hat{\phi}_2^{(u=1)} - \phi_2^{(0)})^2]$,” “Simulation $E[(\hat{\phi}_2^{(u=1, v)} - \phi_2^{(0)})^2]$,” and “Analytic $E[(\hat{\phi}_2^{(u=1, v)} - \phi_2^{(0)})^2]$ ” are obtained using (66) and (51), respectively. It is clear that the observation on the various estimates of ϕ_1 , in Figure 2(c), also applies to the various estimates of ϕ_2 in Figure 2(d). The CRLB of ϕ_2 is obtained from the (4, 4) element of \mathbf{B}_{STO} in (63).

In Figures 3–5, the results with respect to SNR are shown. It has been shown in the new numerical results that a gap between the MSE of the MLE and the Cramer-Rao lower bound gets smaller as the SNR varies from -20 dB to 20 dB

in increments of 10 dB. Note that, in Figure 3, the gap for SNR = 20 dB is much smaller than that for SNR = -20 dB, which implies that the MSE of the MLE attains CRLB as SNR increases. Similar observation can be found in Figures 4 and 5.

Closed-form expression is only available for the estimate both with U -approximation and V -approximation. U -approximation in our scheme is based on the first-order Taylor series expansion, which implies that U -approximation becomes less accurate when the variance of the noise is large since the first-order Taylor series expansion does not take into account higher-order terms. Note that high variance of noise

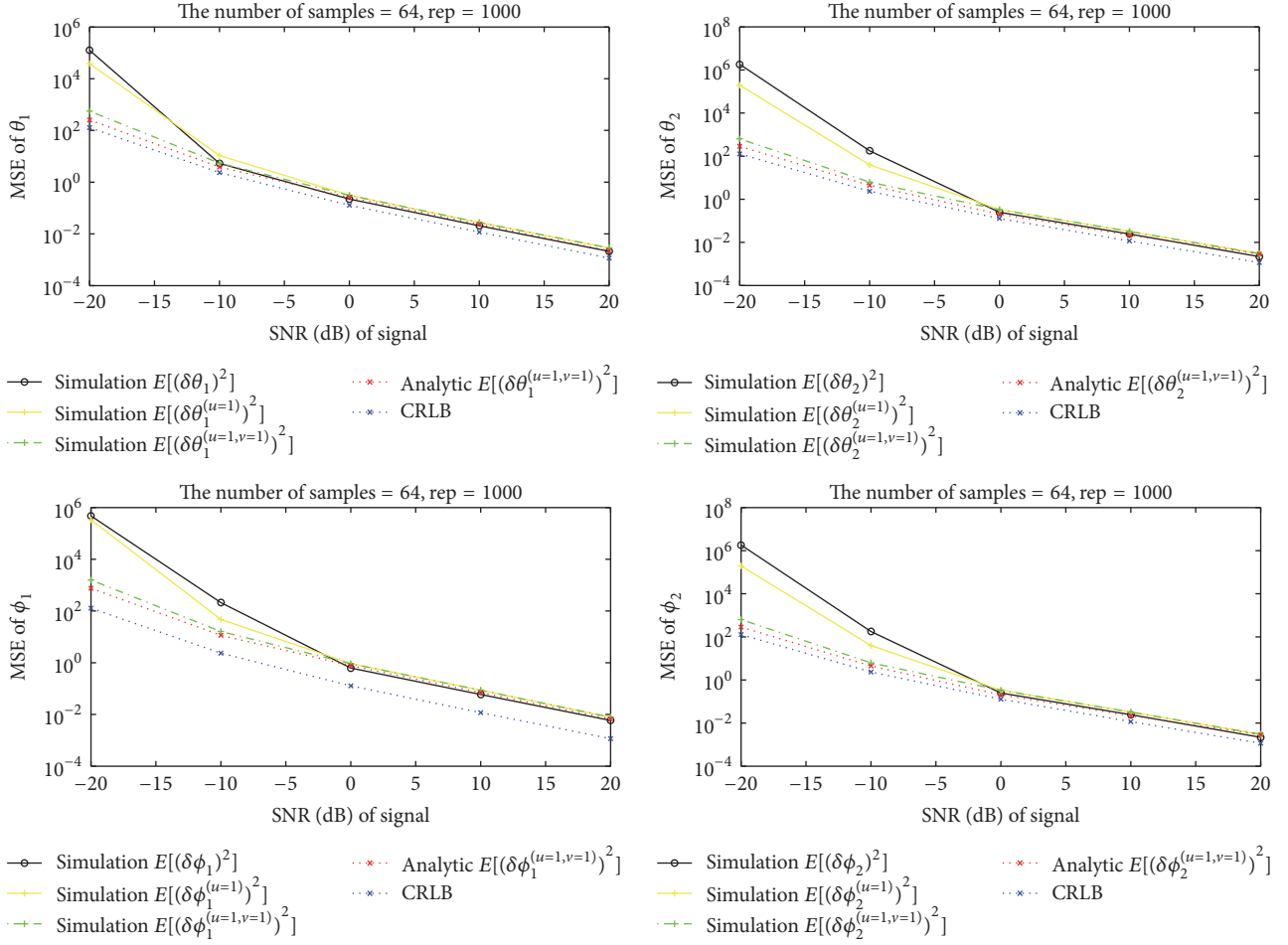


FIGURE 3: MSE of θ_1 , θ_2 , ϕ_1 , and ϕ_2 for SNR -20 dB to 20 dB (the number of samples = 2^6).

corresponds to low SNR. V -approximation in our scheme is based on the fact that the difference between the covariance matrix with noisy array response and that with noiseless antenna response is much smaller than the covariance matrix with noiseless antenna response. V -approximation is accurate when the noisy antenna response is similar to the noiseless antenna response, which is true for high SNR. That is, V -approximation is valid for high SNR.

In conclusion, both U -approximation and V -approximation are valid for high SNR, and therefore the closed-form expression for the estimate with U -approximation and V -approximation is also valid for high SNR.

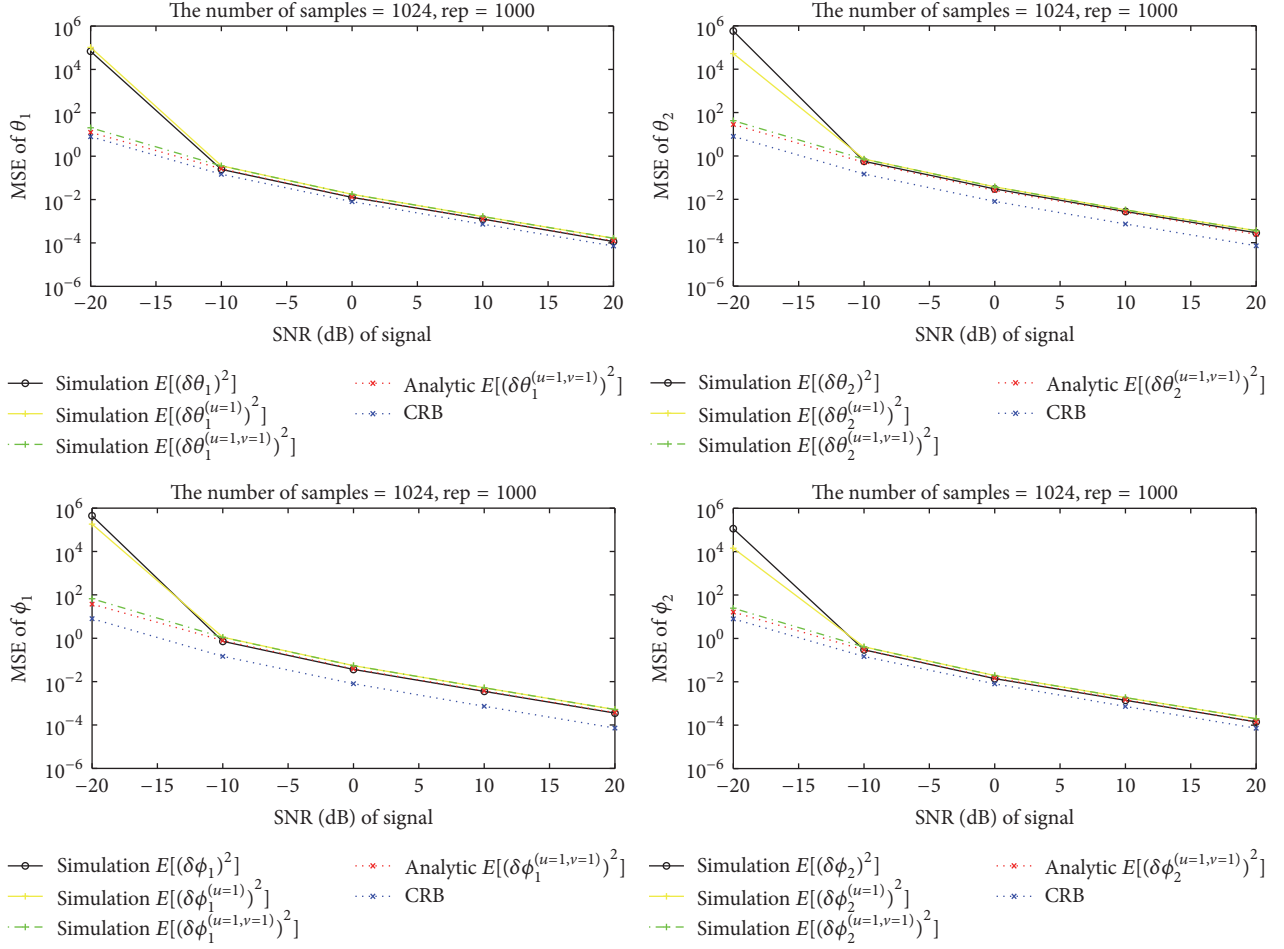
6. Summary and Conclusion

In Figures 6 and 7, we illustrate the outline of our derivation and how the performance analysis of the ML algorithm method is conducted.

In the case of azimuth/elevation estimation of multiple incident signals using the UCA, it has been shown that the bias of the estimate associated with the ML algorithm can be expressed in the closed-form at high SNR where the estimation error is small. The closed-form expression of the MSE of

the one of the estimates has been derived, which implies that the MSE of the estimates can be obtained without computationally intensive Monte-Carlo simulation. The derivation is based on the fact that, for small estimation error, we can make the Taylor series approximation of the array vector, which makes it possible for us to get a closed-form expression of the MSE of the estimate.

We assume that an additive noise on the antenna elements is complex Gaussian distributed and that noise at each antenna is spatially white. Future works include how to extend the results in this paper to the case of non-Gaussian noise and spatially correlated noise. Although the formulation and the numerical results for two incident signals are presented in this paper, an extension to multiple incident signals is quite intuitively clear and straightforward. The number of columns $\mathbf{A}(\Theta)$ in (4) is equal to the number of incident signals. For N incident signals, $\mathbf{A}^H(\Theta)\mathbf{A}(\Theta)$ in (14) is $N \times N$ matrix and $(\mathbf{A}^H(\Theta)\mathbf{A}(\Theta))^{-1}$ in (17) can be explicitly expressed using the adjoint method. More specifically, $D(\Theta)$ in (18), which is a determinant of $\mathbf{A}^H(\Theta)\mathbf{A}(\Theta)$, can be obtained from the cofactor expansion along any row or any column of $\mathbf{A}^H(\Theta)\mathbf{A}(\Theta)$. The entry at the k th row and the l th column of \mathbf{S} , $S_{kl}(\Theta)$ in (21), is the entry at the k th row and the l th column


 FIGURE 4: MSE of θ_1 , θ_2 , ϕ_1 , and ϕ_2 for SNR -20 dB to 20 dB (the number of samples = 2^{10}).

of the adjoint matrix of $\mathbf{A}^H(\Theta)\mathbf{A}(\Theta)$. Note also that $\mathbf{P}_{\mathbf{A}(\Theta)} = \mathbf{A}(\Theta)(\mathbf{A}^H(\Theta)\mathbf{A}(\Theta))^{-1}\mathbf{A}^H(\Theta)$ is $M \times M$ matrix, where M is the number of antenna elements. Therefore, the number of rows and the number of columns of $\mathbf{P}_{\mathbf{A}(\Theta)}$ are not dependent on the number of incident signals, N . Therefore, simple modification of the scheme presented in this paper results in more general scheme, which can be used irrespective of the number of incident signals.

Equation (7) of this manuscript is valid only for the uniform circular array. For different array structure, (7) should be modified appropriately. In that case, we only have to simply modify

- (i) the expressions associated with the first derivatives of (7), which are (D.1),
- (ii) the expressions associated with the second derivatives of (7), which are (K.1).

Simply modifying (D.1) and (K.1) for specific array structure is not so hard. Therefore, although we presented the formulation for the UCA structure, it can be very easily extended to any array structure.

Appendix

A. The First-Order Derivatives of $D(\Theta)$ with respect to θ_1 , θ_2 , ϕ_1 , and ϕ_2

For use in (27), Appendices F and G, the first-order partial derivatives of $D(\Theta)$ in (20) with respect to each argument are expressed as

$$\begin{aligned} \frac{\partial}{\partial \theta_1} D(\Theta) &= -\sum_{k=1}^M \sum_{k'=1}^M \left(\left(\frac{\partial}{\partial \theta_1} (a_{k,1})^* \right) a_{k,2} a_{k',1} (a_{k',2})^* \right. \\ &\quad \left. + (a_{k,1})^* a_{k,2} \left(\frac{\partial}{\partial \theta_1} a_{k',1} \right) (a_{k',2})^* \right), \end{aligned}$$

$$\begin{aligned} \frac{\partial}{\partial \theta_2} D(\Theta) &= -\sum_{k=1}^M \sum_{k'=1}^M \left((a_{k,1})^* \left(\frac{\partial}{\partial \theta_2} a_{k,2} \right) a_{k',1} (a_{k',2})^* \right. \\ &\quad \left. + (a_{k,1})^* a_{k,2} \left(\frac{\partial}{\partial \theta_2} a_{k',1} \right) (a_{k',2})^* \right), \end{aligned}$$

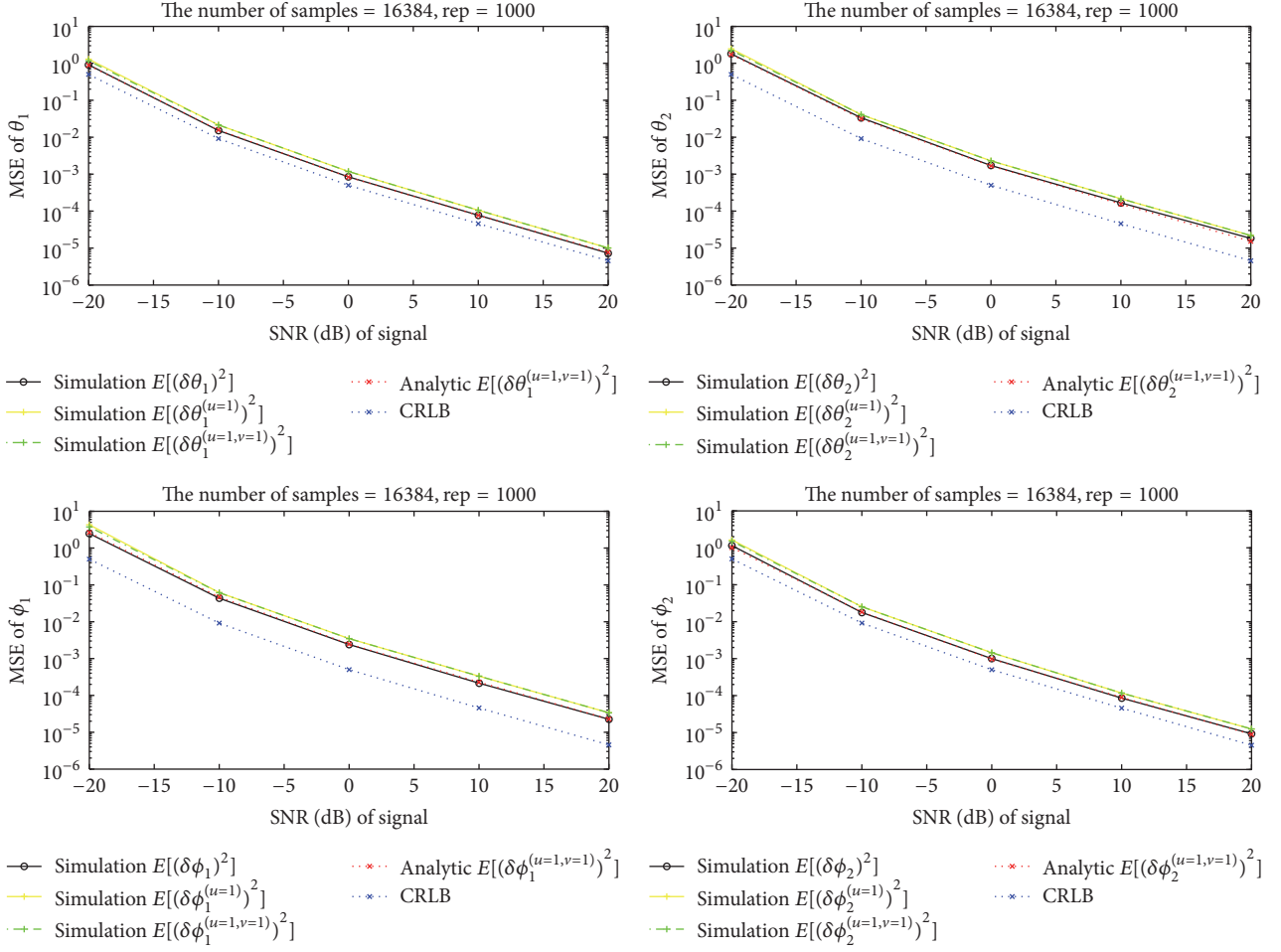


FIGURE 5: MSE of θ_1 , θ_2 , ϕ_1 , and ϕ_2 for SNR -20 dB to 20 dB (the number of samples = 2^{14}).

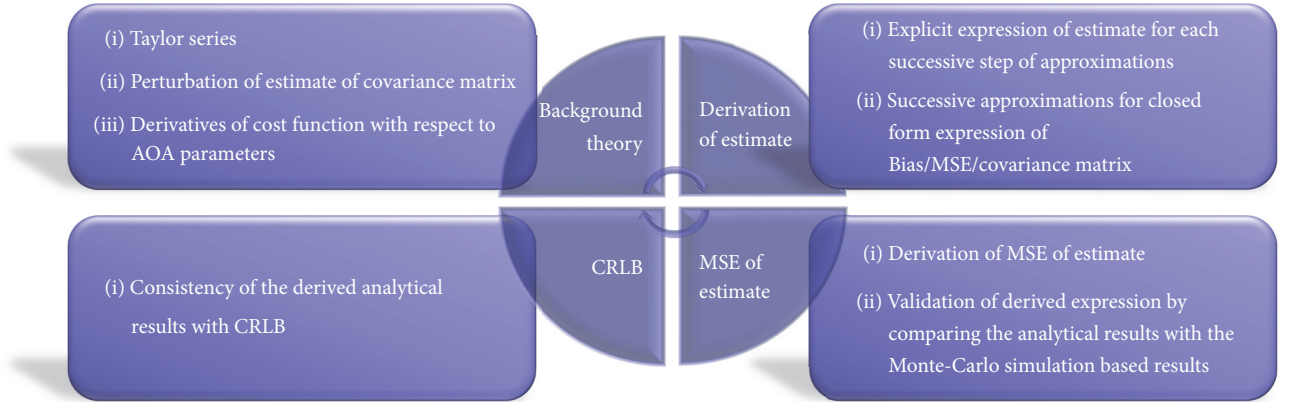


FIGURE 6: Overview of the proposed analytical performance analysis of ML algorithm.

$$\begin{aligned}
 & + (a_{k,1})^* a_{k,2} a_{k',1} \left(\frac{\partial}{\partial \theta_2} (a_{k',2})^* \right), \\
 \frac{\partial}{\partial \phi_1} D(\Theta) & = - \sum_{k=1}^M \sum_{k'=1}^M \left(\left(\frac{\partial}{\partial \phi_1} (a_{k,1})^* \right) a_{k,2} a_{k',1} (a_{k',2})^* \right. \\
 & \left. + (a_{k,1})^* a_{k,2} \left(\frac{\partial}{\partial \phi_1} a_{k',1} \right) (a_{k',2})^* \right),
 \end{aligned}$$

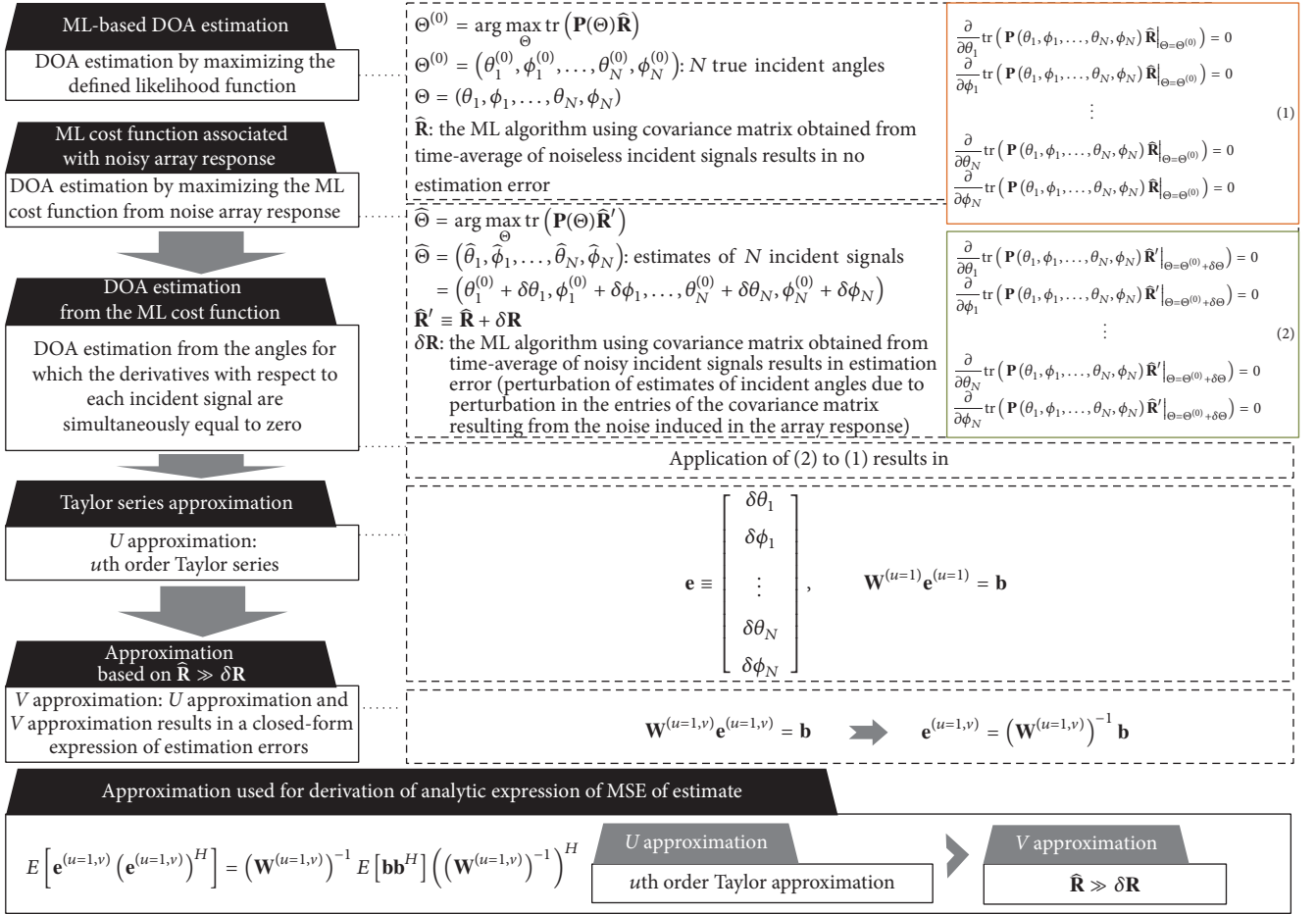


FIGURE 7: Summary of performance analysis of ML DOA estimation algorithm.

$$\begin{aligned} \frac{\partial}{\partial\phi_2} D(\Theta) &= \sum_{k=1}^M \sum_{k'=1}^M \left((a_{k,1})^* \left(\frac{\partial}{\partial\phi_2} a_{k,2} \right) a_{k',1} (a_{k',2})^* \right. \\ &\quad \left. + (a_{k,1})^* a_{k,2} a_{k',1} \left(\frac{\partial}{\partial\phi_2} (a_{k',2})^* \right) \right). \end{aligned} \quad (\text{A.1})$$

B. The First-Order Derivatives of $S_{kl}(\Theta)$ with respect to $\theta_1, \theta_2, \phi_1,$ and ϕ_2

For use in (27), Appendices E and G, the first-order partial derivatives of S_{kl} in (23) with respect to each argument are expressed as

$$\begin{aligned} \frac{\partial}{\partial\theta_1} S_{kl}(\Theta) &= \left(\frac{\partial}{\partial\theta_1} (a_{l,1})^* \right) (a_{k,1}M - a_{k,2} (Q(\Theta))^*) \\ &\quad + (a_{l,1})^* \left(\left(\frac{\partial}{\partial\theta_1} a_{k,1} \right) M - a_{k,2} \left(\frac{\partial}{\partial\theta_1} (Q(\Theta))^* \right) \right) \\ &\quad + (a_{l,2})^* \left(- \left(\frac{\partial}{\partial\theta_1} a_{k,1} \right) Q(\Theta) \right) \end{aligned}$$

$$- a_{k,1} \left(\frac{\partial}{\partial\theta_1} Q(\Theta) \right),$$

$$\begin{aligned} \frac{\partial}{\partial\theta_2} S_{kl}(\Theta) &= (a_{l,1})^* \left(- \left(\frac{\partial}{\partial\theta_2} a_{k,2} \right) (Q(\Theta))^* \right. \\ &\quad \left. - a_{k,2} \left(\frac{\partial}{\partial\theta_2} (Q(\Theta))^* \right) \right) + \left(\frac{\partial}{\partial\theta_2} (a_{l,2})^* \right) (a_{k,2}M \\ &\quad - a_{k,1}Q(\Theta)) + (a_{l,2})^* \left(\left(\frac{\partial}{\partial\theta_2} a_{k,2} \right) M \right. \\ &\quad \left. - a_{k,1} \left(\frac{\partial}{\partial\theta_2} Q(\Theta) \right) \right), \end{aligned}$$

$$\begin{aligned} \frac{\partial}{\partial\phi_1} S_{kl}(\Theta) &= \left(\frac{\partial}{\partial\phi_1} (a_{l,1})^* \right) (a_{k,1}M - a_{k,2} (Q(\Theta))^*) \\ &\quad + (a_{l,1})^* \left(\left(\frac{\partial}{\partial\phi_1} a_{k,1} \right) M - a_{k,2} \left(\frac{\partial}{\partial\phi_1} (Q(\Theta))^* \right) \right) \\ &\quad + (a_{l,2})^* \left(- \left(\frac{\partial}{\partial\phi_1} a_{k,1} \right) Q(\Theta) \right. \\ &\quad \left. - a_{k,1} \left(\frac{\partial}{\partial\phi_1} Q(\Theta) \right) \right), \end{aligned}$$

$$\begin{aligned}
\frac{\partial}{\partial \phi_2} S_{kl}(\Theta) &= (a_{l,1})^* \left(- \left(\frac{\partial}{\partial \phi_2} a_{k,2} \right) (Q(\Theta))^* \right. \\
&\quad \left. - a_{k,2} \left(\frac{\partial}{\partial \phi_2} (Q(\Theta))^* \right) \right) + \left(\frac{\partial}{\partial \phi_2} (a_{l,2})^* \right) (a_{k,2} M \\
&\quad - a_{k,1} Q(\Theta)) + (a_{l,2})^* \left(\left(\frac{\partial}{\partial \phi_2} a_{k,2} \right) M \right. \\
&\quad \left. - a_{k,1} \left(\frac{\partial}{\partial \phi_2} Q(\Theta) \right) \right). \tag{B.1}
\end{aligned}$$

C. The First-Order Derivatives of $Q(\Theta)$ with respect to $\theta_1, \theta_2, \phi_1,$ and ϕ_2

For use in Appendices B and L, the first-order partial derivatives of $Q(\Theta)$ in (17) with respect to each argument are expressed as

$$\begin{aligned}
\frac{\partial}{\partial \theta_1} Q(\Theta) &= \sum_{k=1}^M \left(\left(\frac{\partial}{\partial \theta_1} (a_{k,1})^* \right) a_{k,2} \right), \\
\frac{\partial}{\partial \theta_2} Q(\Theta) &= \sum_{k=1}^M \left((a_{k,1})^* \left(\frac{\partial}{\partial \theta_2} a_{k,2} \right) \right), \\
\frac{\partial}{\partial \phi_1} Q(\Theta) &= \sum_{k=1}^M \left(\left(\frac{\partial}{\partial \phi_1} (a_{k,1})^* \right) a_{k,2} \right), \\
\frac{\partial}{\partial \phi_2} Q(\Theta) &= \sum_{k=1}^M \left((a_{k,1})^* \left(\frac{\partial}{\partial \phi_2} a_{k,2} \right) \right). \tag{C.1}
\end{aligned}$$

D. The First-Order Derivatives of $a_m(\theta_n, \phi_n)$ with respect to θ_n and ϕ_n

For use in Appendices A, B, C, E, F, I, J, K, and L, the first-order partial derivatives of $a_m(\theta_n, \phi_n)$ in (18) with respect to each argument are expressed as

$$\begin{aligned}
\frac{\partial}{\partial \theta_n} a_m(\theta_n, \phi_n) &= -j \frac{2\pi r}{\lambda} \sin \left(\theta_n - \frac{2\pi}{M} (m-1) \right) \cos \phi_n a_m(\theta_n, \phi_n), \\
\frac{\partial}{\partial \phi_n} a_m(\theta_n, \phi_n) &= -j \frac{2\pi r}{\lambda} \cos \left(\theta_n - \frac{2\pi}{M} (m-1) \right) \sin \phi_n a_m(\theta_n, \phi_n). \tag{D.1}
\end{aligned}$$

E. The Second-Order Partial Derivatives of $S_{kl}(\Theta)$

For use in Appendix G, the second partial derivatives of $S_{kl}(\Theta)$ in (23) with respect to each argument are expressed as

$$\begin{aligned}
\frac{\partial^2}{\partial \theta_1^2} S_{kl}(\Theta) &= \left(\frac{\partial^2}{\partial \theta_1^2} (a_{l,1})^* \right) (a_{k,1} M - a_{k,2} (Q(\Theta))^*) \\
&\quad + (a_{l,1})^* \left(\left(\frac{\partial^2}{\partial \theta_1^2} a_{k,1} \right) M - a_{k,2} \left(\frac{\partial^2}{\partial \theta_1^2} (Q(\Theta))^* \right) \right) \\
&\quad + \left(\frac{\partial}{\partial \theta_1} (a_{l,1})^* \right) \left(\left(\frac{\partial}{\partial \theta_1} a_{k,1} \right) M \right. \\
&\quad \left. - a_{k,2} \left(\frac{\partial}{\partial \theta_1} (Q(\Theta))^* \right) \right) + \left(\frac{\partial}{\partial \theta_1} (a_{l,1})^* \right) \\
&\quad \cdot \left(\left(\frac{\partial}{\partial \theta_1} a_{k,1} \right) M - a_{k,2} \left(\frac{\partial}{\partial \theta_1} (Q(\Theta))^* \right) \right) \\
&\quad + (a_{l,2})^* \left(- \left(\frac{\partial^2}{\partial \theta_1^2} a_{k,1} \right) Q(\Theta) \right. \\
&\quad \left. - \left(\frac{\partial}{\partial \theta_1} a_{k,1} \right) \left(\frac{\partial}{\partial \theta_1} Q(\Theta) \right) \right) + (a_{l,2})^* \\
&\quad \cdot \left(- \left(\frac{\partial}{\partial \theta_1} a_{k,1} \right) \left(\frac{\partial}{\partial \theta_1} Q(\Theta) \right) \right. \\
&\quad \left. - a_{k,1} \left(\frac{\partial^2}{\partial \theta_1^2} Q(\Theta) \right) \right), \\
\frac{\partial}{\partial \theta_2} \frac{\partial}{\partial \theta_1} S_{kl}(\Theta) &= \left(\frac{\partial}{\partial \theta_1} (a_{l,1})^* \right) \\
&\quad \cdot \left(- \left(\frac{\partial}{\partial \theta_2} a_{k,2} \right) (Q(\Theta))^* - a_{k,2} \left(\frac{\partial}{\partial \theta_2} (Q(\Theta))^* \right) \right) \\
&\quad + (a_{l,1})^* \left(\left(\frac{\partial}{\partial \theta_2} a_{k,2} \right) \left(\frac{\partial}{\partial \theta_1} (Q(\Theta))^* \right) \right. \\
&\quad \left. - a_{k,2} \left(\frac{\partial}{\partial \theta_2} \frac{\partial}{\partial \theta_1} (Q(\Theta))^* \right) \right) + \left(\frac{\partial}{\partial \theta_2} (a_{l,2})^* \right) \\
&\quad \cdot \left(- \left(\frac{\partial}{\partial \theta_1} a_{k,1} \right) Q(\Theta) - a_{k,1} \left(\frac{\partial}{\partial \theta_1} Q(\Theta) \right) \right) \\
&\quad + (a_{l,2})^* \left(- \left(\frac{\partial}{\partial \theta_1} a_{k,1} \right) \left(\frac{\partial}{\partial \theta_2} Q(\Theta) \right) \right. \\
&\quad \left. - a_{k,1} \left(\frac{\partial}{\partial \theta_2} \frac{\partial}{\partial \theta_1} Q(\Theta) \right) \right), \\
\frac{\partial}{\partial \phi_1} \frac{\partial}{\partial \theta_1} S_{kl}(\Theta) &= \left(\frac{\partial}{\partial \phi_1} \frac{\partial}{\partial \theta_1} (a_{l,1})^* \right) (a_{k,1} M \\
&\quad - a_{k,2} (Q(\Theta))^*) + \left(\frac{\partial}{\partial \theta_1} (a_{l,1})^* \right) \left(\left(\frac{\partial}{\partial \phi_1} a_{k,1} \right) M \right. \\
&\quad \left. - a_{k,2} \left(\frac{\partial}{\partial \phi_1} (Q(\Theta))^* \right) \right) + \left(\frac{\partial}{\partial \phi_1} (a_{l,1})^* \right) \\
&\quad \cdot \left(\left(\frac{\partial}{\partial \theta_1} a_{k,1} \right) M - a_{k,2} \left(\frac{\partial}{\partial \theta_1} (Q(\Theta))^* \right) \right) \\
&\quad + (a_{l,1})^* \left(\left(\frac{\partial}{\partial \phi_1} \frac{\partial}{\partial \theta_1} a_{k,1} \right) M \right.
\end{aligned}$$

$$\begin{aligned}
& + (a_{i,2})^* \left(- \left(\frac{\partial^2}{\partial \phi_1^2} a_{k,1} \right) Q(\Theta) \right. \\
& - \left. \left(\frac{\partial}{\partial \phi_1} a_{k,1} \right) \left(\frac{\partial}{\partial \phi_1} Q(\Theta) \right) \right) + (a_{i,2})^* \\
& \cdot \left(- \left(\frac{\partial^2}{\partial \phi_1^2} a_{k,1} \right) Q(\Theta) \right. \\
& - \left. \left(\frac{\partial}{\partial \phi_1} a_{k,1} \right) \left(\frac{\partial}{\partial \phi_1} Q(\Theta) \right) \right), \\
\frac{\partial}{\partial \phi_2} \frac{\partial}{\partial \phi_1} S_{kl}(\Theta) & = \left(\frac{\partial}{\partial \phi_1} (a_{i,1})^* \right) \\
& \cdot \left(- \left(\frac{\partial}{\partial \phi_2} a_{k,2} \right) (Q(\Theta))^* \right. \\
& - \left. a_{k,2} \left(\frac{\partial}{\partial \phi_2} (Q(\Theta))^* \right) \right) + (a_{i,1})^* \\
& \cdot \left(- \left(\frac{\partial}{\partial \phi_2} a_{k,2} \right) \left(\frac{\partial}{\partial \phi_1} (Q(\Theta))^* \right) \right. \\
& - \left. a_{k,2} \left(\frac{\partial}{\partial \phi_2} \frac{\partial}{\partial \phi_1} (Q(\Theta))^* \right) \right) + \left(\frac{\partial}{\partial \phi_2} (a_{i,2})^* \right) \\
& \cdot \left(- \left(\frac{\partial}{\partial \phi_1} a_{k,1} \right) Q(\Theta) - a_{k,1} \left(\frac{\partial}{\partial \phi_1} Q(\Theta) \right) \right) \\
& + (a_{i,2})^* \left(- \left(\frac{\partial}{\partial \phi_1} a_{k,1} \right) \left(\frac{\partial}{\partial \phi_2} Q(\Theta) \right) \right. \\
& - \left. a_{k,1} \left(\frac{\partial}{\partial \phi_2} \frac{\partial}{\partial \phi_1} Q(\Theta) \right) \right), \\
\frac{\partial^2}{\partial \phi_2^2} S_{kl}(\Theta) & = (a_{i,1})^* \left(- \left(\frac{\partial^2}{\partial \phi_2^2} a_{k,2} \right) (Q(\Theta))^* \right. \\
& - \left. \left(\frac{\partial}{\partial \phi_2} a_{k,2} \right) \left(\frac{\partial}{\partial \phi_2} (Q(\Theta))^* \right) \right) + (a_{i,1})^* \\
& \cdot \left(- \left(\frac{\partial}{\partial \phi_2} a_{k,2} \right) \left(\frac{\partial}{\partial \phi_2} (Q(\Theta))^* \right) \right. \\
& - \left. a_{k,2} \left(\frac{\partial^2}{\partial \phi_2^2} (Q(\Theta))^* \right) \right) + \left(\frac{\partial^2}{\partial \phi_2^2} (a_{i,2})^* \right) (a_{k,2} M \\
& - a_{k,1} Q(\Theta)) + \left(\frac{\partial}{\partial \phi_2} (a_{i,2})^* \right) \left(\left(\frac{\partial}{\partial \phi_2} a_{k,2} \right) M \right. \\
& - \left. a_{k,1} \left(\frac{\partial}{\partial \phi_2} Q(\Theta) \right) \right) + \left(\frac{\partial}{\partial \phi_2} (a_{i,2})^* \right) \\
& \cdot \left(\left(\frac{\partial}{\partial \phi_2} a_{k,2} \right) M - a_{k,1} \left(\frac{\partial}{\partial \phi_2} Q(\Theta) \right) \right) + (a_{i,2})^* \\
& \cdot \left(\left(\frac{\partial^2}{\partial \phi_2^2} a_{k,2} \right) M - a_{k,1} \left(\frac{\partial^2}{\partial \phi_2^2} Q(\Theta) \right) \right).
\end{aligned} \tag{E.1}$$

F. The Second-Order Partial Derivatives of $D(\Theta)$

For use in Appendix G, the second-order partial derivatives of $D(\Theta)$ in (20) with respect to each argument are expressed as

$$\begin{aligned}
\frac{\partial^2}{\partial \theta_1^2} D(\Theta) & = - \sum_{k=1}^M \sum_{k'=1}^M \left(\left(\frac{\partial^2}{\partial \theta_1^2} (a_{k,1})^* \right) \right. \\
& \cdot a_{k,2} a_{k',1} (a_{k',2})^* + \left(\frac{\partial}{\partial \theta_1} (a_{k,1})^* \right) a_{k,2} \left(\frac{\partial}{\partial \theta_1} a_{k',1} \right) \\
& \cdot (a_{k',2})^* + \left(\frac{\partial}{\partial \theta_1} (a_{k,1})^* \right) a_{k,2} \left(\frac{\partial}{\partial \theta_1} a_{k',1} \right) (a_{k',2})^* \\
& \left. + (a_{k,1})^* a_{k,2} \left(\frac{\partial^2}{\partial \theta_1^2} a_{k',1} \right) (a_{k',2})^* \right), \\
\frac{\partial}{\partial \theta_2} \left(\frac{\partial}{\partial \theta_1} D(\Theta) \right) & = - \sum_{k=1}^M \sum_{k'=1}^M \left(\left(\frac{\partial}{\partial \theta_1} (a_{k,1})^* \right) \right. \\
& \cdot \left(\frac{\partial}{\partial \theta_2} a_{k,2} \right) a_{k',1} (a_{k',2})^* + \left(\frac{\partial}{\partial \theta_1} (a_{k,1})^* \right) \\
& \cdot a_{k,2} a_{k',1} \left(\frac{\partial}{\partial \theta_2} (a_{k',2})^* \right) + (a_{k,1})^* \left(\frac{\partial}{\partial \theta_2} a_{k,2} \right) \\
& \cdot \left(\frac{\partial}{\partial \theta_1} a_{k',1} \right) (a_{k',2})^* + (a_{k,1})^* a_{k,2} \left(\frac{\partial}{\partial \theta_1} a_{k',1} \right) \\
& \left. \cdot \left(\frac{\partial}{\partial \theta_2} (a_{k',2})^* \right) \right), \\
\frac{\partial}{\partial \phi_1} \left(\frac{\partial}{\partial \theta_1} D(\Theta) \right) & = - \sum_{k=1}^M \sum_{k'=1}^M \left(\left(\frac{\partial}{\partial \phi_1} \left(\frac{\partial}{\partial \theta_1} (a_{k,1})^* \right) \right) \right. \\
& \cdot a_{k,2} a_{k',1} (a_{k',2})^* + \left(\frac{\partial}{\partial \theta_1} (a_{k,1})^* \right) a_{k,2} \left(\frac{\partial}{\partial \phi_1} a_{k',1} \right) \\
& \cdot (a_{k',2})^* + \left(\frac{\partial}{\partial \phi_1} (a_{k,1})^* \right) a_{k,2} \left(\frac{\partial}{\partial \theta_1} a_{k',1} \right) (a_{k',2})^* \\
& \left. + (a_{k,1})^* a_{k,2} \left(\frac{\partial}{\partial \phi_1} \left(\frac{\partial}{\partial \theta_1} a_{k',1} \right) \right) (a_{k',2})^* \right), \\
\frac{\partial}{\partial \phi_2} \left(\frac{\partial}{\partial \theta_1} D(\Theta) \right) & = - \sum_{k=1}^M \sum_{k'=1}^M \left(\left(\frac{\partial}{\partial \theta_1} (a_{k,1})^* \right) \right. \\
& \cdot \left(\frac{\partial}{\partial \phi_2} a_{k,2} \right) a_{k',1} (a_{k',2})^* + \left(\frac{\partial}{\partial \theta_1} (a_{k,1})^* \right) \\
& \cdot a_{k,2} a_{k',1} \left(\frac{\partial}{\partial \phi_2} (a_{k',2})^* \right) + (a_{k,1})^* \left(\frac{\partial}{\partial \phi_2} a_{k,2} \right) \\
& \cdot \left(\frac{\partial}{\partial \theta_1} a_{k',1} \right) (a_{k',2})^* + (a_{k,1})^* a_{k,2} \left(\frac{\partial}{\partial \theta_1} a_{k',1} \right) \\
& \left. \cdot \left(\frac{\partial}{\partial \phi_2} (a_{k',2})^* \right) \right).
\end{aligned}$$

$$\begin{aligned}
& \cdot \left(\frac{\partial}{\partial \phi_2} (a_{k',2})^* \right), \\
\frac{\partial}{\partial \theta_1} \left(\frac{\partial}{\partial \theta_2} D(\Theta) \right) &= \frac{\partial}{\partial \theta_2} \left(\frac{\partial}{\partial \theta_1} D(\Theta) \right), \\
\frac{\partial^2}{\partial \theta_2^2} D(\Theta) &= - \sum_{k=1}^M \sum_{k'=1}^M \left((a_{k,1})^* \left(\frac{\partial^2}{\partial \theta_2^2} a_{k,2} \right) \right. \\
& \cdot a_{k',1} (a_{k',2})^* + (a_{k,1})^* \left(\frac{\partial}{\partial \theta_2} a_{k,2} \right) \\
& \cdot a_{k',1} \left(\frac{\partial}{\partial \theta_2} (a_{k',2})^* \right) + (a_{k,1})^* \left(\frac{\partial}{\partial \theta_2} a_{k,2} \right) \\
& \cdot a_{k',1} \left(\frac{\partial}{\partial \theta_2} (a_{k',2})^* \right) + (a_{k,1})^* \\
& \cdot a_{k,2} a_{k',1} \left(\frac{\partial^2}{\partial \theta_2^2} (a_{k',2})^* \right) \left. \right), \\
\frac{\partial}{\partial \phi_1} \left(\frac{\partial}{\partial \theta_2} D(\Theta) \right) &= - \sum_{k=1}^M \sum_{k'=1}^M \left(\left(\frac{\partial}{\partial \phi_1} (a_{k,1})^* \right) \right. \\
& \cdot \left(\frac{\partial}{\partial \theta_2} a_{k,2} \right) a_{k',1} (a_{k',2})^* + (a_{k,1})^* \left(\frac{\partial}{\partial \theta_2} a_{k,2} \right) \\
& \cdot \left(\frac{\partial}{\partial \phi_1} a_{k',1} \right) (a_{k',2})^* + \left(\frac{\partial}{\partial \phi_1} (a_{k,1})^* \right) \\
& \cdot a_{k,2} a_{k',1} \left(\frac{\partial}{\partial \theta_2} (a_{k',2})^* \right) + (a_{k,1})^* a_{k,2} \left(\frac{\partial}{\partial \phi_1} a_{k',1} \right) \\
& \cdot \left. \left(\frac{\partial}{\partial \theta_2} (a_{k',2})^* \right) \right), \\
\frac{\partial}{\partial \phi_2} \left(\frac{\partial}{\partial \theta_2} D(\Theta) \right) &= - \sum_{k=1}^M \sum_{k'=1}^M \left((a_{k,1})^* \right. \\
& \cdot \left(\frac{\partial}{\partial \phi_2} \left(\frac{\partial}{\partial \theta_2} a_{k,2} \right) \right) a_{k',1} (a_{k',2})^* + (a_{k,1})^* \\
& \cdot \left(\frac{\partial}{\partial \phi_1} a_{k',1} \right) (a_{k',2})^* + \left(\frac{\partial}{\partial \phi_1} (a_{k,1})^* \right) \\
& \cdot a_{k,2} a_{k',1} \left(\frac{\partial}{\partial \theta_2} (a_{k',2})^* \right) + (a_{k,1})^* a_{k,2} \left(\frac{\partial}{\partial \phi_1} a_{k',1} \right) \\
& \cdot \left. \left(\frac{\partial}{\partial \theta_2} (a_{k',2})^* \right) \right), \\
\frac{\partial}{\partial \phi_2} \left(\frac{\partial}{\partial \theta_2} D(\Theta) \right) &= - \sum_{k=1}^M \sum_{k'=1}^M \left((a_{k,1})^* \right. \\
& \cdot \left(\frac{\partial}{\partial \phi_2} \left(\frac{\partial}{\partial \theta_2} a_{k,2} \right) \right) a_{k',1} (a_{k',2})^* + (a_{k,1})^* \\
& \cdot \left(\frac{\partial}{\partial \theta_2} a_{k,2} \right) a_{k',1} \left(\frac{\partial}{\partial \phi_2} (a_{k',2})^* \right) + (a_{k,1})^* \\
& \cdot \left(\frac{\partial}{\partial \phi_2} a_{k,2} \right) a_{k',1} \left(\frac{\partial}{\partial \theta_2} (a_{k',2})^* \right) + (a_{k,1})^* \\
& \cdot a_{k,2} a_{k',1} \left(\frac{\partial}{\partial \phi_2} \left(\frac{\partial}{\partial \theta_2} (a_{k',2})^* \right) \right) \left. \right), \\
\frac{\partial}{\partial \theta_1} \left(\frac{\partial}{\partial \phi_1} D(\Theta) \right) &= \frac{\partial}{\partial \phi_1} \left(\frac{\partial}{\partial \theta_1} D(\Theta) \right), \\
\frac{\partial}{\partial \theta_2} \left(\frac{\partial}{\partial \phi_1} D(\Theta) \right) &= \frac{\partial}{\partial \phi_1} \left(\frac{\partial}{\partial \theta_2} D(\Theta) \right), \\
\frac{\partial}{\partial \phi_1} \left(\frac{\partial}{\partial \phi_2} D(\Theta) \right) &= \frac{\partial}{\partial \phi_2} \left(\frac{\partial}{\partial \phi_1} D(\Theta) \right), \\
\frac{\partial^2}{\partial \phi_2^2} D(\Theta) &= \sum_{k=1}^M \sum_{k'=1}^M \left((a_{k,1})^* \left(\frac{\partial^2}{\partial \phi_2^2} a_{k,2} \right) a_{k',1} (a_{k',2})^* \right. \\
& + (a_{k,1})^* \left(\frac{\partial}{\partial \phi_2} a_{k,2} \right) a_{k',1} \left(\frac{\partial}{\partial \phi_2} (a_{k',2})^* \right) + (a_{k,1})^* \\
& \cdot \left(\frac{\partial}{\partial \phi_2} a_{k,2} \right) a_{k',1} \left(\frac{\partial}{\partial \phi_2} (a_{k',2})^* \right) + (a_{k,1})^* \\
& \cdot a_{k,2} a_{k',1} \left(\frac{\partial^2}{\partial \phi_2^2} (a_{k',2})^* \right) \left. \right).
\end{aligned}$$

(E.1)

G. The First-Order Derivatives of $P_{kl,\theta_1}(\Theta)$, $P_{kl,\theta_2}(\Theta)$, $P_{kl,\phi_1}(\Theta)$, and $P_{kl,\phi_2}(\Theta)$

The first partial derivatives of $P_{kl,\theta_1}(\Theta)$, $P_{kl,\theta_2}(\Theta)$, $P_{kl,\phi_1}(\Theta)$, and $P_{kl,\phi_2}(\Theta)$ in (27) with respect to each argument can be expressed as

$$\frac{\partial}{\partial \theta_i} P_{kl,\theta_1}(\Theta) = \frac{(((\partial/\partial \theta_i)(\partial/\partial \theta_1) S_{kl}(\Theta)) D(\Theta) + ((\partial/\partial \theta_1) S_{kl}(\Theta)) ((\partial/\partial \theta_i) D(\Theta))) (D(\Theta))^2}{(D(\Theta))^4}$$

$$\begin{aligned}
& - \frac{(((\partial/\partial\theta_i) S_{kl}(\Theta))((\partial/\partial\theta_1) D(\Theta)) + S_{kl}(\Theta)((\partial/\partial\theta_i)(\partial/\partial\theta_1) D(\Theta)))(D(\Theta))^2}{(D(\Theta))^4} \\
& - \frac{(((\partial/\partial\theta_1) S_{kl}(\Theta)) D(\Theta) - S_{kl}(\Theta)((\partial/\partial\theta_1) D(\Theta))((\partial/\partial\theta_i) D(\Theta)))^2}{(D(\Theta))^4} \quad i = 1, 2, \\
\frac{\partial}{\partial\phi_i} P_{kl,\theta_1}(\Theta) &= \frac{(((\partial/\partial\phi_i)(\partial/\partial\theta_1) S_{kl}(\Theta)) D(\Theta) + ((\partial/\partial\theta_1) S_{kl}(\Theta))((\partial/\partial\phi_i) D(\Theta)))(D(\Theta))^2}{(D(\Theta))^4} \\
& - \frac{(((\partial/\partial\phi_i) S_{kl}(\Theta))((\partial/\partial\theta_1) D(\Theta)) + S_{kl}(\Theta)((\partial/\partial\phi_i)(\partial/\partial\theta_1) D(\Theta)))(D(\Theta))^2}{(D(\Theta))^4} \\
& - \frac{(((\partial/\partial\theta_1) S_{kl}(\Theta)) D(\Theta) - S_{kl}(\Theta)((\partial/\partial\theta_1) D(\Theta))((\partial/\partial\phi_i) D(\Theta)))^2}{(D(\Theta))^4} \quad i = 1, 2, \\
\frac{\partial}{\partial\theta_1} P_{kl,\theta_2}(\Theta) &= \frac{\partial}{\partial\theta_1} \left(\frac{\partial}{\partial\theta_2} P_{kl}(\Theta) \right) = \frac{\partial}{\partial\theta_2} \left(\frac{\partial}{\partial\theta_1} P_{kl}(\Theta) \right) = \frac{\partial}{\partial\theta_2} P_{kl,\theta_1}(\Theta), \\
\frac{\partial}{\partial\phi_i} P_{kl,\theta_2}(\Theta) &= \frac{(((\partial/\partial\phi_i)(\partial/\partial\theta_2) S_{kl}(\Theta)) D(\Theta) + ((\partial/\partial\theta_2) S_{kl}(\Theta))((\partial/\partial\phi_i) D(\Theta)))(D(\Theta))^2}{(D(\Theta))^4} \\
& - \frac{(((\partial/\partial\phi_i) S_{kl}(\Theta))((\partial/\partial\theta_2) D(\Theta)) + S_{kl}(\Theta)((\partial/\partial\phi_i)(\partial/\partial\theta_2) D(\Theta)))(D(\Theta))^2}{(D(\Theta))^4} \\
& - \frac{(((\partial/\partial\theta_2) S_{kl}(\Theta)) D(\Theta) - S_{kl}(\Theta)((\partial/\partial\theta_2) D(\Theta))((\partial/\partial\phi_i) D(\Theta)))^2}{(D(\Theta))^4} \quad i = 1, 2, \\
\frac{\partial}{\partial\theta_1} P_{kl,\phi_1}(\Theta) &= \frac{\partial}{\partial\theta_1} \left(\frac{\partial}{\partial\phi_1} P_{kl}(\Theta) \right) = \frac{\partial}{\partial\phi_1} \left(\frac{\partial}{\partial\theta_1} P_{kl}(\Theta) \right) = \frac{\partial}{\partial\phi_1} P_{kl,\theta_1}(\Theta), \\
\frac{\partial}{\partial\theta_2} P_{kl,\phi_1}(\Theta) &= \frac{\partial}{\partial\theta_2} \left(\frac{\partial}{\partial\phi_1} P_{kl}(\Theta) \right) = \frac{\partial}{\partial\phi_1} \left(\frac{\partial}{\partial\theta_2} P_{kl}(\Theta) \right) = \frac{\partial}{\partial\phi_1} P_{kl,\theta_2}(\Theta), \\
\frac{\partial}{\partial\phi_i} P_{kl,\phi_1}(\Theta) &= \frac{(((\partial/\partial\phi_i)(\partial/\partial\phi_1) S_{kl}(\Theta)) D(\Theta) + ((\partial/\partial\phi_1) S_{kl}(\Theta))((\partial/\partial\phi_i) D(\Theta)))(D(\Theta))^2}{(D(\Theta))^4} \\
& - \frac{(((\partial/\partial\phi_i) S_{kl}(\Theta))((\partial/\partial\phi_1) D(\Theta)) + S_{kl}(\Theta)((\partial/\partial\phi_i)(\partial/\partial\phi_1) D(\Theta)))(D(\Theta))^2}{(D(\Theta))^4} \\
& - \frac{(((\partial/\partial\phi_1) S_{kl}(\Theta)) D(\Theta) - S_{kl}(\Theta)((\partial/\partial\phi_1) D(\Theta))((\partial/\partial\phi_i) D(\Theta)))^2}{(D(\Theta))^4} \quad i = 1, 2, \\
\frac{\partial}{\partial\theta_1} P_{kl,\phi_2}(\Theta) &= \frac{\partial}{\partial\theta_1} \left(\frac{\partial}{\partial\phi_2} P_{kl}(\Theta) \right) = \frac{\partial}{\partial\phi_2} \left(\frac{\partial}{\partial\theta_1} P_{kl}(\Theta) \right) = \frac{\partial}{\partial\phi_2} P_{kl,\theta_1}(\Theta), \\
\frac{\partial}{\partial\theta_2} P_{kl,\phi_2}(\Theta) &= \frac{\partial}{\partial\theta_2} \left(\frac{\partial}{\partial\phi_2} P_{kl}(\Theta) \right) = \frac{\partial}{\partial\phi_2} \left(\frac{\partial}{\partial\theta_2} P_{kl}(\Theta) \right) = \frac{\partial}{\partial\phi_2} P_{kl,\theta_2}(\Theta), \\
\frac{\partial}{\partial\phi_1} P_{kl,\phi_2}(\Theta) &= \frac{\partial}{\partial\phi_1} \left(\frac{\partial}{\partial\phi_2} P_{kl}(\Theta) \right) = \frac{\partial}{\partial\phi_2} \left(\frac{\partial}{\partial\phi_1} P_{kl}(\Theta) \right) = \frac{\partial}{\partial\phi_2} P_{kl,\phi_1}(\Theta).
\end{aligned}$$

H. The First-Order Derivatives of $(D(\Theta))^2$

For use in Appendix G, the first partial derivatives of $(D(\Theta))^2$ in (28) with respect to each argument are expressed as

$$\begin{aligned} \frac{\partial}{\partial \theta_i} (D(\Theta))^2 &= -2M^2 \frac{\partial}{\partial \theta_i} |Q(\Theta)|^2 \\ &\quad + \left(\frac{\partial}{\partial \theta_i} |Q(\Theta)|^4 \right) \quad i = 1, 2, \\ \frac{\partial}{\partial \phi_i} (D(\Theta))^2 &= -2M^2 \frac{\partial}{\partial \phi_i} |Q(\Theta)|^2 \\ &\quad + \left(\frac{\partial}{\partial \phi_i} |Q(\Theta)|^4 \right) \quad i = 1, 2. \end{aligned} \quad (\text{H.1})$$

I. The First-Order Derivatives of $|Q(\Theta)|^2$

For use in Appendix H, the first-order partial derivatives of $|Q(\Theta)|^2$ in (21) with respect to each argument are expressed as

$$\begin{aligned} \frac{\partial}{\partial \theta_i} (Q(\Theta))^2 &= \sum_{k=1}^M \sum_{k'=1}^M \left(\left(\frac{\partial}{\partial \theta_i} (a_{k,1})^* \right) a_{k,2} a_{k',1} (a_{k',2})^* \right. \\ &\quad \left. + (a_{k,1})^* a_{k,2} \left(\frac{\partial}{\partial \theta_i} a_{k',1} \right) (a_{k',2})^* \right) \quad i = 1, 2, \\ \frac{\partial}{\partial \phi_i} (Q(\Theta))^2 &= \sum_{k=1}^M \sum_{k'=1}^M \left(\left(\frac{\partial}{\partial \phi_i} (a_{k,1})^* \right) a_{k,2} a_{k',1} (a_{k',2})^* \right. \\ &\quad \left. + (a_{k,1})^* a_{k,2} \left(\frac{\partial}{\partial \phi_i} a_{k',1} \right) (a_{k',2})^* \right) \quad i = 1, 2. \end{aligned} \quad (\text{I.1})$$

J. The First-Order Derivatives of $|Q(\Theta)|^4$

For use in Appendix H, the first-order partial derivatives of $|Q(\Theta)|^4$ in (29) with respect to each argument are expressed as

$$\begin{aligned} \frac{\partial}{\partial \theta_i} (Q(\Theta))^4 &= \sum_{k=1}^M \sum_{k'=1}^M \sum_{q=1}^M \sum_{q'=1}^M \left(\left(\frac{\partial}{\partial \theta_i} (a_{k,1})^* \right) a_{k,2} a_{k',1} (a_{k,2})^* (a_{q,1})^* a_{q,2} a_{q',1} (a_{q',2})^* \right. \\ &\quad \left. + (a_{k,1})^* a_{k,2} \left(\frac{\partial}{\partial \theta_i} a_{k',1} \right) (a_{k,2})^* (a_{q,1})^* a_{q,2} a_{q',1} (a_{q',2})^* \right. \\ &\quad \left. + (a_{k,1})^* a_{k,2} a_{k',1} (a_{k,2})^* \left(\frac{\partial}{\partial \theta_i} (a_{q,1})^* \right) a_{q,2} a_{q',1} (a_{q',2})^* \right. \\ &\quad \left. + (a_{k,1})^* a_{k,2} a_{k',1} (a_{k,2})^* (a_{q,1})^* a_{q,2} \left(\frac{\partial}{\partial \theta_i} (a_{q,1}) \right) (a_{q',2})^* \right) \quad i = 1, 2, \end{aligned}$$

$$\begin{aligned} \frac{\partial}{\partial \phi_i} (Q(\Theta))^4 &= \sum_{k=1}^M \sum_{k'=1}^M \sum_{q=1}^M \sum_{q'=1}^M \left(\left(\frac{\partial}{\partial \phi_i} (a_{k,1})^* \right) a_{k,2} a_{k',1} (a_{k,2})^* (a_{q,1})^* a_{q,2} a_{q',1} (a_{q',2})^* \right. \\ &\quad \left. + (a_{k,1})^* a_{k,2} \left(\frac{\partial}{\partial \phi_i} a_{k',1} \right) (a_{k,2})^* (a_{q,1})^* a_{q,2} a_{q',1} (a_{q',2})^* \right. \\ &\quad \left. + (a_{k,1})^* a_{k,2} a_{k',1} (a_{k,2})^* \left(\frac{\partial}{\partial \phi_i} (a_{q,1})^* \right) a_{q,2} a_{q',1} (a_{q',2})^* \right. \\ &\quad \left. + (a_{k,1})^* a_{k,2} a_{k',1} (a_{k,2})^* (a_{q,1})^* a_{q,2} \left(\frac{\partial}{\partial \phi_i} (a_{q,1}) \right) (a_{q',2})^* \right) \quad i = 1, 2. \end{aligned} \quad (\text{J.1})$$

K. The Second-Order Derivatives of $a_m(\theta_i, \phi_i)$

For use in Appendices E, F, and L, the second partial derivatives of $a_m(\theta_i, \phi_i)$ in (18) with respect to each argument are expressed as

$$\begin{aligned} \frac{\partial^2}{\partial \theta_i^2} a_m(\theta_i, \phi_i) &= -j \frac{2\pi r}{\lambda} \\ &\quad \cdot \cos \phi_i \left(\cos \left(\theta_i - \frac{2\pi}{M} (m-1) \right) a_m(\theta_i, \phi_i) \right. \\ &\quad \left. - \sin \left(\theta_i - \frac{2\pi}{M} (m-1) \right) \frac{\partial}{\partial \theta_i} a_m(\theta_i, \phi_i) \right), \\ \frac{\partial^2}{\partial \phi_i^2} a_m(\theta_i, \phi_i) &= -j \frac{2\pi r}{\lambda} \cos \left(\theta_i - \frac{2\pi}{M} (m-1) \right) \\ &\quad \cdot \left(\cos \phi_i a_m(\theta_i, \phi_i) - \sin \phi_i \frac{\partial}{\partial \phi_i} a_m(\theta_i, \phi_i) \right), \\ \frac{\partial}{\partial \phi_i} \frac{\partial}{\partial \theta_i} a_m(\theta_i, \phi_i) &= j \frac{2\pi r}{\lambda} \sin \left(\theta_i - \frac{2\pi}{M} (m-1) \right) \\ &\quad \cdot \left(\sin \phi_i a_m(\theta_i, \phi_i) - \cos \phi_i \frac{\partial}{\partial \phi_i} a_m(\theta_i, \phi_i) \right). \end{aligned} \quad (\text{K.1})$$

L. The Second-Order Derivatives of $Q(\Theta)$

For use in Appendix F, the second partial derivatives of $Q(\Theta)$ in (17) with respect to each argument are expressed as

$$\begin{aligned} \frac{\partial}{\partial \theta_i} \frac{\partial}{\partial \theta_1} Q(\Theta) &= \sum_{k=1}^M \left(\left(\frac{\partial}{\partial \theta_1} (a_{k,1})^* \right) \left(\frac{\partial}{\partial \theta_i} a_{k,2} \right) \right) \\ &\quad i = 1, 2, \\ \frac{\partial}{\partial \phi_i} \frac{\partial}{\partial \theta_1} Q(\Theta) &= \sum_{k=1}^M \left(\left(\frac{\partial}{\partial \phi_1} (a_{k,1})^* \right) \left(\frac{\partial}{\partial \theta_i} a_{k,2} \right) \right) \\ &\quad i = 1, 2, \end{aligned}$$

$$\begin{aligned} \frac{\partial}{\partial \theta_1} \left(\frac{\partial}{\partial \theta_2} Q(\Theta) \right) &= \frac{\partial}{\partial \theta_2} \left(\frac{\partial}{\partial \theta_1} Q(\Theta) \right), \\ \frac{\partial^2}{\partial \theta_2^2} Q(\Theta) &= \sum_{k=1}^M \left((a_{k,1})^* \left(\frac{\partial^2}{\partial \theta_2^2} a_{k,2} \right) \right), \\ \frac{\partial}{\partial \phi_i} \frac{\partial}{\partial \theta_1} Q(\Theta) &= \sum_{k=1}^M \left(\left(\frac{\partial}{\partial \phi_i} (a_{k,1})^* \right) \left(\frac{\partial}{\partial \theta_2} a_{k,2} \right) \right) \\ & \quad i = 1, 2, \\ \frac{\partial}{\partial \theta_i} \left(\frac{\partial}{\partial \phi_1} Q(\Theta) \right) &= \frac{\partial}{\partial \phi_1} \left(\frac{\partial}{\partial \theta_i} Q(\Theta) \right) \quad i = 1, 2, \\ \frac{\partial}{\partial \phi_i} \left(\frac{\partial}{\partial \phi_1} Q(\Theta) \right) &= \sum_{k=1}^M \left(\left(\frac{\partial}{\partial \phi_i} (a_{k,1})^* \right) \left(\frac{\partial}{\partial \phi_1} a_{k,2} \right) \right) \\ & \quad i = 1, 2, \\ \frac{\partial}{\partial \theta_i} \left(\frac{\partial}{\partial \phi_2} Q(\Theta) \right) &= \frac{\partial}{\partial \phi_2} \left(\frac{\partial}{\partial \theta_i} Q(\Theta) \right) \quad i = 1, 2, \end{aligned}$$

M. Second-Order Central Moment of Zero-Mean Complex Gaussian Random Variable with Variance σ^2

Depending on how a , b , d , and e are related, we define four cases.

Case 1. $a = b$ and $d = e$.

Case 2. $a \neq b$ and $d = e$.

Case 3. $a = b$ and $d \neq e$.

Case 4. $a \neq b$ and $d \neq e$.

(i) $E[n_a(t_d)n_b^*(t_e)]$:

$$\begin{aligned} E[n_a(t_d)n_b^*(t_e)] &= E[(\text{Re}[n_a(t_d)] + j\text{Im}[n_a(t_d)])(\text{Re}[n_b(t_e)] - j\text{Im}[n_b(t_e)])] \\ &= E[\text{Re}[n_a(t_d)]\text{Re}[n_b(t_e)] - j\text{Re}[n_a(t_d)]\text{Im}[n_b(t_e)] + j\text{Im}[n_a(t_d)]\text{Re}[n_b(t_e)] + \text{Im}[n_a(t_d)]\text{Im}[n_b(t_e)]]]. \end{aligned} \quad (\text{M.1})$$

For Case 1, $E[n_a(t_d)n_b^*(t_e)]$ is given by

$$\begin{aligned} E[n_a(t_d)n_b^*(t_e)] &= E[n_a(t_d)n_a^*(t_d)] \\ &= E[\text{Re}[n_a(t_d)]\text{Re}[n_a(t_d)]] \\ & \quad + E[\text{Im}[n_a(t_d)]\text{Im}[n_a(t_d)]] \\ & \quad - jE[\text{Re}[n_a(t_d)]\text{Im}[n_a(t_d)]] \\ & \quad + jE[\text{Im}[n_a(t_d)]\text{Re}[n_a(t_d)]] \\ &= \frac{\sigma^2}{2} + \frac{\sigma^2}{2} - 0 + 0 = \sigma^2. \end{aligned} \quad (\text{M.2})$$

Similarly, it can be shown that $E[n_a(t_d)n_b^*(t_e)]$ is identically zero for Cases 2–4:

$$E[n_a(t_d)n_b^*(t_e)] = 0 \quad \text{for Cases 2–4.} \quad (\text{M.3})$$

Note that, in deriving (M.1)–(M.3), we used the fact that the real part and the imaginary part of noise are independent and identically distributed with $N(0, \sigma^2/2)$.

(ii) $E[n_a^*(t_d)n_b^*(t_e)]$:

Using the same algebraic manipulation used in evaluating $E[n_a(t_d)n_b^*(t_e)]$, it can be shown that $E[n_a^*(t_d)n_b^*(t_e)]$ is equal to zero for Cases 1–4:

$$E[n_a^*(t_d)n_b^*(t_e)] = 0 \quad \text{for Cases 1–4.} \quad (\text{M.4})$$

(iii) $E[n_a(t_d)n_b(t_e)]$:

Using the same algebraic manipulation used in evaluating $E[n_a(t_d)n_b^*(t_e)]$, it can be shown that $E[n_a(t_d)n_b(t_e)]$ is equal to zero for Cases 1–4:

$$E[n_a(t_d)n_b(t_e)] = 0 \quad \text{for Cases 1–4.} \quad (\text{M.5})$$

N. Third-Order Central Moment of Zero-Mean Complex Gaussian Random Variable with Variance σ^2

We define ten cases depending on how a , b , c , d , and e are related.

Case 1. $a = b$ and $b = c$ and $e = d$.

Case 2. $a = b$ and $b \neq c$ and $e = d$.

Case 3. $a \neq b$ and $b = c$ and $e = d$.

Case 4. $a = c$ and $c \neq b$ and $e = d$.

Case 5. $a \neq b$ and $b \neq c$ and $e = d$.

Case 6. $a = b$ and $b = c$ and $e \neq d$.

Case 7. $a = b$ and $b \neq c$ and $e \neq d$.

Case 8. $a \neq b$ and $b = c$ and $e \neq d$.

Case 9. $a = c$ and $c \neq b$ and $e \neq d$.

Case 10. $a \neq b$ and $b \neq c$ and $e \neq d$.

(i) $E[n_a(t_d)n_b^*(t_e)n_c(t_e)]$:

$$\begin{aligned}
& E[n_a(t_d)n_b^*(t_e)n_c(t_e)] \\
&= E[(\text{Re}[n_a(t_d)] + j \text{Im}[n_a(t_d)]) \\
&\cdot (\text{Re}[n_b(t_e)] - j \text{Im}[n_b(t_e)]) \\
&\cdot (\text{Re}[n_c(t_e)] + j \text{Im}[n_c(t_e)])] = E[\text{Re}[n_a(t_d)] \\
&\cdot \text{Re}[n_b(t_e)] \text{Re}[n_c(t_e)] + jE[\text{Re}[n_a(t_d)] \\
&\cdot \text{Re}[n_b(t_e)] \text{Im}[n_c(t_e)] - jE[\text{Re}[n_a(t_d)] \\
&\cdot \text{Im}[n_b(t_e)] \text{Re}[n_c(t_e)] + jE[\text{Im}[n_a(t_d)] \\
&\cdot \text{Re}[n_b(t_e)] \text{Re}[n_c(t_e)] + E[\text{Re}[n_a(t_d)] \\
&\cdot \text{Im}[n_b(t_e)] \text{Im}[n_c(t_e)]] - E[\text{Im}[n_a(t_d)] \\
&\cdot \text{Re}[n_b(t_e)] \text{Im}[n_c(t_e)] + E[\text{Im}[n_a(t_d)] \\
&\cdot \text{Im}[n_b(t_e)] \text{Re}[n_c(t_e)] + jE[\text{Im}[n_a(t_d)] \\
&\cdot \text{Im}[n_b(t_e)] \text{Im}[n_c(t_e)]]]. \tag{N.1}
\end{aligned}$$

$E[n_a(t_d)n_b^*(t_e)n_c(t_e)]$ for Case 1 is identically zero:

$$\begin{aligned}
& E[n_a(t_d)n_b^*(t_e)n_c(t_e)] \\
&= E[n_a(t_d)n_a^*(t_d)n_a(t_d)] \\
&= E[\text{Re}[n_a(t_d)] \text{Re}[n_a(t_d)] \text{Re}[n_a(t_d)] \\
&\quad + jE[\text{Re}[n_a(t_d)] \text{Re}[n_a(t_d)] E[\text{Im}[n_a(t_d)]] \\
&\quad - jE[\text{Re}[n_a(t_d)] \text{Re}[n_a(t_d)] E[\text{Im}[n_a(t_d)]] \\
&\quad + jE[\text{Im}[n_a(t_d)] E[\text{Re}[n_a(t_d)] \text{Re}[n_a(t_d)]] \\
&\quad + E[\text{Re}[n_a(t_d)] E[\text{Im}[n_a(t_d)] \text{Im}[n_a(t_d)]] \\
&\quad - E[\text{Im}[n_a(t_d)] \text{Im}[n_a(t_d)] E[\text{Re}[n_a(t_d)]] \\
&\quad + E[\text{Im}[n_a(t_d)] \text{Im}[n_a(t_d)] E[\text{Re}[n_a(t_d)]] \\
&\quad + jE[\text{Im}[n_a(t_d)] \text{Im}[n_a(t_d)] \text{Im}[n_a(t_d)]] \\
&= 0 + j\left(\frac{\sigma^2}{2}\right) \times 0 - j\left(\frac{\sigma^2}{2}\right) \times 0 + j\left(\frac{\sigma^2}{2}\right) \times 0 \\
&\quad + \left(\frac{\sigma^2}{2}\right) \times 0 - \left(\frac{\sigma^2}{2}\right) \times 0 + \left(\frac{\sigma^2}{2}\right) \times 0 + j \times 0 \\
&= 0. \tag{N.2}
\end{aligned}$$

Note that, in deriving (N.1)-(N.2), we used the fact that the real part and the imaginary part of noise

are independent and identically distributed with $N(0, \sigma^2/2)$.

Using the same manipulation used in obtaining (N.2), it can be shown that $E[n_a(t_d)n_b^*(t_e)n_c(t_e)]$ is identically zero for Cases 2–10:

$$E[n_a(t_d)n_b^*(t_e)n_c(t_e)] = 0 \quad \text{for Cases 2–10.} \tag{N.3}$$

From (N.2) and (N.3), $E[n_a(t_d)n_b^*(t_e)n_c(t_e)]$ is zero for all ten cases defined in Case 1–Case 10:

$$E[n_a(t_d)n_b^*(t_e)n_c(t_e)] = 0 \quad \text{for Cases 1–10.} \tag{N.4}$$

(ii) $E[n_a^*(t_d)n_b^*(t_e)n_c(t_e)]$:

$$\begin{aligned}
& E[n_a^*(t_d)n_b^*(t_e)n_c(t_e)] \\
&= E[(\text{Re}[n_a(t_d)] - j \text{Im}[n_a(t_d)]) \\
&\cdot (\text{Re}[n_b(t_e)] - j \text{Im}[n_b(t_e)]) \\
&\cdot (\text{Re}[n_c(t_e)] + j \text{Im}[n_c(t_e)])] = E[\text{Re}[n_a(t_d)] \\
&\cdot \text{Re}[n_b(t_e)] \text{Re}[n_c(t_e)] + jE[\text{Re}[n_a(t_d)] \\
&\cdot \text{Re}[n_b(t_e)] \text{Im}[n_c(t_e)] - jE[\text{Re}[n_a(t_d)] \\
&\cdot \text{Im}[n_b(t_e)] \text{Re}[n_c(t_e)] - jE[\text{Im}[n_a(t_d)] \\
&\cdot \text{Re}[n_b(t_e)] \text{Re}[n_c(t_e)] + E[\text{Re}[n_a(t_d)] \\
&\cdot \text{Im}[n_b(t_e)] \text{Im}[n_c(t_e)]] + E[\text{Im}[n_a(t_d)] \\
&\cdot \text{Re}[n_b(t_e)] \text{Im}[n_c(t_e)] - E[\text{Im}[n_a(t_d)] \\
&\cdot \text{Im}[n_b(t_e)] \text{Re}[n_c(t_e)] - jE[\text{Im}[n_a(t_d)] \\
&\cdot \text{Im}[n_b(t_e)] \text{Im}[n_c(t_e)]]]. \tag{N.5}
\end{aligned}$$

In a similar way to get (N.4), we get

$$E[n_a^*(t_d)n_b^*(t_e)n_c(t_e)] = 0 \quad \text{for Cases 1–10.} \tag{N.6}$$

O. Fourth-Order Central Moment of Zero-Mean Complex Gaussian Random Variable with Variance σ^2

$$\begin{aligned}
& E[n_l(t_i)n_k^*(t_i)n_{l'}(t_{i'})n_{k'}(t_{i'})] \\
&= E[(\text{Re}[n_l(t_i)] + j \text{Im}[n_l(t_i)]) \\
&\cdot (\text{Re}[n_k(t_i)] - j \text{Im}[n_k(t_i)]) \\
&\cdot (\text{Re}[n_{l'}(t_{i'})] - j \text{Im}[n_{l'}(t_{i'})]) \\
&\cdot (\text{Re}[n_{k'}(t_{i'})] + j \text{Im}[n_{k'}(t_{i'})])]. \tag{O.1}
\end{aligned}$$

(a) $i = i'$:For $i = i'$, (O.1) can be written as

$$\begin{aligned}
E [n_l(t_i) n_k^*(t_i) n_{l'}^*(t_i) n_{k'}(t_i)] &= E [\text{Re} [n_l(t_i)] \\
&\cdot \text{Re} [n_k(t_i)] \text{Re} [n_{l'}(t_i)] \text{Re} [n_{k'}(t_i)]] \\
&+ E [\text{Re} [n_l(t_i)] \text{Re} [n_k(t_i)] E [\text{Im} [n_{l'}(t_i)] \\
&\cdot \text{Im} [n_{k'}(t_i)]] - E [\text{Re} [n_l(t_i)] \text{Re} [n_{k'}(t_i)]] \\
&\cdot E [\text{Im} [n_k(t_i)] \text{Im} [n_{l'}(t_i)]] + E [\text{Im} [n_l(t_i)] \\
&\cdot \text{Im} [n_k(t_i)]] E [\text{Re} [n_{l'}(t_i)] \text{Re} [n_{k'}(t_i)]]
\end{aligned}$$

$$\begin{aligned}
&+ E [\text{Re} [n_k(t_i)] \text{Re} [n_{k'}(t_i)]] E [\text{Im} [n_l(t_i)] \\
&\cdot \text{Im} [n_{l'}(t_i)]] - E [\text{Re} [n_k(t_i)] \text{Re} [n_{l'}(t_i)]] \\
&\cdot E [\text{Im} [n_l(t_i)] \text{Im} [n_{k'}(t_i)]] + E [\text{Re} [n_l(t_i)] \\
&\cdot \text{Re} [n_{l'}(t_i)]] E [\text{Im} [n_k(t_i)] \text{Im} [n_{k'}(t_i)]] \\
&+ E [\text{Im} [n_l(t_i)] \text{Im} [n_k(t_i)] \text{Im} [n_{l'}(t_i)] \\
&\cdot \text{Im} [n_{k'}(t_i)]] .
\end{aligned}$$

(O.2)

The first term of (O.2) is given by

$$E [\text{Re} [n_l(t_i)] \text{Re} [n_k(t_i)] \text{Re} [n_{l'}(t_i)] \text{Re} [n_{k'}(t_i)]]$$

$$\begin{aligned}
&E [\text{Re} [n_l(t_i)] \text{Re} [n_k(t_i)] \text{Re} [n_{l'}(t_i)] \text{Re} [n_{k'}(t_i)]] = 3 \left(\frac{\sigma^2}{2} \right)^2 = \frac{3}{4} \sigma^4 & l = k, k = l', l' = k' \\
&E [\text{Re} [n_l(t_i)] \text{Re} [n_k(t_i)] \text{Re} [n_{l'}(t_i)] E [\text{Re} [n_{k'}(t_i)]]] = 0 & l = k, k = l', l' \neq k' \\
&E [\text{Re} [n_l(t_i)] \text{Re} [n_k(t_i)] \text{Re} [n_{k'}(t_i)] E [\text{Re} [n_{l'}(t_i)]]] = 0 & l = k, k = k', k' \neq l' \\
&E [\text{Re} [n_l(t_i)] \text{Re} [n_{l'}(t_i)] \text{Re} [n_{k'}(t_i)] E [\text{Re} [n_k(t_i)]]] = 0 & l = l', l' = k', k' \neq k \\
&E [\text{Re} [n_k(t_i)] \text{Re} [n_{l'}(t_i)] \text{Re} [n_{k'}(t_i)] E [\text{Re} [n_l(t_i)]]] = 0 & k = l', l' = k', k' \neq l \\
&E [\text{Re} [n_l(t_i)] \text{Re} [n_k(t_i)] E [\text{Re} [n_{l'}(t_i)] \text{Re} [n_{k'}(t_i)]]] = \left(\frac{\sigma^2}{2} \right)^2 = \frac{1}{4} \sigma^4 & l = k, k \neq l', l' = k' \\
&E [\text{Re} [n_l(t_i)] \text{Re} [n_{l'}(t_i)] E [\text{Re} [n_k(t_i)] \text{Re} [n_{k'}(t_i)]]] = \left(\frac{\sigma^2}{2} \right)^2 = \frac{1}{4} \sigma^4 & l = l', l' \neq k, k = k' \\
&E [\text{Re} [n_l(t_i)] \text{Re} [n_{k'}(t_i)] E [\text{Re} [n_k(t_i)] \text{Re} [n_{l'}(t_i)]]] = \left(\frac{\sigma^2}{2} \right)^2 = \frac{1}{4} \sigma^4 & l = k', k' \neq k, k = l' \\
&E [\text{Re} [n_l(t_i)] \text{Re} [n_k(t_i)] E [\text{Re} [n_{l'}(t_i)]] E [\text{Re} [n_{k'}(t_i)]]] = \left(\frac{\sigma^2}{2} \right) \times 0 = 0 & l = k, k \neq l', l' \neq k', k' \neq l \\
&E [\text{Re} [n_l(t_i)] \text{Re} [n_{l'}(t_i)] E [\text{Re} [n_k(t_i)]] E [\text{Re} [n_{k'}(t_i)]]] = \left(\frac{\sigma^2}{2} \right) \times 0 = 0 & l = l', l' \neq k, k \neq k', k' \neq l \\
&E [\text{Re} [n_l(t_i)] \text{Re} [n_{k'}(t_i)] E [\text{Re} [n_k(t_i)]] E [\text{Re} [n_{l'}(t_i)]]] = \left(\frac{\sigma^2}{2} \right) \times 0 = 0 & l = k', k' \neq k, k \neq l', l' \neq l \\
&E [\text{Re} [n_k(t_i)] \text{Re} [n_{l'}(t_i)] E [\text{Re} [n_{k'}(t_i)]] E [\text{Re} [n_l(t_i)]]] = \left(\frac{\sigma^2}{2} \right) \times 0 = 0 & k = l', l' \neq l, l \neq k', k' \neq k \\
&E [\text{Re} [n_k(t_i)] \text{Re} [n_{l'}(t_i)] E [\text{Re} [n_{k'}(t_i)]] E [\text{Re} [n_l(t_i)]]] = \left(\frac{\sigma^2}{2} \right) \times 0 = 0 & k = k', k' \neq l, l \neq l', l' \neq k \\
&E [\text{Re} [n_{l'}(t_i)] \text{Re} [n_{k'}(t_i)] E [\text{Re} [n_l(t_i)]] E [\text{Re} [n_k(t_i)]]] = \left(\frac{\sigma^2}{2} \right) \times 0 = 0 & l' = k', k' \neq l, l \neq k, l' \neq k \\
&E [\text{Re} [n_l(t_i)] E [\text{Re} [n_k(t_i)]] E [\text{Re} [n_{l'}(t_i)]] E [\text{Re} [n_{k'}(t_i)]]] = 0 & \text{otherwise,}
\end{aligned} \tag{O.3}$$

where the results in Appendices M and N are used.

Using the same scheme in getting (O.3), the other terms of (O.2) are given by

From (O.3)–(O.10), $E[n_l(t_i)n_k^*(t_i)n_{l'}^*(t_i)n_{k'}(t_i)]$ in (O.2) is given by

$$E[n_l(t_i)n_k^*(t_i)n_{l'}^*(t_i)n_{k'}(t_i)] = \begin{cases} \frac{3}{4}\sigma^4 + \frac{1}{4}\sigma^4 - \frac{1}{4}\sigma^4 + \frac{1}{4}\sigma^4 + \frac{1}{4}\sigma^4 - \frac{1}{4}\sigma^4 + \frac{1}{4}\sigma^4 + \frac{3}{4}\sigma^4 = 2\sigma^4 & l = k, k = l', l' = k' \\ \frac{1}{4}\sigma^4 + \frac{1}{4}\sigma^4 + \frac{1}{4}\sigma^4 + \frac{1}{4}\sigma^4 = \sigma^4 & l = k, k \neq l', l' = k' \\ \frac{1}{4}\sigma^4 + \frac{1}{4}\sigma^4 + \frac{1}{4}\sigma^4 + \frac{1}{4}\sigma^4 = \sigma^4 & l = l', l' \neq k, k = k' \\ 0 & \text{otherwise.} \end{cases} \quad (\text{O.11})$$

(b) $i \neq i'$:

$$\begin{aligned} E[n_l(t_i)n_k^*(t_i)n_{l'}^*(t_{i'})n_{k'}(t_{i'})] &= E[\text{Re}[n_l(t_i)] \\ &\cdot \text{Re}[n_k(t_i)] \text{Re}[n_{l'}(t_{i'})] \text{Re}[n_{k'}(t_{i'})]] \\ &+ E[\text{Re}[n_l(t_i)] \text{Re}[n_k(t_i)] \text{Im}[n_{l'}(t_{i'})] \\ &\cdot \text{Im}[n_{k'}(t_{i'})]] + E[\text{Im}[n_l(t_i)] \text{Im}[n_k(t_i)] \\ &\cdot \text{Re}[n_{l'}(t_{i'})] \text{Re}[n_{k'}(t_{i'})]] + E[\text{Im}[n_l(t_i)] \\ &\cdot \text{Im}[n_k(t_i)] \text{Im}[n_{l'}(t_{i'})] \text{Im}[n_{k'}(t_{i'})]]. \end{aligned} \quad (\text{O.12})$$

Using a similar way to get (O.11), for $i \neq i'$, $E[n_l(t_i)n_k^*(t_i)n_{l'}^*(t_{i'})n_{k'}(t_{i'})]$ is given by

$$E[n_l(t_i)n_k^*(t_i)n_{l'}^*(t_{i'})n_{k'}(t_{i'})] = \begin{cases} \frac{1}{4}\sigma^4 + \frac{1}{4}\sigma^4 + \frac{1}{4}\sigma^4 + \frac{1}{4}\sigma^4 = \sigma^4 & l = k, k = l', l' = k' \\ \frac{1}{4}\sigma^4 + \frac{1}{4}\sigma^4 + \frac{1}{4}\sigma^4 + \frac{1}{4}\sigma^4 = \sigma^4 & l = k, k \neq l', l' = k' \\ 0 & \text{otherwise.} \end{cases} \quad (\text{O.13})$$

P. Derivation of $E[\delta R_{lk}\delta R_{l'k'}^*]$

$$\hat{R}'_{lk} = \frac{1}{L} \sum_{i=1}^L (x_i(t_i)x_k^*(t_i) + x_i(t_i)n_k^*(t_i)) \quad (\text{P.1})$$

$$+ n_l(t_i)x_k^*(t_i) + n_l(t_i)n_k^*(t_i)),$$

$$\hat{R}_{lk} = \frac{1}{L} \sum_{i=1}^L (x_i(t_i)x_k^*(t_i)), \quad (\text{P.2})$$

$$\delta R_{lk} = \frac{1}{L} \sum_{i=1}^L (x_i(t_i)n_k^*(t_i) + n_l(t_i)x_k^*(t_i)) \quad (\text{P.3})$$

$$+ n_l(t_i)n_k^*(t_i).$$

From (P.3), $E[\delta R_{lk}\delta R_{l'k'}^*]$ is given by

$$\begin{aligned} E[\delta R_{lk}\delta R_{l'k'}^*] &= \frac{1}{L^2} \left(\sum_{i=1}^L \sum_{i'=1}^L (x_l(t_i)x_{l'}^*(t_{i'})E(n_k^*(t_i)n_{k'}(t_{i'})) \right. \\ &+ x_l(t_i)x_{k'}(t_{i'})E(n_k^*(t_i)n_{l'}^*(t_{i'})) \\ &+ x_l(t_i)E(n_k^*(t_i)n_{l'}^*(t_{i'})n_{k'}(t_{i'})) \\ &+ x_k^*(t_i)x_{l'}^*(t_{i'})E(n_l(t_i)n_{k'}(t_{i'})) \\ &+ x_k^*(t_i)x_{k'}(t_{i'})E(n_l(t_i)n_{l'}^*(t_{i'})) \\ &+ x_k^*(t_i)E(n_l(t_i)n_{l'}^*(t_{i'})n_{k'}(t_{i'})) \\ &+ x_{l'}^*(t_{i'})E(n_l(t_i)n_k^*(t_i)n_{k'}(t_{i'})) \\ &+ x_{k'}(t_{i'})E(n_l(t_i)n_k^*(t_i)n_{l'}^*(t_{i'})) \\ &\left. + E(n_l(t_i)n_k^*(t_i)n_{l'}^*(t_{i'})n_{k'}(t_{i'})) \right), \end{aligned} \quad (\text{P.4})$$

where the last equality follows since the noiseless signals are not stochastic.

In Appendices M and N, it is shown that the followings are identically zero:

$$E(n_k(t_i)n_{l'}(t_{i'})) = 0,$$

$$E(n_k(t_i)n_l^*(t_i)n_{l'}(t_{i'})) = 0,$$

$$E(n_k(t_i)n_{k'}^*(t_{i'})n_{l'}(t_{i'})) = 0,$$

(P.5)

$$E(n_l^*(t_i)n_{k'}^*(t_{i'})) = 0,$$

$$E(n_k(t_i)n_l^*(t_i)n_{k'}^*(t_{i'})) = 0,$$

$$E(n_l^*(t_i)n_k^*(t_i)n_{l'}(t_{i'})n_{k'}(t_{i'})) = 0.$$

Using (P.5) in (P.4), (P.4) is simplified to $E[\delta R_{lk} \delta R_{l'k'}^*]$,

$$\frac{1}{L^2} \left(\sum_{i=1}^L \sum_{i'=1}^L (x_l(t_i) x_{l'}^*(t_{i'}) E(n_k^*(t_i) n_{k'}(t_{i'})) + x_k^*(t_i) x_{k'}(t_{i'}) E(n_l(t_i) n_{l'}^*(t_{i'})) + E(n_l(t_i) n_k^*(t_i) n_{l'}^*(t_{i'}) n_{k'}(t_{i'}))) \right), \quad (\text{P.6})$$

where the second moments and the fourth moment in (P.6) are derived in Appendices M and O, respectively. Finally,

$E[(\delta R)_{lk} (\delta R)_{l'k'}^*]$ is given by

$$E[(\delta R)_{lk} (\delta R)_{l'k'}^*] = \begin{cases} \frac{1}{L^2} \left(\sigma^2 \sum_{i=1}^L (x_l(t_i) x_{l'}^*(t_i) + x_k^*(t_i) x_{k'}(t_i)) + (L^2 + L) \sigma^4 \right) & (l = k, k = l', l' = k') \\ \frac{1}{L^2} \left(\sigma^2 \sum_{i=1}^L (x_k^*(t_i) x_{k'}(t_i)) \right) & (l = k, k = l', l' \neq k') \\ \frac{1}{L^2} \left(\sigma^2 \sum_{i=1}^L (x_l(t_i) x_{l'}^*(t_i)) \right) & (l = l', l' = k', k' \neq k) \\ \frac{1}{L^2} \left(\sigma^2 \sum_{i=1}^L (x_k^*(t_i) x_{k'}(t_i)) \right) & (l = k', k' = l', l' \neq k) \\ \frac{1}{L^2} \left(\sigma^2 \sum_{i=1}^L (x_l(t_i) x_{l'}^*(t_i)) \right) & (l = k, k = k', k' \neq l') \\ \frac{1}{L^2} (L^2 \sigma^4) & (l = k, k \neq l', l' = k') \\ \frac{1}{L^2} \left(\sigma^2 \sum_{i=1}^L (x_l(t_i) x_{l'}^*(t_i) + x_k^*(t_i) x_{k'}(t_i)) + L \sigma^4 \right) & (l = l', l' \neq k, k = k') \\ \frac{1}{L^2} \left(\sigma^2 \sum_{i=1}^L (x_k^*(t_i) x_{k'}(t_i)) \right) & (l = l', l' \neq k, k \neq k') \\ \frac{1}{L^2} \left(\sigma^2 \sum_{i=1}^L (x_l(t_i) x_{l'}^*(t_i)) \right) & (k = k', k' \neq l, l \neq l'). \end{cases} \quad (\text{P.7})$$

Competing Interests

The authors declare that they have no competing interests.

References

- [1] Z.-M. Liu, Z.-T. Huang, Y.-Y. Zhou, and J. Liu, "Direction-of-arrival estimation of noncircular signals via sparse representation," *IEEE Transactions on Aerospace and Electronic Systems*, vol. 48, no. 3, pp. 2690–2698, 2012.
- [2] B. Liao and S.-C. Chan, "Direction-of-arrival estimation in subarrays-based linear sparse arrays with gain/phase uncertainties," *IEEE Transactions on Aerospace and Electronic Systems*, vol. 49, no. 4, pp. 2268–2280, 2013.
- [3] T. N. Ferreira, S. L. Netto, and P. S. R. Diniz, "Direction-of-arrival estimation using a low-complexity covariance-based approach," *IEEE Transactions on Aerospace and Electronic Systems*, vol. 48, no. 3, pp. 1924–1934, 2012.
- [4] Y. Song, "Decoupled 2D direction-of-arrival estimation using partly calibrated vector hydrophones," *IEEE Transactions on Aerospace and Electronic Systems*, vol. 49, no. 4, pp. 2470–2477, 2013.
- [5] Y. Song and K. T. Wong, "A lower bound of direction-of-arrival estimation for an acoustic vector sensor subject to sensor breakdown," *IEEE Transactions on Aerospace and Electronic Systems*, vol. 48, no. 4, pp. 3703–3708, 2012.
- [6] P. Stoica and A. Nehorai, "MUSIC, maximum likelihood, and Cramer-Rao bound," *IEEE Transactions on Acoustics, Speech, and Signal Processing*, vol. 37, no. 5, pp. 720–741, 1989.

- [7] P. Stoica and A. Nehorai, "MUSIC, maximum likelihood, and Cramer-Rao bound: further results and comparisons," *IEEE Transactions on Acoustics, Speech, and Signal Processing*, vol. 38, no. 12, pp. 2140–2150, 1990.
- [8] P. Stoica and A. Nehorai, "Performance study of conditional and unconditional direction-of-arrival estimation," *IEEE Transactions on Acoustics, Speech, and Signal Processing*, vol. 38, no. 10, pp. 1783–1795, 1990.
- [9] B. G. Quinn and P. J. Kootsookos, "Threshold behavior of the maximum likelihood estimator of frequency," *IEEE Transactions on Signal Processing*, vol. 42, no. 11, pp. 3291–3294, 1994.
- [10] F. Athley, "Threshold region performance of maximum likelihood direction of arrival estimators," *IEEE Transactions on Signal Processing*, vol. 53, no. 4, pp. 1359–1373, 2005.
- [11] P. Forster, P. Larzabal, and E. Boyer, "Threshold performance analysis of maximum likelihood DOA estimation," *IEEE Transactions on Signal Processing*, vol. 52, no. 11, pp. 3183–3191, 2004.
- [12] F. Athley, "Performance analysis of DOA estimation in the threshold region," in *Proceedings of the 2002 IEEE International Conference on Acoustic, Speech, and Signal Processing (ICASSP '02)*, vol. 3, pp. 3017–3020, Orlando, Fla, USA, May 2002.
- [13] B. Ottersten, M. Viberg, P. Stoica, and A. Nehorai, "Exact and large sample maximum likelihood techniques for parameter estimation and detection in array processing," in *Radar Array Processing*, vol. 25 of *Springer Series in Information Sciences*, pp. 99–151, Springer, Berlin, Germany, 1993.
- [14] H. C. So, Y. T. Chan, K. C. Ho, and Y. Chen, "Simple formulae for bias and mean square error computation [DSP Tips and Tricks]," *IEEE Signal Processing Magazine*, vol. 30, no. 4, pp. 162–165, 2013.
- [15] H. Anton and C. Rorres, *Elementary Linear Algebra*, John Wiley & Sons, New York, NY, USA, 10th edition, 2011.
- [16] Z. Chen, G. Gokeda, and Y. Yu, *Introduction to Direction-of-Arrival Estimation*, Artech House, 2010.

Research Article

Azimuth/Elevation Directional Finding with Automatic Pair Matching

Nizar Tayem

Department of Electrical Engineering, Prince Mohamed Bin Fahd University, Al Khobar, Saudi Arabia

Correspondence should be addressed to Nizar Tayem; ntayem@pmu.edu.sa

Received 11 April 2016; Revised 21 September 2016; Accepted 15 November 2016

Academic Editor: Aboulnasr Hassanien

Copyright © 2016 Nizar Tayem. This is an open access article distributed under the Creative Commons Attribution License, which permits unrestricted use, distribution, and reproduction in any medium, provided the original work is properly cited.

We addressed the problem of two-dimensional (2D) direction-of-arrival (DOA) elevation and azimuth angles estimation for multiple uncorrelated signals using L-shaped antenna array configuration. The key points of the proposed method are the following: (1) it obtains azimuth and elevation angles through construction of three cross-correlation matrices from the collected data of the received signals; this implies that the noise reduces significantly in the reconstructed data matrices; (2) it derives a parallel factor analysis (PARAFAC) model and applies trilinear least squares method to avoid pair matching problem between 2D DOA azimuth and elevation angles for multiple sources; (3) it does not require spectral peak searching; and (4) it has better 2D DOA estimation compared with signal parameters via rotational invariance technique and fourth-order signal parameters via rotational invariance technique. Simulation results demonstrate the estimation accuracy and the effectiveness of the proposed method.

1. Introduction

The problem of estimating the two-dimensional direction-of-arrival (2D DOA) azimuth and elevation (ϕ, θ) angles of multiple incident sources plays an important role in many practical applications in the fields of wireless communication and signal processing such as radar, sonar, and multiple-input-multiple-output (MIMO) systems. Several 2D DOA estimation methods have been proposed in the literature considering different geometries of the antenna arrays such as circular array [1], parallel uniform linear array [2], uniform rectangular array [3], and L-shaped array [4, 5]. In particular, the L-shaped array which is composed of two orthogonal uniform linear arrays with one placed on the x -axis and the other on the z -axis has received considerable attention due to its geometric configuration, ease of implementation, use of less number of antennas, and higher estimation accuracy compared with other geometrical arrays.

Conventional methods of DOA estimation rely on the decomposition of the observation space into a signal subspace and a noise subspace. Two widely used subspace techniques, MUSIC [6] and ESPRIT [7], are computationally complex as they require either eigenvalue decomposition (EVD) of the sample covariance matrix or the singular value

decomposition (SVD) of the received data matrix. Improved techniques which are simpler and less complex have been reported in the literature [6–11] which do not rely on either EVD or SVD. However, some of these methods [6, 7] suffer from heavy losses of the array aperture and encounter an estimation failure problem. To avoid aperture loss problem many cumulant-based methods [12–17] have been proposed. But these methods are computationally intensive and require parameter pairing.

The 2D DOA methods using L-shaped array [3, 4] fail to resolve the pair matching problem for multiple incident sources which result in incorrect 2D estimation of azimuth and elevation (ϕ, θ) angles and hence severe performance degradation. Many schemes have been proposed to solve the problem of pair matching [11, 18–21]. These pair matching techniques have high computational cost and complexity and they do not always provide accurate pairing results.

A parallel factor analysis (PARAFAC) [22] model is a method that transfers low rank matrix decomposition to three-way arrays (TWAs); it was first introduced in psychometrics and flow injection analysis. It has been widely used in subspace domain in array signal processing and wireless communication areas [23, 24]. Several methods have applied PARAFAC model to alleviate the problem of

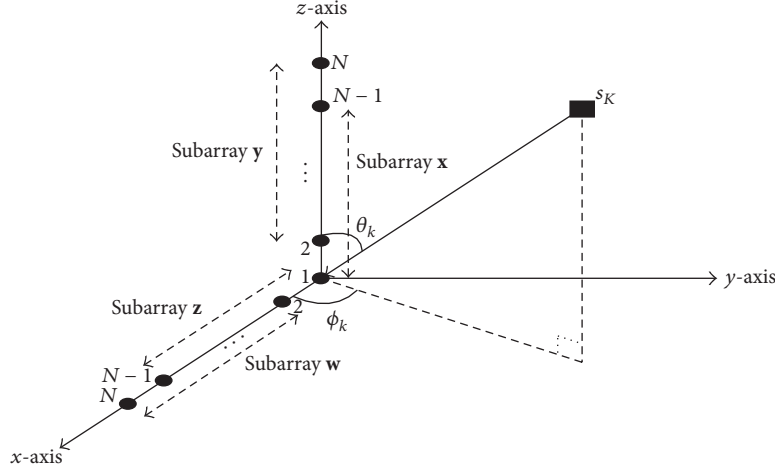


FIGURE 1: Configuration of array geometry for 2D DOA azimuth and elevation angles.

parameter pairing (or pair matching) for 2D DOA estimation for azimuth and elevation angles [25–29]. A trilinear decomposition-based blind 2D DOA estimation algorithm employing PARAFAC data model for parallel shaped array has been proposed in [17] to achieve automatic pair matching. One drawback of this method is that it requires high number of snapshots and has high computational complexity.

In this paper, we propose a novel 2D DOA estimation method that employs an L-shaped uniform antenna array based on a new computationally efficient cross-correlation with automatic pair matching based on PARAFAC data model. The constructed data consists of three cross-correlation matrices which contain information about azimuth and elevation angles of multiple uncorrelated signals that are spatially independent; this implies that the noise significantly reduces in the constructed data matrices. Further, we derive a PARAFAC model and apply trilinear least squares method to avoid pair matching problem. Compared with existing methods, the proposed method works with less than a hundred snapshots and has very accurate estimation and has lower computational complexity.

The rest of the paper is structured as follows. The signal model and proposed method are presented and developed in Section 2. Analysis of computational complexity is presented in Section 3. Simulation results are presented in Section 4. Conclusions are drawn in Section 5.

2. Signal Model and Proposed Method

The geometry of the proposed L-shaped array is shown in Figure 1. The distance between adjacent antenna elements is d where $d = \lambda/2$ with λ being the wavelength of the incident waveform. The arrays are divided into four subarrays: \mathbf{x} , \mathbf{y} , \mathbf{z} , and \mathbf{w} . Each linear subarray consists of $(N - 1)$ antenna elements. The element located at point $(0, 0, 0)$ is considered as a reference element. Hence, the total number of antenna elements in both z -axis and x -axis is $(2N - 1)$. Consider K narrowband noncoherent sources in far-field of the antenna array.

$(N - 1) \times 1$ collected signal vectors received at \mathbf{x} , \mathbf{y} , \mathbf{z} , and \mathbf{w} subarrays are defined as follows:

$$\begin{aligned} \mathbf{x}(t) &= [x_1(t) \ x_2(t) \ \cdots \ x_{N-1}(t)]^T, \\ \mathbf{y}(t) &= [y_2(t) \ y_3(t) \ \cdots \ y_N(t)]^T, \\ \mathbf{z}(t) &= [z_1(t) \ z_2(t) \ \cdots \ z_{N-1}(t)]^T, \\ \mathbf{w}(t) &= [w_2(t) \ w_3(t) \ \cdots \ w_N(t)]^T, \end{aligned} \quad (1)$$

where t represents the snapshot index and superscript T represents the transpose operation. The received $(N - 1) \times 1$ signal vectors in (1) can be represented as follows:

$$\mathbf{x}(t) = \mathbf{A}_z(\theta) \mathbf{s}(t) + \mathbf{n}_x(t), \quad (2)$$

$$\mathbf{y}(t) = \mathbf{A}_z(\theta) \Phi_z(\theta) \mathbf{s}(t) + \mathbf{n}_y(t), \quad (3)$$

$$\mathbf{z}(t) = \mathbf{A}_x(\theta, \phi) \mathbf{s}(t) + \mathbf{n}_z(t), \quad (4)$$

$$\mathbf{w}(t) = \mathbf{A}_x(\theta, \phi) \Phi_x(\theta, \phi) \mathbf{s}(t) + \mathbf{n}_w(t), \quad (5)$$

$$\mathbf{A}_z(\theta) = [\mathbf{a}_z(\theta_1) \ \mathbf{a}_z(\theta_2) \ \cdots \ \mathbf{a}_z(\theta_K)], \quad (6)$$

$$\mathbf{A}_x(\theta, \phi) = [\mathbf{a}_x(\theta_1, \phi_1) \ \mathbf{a}_x(\theta_2, \phi_2) \ \cdots \ \mathbf{a}_x(\theta_K, \phi_K)], \quad (7)$$

$$\mathbf{s}(t) = [s_1(t) \ s_2(t) \ \cdots \ s_K(t)]^T, \quad (8)$$

where the array manifold vector for k th source $\mathbf{a}_z(\theta_k) = [1 \ e^{-j\alpha_k} \ \cdots \ e^{-j(N-1)\alpha_k}]$, $\alpha_k = 2\pi d \cos \theta_k / \lambda$, and $\mathbf{a}_x(\theta_k, \phi_k) = [1 \ e^{-j\beta_k} \ \cdots \ e^{-j(N-1)\beta_k}]^T$, $\beta_k = 2\pi d \sin \theta_k \cos \phi_k / \lambda$. $\mathbf{s}(t)$ is the complex envelope vector of k incident sources and at snapshot t , $\mathbf{n}_x(t)$, $\mathbf{n}_y(t)$, $\mathbf{n}_z(t)$, and $\mathbf{n}_w(t)$ are the Gaussian white noise vectors of zero mean and variance σ^2 . $\mathbf{A}_z(\theta)$ and $\mathbf{A}_x(\theta, \phi)$ are array manifold matrices.

The matrices $\Phi_z(\theta)$ in (3) and $\Phi_x(\theta, \phi)$ in (5) are $K \times K$ diagonal matrices containing information about the azimuth

angle ϕ_k and elevation angle θ_k which can be presented as follows:

$$\begin{aligned}\Phi_z(\theta) &= \text{diag} [e^{-i\alpha_1} \ e^{-i\alpha_2} \ \dots \ e^{-i\alpha_K}], \\ \Phi_x(\theta, \phi) &= \text{diag} [e^{-i\beta_1} \ e^{-i\beta_2} \ \dots \ e^{-i\beta_K}].\end{aligned}\quad (9)$$

In the proposed method, we first construct three cross-correlation matrices (\mathbf{z} subarray, \mathbf{x} subarray), (\mathbf{w} subarray, \mathbf{x} subarray), and (\mathbf{z} subarray, \mathbf{y} subarray) as follows:

$$\begin{aligned}\mathbf{R}_{zx} &= E [\mathbf{z}(t) \mathbf{x}(t)^H] \\ &= \mathbf{A}_x(\theta, \phi) E [\mathbf{s}(t) \mathbf{s}^H(t)] \mathbf{A}_z^H(\theta) \\ &\quad + E [\mathbf{n}_z(t) \mathbf{n}_x^H(t)] \\ &= \mathbf{A}_x(\theta, \phi) \mathbf{R}_s \mathbf{A}_z^H(\theta) + \mathbf{N}_{zx}, \\ \text{where } \mathbf{N}_{zx} &= \begin{bmatrix} \sigma^2 & 0 & \dots & 0 \\ 0 & 0 & \dots & 0 \\ \vdots & \vdots & \ddots & \vdots \\ 0 & 0 & \dots & 0 \end{bmatrix} \in \mathbb{C}^{(N-1) \times (N-1)}, \\ \mathbf{R}_{wx} &= E [\mathbf{w}(t) \mathbf{x}(t)^H] \\ &= \mathbf{A}_x(\theta, \phi) \Phi_x(\theta, \phi) E [\mathbf{s}(t) \mathbf{s}^H(t)] \mathbf{A}_z^H(\theta) \\ &\quad + E [\mathbf{n}_w(t) \mathbf{n}_x^H(t)] \\ &= \mathbf{A}_x(\theta, \phi) \Phi_x(\theta, \phi) \mathbf{R}_s \mathbf{A}_z^H(\theta) + \mathbf{N}_{wx}, \\ \mathbf{R}_{zy} &= E [\mathbf{z}(t) \mathbf{y}(t)^H] \\ &= \mathbf{A}_x(\theta, \phi) E [\mathbf{s}(t) \mathbf{s}^H(t)] \Phi_z^H(\theta) \mathbf{A}_z^H(\theta) \\ &\quad + E [\mathbf{n}_z(t) \mathbf{n}_y^H(t)] \\ &= \mathbf{A}_x(\theta, \phi) \mathbf{R}_s \Phi_z^H(\theta) \mathbf{A}_z^H(\theta) \\ &= \mathbf{A}_x(\theta, \phi) \Phi_z^H(\theta) \mathbf{R}_s \mathbf{A}_z^H(\theta) + \mathbf{N}_{zy},\end{aligned}\quad (10)$$

where the superscript H represents the conjugate and transpose operations. Note that $\{\mathbf{n}_w(t), \mathbf{n}_x(t)\}$ and $\{\mathbf{n}_z(t), \mathbf{n}_x(t)\}$ are spatially independent of each other. Therefore, $\mathbf{N}_{wx} = E[\mathbf{n}_w(t) \mathbf{n}_x^H(t)] = \mathbf{0}$ and $\mathbf{N}_{zy} = E[\mathbf{n}_z(t) \mathbf{n}_y^H(t)] = \mathbf{0}$, where $\mathbf{0}$ matrix has a dimension of $(N-1) \times (N-1)$ with all entries zero. Additive noises are not correlated with incident signals. For uncorrelated sources $\mathbf{s}(t) = [s_1(t) \ s_2(t) \ \dots \ s_K(t)]^T$, $\{\mathbf{z}(t), \mathbf{x}(t)\}$, $\{\mathbf{w}(t), \mathbf{x}(t)\}$ and $\{\mathbf{z}(t), \mathbf{y}(t)\}$ are wide-sense stationary sequences. As a consequence, the correlation matrix of the signal sources $\mathbf{R}_s = E[\mathbf{s}(t) \mathbf{s}^H(t)]$ is a diagonal matrix where its entries represent the power of signal sources. The matrices $\{\mathbf{R}_s \Phi_z^H(\theta)\} = \{\Phi_z^H(\theta) \mathbf{R}_s\}$ since both matrices \mathbf{R}_s and $\Phi_z^H(\theta)$ are diagonal.

The cross-correlation matrices in (10) are concatenated to form a new data matrix \mathbf{R} as follows:

$$\begin{aligned}\mathbf{R} &= \begin{bmatrix} \mathbf{R}_{zx} \\ \mathbf{R}_{zy} \\ \mathbf{R}_{wx} \end{bmatrix} \\ &= \begin{bmatrix} \mathbf{A}_x(\theta, \phi) \mathbf{R}_s \mathbf{A}_z^H(\theta) \\ \mathbf{A}_x(\theta, \phi) \Phi_z(\theta) \mathbf{R}_s \mathbf{A}_z^H(\theta) \\ \mathbf{A}_x(\theta, \phi) \Phi_x^H(\theta, \phi) \mathbf{R}_s \mathbf{A}_z^H(\theta) \end{bmatrix} + \begin{bmatrix} \mathbf{N}_{zx} \\ \mathbf{N}_{zy} \\ \mathbf{N}_{wx} \end{bmatrix}.\end{aligned}\quad (11)$$

Parallel factor (PARAFAC) model is applied on the data in (11) along with trilinear least squares method to jointly estimate the correct pair of azimuth ϕ_k and elevation θ_k angles for each signal source.

Using the definition of PARAFAC model, the outer product ($\mathbf{a} \circ \mathbf{b} \circ \mathbf{c}$) of the three vectors $\mathbf{a} \in \mathbb{C}^{I \times 1}$, $\mathbf{b} \in \mathbb{C}^{J \times 1}$ and $\mathbf{c} \in \mathbb{C}^{K \times 1}$ can be expressed in a third-order tensor form as $\mathbf{Q} \in \mathbb{C}^{I \times J \times K}$ with typical elements defined as $q_{ijk} = a_i b_j c_k$. \mathbf{Q} can be expressed as a sum of tensor product:

$$\mathbf{Q} = \sum_{u=1}^U (\mathbf{a}_u \circ \mathbf{b}_u \circ \mathbf{c}_u), \quad (12)$$

where \mathbf{a}_u , \mathbf{b}_u , and \mathbf{c}_u are u th columns of the following load matrices \mathbf{A} , \mathbf{B} , and \mathbf{C} . These matrices for a given PARAFAC model can be defined as follows:

$$\begin{aligned}\mathbf{A} &= [\mathbf{a}_1 \ \mathbf{a}_2 \ \dots \ \mathbf{a}_U], \quad \mathbf{A} \in \mathbb{C}^{I \times U}, \\ \mathbf{B} &= [\mathbf{b}_1 \ \mathbf{b}_2 \ \dots \ \mathbf{b}_U], \quad \mathbf{B} \in \mathbb{C}^{J \times U}, \\ \mathbf{C} &= [\mathbf{c}_1 \ \mathbf{c}_2 \ \dots \ \mathbf{c}_U], \quad \mathbf{C} \in \mathbb{C}^{K \times U}.\end{aligned}\quad (13)$$

The PARAFAC decomposition in (12) can also be represented in another matrix form of 3D tensor matrix $\mathbf{Q} \in \mathbb{C}^{I \times J \times K}$ and can be represented using three slice matrices $\mathbf{Q}^{(1)}$, $\mathbf{Q}^{(2)}$, $\mathbf{Q}^{(3)}$ as follows:

$$\begin{aligned}\mathbf{Q}^{(1)} &= (\mathbf{A} \circ \mathbf{B}) \mathbf{C}^T, \\ \mathbf{Q}^{(2)} &= (\mathbf{B} \circ \mathbf{C}) \mathbf{A}^T, \\ \mathbf{Q}^{(3)} &= (\mathbf{C} \circ \mathbf{A}) \mathbf{B}^T,\end{aligned}\quad (14)$$

where $(\mathbf{A} \circ \mathbf{B}) = [\mathbf{a}_1 \otimes \mathbf{b}_1 \ \mathbf{a}_2 \otimes \mathbf{b}_2 \ \dots \ \mathbf{a}_U \otimes \mathbf{b}_U]$ is the Khatri-Rao product based on column wise Kronecker products and \otimes is Kronecker product.

The PARAFAC decomposition in (14) is considered to be essentially unique to arbitrary permutation and scaling under the condition ([31, 32]):

$$\kappa_A + \kappa_B + \kappa_C \geq 2K + 1, \quad (15)$$

where κ_A , κ_B , κ_C denote the maximum number of arbitrary linearly independent columns of matrices \mathbf{A} , \mathbf{B} , and \mathbf{C} , respectively. The arbitrary permutation and scaling implies

that there exists a triplet matrix $(\tilde{\mathbf{A}}, \tilde{\mathbf{B}}, \tilde{\mathbf{C}})$ related to $(\mathbf{A}, \mathbf{B}, \mathbf{C})$ as follows:

$$\begin{aligned}\mathbf{A} &= \tilde{\mathbf{A}}\mathbf{\Pi}\Delta_1, \\ \mathbf{B} &= \tilde{\mathbf{B}}\mathbf{\Pi}\Delta_2, \\ \mathbf{C} &= \tilde{\mathbf{C}}\mathbf{\Pi}\Delta_3,\end{aligned}\quad (16)$$

where $\mathbf{\Pi}$ is a permutation matrix and $\{\Delta_1, \Delta_2, \Delta_3\}$ are arbitrary diagonal matrices satisfying $\Delta_1\Delta_2\Delta_3 = \mathbf{I}$.

On the basis of PARAFAC theorem, three-way array (TWA) $(N-1) \times (N-1) \times 3$ can be constructed using (11) as follows:

$$\begin{aligned}\begin{bmatrix} \mathbf{R}(:, :, 1) \\ \mathbf{R}(:, :, 2) \\ \mathbf{R}(:, :, 3) \end{bmatrix} &= \begin{bmatrix} \mathbf{R}_{zx} \\ \mathbf{R}_{zy} \\ \mathbf{R}_{wx} \end{bmatrix} \\ &= \begin{bmatrix} \mathbf{A}_x(\theta, \phi) \mathbf{R}_s \mathbf{A}_z^H(\theta) \\ \mathbf{A}_x(\theta, \phi) \mathbf{\Phi}_z(\theta) \mathbf{R}_s \mathbf{A}_z^H(\theta) \\ \mathbf{A}_x(\theta, \phi) \mathbf{\Phi}_x^H(\theta, \phi) \mathbf{R}_s \mathbf{A}_z^H(\theta) \end{bmatrix} \\ &\quad + \begin{bmatrix} \mathbf{N}_{zx} \\ \mathbf{N}_{zy} \\ \mathbf{N}_{wx} \end{bmatrix}.\end{aligned}\quad (17)$$

Let $\mathbf{C} = \mathbf{A}_z^H(\theta)$; according to the definition of Khatri-Rao product the matrix in (17) can be transformed as follows:

$$\mathbf{R}^{(1)} = (\mathbf{A}_x \odot \mathbf{C}^T) \mathbf{D}^T, \quad (18)$$

$$\mathbf{R}^{(2)} = (\mathbf{C}^T \odot \mathbf{D}) \mathbf{A}_x^T, \quad (19)$$

$$\mathbf{R}^{(3)} = (\mathbf{D} \odot \mathbf{A}_x) \mathbf{C}, \quad (20)$$

$$\mathbf{D} = \begin{bmatrix} \mathbf{d}_1 \\ \mathbf{d}_2 \\ \mathbf{d}_3 \end{bmatrix} = \begin{bmatrix} \Lambda^{-1}(\mathbf{R}_s) \\ \Lambda^{-1}(\mathbf{\Phi}_z(\theta) \mathbf{R}_s) \\ \Lambda^{-1}(\mathbf{\Phi}_x(\theta, \Phi) \mathbf{R}_s) \end{bmatrix}, \quad (21)$$

where $\Lambda^{-1}(\mathbf{R}_s)$ represents the row vector data built from the diagonal elements of the diagonal matrix \mathbf{R}_s . The uniqueness of (18), (19), and (20) will be guaranteed if the following inequality holds:

$$\text{rank}(\mathbf{D}) + \text{rank}(\mathbf{A}) + \text{rank}(\mathbf{C}) \geq 2K + 2. \quad (22)$$

For different DOAs and independent sources \mathbf{C} and \mathbf{A}_x have Vandermonde structure with minimum rank equal to the number of sources, and \mathbf{D} also is a nonsingular matrix whose rank equals the number of incident sources. This implies that the minimum rank of $\text{rank}(\mathbf{D}) + \text{rank}(\mathbf{A}) + \text{rank}(\mathbf{C}) = 3K$; for multiple incident sources $K \geq 2$ and therefore, (22) will be always guaranteed.

One of the methods of solving PARAFAC model in (18), (19), and (20) is trilinear alternative least squares (TALS) approach [24, 31–33]. TALS method can be applied to solve

the matrices \mathbf{D} , \mathbf{C} , and \mathbf{A}_x and then estimate the azimuth and elevation angles. There are three basic steps behind TALS method: (a) update one of the matrices \mathbf{D} , \mathbf{C} , and \mathbf{A}_x each time using least squares (LS) method, (b) continue updating the remaining matrices based on the LS results from the previous estimation step, and (c) repeat previous steps (a) and (b) until convergence of the LS cost function. The detailed procedure of estimating \mathbf{D} , \mathbf{C} , and \mathbf{A}_x using TALS is as follows.

Define the cost functions for finding the matrices \mathbf{D} , \mathbf{C} , and \mathbf{A}_x as

$$F_1(\mathbf{D}, \mathbf{C}, \mathbf{A}_x; \mathbf{R}^{(1)}) = \|\mathbf{R}^{(1)} - (\mathbf{A}_x \odot \mathbf{C}^T) \mathbf{D}^T\|_F, \quad (23)$$

$$F_2(\mathbf{D}, \mathbf{C}, \mathbf{A}_x; \mathbf{R}^{(2)}) = \|\mathbf{R}^{(2)} - (\mathbf{C}^T \odot \mathbf{D}) \mathbf{A}_x^T\|_F, \quad (24)$$

$$F_3(\mathbf{D}, \mathbf{C}, \mathbf{A}_x; \mathbf{R}^{(3)}) = \|\mathbf{R}^{(3)} - (\mathbf{D} \odot \mathbf{A}_x) \mathbf{C}\|_F, \quad (25)$$

where $\|\cdot\|_F$ stands for Frobenius norm. Given the estimation of matrices $\tilde{\mathbf{C}}$ and $\tilde{\mathbf{A}}_x$, the matrix \mathbf{D} can be found from (23) as follows:

$$\mathbf{D}^T = \arg \min_{(\mathbf{D})} \|\mathbf{R}^{(1)} - (\tilde{\mathbf{A}}_x \odot \tilde{\mathbf{C}}^T) \mathbf{D}^T\|_F^2, \quad (26)$$

$$\hat{\mathbf{D}} = [(\hat{\mathbf{A}}_x \odot \hat{\mathbf{C}})^\dagger \mathbf{R}^{(1)}]^T, \quad (27)$$

where $(\mathbf{J})^\dagger$ represents the pseudoinverse of matrix \mathbf{J} . \mathbf{A}_x can be also obtained by minimizing the cost function in (24) and keeping $\hat{\mathbf{C}}$ and $\hat{\mathbf{D}}$ fixed.

$$\hat{\mathbf{A}}_x = [(\mathbf{C}^T \odot \mathbf{D})^\dagger \mathbf{R}^{(2)}]^T. \quad (28)$$

Similarly, an estimation of matrix $\hat{\mathbf{C}}$ can be obtained as

$$\hat{\mathbf{C}} = (\hat{\mathbf{D}} \odot \hat{\mathbf{A}}_x)^\dagger \mathbf{R}^{(3)}. \quad (29)$$

The process in (27), (28), and (29) will continue until matrices $\hat{\mathbf{D}}$, $\hat{\mathbf{C}}$, and $\hat{\mathbf{A}}_x$ converge. PARAFAC along with TALS method can be initialized to speed up the convergence by exploiting an ESPRIT method idea on the concatenated data formed in (11).

The estimated matrix $\hat{\mathbf{D}}$ in (27) will be sufficient for 2D DOA estimation of azimuth and elevation angles. The TALS method guarantees the convergence but it is slow. For fast implementation of alternative least squares method to solve PARAFAC model in (23), (24), and (25), the COMFAC algorithm is employed which speeds up the least square fitting by utilizing a compressed version of the three-way data into smaller matrix dimensions. COMFAC MATLAB function will be used to estimate the matrices $\hat{\mathbf{D}}$, $\hat{\mathbf{C}}$, and $\hat{\mathbf{A}}_x$ (as described in [24]) as follows:

$$[\mathbf{D} \ \mathbf{A}_x \ \mathbf{C} \ i] = \text{comfac}(\mathbf{R}, K), \quad (30)$$

where \mathbf{R} is the input data, K is the number of sources, i represents the number of iterations, and $[\mathbf{D} \ \mathbf{A}_x \ \mathbf{C}]$ are the output identification matrices.

Now the diagonal matrices $\Phi_z(\theta)$ in (3) and $\Phi_x(\theta, \phi)$ are estimated from the identification matrix $\widehat{\mathbf{D}} = [\widehat{\mathbf{d}}_1 \ \widehat{\mathbf{d}}_2 \ \widehat{\mathbf{d}}_3]^T$ as follows:

$$\widehat{\varphi}_z(k) = \frac{\widehat{\mathbf{d}}_2(k)}{\widehat{\mathbf{d}}_1(k)}, \quad (31)$$

where $\widehat{\varphi}_z(k)$ is the estimated k th entry of the diagonal matrix $\widehat{\Phi}_z(\theta)$. Similarly, k th diagonal entry of $\widehat{\Phi}_x(\theta, \phi)$ can be obtained as follows:

$$\widehat{\varphi}_x(k) = \frac{\widehat{\mathbf{d}}_3(k)}{\widehat{\mathbf{d}}_1(k)}. \quad (32)$$

The azimuth angle $\widehat{\theta}_k$ and elevation angle $\widehat{\theta}_k$ for k th source can be estimated as follows:

$$\begin{aligned} \widehat{\theta}_k &= \cos^{-1} \left[\frac{\angle \widehat{\varphi}_z(k) \times \lambda}{2\pi d} \right], \\ \widehat{\phi}_k &= \cos^{-1} \left[\frac{\angle \widehat{\varphi}_x(k) \times \lambda}{2\pi d \sin(\widehat{\theta}_k)} \right]. \end{aligned} \quad (33)$$

The estimated azimuth and elevation angles in (33) are for k th source. In case of multiple sources, the following pairs are obtained: $(\widehat{\theta}_1, \widehat{\phi}_1), (\widehat{\theta}_2, \widehat{\phi}_2), \dots, (\widehat{\theta}_K, \widehat{\phi}_K)$. The estimated matrices $\widehat{\mathbf{D}}$, $\widehat{\mathbf{C}}$, and $\widehat{\mathbf{A}}_x$ have the same column permutation matrix. This implies automatic pair matching since k th column of the steering matrix \mathbf{A}_x corresponds to k th column of matrix $\widehat{\mathbf{D}}$.

The procedure of the 2D DOA proposed method is summarized as follows.

Step 1. Construct $\mathbf{x}, \mathbf{y}, \mathbf{z}$, and \mathbf{w} subarrays according to (2), (3), (4), and (5) from multiple snapshots of the array data $\{x(t) \ y(t) \ z(t) \ w(t)\}$, for $t = 1, \dots, L$.

Step 2. Estimate the cross-correlation matrices $\widehat{\mathbf{R}}_{zx}$, $\widehat{\mathbf{R}}_{wx}$, and $\widehat{\mathbf{R}}_{zy}$ from multiple snapshots in (10) as follows:

$$\begin{aligned} \widehat{\mathbf{R}}_{zx} &= \frac{1}{L} \sum_{t=1}^L \mathbf{z}(t) \mathbf{x}^H(t), \\ \widehat{\mathbf{R}}_{wx} &= \frac{1}{L} \sum_{t=1}^L \mathbf{w}(t) \mathbf{x}^H(t), \\ \widehat{\mathbf{R}}_{zy} &= \frac{1}{L} \sum_{t=1}^L \mathbf{z}(t) \mathbf{y}^H(t). \end{aligned} \quad (34)$$

Step 3. Concatenate the estimated cross-correlation matrices $\{\widehat{\mathbf{R}}_{zx}, \widehat{\mathbf{R}}_{wx}, \widehat{\mathbf{R}}_{zy}\}$ according to (34).

Step 4. Construct the three-way array (TWA) $(N-1) \times (N-1) \times 3$ according to (17).

Step 5. Apply alternative least squares method to estimate $\widehat{\mathbf{D}}$, $\widehat{\mathbf{C}}$, and $\widehat{\mathbf{A}}_x$ which minimize the cost function in (23), (24), and (25).

Step 6. Repeat Step 5 until convergence.

Step 7. Obtain the estimated diagonal matrices $\widehat{\varphi}_z(k)$ and $\widehat{\varphi}_x(k)$ from the identification matrix $\widehat{\mathbf{D}}$.

Step 8. Estimate the 2D DOA azimuth and elevation angles according to (33).

3. Analysis of the Computational Complexity of the Proposed Method

The computational complexity of the proposed method is compared with that of 2D DOA fourth-order cumulant method [17] and novel 2D DOA with L-shaped array [30]. For L total snapshots, N number of antenna elements, n number of iterations, and K number of sources, considering major processing operations like forming the sample covariance or cross-correlation matrices and applying the alternative least squares method, the total computational complexity of the proposed method is in the order of $O(3(N-1)L + n(3K^3) + 9(N-1)^2K)$. The complexity of the novel L-shaped array method is in the order of $O(4(N-1)L + n(3K^3) + 12(N-1)^2K)$ and the complexity of the fourth-order cumulant method is in the order of $O(21(2N+1)^2L + n(3K^3) + 12(2N+1)^2K)$. Upon comparison, it can be seen that the proposed method requires slightly less computational complexity compared to the method in [17] and significantly less computational complexity compared with the method in [30].

4. Simulation Results

The performance of the proposed method is presented in the section and compared with the novel L-shaped method in [30] and cumulant-based method in [17]. The performance is measured in terms of root mean square error (RMSE) for the azimuth and elevation angles estimation. We consider 21 antenna elements in total for the first three experiments. The distance between the adjacent elements is taken to be half the wave length of the incoming signal, and the number of uncorrelated sources is taken as $(K = 1, K = 2$ and $K = 4)$. Several simulation experiments have been conducted to evaluate the performance of the proposed method. The RMSE for the joint 2D DOA estimation azimuth and elevation angles is defined as follows:

$$\text{RMSE} = \sqrt{E[(\widehat{\theta}_i - \theta_i) + (\widehat{\phi}_i - \phi_i)]}, \quad (35)$$

where i represents the source index, $E[Q']$ represents the expectation value of a random variable Q' , and $(\widehat{\theta}_i, \widehat{\phi}_i)$ are the pair of the estimated elevation and azimuth angles.

In the first experiment, we consider two uncorrelated sources with direction-of-arrival azimuth and elevation angles $(\theta, \phi) = (75^\circ, 60^\circ)$ and $(80^\circ, 70^\circ)$, SNR range is set from -5 to 30 dB, and the number of snapshots is 200. Monte-Carlo trials of 500 are used. The RMSE values for source 1 and source 2 are shown in Figures 2 and 3 versus SNR for both novel L-shaped and cumulant methods and compared with the proposed method. We observe that the proposed

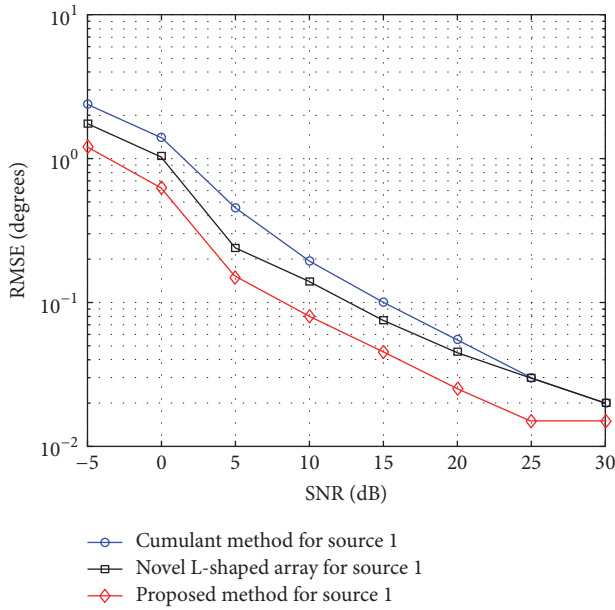


FIGURE 2: Comparison of RMSE of joint azimuth-elevation versus SNR for source 1 located at $(75^\circ, 60^\circ)$ using proposed method, novel L-shaped, and cumulant method.

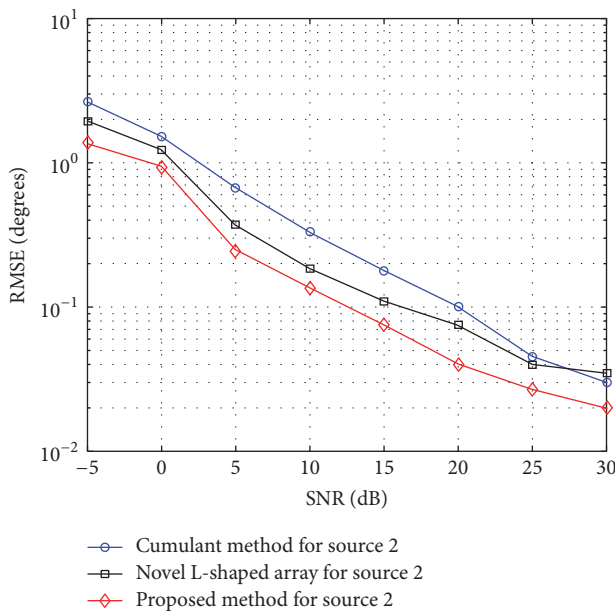


FIGURE 3: Comparison of RMSE of joint azimuth-elevation versus SNR for source 2 located at $(80^\circ, 70^\circ)$ using proposed method, novel L-shaped, and cumulant method.

method has better performance which is indicated through lower RMSE especially at low SNR. For a given RMSE value of 0.15 degrees for source 1 and 0.25 degrees for source 2, it is clear that the proposed method is 5 dB better compared with novel L-shaped for source 1 and around 2.5 dB for source 2. It is also 7.5 and 8 dB better when compared with cumulant method for source 1 and source 2, respectively. We observe also that proposed method has better performance compared

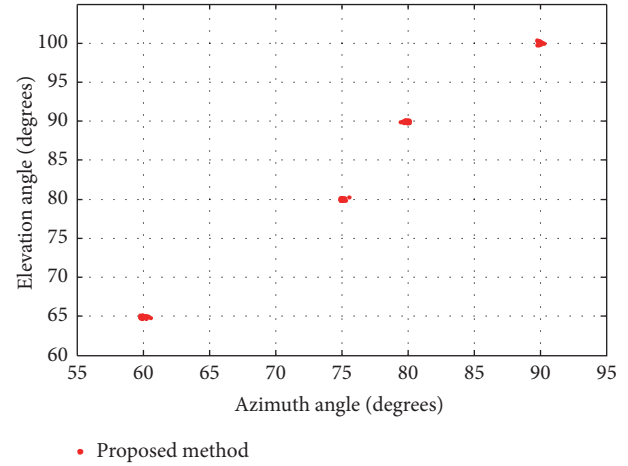


FIGURE 4: Scatter plot for azimuth and elevation for four uncorrelated sources at $(65^\circ, 60^\circ)$, $(80^\circ, 75^\circ)$, $(90^\circ, 80^\circ)$, and $(100^\circ, 90^\circ)$ at SNR = 10 dB using proposed method.

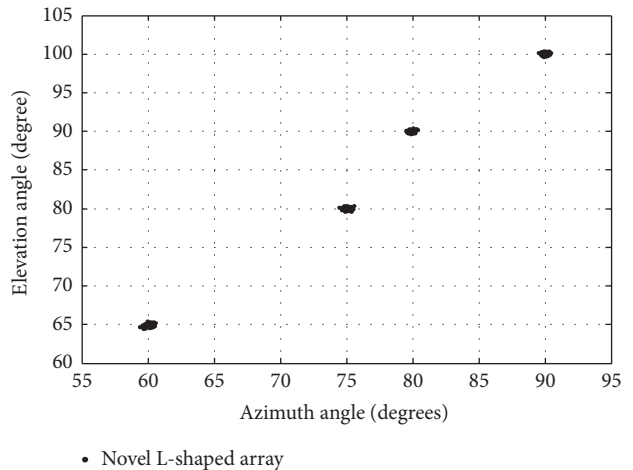


FIGURE 5: Scatter plot for azimuth and elevation for four uncorrelated sources at $(65^\circ, 60^\circ)$, $(80^\circ, 75^\circ)$, $(90^\circ, 80^\circ)$, and $(100^\circ, 90^\circ)$ at SNR = 10 dB using novel L-shaped method [30].

with [17, 30] even at low SNR. It can be deduced from Figures 2 and 3 that the performance of the proposed method will be affected due to noise. For example, for the proposed method the RMSE at SNR of -5 dB for source 1 is about 1.3 degrees and for source 2 is about 1.5 degrees.

In the second experiment, four uncorrelated sources with DOAs at $(\theta, \phi) = (65^\circ, 60^\circ)$, $(80^\circ, 75^\circ)$, $(90^\circ, 80^\circ)$, and $(100^\circ, 90^\circ)$ are considered and the number of snapshots is set to 200. Monte-Carlo trials of 200 are conducted. SNR is set to 10 dB. Figures 4, 5, and 6 illustrate joint azimuth and elevation scatter diagrams of 2D DOA estimation for the proposed method, novel L-shaped, and cumulant method, respectively. It is shown that the four incoming sources can be clearly observed by all methods. The proposed method in Figure 4 gives better and precise estimation compared to the other two methods in [17, 30]. It is also observed that

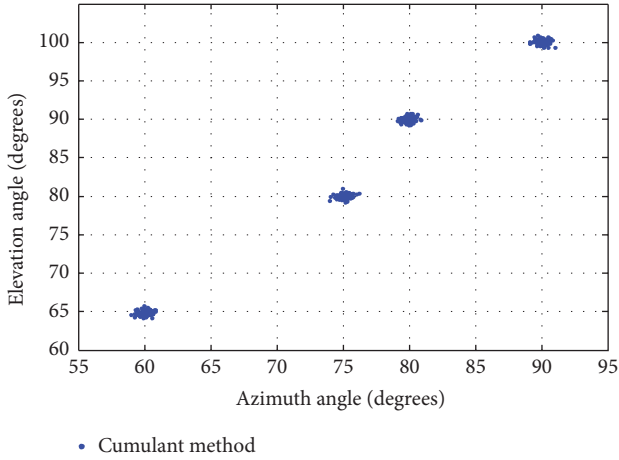


FIGURE 6: Scatter plot for azimuth and elevation for four uncorrelated sources at $(65^\circ, 60^\circ)$, $(80^\circ, 75^\circ)$, $(90^\circ, 80^\circ)$ and $(100^\circ, 90^\circ)$ at SNR = 10 dB using cumulant method [17].

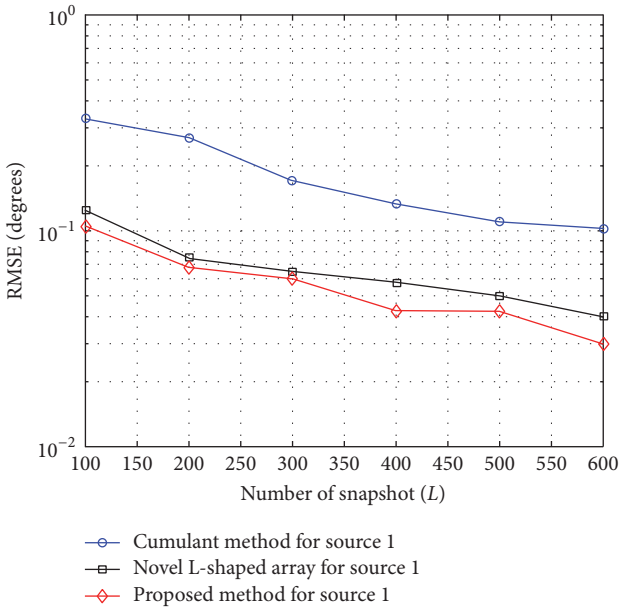


FIGURE 7: RMSE of azimuth-elevation versus number of snapshots at SNR = 10 dB for source 1 located at $(45^\circ, 50^\circ)$ using proposed method, novel L-shaped, and cumulant method.

the cumulant method in Figure 6 has the worst azimuth and elevation estimation for the four sources.

In the third experiment, the effect of the number of snapshots on the performance of the proposed method is evaluated. We consider two uncorrelated sources with DOAs at $(\theta, \phi) = (45^\circ, 50^\circ)$ and $(65^\circ, 80^\circ)$, SNR is set to 10 dB, and the number of snapshots L range is set from 100 to 600. Monte-Carlo trials of 500 are used. The average RMSE of azimuth and elevation angles estimation versus the number of snapshots for the two sources is shown in Figures 7 and 8. From these figures, we observe that RMSE of joint azimuth and elevation angles for source 1 and source 2 decrease with increasing number of snapshots. We can also clearly see

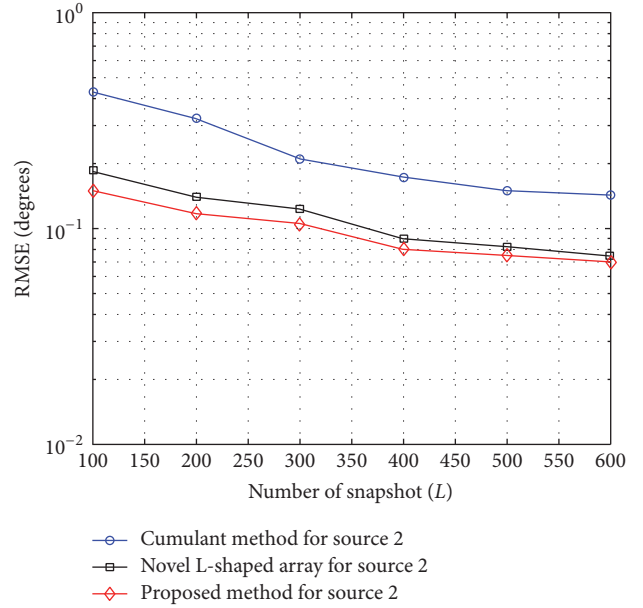


FIGURE 8: RMSE of azimuth-elevation versus number of snapshots at SNR = 10 dB for source 2 located at $(65^\circ, 80^\circ)$ using proposed method, novel L-shaped, and cumulant method.

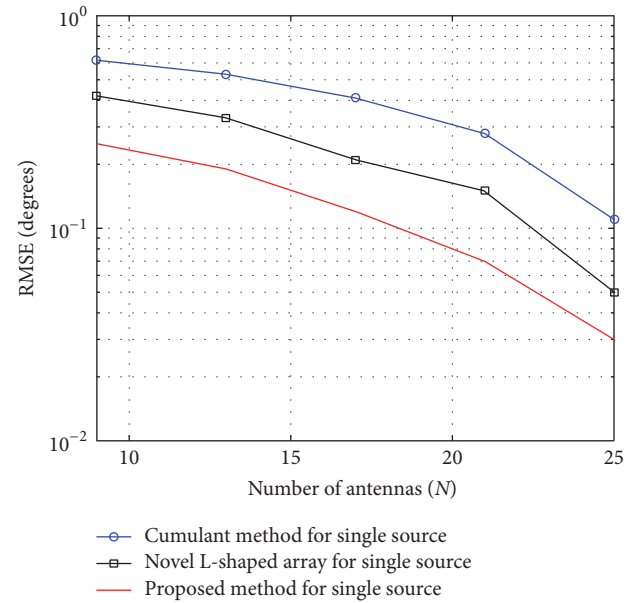


FIGURE 9: RMSE of azimuth-elevation versus number of antennas at SNR = 6 dB for single source located at $(65^\circ, 72^\circ)$ using proposed method, novel L-shaped, and cumulant method.

that the proposed method has higher estimation accuracy compared to the methods in [17, 30].

In the fourth experiment, the effect of the number of antennas on the performance of the proposed method is evaluated. We consider a single source located at $(\theta, \phi) = (65^\circ, 72^\circ)$, SNR set to 6 dB, and the number of snapshots set to 300. Monte-Carlo trials of 400 are used. The average RMSE of azimuth and elevation angles estimation versus the number of antennas is shown in Figure 9. From the figure, we observe

that RMSE of joint azimuth and elevation angles decrease with increasing number of antennas. We can also clearly see that the proposed method has better performance compared to the methods in [17, 30].

5. Conclusions

We have proposed a new method for 2D DOA azimuth and elevation angles estimation using L-shaped array. The proposed method has lower complexity and better performance compared with existing methods since constructed data matrices from cross-correlation are almost free of noise. PARAFAC model is derived for automatic pair matching of azimuth and elevation angles for multiple incident sources. In addition, the proposed method does not require spectral peak searching.

Competing Interests

The author declares that there is no conflict of interests regarding the publication of this paper.

References

- [1] Y. Wu and H. C. So, "Simple and accurate two-dimensional angle estimation for a single source with uniform circular array," *IEEE Antennas and Wireless Propagation Letters*, vol. 7, pp. 78–80, 2008.
- [2] Y. Wu, G. Liao, and H. C. So, "A fast algorithm for 2-D direction-of-arrival estimation," *Signal Processing*, vol. 83, no. 8, pp. 1827–1831, 2003.
- [3] P. Heidenreich, A. M. Zoubir, and M. Rubsamen, "Joint 2-D DOA estimation and phase calibration for uniform rectangular arrays," *IEEE Transactions on Signal Processing*, vol. 60, no. 9, pp. 4683–4693, 2012.
- [4] N. Tayem and H. M. Kwon, "L-shape 2-dimensional arrival angle estimation with propagator method," *IEEE Transactions on Antennas and Propagation*, vol. 53, no. 5, pp. 1622–1630, 2005.
- [5] Y. Hua, T. K. Sarkar, and D. D. Weiner, "An L-shaped array for estimating 2-D directions of wave arrival," *IEEE Transactions on Antennas and Propagation*, vol. 39, no. 2, pp. 143–146, 1991.
- [6] S. Marcos, A. Marsal, and M. Benidir, "The propagator method for source bearing estimation," *Signal Processing*, vol. 42, no. 2, pp. 121–138, 1995.
- [7] J. E. F. Del Rio and M. F. Càtedra-Pérez, "The matrix pencil method for two-dimensional direction of arrival estimation employing an l-shaped array," *IEEE Transactions on Antennas and Propagation*, vol. 45, no. 11, pp. 1693–1694, 1997.
- [8] F.-J. Chen, S. Kwong, and C.-W. Kok, "ESPRIT-like two-dimensional DOA estimation for coherent signals," *IEEE Transactions on Aerospace and Electronic Systems*, vol. 46, no. 3, pp. 1477–1484, 2010.
- [9] Y. Zhang, Z. Ye, X. Xu, and J. Cui, "Estimation of two-dimensional direction-of-arrival for uncorrelated and coherent signals with low complexity," *IET Radar, Sonar and Navigation*, vol. 4, no. 4, pp. 507–519, 2010.
- [10] N. Tayem, M. Omer, and A. Abul Hussain, "DOA estimation method using R matrix of the QR factorized data and its prototype implementation on NI-PXI platform," in *Proceedings of the 33rd Annual IEEE Military Communications Conference (MILCOM '14)*, pp. 333–337, Baltimore, Md, USA, October 2014.
- [11] T.-H. Liu and J. M. Mendel, "Azimuth and elevation direction finding using arbitrary array geometries," *IEEE Transactions on Signal Processing*, vol. 46, no. 7, pp. 2061–2065, 1998.
- [12] B. Porat and B. Friedlander, "Direction finding algorithms based on high-order statistics," *IEEE Transactions on Signal Processing*, vol. 39, no. 9, pp. 2016–2024, 1991.
- [13] P. Chevalier, L. Albera, A. Ferréol, and P. Comon, "On the virtual array concept for higher order array processing," *IEEE Transactions on Signal Processing*, vol. 53, no. 4, pp. 1254–1271, 2005.
- [14] M. C. Dogan and J. M. Mendel, "Applications of cumulants to array Processing-Part I: aperture extension and array calibration," *IEEE Transactions on Signal Processing*, vol. 43, no. 5, pp. 1200–1216, 1995.
- [15] P. Chevalier and A. Ferréol, "On the virtual array concept for the fourth-order direction finding problem," *IEEE Transactions on Signal Processing*, vol. 47, no. 9, pp. 2592–2595, 1999.
- [16] P. Chevalier, A. Ferréol, and L. Albera, "High-resolution direction finding from higher order statistics: the 2q-MUSIC algorithm," *IEEE Transactions on Signal Processing*, vol. 54, no. 8, pp. 2986–2997, 2006.
- [17] J. Liang, "Joint azimuth and elevation direction finding using cumulant," *IEEE Sensors Journal*, vol. 9, no. 4, pp. 390–398, 2009.
- [18] A. J. van der Veen, P. B. Ober, and E. F. Deprettere, "Azimuth and elevation computation in high resolution DOA estimation," *IEEE Transactions on Signal Processing*, vol. 40, no. 7, pp. 1828–1832, 1992.
- [19] A. L. Swindlehurst and T. Kailath, "Azimuth/elevation direction finding using regular array geometries," *IEEE Transactions on Aerospace and Electronic Systems*, vol. 29, no. 1, pp. 145–156, 1993.
- [20] S. Kikuchi, H. Tsuji, and A. Sano, "Pair-matching method for estimating 2-D angle of arrival with a cross-correlation matrix," *IEEE Antennas and Wireless Propagation Letters*, vol. 5, no. 1, pp. 35–40, 2006.
- [21] R. Bro, N. D. Sidiropoulos, and G. B. Giannakis, "Optimal joint azimuth-elevation and signal-array response estimation using parallel factor analysis," in *Proceedings of the 32nd Asilomar Conference on Signals, Systems & Computers*, pp. 1594–1598, November 1998.
- [22] R. Bro, "PARAFAC: tutorials and applications," *Chemometrics and Intelligent Laboratory Systems*, vol. 38, no. 2, pp. 149–171, 1997.
- [23] N. D. Sidiropoulos, R. Bro, and G. B. Giannakis, "Parallel factor analysis in sensor array processing," *IEEE Transactions on Signal Processing*, vol. 48, no. 8, pp. 2377–2388, 2000.
- [24] N. D. Sidiropoulos, G. B. Giannakis, and R. Bro, "Blind PARAFAC receivers for DS-CDMA systems," *IEEE Transactions on Signal Processing*, vol. 48, no. 3, pp. 810–823, 2000.
- [25] Z.-S. Qi, Y. Guo, and B.-H. Wang, "Blind direction-of-arrival estimation algorithm for conformal array antenna with respect to polarisation diversity," *IET Microwaves, Antennas and Propagation*, vol. 5, no. 4, pp. 433–442, 2011.
- [26] L. Zou, J. Lasenby, and Z. He, "Direction and polarisation estimation using polarised cylindrical conformal arrays," *IET Signal Processing*, vol. 6, no. 5, pp. 395–403, 2012.
- [27] W. Si, L. Wan, L. Liu, and Z. Tian, "Fast estimation of frequency and 2-D doas for cylindrical conformal array antenna using state-space and propagator method," *Progress in Electromagnetics Research*, vol. 137, pp. 51–71, 2013.
- [28] R. A. Harshman, "Foundation of the PARAFAC procedure: model and conditions for an 'explanatory' multi-mode factor

- analysis," *UCLA Working Papers in Phonetics*, vol. 16, pp. 1–84, 1970.
- [29] L. Wan, W. Si, L. Liu, Z. Tian, and N. Feng, "High accuracy 2D-DOA estimation for conformal array using PARAFAC," *International Journal of Antennas and Propagation*, vol. 2014, Article ID 394707, 14 pages, 2014.
- [30] Z. Xiaofei, L. Jianfeng, and X. Lingyun, "Novel two-dimensional DOA estimation with L-shaped array," *EURASIP Journal on Advances in Signal Processing*, vol. 2011, article 50, 2011.
- [31] A. Stegeman and N. D. Sidiropoulos, "On Kruskal's uniqueness condition for the Candecomp/Parafac decomposition," *Linear Algebra and Its Applications*, vol. 420, no. 2-3, pp. 540–552, 2007.
- [32] J. B. Kruskal, "Three-way arrays: rank and uniqueness of trilinear decompositions, with application to arithmetic complexity and statistics," *Linear Algebra and Its Applications*, vol. 18, no. 2, pp. 95–138, 1977.
- [33] R. Bro, "PARAFAC. Tutorial and applications," *Chemometrics and Intelligent Laboratory Systems*, vol. 38, no. 2, pp. 149–171, 1997.

Research Article

Application Research of the Sparse Representation of Eigenvector on the PD Positioning in the Transformer Oil

**Qing Xie,^{1,2} Dan Liu,² Ying Zhang,² Shuguo Gao,³ Tong Li,²
Xinjie Wang,⁴ and Fangcheng Lü²**

¹State Key Laboratory of Alternate Electrical Power System with Renewable Energy Sources,
North China Electric Power University, Baoding, Hebei 071003, China

²Hebei Provincial Key Laboratory of Power Transmission Equipment Security Defense,
North China Electric Power University, Baoding, Hebei 071003, China

³State Grid Hebei Electric Power Research Institute, Shijiazhuang 050021, China

⁴Department of English, North China Electric Power University, Baoding, Hebei 071003, China

Correspondence should be addressed to Qing Xie; xq_ncepu@126.com

Received 8 April 2016; Revised 23 August 2016; Accepted 27 September 2016

Academic Editor: Elias Aboutanios

Copyright © 2016 Qing Xie et al. This is an open access article distributed under the Creative Commons Attribution License, which permits unrestricted use, distribution, and reproduction in any medium, provided the original work is properly cited.

The partial discharge (PD) detection of electrical equipment is important for the safe operation of power system. The ultrasonic signal generated by the PD in the oil is a broadband signal. However, most methods of the array signal processing are used for the narrowband signal at present, and the effect of some methods for processing wideband signals is not satisfactory. Therefore, it is necessary to find new broadband signal processing methods to improve detection ability of the PD source. In this paper, the direction of arrival (DOA) estimation method based on sparse representation of eigenvector is proposed, and this method can further reduce the noise interference. Moreover, the simulation results show that this direction finding method is feasible for broadband signal and thus improve the following positioning accuracy of the three-array localization method. And experimental results verify that the direction finding method based on sparse representation of eigenvector is feasible for the ultrasonic array, which can achieve accurate estimation of direction of arrival and improve the following positioning accuracy. This can provide important guidance information for the equipment maintenance in the practical application.

1. Introduction

Electrical equipment working status is directly related to the reliable operation of power system. And the practice has proved that the PD is the main reason for the high voltage electrical equipment insulation breakdown finally. In order to avoid accidents and timely find the potential danger, it is necessary for the electrical equipment partial discharge testing to ensure system reliability [1–6].

In the PD detection, an array sensor is used to collect ultrasonic signals generated by the PD. Then the array signal processing technology is used to complete the source direction of arrival (DOA) estimation and positioning. This method not only has strong anti-interference ability, but also has high positioning accuracy, and it has been widely used in many areas [7–9]. However, the main processing

object of the traditional array signal processing methods is a narrowband signal, and the corresponding variety of space spectrum estimation (direction of arrival, DOA) methods that have high resolution and fast computing speed have been successfully applied. The electrical equipment ultrasonic signal generated by the PD in transformer oil is a typical broadband signal [10, 11], so the study on the DOA estimation algorithm that is suitable for wideband signal has extremely important significance.

The more classical wideband direction finding algorithm is mainly divided into two categories.

The first kind of method is incoherent subspace algorithm (ISM algorithm) [12, 13]. It is that a broadband signal is divided into a number of narrowband signals, and the average value is obtained after estimating the DOA of each narrowband signal. This method is a simple average of the

narrowband signal processing results, which has a large amount of calculation, and cannot overcome the shortcomings of subspace algorithms adopted by the narrowband signal, such that it is easily affected by noise and sampling points and cannot solve the coherent sources. The second method is the coherent signal subspace algorithm (CSM algorithm) [14–17]. A focusing matrix is used to focus on all frequency components on a single reference frequency. Narrowband signal processing method is used to estimate the DOA of the covariance matrix after focusing, which reduces the correlation coefficient between signals, and can achieve the goal of coherent solution. Moreover, the existing CSM algorithm has to use the traditional narrowband signal processing method after focusing, which is still unable to avoid the disadvantages of subspace algorithms.

Mallat and Zhang in 1990s proposed the theory of signal sparse decomposition [18, 19]. It can be constructed by using different ways according to the specific signal form and different research purposes. Although, the signal is represented by a handful of basis functions, the information in the signal also focuses on these few basis functions, so it is more conducive to extract and explain the essential characteristics of signals. At present, the signal sparse decomposition has been widely used in signal noise reduction, compression, coding and image processing, and other fields [11]. In this paper, the sparse decomposition theory is applied to the PD signal DOA estimation. According to the array signal direction vectors, an overcomplete atom dictionary is established. The matching pursuit (MP) algorithm is used to choose the appropriate atoms, and the angle information contained in the atoms is the DOA of signal sources.

This work studies the PD positioning method in the transformer oil based on the sparse representation of eigenvectors. Taking a nine-element circular ultrasonic array sensor as an example, the mathematical model of ultrasonic array signals is given. Firstly, the broadband PD signals are received by an ultrasonic array sensor, and the covariance matrix of a single frequency is obtained by using RSS focusing method [20]. Then an eigenvector corresponding to the maximum eigenvalue is obtained through eigendecomposition of the covariance matrix obtained; the eigenvector is as the amount to be decomposed. According to the reference frequency and the steering vector form of an array signal, a step and step overcomplete dictionary is established, and thus the DOA estimation of the PD signal can be obtained by MP. Moreover, this method can further reduce the noise interference. Finally, according to the results, the PD source is located by using the three-array cross positioning principle. The simulation and experimental results show that the direction finding method based on sparse representation of eigenvectors can get higher accuracy of the DOA estimation results and improve the subsequent positioning precision.

2. Broadband PD Ultrasonic Array Signal

2.1. The Mathematical Model of Array Signal. The research results show that the ultrasonic frequency produced by the PD in transformer oil is mainly concentrated in the range of

50 kHz to 400 kHz, the center frequency is between 70 kHz and 200 kHz, and so the PD ultrasonic signal source is a typical broadband signal.

Assuming that a uniform array consists of M equally spaced elements and there is a space with P broadband signals, the incident angle is, respectively, $\varphi_1, \varphi_2, \dots, \varphi_P$, and the signal received from the K th element can be expressed as

$$x_k(t) = \sum_{i=1}^P s_i [t - \tau_k(\varphi_i)] + n_k(t), \quad (1)$$

where $s_i(t)$ ($i = 1, 2, \dots, P$) is incident broadband signal; $n_k(t)$ is additive noise; $\tau_k(\varphi_i)$ is time difference relative to the reference node when the i th signal source is received by the k th element.

The time shift theorem of Fourier transform is as follows: a signal is carried on Fourier transform after the signal has a time shift equal to that of the signal that has a phase delay after Fourier transform. If $s(f)$ is the Fourier transform form of $s(t)$, that is,

$$\text{FFT}[s(t)] = s(f), \quad (2)$$

then the Fourier transform form of $s(t + \tau)$ is

$$\text{FFT}[s(t - \tau)] = s(f) e^{-j2\pi f\tau}. \quad (3)$$

For the signal received by the k th element, both sides of (1) are analyzed based on Fourier transform:

$$x_k(f) = \sum_{i=1}^P s_i(f) e^{-j2\pi f\tau_k(\varphi_i)} + n_k(f). \quad (4)$$

The Fourier transform for M elements can be written in matrix form, which is

$$\begin{bmatrix} x_1(f) \\ x_2(f) \\ \vdots \\ x_M(f) \end{bmatrix} = \begin{bmatrix} e^{-j\omega\tau_1(\varphi_1)} & e^{-j\omega\tau_1(\varphi_2)} & \dots & e^{-j\omega\tau_1(\varphi_P)} \\ e^{-j\omega\tau_2(\varphi_1)} & e^{-j\omega\tau_2(\varphi_2)} & \dots & e^{-j\omega\tau_2(\varphi_P)} \\ \vdots & \vdots & \ddots & \vdots \\ e^{-j\omega\tau_M(\varphi_1)} & e^{-j\omega\tau_M(\varphi_2)} & \dots & e^{-j\omega\tau_M(\varphi_P)} \end{bmatrix} \begin{bmatrix} s_1(f) \\ s_2(f) \\ \vdots \\ s_P(f) \end{bmatrix} + \begin{bmatrix} n_1(f) \\ n_2(f) \\ \vdots \\ n_M(f) \end{bmatrix}. \quad (5)$$

And they can be written as

$$\mathbf{X}(f) = \mathbf{A}(f, \theta) \mathbf{S}(f) + \mathbf{N}(f). \quad (6)$$

Among them, the steering vector matrix is

$$A(f, \varphi) = \begin{bmatrix} e^{-j\omega\tau_1(\varphi_1)} & e^{-j\omega\tau_1(\varphi_2)} & \dots & e^{-j\omega\tau_1(\varphi_P)} \\ e^{-j\omega\tau_2(\varphi_1)} & e^{-j\omega\tau_2(\varphi_2)} & \dots & e^{-j\omega\tau_2(\varphi_P)} \\ \vdots & \vdots & \ddots & \vdots \\ e^{-j\omega\tau_M(\varphi_1)} & e^{-j\omega\tau_M(\varphi_2)} & \dots & e^{-j\omega\tau_M(\varphi_P)} \end{bmatrix}. \quad (7)$$

The signal direction matrix $A(f, \varphi)$ is different from narrowband direction matrix. Here, the frequency is the whole band of the signal, while the frequency is a single fixed value in a narrowband model.

When the signal is analyzed based on the discrete Fourier transform (DFT) with J points, the frequencies are J discrete points, and then (6) can be discrete as

$$X(f_j) = A(f_j)S(f_j) + N(f_j) \quad j = 1, 2, \dots, J. \quad (8)$$

The steering vector matrix is

$$A(f_j, \varphi) = [a(\varphi_1, f_j) \ a(\varphi_2, f_j) \ \dots \ a(\varphi_P, f_j)], \quad (9)$$

where $\mathbf{a}(\varphi_i, f_i)$ ($i = 1, 2, \dots, k$) is a steering vector:

$$\mathbf{a}(\varphi_i, \mathbf{f}_j) = \begin{bmatrix} e^{-j2\pi\mathbf{f}_j\tau_1(\varphi_i)} \\ e^{-j2\pi\mathbf{f}_j\tau_2(\varphi_i)} \\ \vdots \\ e^{-j2\pi\mathbf{f}_j\tau_M(\varphi_i)} \end{bmatrix}. \quad (10)$$

2.2. The Structure of the Circular Ultrasonic Array Sensor. The circular ultrasonic array sensor is composed of M identical elements evenly distributed on the circumference with a radius of R in the x - y plane; the elements are arranged as shown in Figure 1 (e.g., taking nine element). The coordinate system of the sphere is used to express the DOA of the incident plane wave, and o is in the center of the array, which is the origin of the coordinate system. Consequently, it is taken as a reference point. In addition, when the incident signal direction is (α, θ) , azimuth α is expressed as the angle between the x -axis and a projection in the x - y plane, and the projection is wired from the reference point to the source of the signal. The pitch angle θ is the angle between the z -axis and the wired one that is from the reference point to the source of signal. Then the delay time τ_m in which the signal arrives at the m th element relative to the reference element is

$$\tau_m = \frac{r}{c} \left(\cos \left(\frac{2\pi(m-1)}{M} - \alpha \right) \sin \theta \right) \quad (11)$$

$m = 1, 2, \dots, M.$

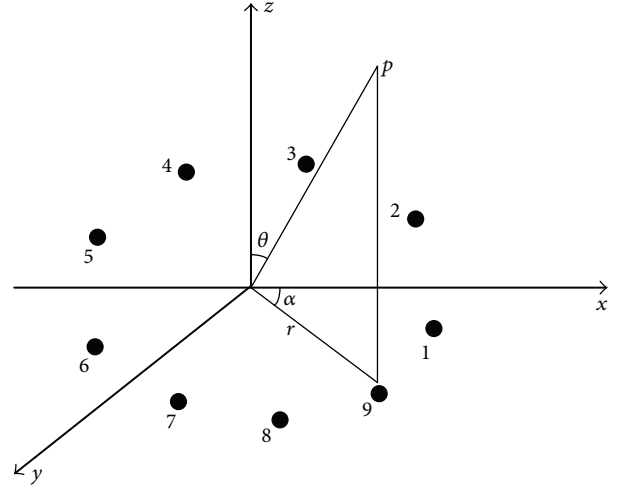


FIGURE 1: The structure of a nine-element circular ultrasonic array.

Then, according to (10) and (11), the steering vector of an m -element circular array can be expressed as

$$\mathbf{a}(\alpha, \theta, f) = \begin{bmatrix} \exp \left[-j2\pi f \cos \alpha \frac{\sin \theta r}{c} \right] \\ \exp \left[-j2\pi f \cos \left(\frac{2\pi}{M} - \alpha \right) \frac{\sin \theta r}{c} \right] \\ \vdots \\ \exp \left[-j2\pi f \cos \left(\frac{2\pi(m-1)}{M} - \alpha \right) \frac{\sin \theta r}{c} \right] \end{bmatrix}, \quad (12)$$

where the frequency f is the whole frequency band of the signal.

3. DOA Estimation Based on Sparse Decomposition

3.1. The Mathematical Expression of Sparse Representation. Given an overcomplete dictionary $\mathbf{D} = \{\Phi_i, i = 1, 2, \dots, I\}$, there are I atoms, which is a whole Hilbert space $H = R^d$, and $I > d$. Therefore, for any signal expressed as y , $y \in H$, the k atoms can be selected adaptively in \mathbf{D} , to make sparse approximation with the signal y ; that is,

$$y = \sum_{r \in I_k} c_r \Phi_r, \quad (13)$$

where I_k is index set of Φ_r and the corresponding coefficients are expressed as $C = \{c_r\}_{r \in I_k}$. The atomic number k selected is usually much smaller than the atomic number I in the atom dictionary. A few atoms can express the signal, so-called sparse representation.

The matrix is used to express $y \in R^d$ and $\mathbf{D} \in R^{d \times I}$; the i th column of \mathbf{D} is Φ_i , and then (13) can be written as

$$\mathbf{Y} = \mathbf{D}\mathbf{c}, \quad (14)$$

where $\mathbf{c} \in R^I$ is a sparse vector.

The ways in which the atoms in the overcomplete dictionary are used to express the signal have infinite variety of forms. Therefore, how to effectively solve the sparse coefficient vector \mathbf{c} is an important problem, the sparse representation which is the basic problem of sparse representation, and the specific expression is as follows:

$$\begin{aligned} \operatorname{argmin} \quad & \|\mathbf{c}_0\|, \\ \text{s.t.} \quad & \mathbf{y} = \mathbf{D}\mathbf{c}, \end{aligned} \quad (15)$$

where \mathbf{c}_0 is l_0 -norm of \mathbf{c} , which is the number of the nonzero elements in the coefficient vector \mathbf{c} .

3.2. Application of Matching Pursuit Algorithm in DOA Estimation. In the application process of sparse representation method, different overcomplete dictionaries are constructed according to different research purposes. When an ultrasonic array is used to estimate the DOA of the broadband PD signal, the overcomplete dictionary can be structured according to a steering vector matrix form of the received signal. The steering vector matrix contains the wave direction of signals; therefore, constructing a group of atomic vectors covered space at any angle inevitably includes the DOA of signals. Based on sparse representation theory, these atoms that include the DOA of signals can be selected by using matching pursuit (MP) algorithm, and they can be used to realize the direction finding.

The principles of the MP algorithm are similar to the adaptive projection decomposition algorithm. Firstly, the atoms that match with the signal mostly are selected from the overcomplete dictionary, which is the idea that these atoms have the maximum inner product with signal. Here, the projection coefficient is that the signal on the atom is the largest, and the rest of energy on the atom after decomposition is minimum. Next, the same method is used to find out the best matching atoms with the remaining amount and then make decomposition. Repeat the above steps. When the remaining energy of decomposition is small enough or the best matching atom combinations can represent the original signal, stop the decomposition. The flow chart of the sparse representation by using MP algorithm is shown in Figure 2.

When estimating the DOAs of the ultrasonic signal generated by p PD sources, the incidence angles of the signal can be searched on N angle vectors that have been set. In general, the number of the PD sources is much smaller than the number of angles to be searched; that is, $P \ll N$. A search vector of the angle is constructed, and the vector is covering all space angle, which is $\boldsymbol{\beta} = [\beta_1 \ \beta_2 \ \cdots \ \beta_N]$. There are P components equal to $\varphi_1, \varphi_2, \dots, \varphi_P$, respectively. According to (9), the search matrix of angle is constructed as

$$A_s(\boldsymbol{\beta}) = [a_v(\beta_1), a_v(\beta_2), \dots, a_v(\beta_N)]. \quad (16)$$

The direction finding by using the sparse representation theory is to decompose the received signals on the atoms with different directions. The projection value is maximum when the incident signal has the same direction with the atoms. According to the relevant knowledge of the vector projection theory in mathematics, the projection of an array

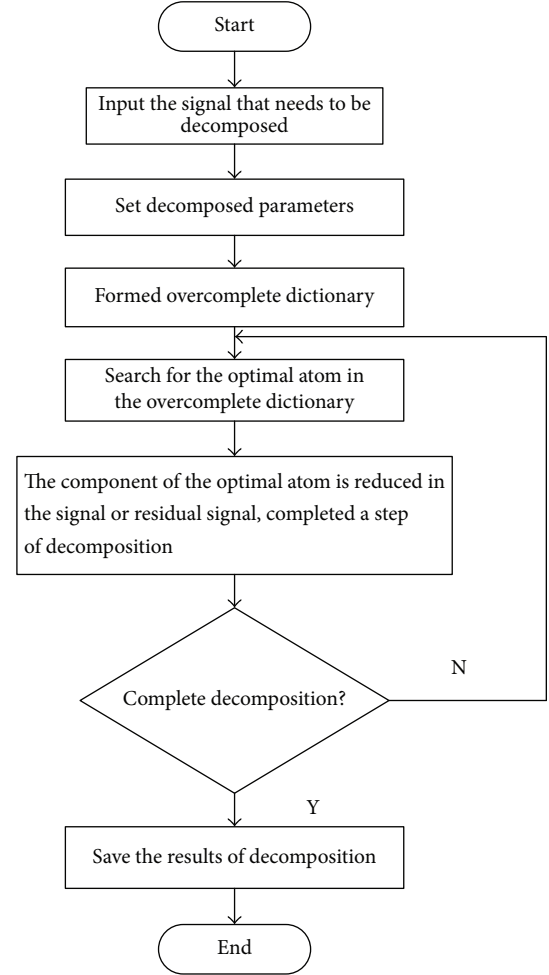


FIGURE 2: The flow chart of sparse representation based on MP algorithm.

signal on the atom is maximum, which means that the inner product module between the array signal and the corresponding atom is maximum. Firstly, the parameter to be decomposed is set to be \mathbf{X} , and \mathbf{X} makes the inner product with each atom $\mathbf{a}_v(\beta_n)$ ($n = 1, 2, \dots, N$); then the optimal atom $a_v(\beta_{\gamma_0})$ $\gamma_0 \in \{1, 2, \dots, P\}$ is selected by the absolute value of the inner product, and the optimal atom meets the following conditions:

$$|\langle \mathbf{X}, \mathbf{a}_v(\beta_{\gamma_0}) \rangle| = \sup |\langle \mathbf{X}, \mathbf{a}_v(\beta_n) \rangle|. \quad (17)$$

The received signal \mathbf{X} is decomposed into the component of projection on $\mathbf{a}_v(\beta_{\gamma_0})$ and the remains of the signal:

$$\mathbf{X} = P_{a_v(\beta_{\gamma_0})}\mathbf{X} + R\mathbf{X}, \quad (18)$$

where $P_{a_v(\beta_{\gamma_0})}\mathbf{X}$ is the projection of signal on the optimal atom. And with the definition of the matrix projection, the

part of projection can be obtained by using the following equation:

$$\begin{aligned} & \mathbf{P}_{\mathbf{a}_v(\beta_{\gamma_0})} \mathbf{X} \\ &= \mathbf{a}_v(\beta_{\gamma_0}) \langle \mathbf{a}_v(\beta_{\gamma_0}), \mathbf{a}_v(\beta_{\gamma_0}) \rangle^{-1} \mathbf{a}_v^H(\beta_{\gamma_0}) \mathbf{X} \quad (19) \\ &= \langle \mathbf{X}, \mathbf{a}_v(\beta_{\gamma_0}) \rangle \mathbf{a}_v(\beta_{\gamma_0}). \end{aligned}$$

Repeat the above steps with the residual signal and, after the decomposition for \mathbf{P} times, the residual signal is small enough to meet the requirements of the allowable error, so the decomposition results of the array signal \mathbf{X} can be obtained:

$$\mathbf{X} = \sum_{n=1}^P \langle \mathbf{R}_n \mathbf{X}, \mathbf{a}_v(\beta_n) \rangle \mathbf{a}_v(\beta_n) + \mathbf{R}_K \mathbf{X}. \quad (20)$$

When the decomposition of the received signal has been finished, a group of orientation matrixes $\beta = [\beta_1 \ \beta_2 \ \cdots \ \beta_P]$ can be obtained. And P elements are wave directions of P signals, respectively.

The number of PD sources is previously unknown and, according to the signal sparse representation in the process of the change in energy, the iterative termination conditions for DOA estimation of ultrasonic array signals based on MP algorithm are obtained. However, if the difference of the energy variation for the adjacent decomposition is particularly large and the value of the energy variation is small in the process of subsequent classification, then the iteration can be terminated.

3.3. The Principle of Direction Finding Based on Sparse Representation of the Eigenvectors. According to the introduction of Section 2.1, assuming that the signal and noise are independent of each other, the center frequency is f , the array covariance matrix of received data is

$$\begin{aligned} \mathbf{R}(f) &= E \{ \mathbf{X}(f) \mathbf{X}^H(f) \} \\ &= \mathbf{A}(f) \mathbf{R}_S(f) \mathbf{A}^H(f) + \delta^2 \mathbf{I}, \end{aligned} \quad (21)$$

where \mathbf{I} is identity matrix, $\sigma^2 \mathbf{I} = E[\mathbf{N}(f) \mathbf{N}(f)^H]$, and $\mathbf{R}_S(f)$ is the covariance matrix of the source signal. Moreover, the signal subspace composed by the signal eigenvector and the noise subspace composed by the noise eigenvector can be obtained, respectively, by the decomposition of the covariance of the ultrasonic array signal.

Theorem 1. Suppose that N ($N \leq M - 1$) narrowband far-field signal is incident on the array that consists of M elements, the order of the array manifold matrix is N , and the order of the signal covariance matrix is K ($K \leq N$). Assuming that the noise covariance matrix \mathbf{R}_N is a matrix with full rank, so the following linear relationship meets

$$\mathbf{R}_N \mathbf{e}_k = \sum_{n=1}^N \alpha_k(n) \mathbf{a}(\theta_n), \quad (22)$$

where $1 \leq k \leq K$, \mathbf{e}_k is an eigenvector of covariance matrix that receives the data, $\alpha_k(n)$ is a factor of linear combination, and

$\mathbf{a}(\theta_n)$ is a steering vector. The proof process is in the literature [21].

Based on the theorem, when the noise covariance matrix is the ideal white noise, (22) can be simplified as

$$\mathbf{e}_k = \sum_{n=1}^N \alpha_k(n) \mathbf{a}(\theta_n) \quad 1 \leq k \leq K. \quad (23)$$

Equation (23) shows that whether the source of signal is coherent, the eigenvectors corresponding to the maximum eigenvalue is a linear combination of the steering vectors for each signal source. And the biggest eigenvector of the data covariance matrix contains the information of all signals.

Consequently, the eigenvector corresponding to the maximum eigenvalue can be sparse representation, thereby the DOA estimation for the signal is obtained. Compared with the DOA estimation of the received data based on sparse representation, the eigenvalue decomposition can weaken the interference caused by noise, and the eigenvector corresponding to the maximum eigenvalue is selected to be as the amount to be decomposed, and the estimation results will be more accurate.

3.4. The Steps of Direction Finding Based on Sparse Representation of Eigenvectors. Firstly, in order to obtain the narrow covariance matrix of a single frequency, the received data need to be focused on, because the ultrasonic signal is a broadband signal. The rotate signal subspace (RSS) algorithm presented in literature [20] is used to focus on the received data of the array in this work.

Therefore, the detailed steps of the DOA estimation based on sparse representation of eigenvectors can be expressed as follows:

- (1) The data \mathbf{X} received by the ultrasonic array sensor is analyzed based on the DFT to obtain the \mathbf{X}' , and this is the preparation for the subsequent focus.
- (2) The reference frequency is selected as f_0 , and \mathbf{X}' is focused by RSS, and the covariance matrix of a single frequency \mathbf{P} is obtained by using the focus algorithm.
- (3) The corresponding eigenvector \mathbf{e}_{\max} of the maximum eigenvalue can be obtained through the eigenvalue decomposition of the covariance matrix \mathbf{P} .
- (4) According to Section 2.2, the overcomplete dictionary is established in the form of the steering vector, and the frequency f of the atom in the step and step overcomplete dictionary is replaced with the reference frequency f_0 .
- (5) By using the MP algorithm, the eigenvector \mathbf{e}_{\max} is to make sparse representation, and the optimal atom is selected. Then the DOA estimation of the signal is obtained, which is contained in the angle (α, θ) of the optimal atom.

3.5. Three-Array Cross Localization Method. After the DOA estimation of the signal, the position of the PD source cannot be sure, because the distance between the PD source and the

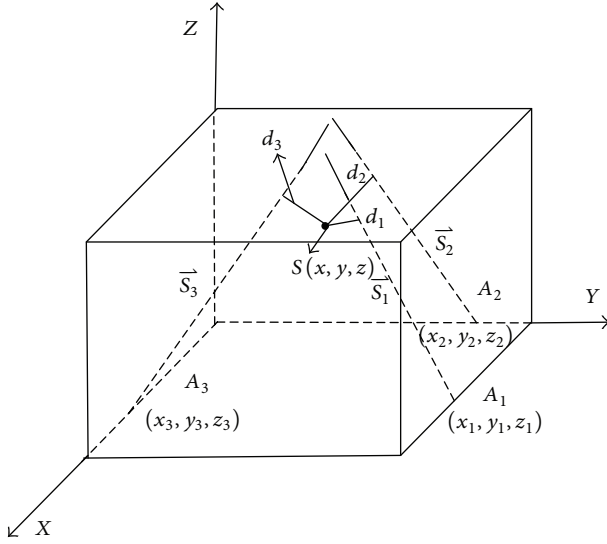


FIGURE 3: The map of three-array cross localization principle.

array sensor is unknown [22, 23]. The space position of the PD source is obtained according to the method of three-array cross localization method and the results of the direction finding. The principle of three-array localization method is shown in Figure 3.

The space positions of the three sets of array sensors are, respectively, $A_1(x_1, y_1, z_1)$, $A_2(x_2, y_2, z_2)$, and $A_3(x_3, y_3, z_3)$ and, using the direction angle and the positions of the ultrasonic array sensor, the equation of the direction line can be obtained. Suppose that spatial coordinates of the signal source are $S(x, y, z)$. In the ideal situation, the three different direction lines should intersect in the $S(x, y, z)$. But these lines are on different surfaces, because there are many actual measurement errors. Therefore, the sum function that is a sum of the vertical distance from a point in the space to the three lines is

$$d = \sum_{t=1}^3 d_t = d_1 + d_2 + d_3. \quad (24)$$

Through searching in the space by using Chaotic Monkey algorithm [24], when the sum of distance is minimum, the point with the minimum value d can be regarded as the space position of the PD source.

4. The Simulation Study

4.1. The Simulation of the PD Signal. The length (x), width (y), and height (z) of the electrical equipment model are, respectively, 150 cm, 100 cm, and 120 cm (they are matched with the size of the experimental equipment). The simulation parameters of signal are set as the wavelength $\lambda = 10$ mm; the amplitude is 5 mm; the center frequency is 150 kHz; the equivalent velocity is 1500 m/s; the acoustic attenuation coefficient of the signal is $\alpha = 50 \times 10^{-7} \text{ cm}^{-1}$; the number of sampling snapshots is 1024; the sampling frequency is 2 MHz; the noise-signal ratio is 10 dB. Moreover, in order to verify

the validity of the array signal direction finding based on sparse representation, the simulation research is carried out on a nine-element circular ultrasonic array sensor, and the interval between array elements is $d = \lambda/2 = 5$ mm.

The form of simulated signal [25, 26] is

$$f(t) = \begin{cases} Ae(k_1(t_0 - t)) \cos(2\pi ft), & 0 \leq t \leq t_0, \\ Ae(k_2(t - t_1)) \cos(2\pi ft), & t_0 \leq t \leq t_1, \end{cases} \quad (25)$$

where f is the central frequency of the signal, A is the amplitude of the signal, and t_0 is the time division point. Firstly, because of the randomness, the PD ultrasonic signal is in electrical equipment, so 100 frequency points of the signal are generated according to the average probability in the bandwidth, and they formed frequency distribution. Then, on the basis of center frequency of ultrasonic signal, the amplitude of the signal corresponding to each frequency point is formed by the normal distribution method. Finally, the initial phase of each frequency point is randomly generated, and the white Gaussian noise is added in the signal, and the PD ultrasonic signal in the oil can be simulated.

The map of the time waveform of the simulated signal is shown in Figure 4(a); by using the Fourier transform, the map of the frequency domain is shown in Figure 4(b); when the noise is large, the PD signal is submerged in the waveform of the time domain, and it is shown in Figure 4(c).

The map of the frequency domain shows that the simulated PD signal is a broadband signal, and the center frequency is 150 kHz.

The oscillogram of the simulated signal received by a nine-element circular ultrasonic array sensor is shown in Figure 5.

4.2. The Simulation of Location. For the broadband signal simulated, the received data by ultrasonic array sensor is segmented according to the observation time, and the array covariance matrix of each frequency point can be obtained by the DFT in every period. f_0 is selected as focusing frequency, and the covariance matrix of a single frequency can be acquired. The step and step overcomplete dictionary is established according to the focusing frequency and the steering vector form of Section 2.2. After the focusing and the eigendecomposition of the covariance matrix, the eigenvector corresponding to the maximum eigenvalue can be acquired, and the eigenvector is the parameter to be decomposed.

Then taking a circular ultrasonic array sensor, for example, the position of the source is set at (35, 50, 60) cm, and the positions of the three-array sensors are set at position #1: (40, 0, 10) cm, position #2: (80, 0, 0) cm, position #3: (0, 30, 50) cm. Therefore, the theoretical values of the DOAs are, respectively, $(5.7^\circ, 45.1^\circ)$, $(132.0^\circ, 48.3^\circ)$, and $(29.7^\circ, 76.1^\circ)$.

In accordance with the steps of the Section 3.4, the process of searching for the optimal atom is that the array signal makes inner products with each atom, respectively, and the value of the inner product is maximum with the optimal atom. In order to figuratively present this process, the scatter gram of absolute value of the inner product in the angle space can be made.

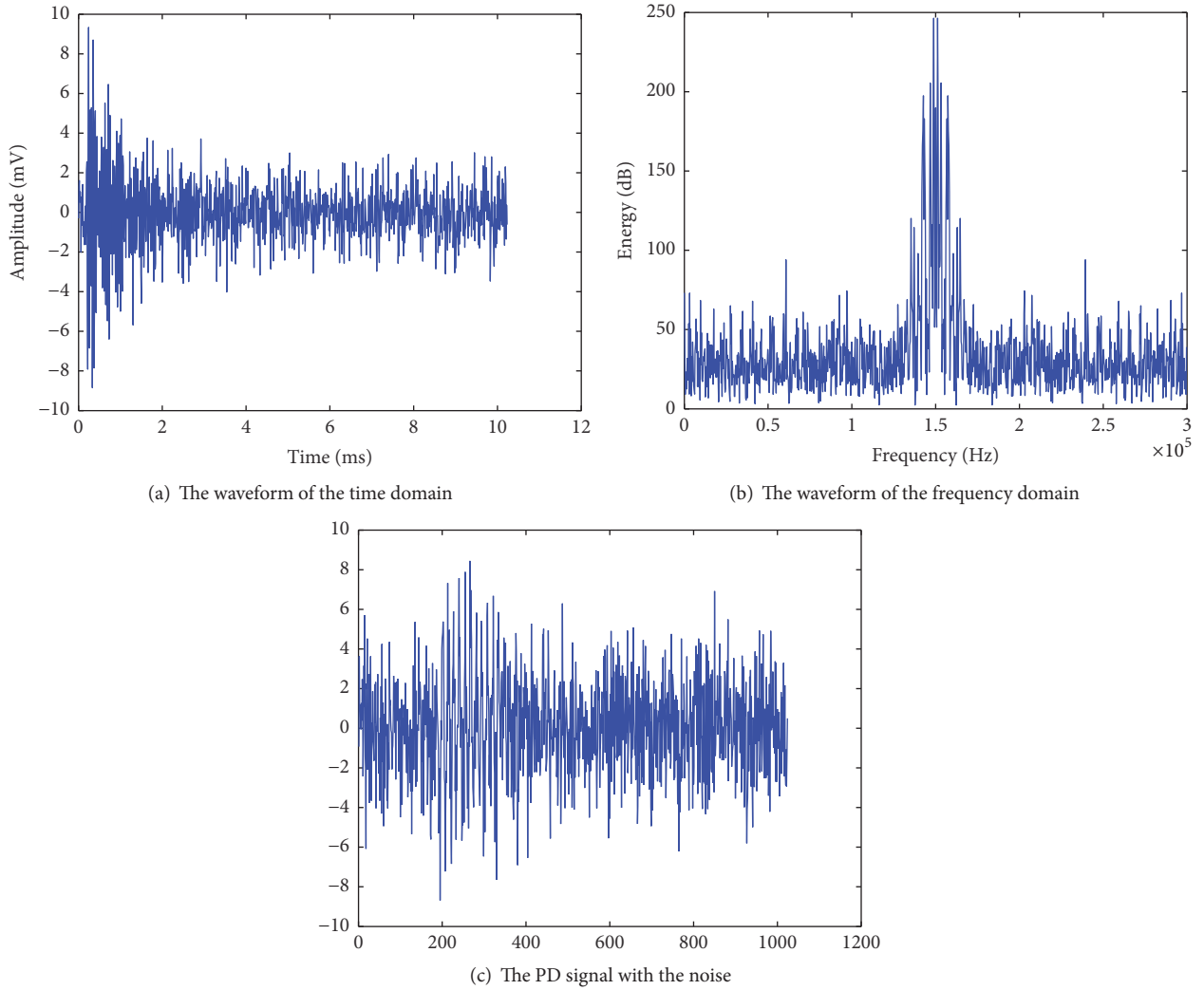


FIGURE 4: The simulated PD signal.

The DOA estimation result of the PD ultrasonic signal received by the array sensor at the position #1 is $(95.9^\circ, 4.8^\circ)$, and the scatter gram of the absolute value of the inner product in the space is shown in Figure 6.

The DOA estimation result of the PD ultrasonic signal received by the array sensor at position #2 is $(131.6^\circ, 8.5^\circ)$, and the scatter gram of the absolute value of the inner product in the space is shown in Figure 7.

The DOA estimation result of the PD ultrasonic signal received by the array sensor at position #3 is $(30.1^\circ, 6.4^\circ)$, and the scatter gram of the absolute value of the inner product in the space is shown in Figure 8.

Then using the three DOA estimation results above, the objective function equation (24) is calculated by the three-array cross positioning principle. And when the objective function is minimum by using the search of the optimization algorithm, the position of the PD source in the space can be acquired. Consequently, the result is $(33.1, 51.8, 58.7)$ cm, the error is 2.9 cm, and the location diagram is shown in Figure 9.

Changing the positions of the PD source and the ultrasonic array sensors, the five groups of the PD source positioning simulation are conducted. The positioning results of the circular ultrasonic array are shown in Table 1.

The table shows that, after direction of the eigenvector with the sparse representation, the average error for positioning is 3.08 cm. And it illustrates that the eigenvector with the sparse representation can obtain the better direction finding results and reduce the errors in the positioning.

5. The Experimental Study

5.1. The Experimental System. The experimental system for research includes discharge device, the array sensor, the data acquisition system, and the data processing system.

The simulated electrical equipment is a tank welded by steel plates, the body length is 150 cm, the width is 100 cm, the height is 120 cm, and the thickness of the steel plate is 5 mm.

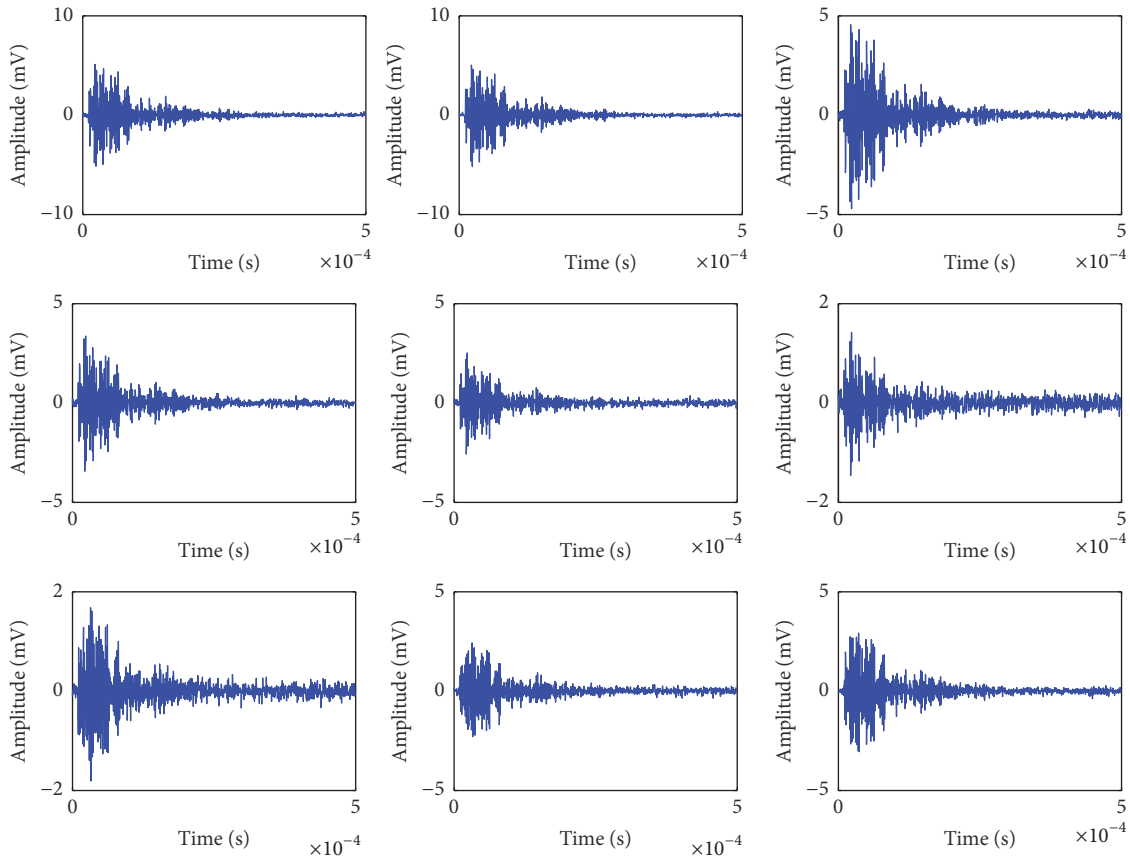


FIGURE 5: The oscillogram of the signal received by a full ultrasonic array.

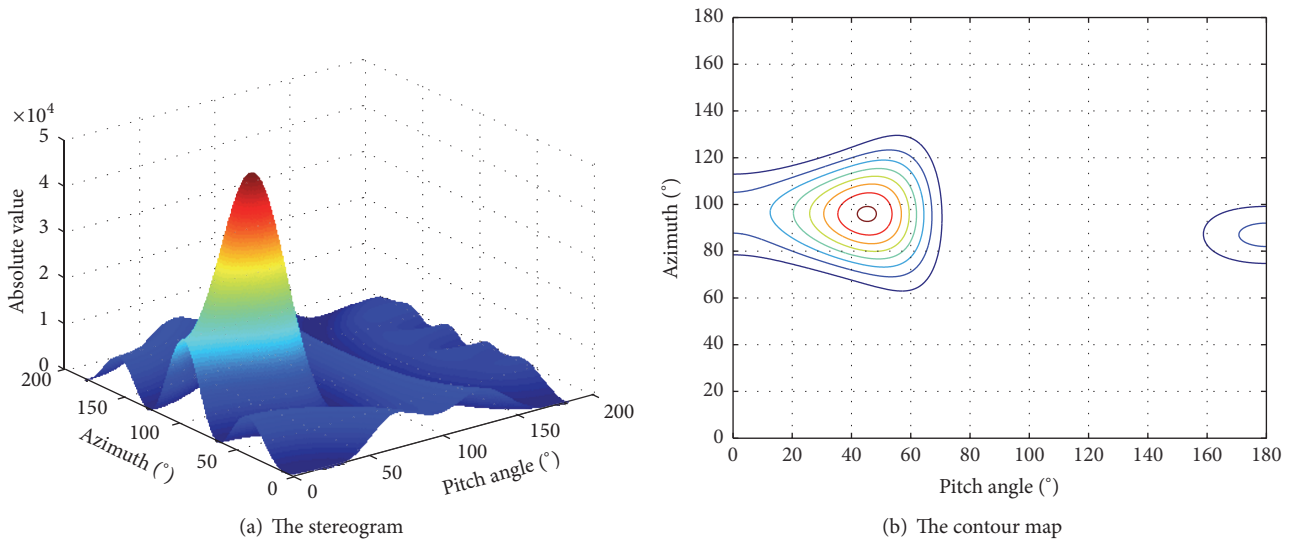


FIGURE 6: The scatter gram of the absolute value of the inner product in the space.

Moreover, a three-capacitor discharge tube is used to simulate the PD source of the internal electrical equipment. And the array sensor is put in the preset position.

A nine-element circular ultrasonic array sensor is used to receive signal, it is fixed on the outer wall of the tank, and the shielding lines are used to transfer the data; then

the data are processed by the computer combined with ultrasonic detection software. The principle diagram of the whole experiment system is shown in Figure 10.

The scale model and the physical map of the nine-element circular ultrasonic array sensor are, respectively, shown in Figures 11(a) and 11(b).

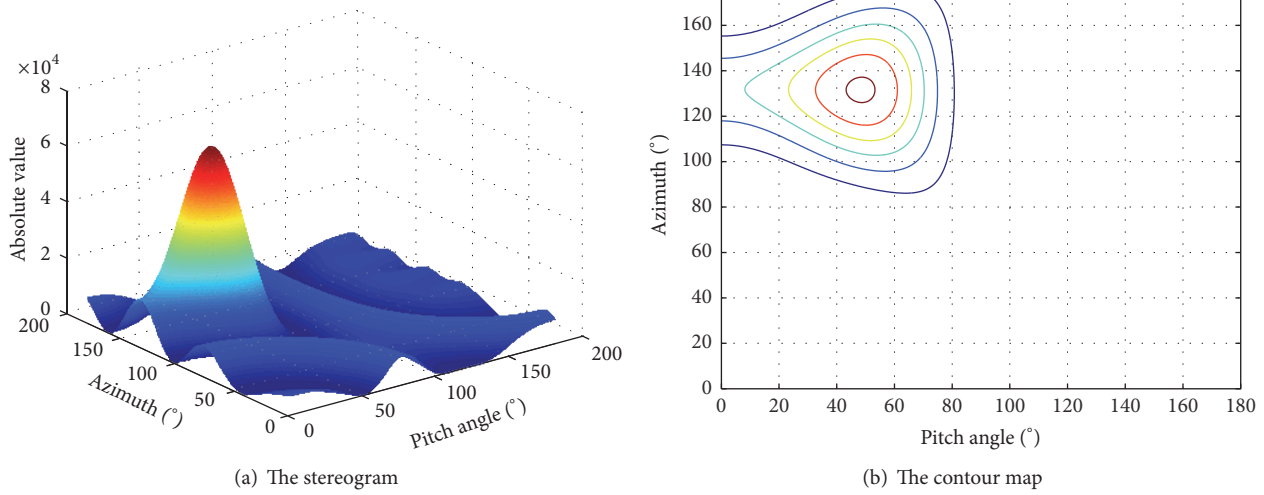


FIGURE 7: The scatter gram of the absolute value of the inner product in the space at position 2.

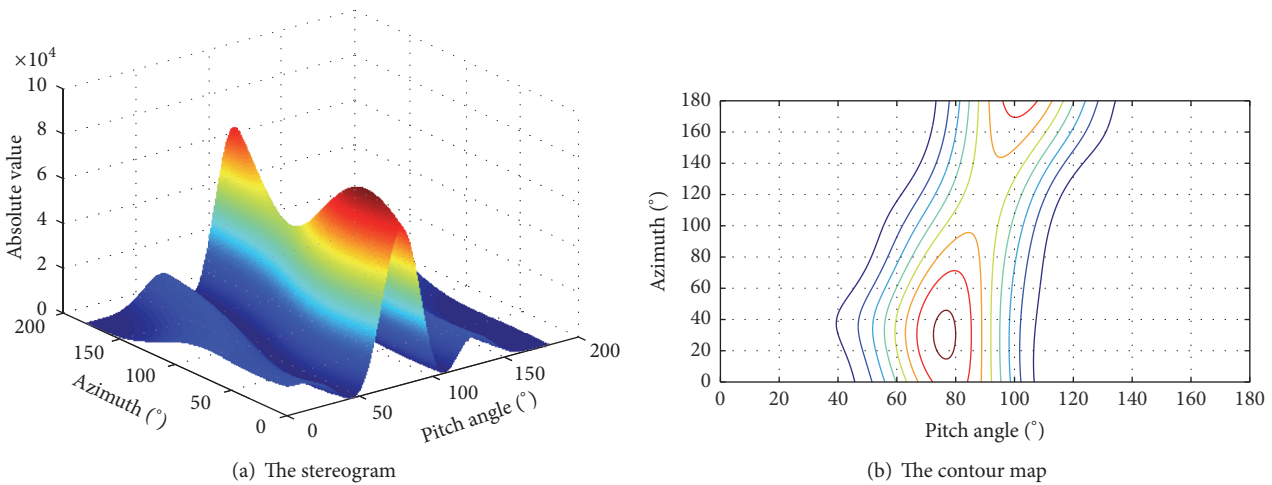


FIGURE 8: The scatter gram of the absolute value of the inner product in the space at position 3.

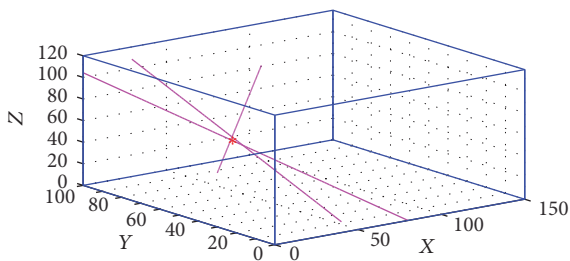


FIGURE 9: The map of simulated location of the circular array sensor. “*” refers to the position of the PD source.

In order to avoid the influences of discharge instability and other factors on the experimental results, a three-capacitor discharge tube is used to simulate the PD source,

it can generate the ultrasonic that is similar to the ultrasonic signal of the real partial discharge, and it has good stability and repeatability, and the discharge voltage is low and easy to meet the insulation. The EPSON discharge tube is used to be a discharge device, and the critical discharge voltage is 230 V. Generally, the discharge frequency of ultrasonic signals emitted by the discharge tube is in the range of 50 kHz to 280 kHz, the center frequency is 150 kHz, and the equivalent velocity is 1500 m/s, while the wavelength is about 10 mm. The diagram of the three-capacitor discharge principle is shown in Figure 12.

In Figure 12, C_0 is a coupling capacitor, and C_1 is equivalent capacitance of the other parts of the insulating medium. C_2 is equivalent capacitance of the insulating medium that is in series with the PD source, and the gas-discharge tube is used to be a discharge device, when the voltage of the tube

TABLE 1: The location results of the circular ultrasonic array.

Group	The position of the PD source/cm	The position of the array sensor/cm	Theoretical angle/(°)	Direction angle/(°)	The result of the three-array cross positioning /cm	The error/cm
1	(35, 50, 60)	(40, 0, 10)	(95.7, 45.1)	(95.9, 44.8)	(33.1, 51.8, 58.7)	2.9
		(80, 0, 0)	(132.0, 48.3)	(131.6, 48.5)		
		(0, 30, 50)	(29.7, 76.1)	(30.1, 76.4)		
2	(30, 80, 95)	(35, 0, 50)	(93.6, 60.7)	(94.1, 60.4)	(32.0, 78.5, 93.2)	3.1
		(40, 0, 0)	(97.1, 40.3)	(97.5, 39.5)		
		(0, 20, 30)	(63.4, 45.9)	(64.3, 46.2)		
3	(25, 70, 20)	(50, 0, 10)	(109.7, 82.3)	(110.3, 81.6)	(23.2, 68.4, 22.3)	3.3
		(0, 50, 0)	(38.7, 58.0)	(38.3, 57.4)		
		(0, 50, 60)	(38.7, 141.3)	(38.3, 139.8)		
4	(60, 30, 50)	(30, 0, 20)	(45.0, 54.7)	(44.3, 54.1)	(62.3, 31.7, 49.0)	3.0
		(65, 0, 35)	(99.5, 63.7)	(98.7, 64.0)		
		(0, 45, 0)	(166.0, 51.0)	(165.2, 50.5)		
5	(75, 20, 45)	(0, 0, 80)	(14.9, 114.3)	(14.4, 114.8)	(73.2, 21.7, 43.1)	3.1
		(40, 0, 0)	(29.7, 41.9)	(30.3, 40.8)		
		(55, 0, 0)	(45.0, 32.2)	(44.1, 32.7)		

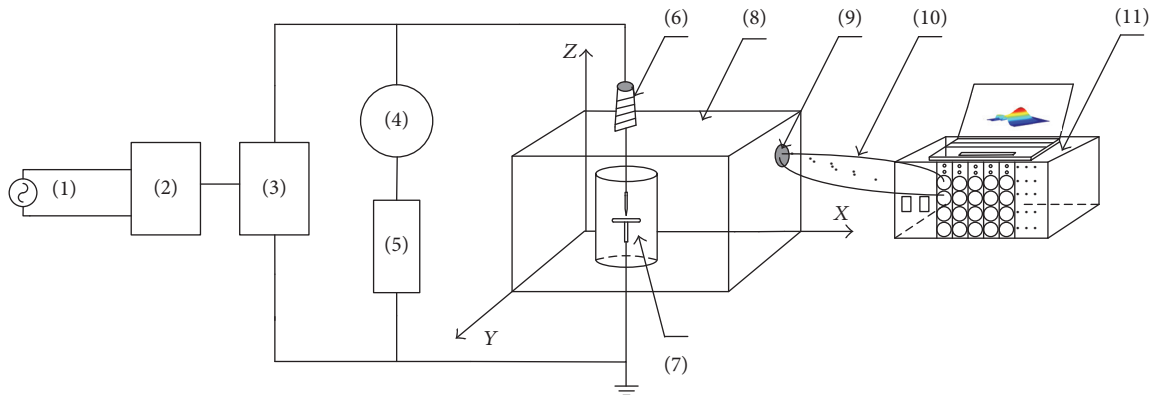
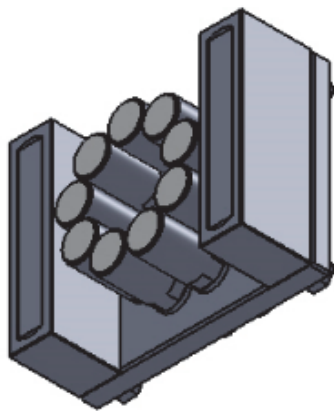
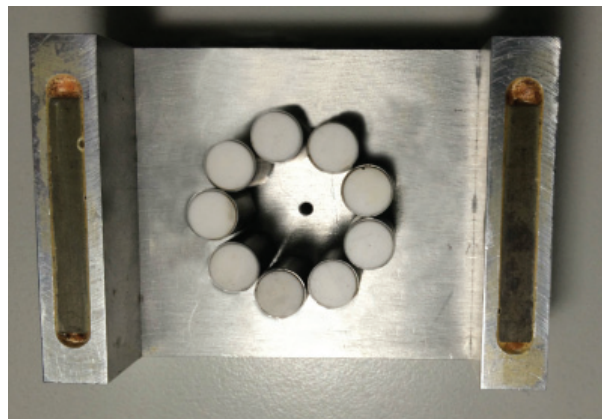


FIGURE 10: The structure of the PD positioning experimental system. (1) AC power regulator; (2) voltage regulator; (3) test transformer; (4) coupling capacitor; (5) impedance measurement; (6) inlet bushing; (7) PD model; (8) oil tank; (9) Partial Discharge Ultrasonic array sensor; (10) transmission lines; (11) data acquisition unit.



(a) The scale model



(b) The physical map

FIGURE 11: A nine-element circular ultrasonic array sensor.

TABLE 2: The positioning results based on sparse representation of the eigenvector.

Group	The position of the PD source/cm	Theoretical angle/(°)	Direction angle/(°)	The result of the three-array cross positioning/cm	The error/cm
1	(45, 0, 20)	(36.9, 32.0)	(36.0, 31.2)	(67.7, 17.4, 62.6)	4.5
	(80, 0, 20)	(135.0, 27.9)	(134.2, 28.9)		
	(0, 30, 40)	(167.0, 73.3)	(168.1, 73.5)		
2	(55, 0, 35)	(56.3, 35.8)	(55.2, 36.6)	(62.5, 12.2, 57.1)	4.7
	(0, 25, 35)	(163.0, 69.8)	(162.1, 69.2)		
	(45, 0, 20)	(36.9, 32.0)	(37.5, 32.9)		
3	(0, 45, 45)	(155.2, 78.2)	(154.0, 79.4)	(62.0, 17.6, 62.2)	4.5
	(70, 0, 45)	(108.3, 46.5)	(107.6, 45.4)		
	(45, 0, 40)	(56.3, 51.4)	(55.6, 52.0)		
4	(55, 0, 45)	(56.3, 50.3)	(55.5, 51.2)	(67.4, 12.5, 62.7)	4.4
	(0, 40, 25)	(158.9, 63.3)	(157.8, 64.0)		
	(45, 0, 20)	(36.9, 32.0)	(37.5, 31.1)		
5	(55, 0, 35)	(56.3, 35.8)	(57.2, 35.0)	(67.8, 17.6, 62.4)	4.5
	(70, 0, 35)	(108.3, 32.3)	(107.4, 31.2)		
	(0, 40, 20)	(158.9, 60.1)	(159.7, 61.2)		

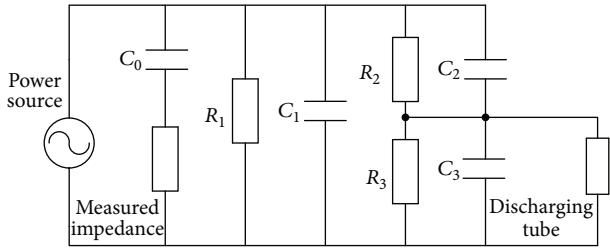


FIGURE 12: The diagram of the three-capacitor discharge principle.

reaches a certain value, the gas is breakdown conduction, and then the discharge effect is produced.

5.2. The Signal Processing. In the process of the experiment, the position of the PD source was preset. And a plurality of preset fixed locations were for the array sensors on the outer wall of the electrical equipment. Then the ultrasonic array sensor was used to collect the PD signal. In order to ensure that the experiment was performed under the same conditions and to facilitate subsequent data processing, the PD source location was fixed during the experiment, only changing the position of ultrasonic array sensor so that the relative space position was changed. The location of the PD source in experiment was (65, 15, 60) cm.

The oscillogram of the PD signal received by the nine-element ultrasonic array sensor is shown in Figure 13.

Three different locations were selected to place ultrasonic array sensors that were used to receive the PD signal, and the ultrasonic signal was used to be focusing and the eigenvector

corresponding to the maximum eigenvalue was acquired by using the eigendecomposition of the covariance matrix with a single frequency. This eigenvector was the amount to be decomposed, and the optimal atom was selected by using MP algorithm; then the DOA estimation can be realized. Besides, the noise interference can be reduced based on sparse representation of the eigenvectors and improve the accuracy of positioning.

Using the methods of direction finding and positioning in the work, the results are shown in Table 2.

The table shows that, in the experimental process, the average error of positioning for the circular ultrasonic array sensor based on sparse representation of the eigenvectors is 4.52 cm, which meets the requirement of practical engineering.

6. Conclusion

The accurate detection of the PD in oil of electrical equipment is the key to the maintenance and repairs of equipment. The positioning method for the PD based on the sparse representation of the eigenvectors is studied in this work. First of all, the mathematical model of a wideband PD signal and the steering vector of a circular ultrasonic array sensor is given. Then the sparse representation theory is applied to the DOA estimation. The principle and process of the sparse presentation of the eigenvectors is introduced in detail, and the three-array cross positioning method is also introduced. Lastly, the simulation study and experimental research are conducted on this method, and the results show that the positioning method in the work can achieve the accurate positioning of the PD source.

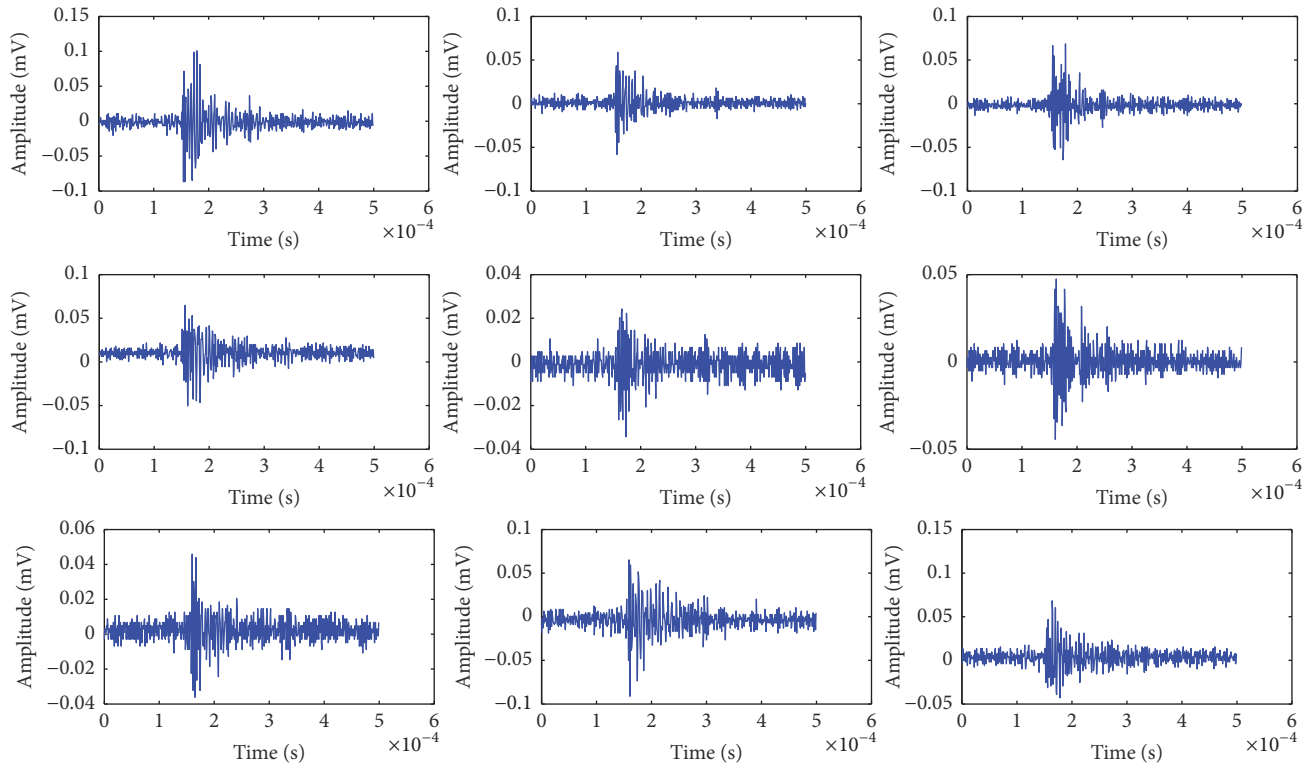


FIGURE 13: Nine channel ultrasonic signal waveforms.

Competing Interests

The authors declare that they have no competing interests.

Acknowledgments

This work was supported by Project Supported by National Natural Science Foundation of China (51307060); Project Supported by Natural Science Foundation of Hebei Province (E2015502081); State Key Laboratory of Alternate Electrical Power System with Renewable Energy Source (LAPS16009).

References

- [1] C. R. Qiu and N. Q. Wang, *Electrician Equipment Local Discharge and Its Test Technology*, Mechanical Industry Publishing House, Beijing, China, 1994.
- [2] Z. Liu, *The Ultra-High Voltage Grid*, China Electric Power Press, Beijing, China, 2005.
- [3] J. Y. Wang, R. J. Liao, Y. Y. Zhang, and F. J. Meng, "Economic life assessment of power transformers using an improved model," *CSEE Journal of Power and Energy Systems*, vol. 1, no. 3, pp. 68–75, 2015.
- [4] W. J. Chen and X. Cui, "Foreword for the special section on AC and DC ultrahigh voltage technologies," *CSEE Journal of Power and Energy Systems*, vol. 1, no. 3, pp. 1–2, 2015.
- [5] Q. Xie, S. Cheng, F. Lü, and Y. Li, "A new sparse design method on phased array-based acoustic emission sensor for partial discharge detection," *Measurement Science & Technology*, vol. 25, no. 3, Article ID 035102, 11 pages, 2014.
- [6] S. Chen, F. Lv, Q. Xie et al., "The transformer partial discharge positioning method based on transient voltage to earth and ultrasonic array signals," *Transactions of China Electrotechnical Society*, vol. 27, no. 4, pp. 255–262, 2012.
- [7] Y. L. Wang, H. Chen, Y. N. Peng et al., *The Spatial Spectrum Estimation Theory and Algorithms*, Tsinghua University Press, 2004.
- [8] E. Skudrzyk, *The Foundations of Acoustics*, Springer, New York, NY, USA, 1971.
- [9] Q. Xie, S. Cheng, F. Lü, and Y. Li, "Location of partial discharge in transformer oil using circular array of ultrasonic sensors," *IEEE Transactions on Dielectrics and Electrical Insulation*, vol. 20, no. 5, pp. 1683–1690, 2013.
- [10] Q. Xie, X. Liu, J. Tao, T. Li, S. Cheng, and F. Lu, "Experimental verification of the sparse design of a square partial discharge acoustic emission array sensor," *Measurement Science & Technology*, vol. 26, no. 4, Article ID 045101, 2015.
- [11] M. R. Rao and B. P. Singh, "Detection and localization of interturn fault in the HV winding of a power transformer using wavelets," *IEEE Transactions on Dielectrics and Electrical Insulation*, vol. 8, no. 4, pp. 652–657, 2001.
- [12] M. Wax, T. J. Shan, and T. Kailath, *Spatio-Temporal Spectral Analysis by Eigenstructure Methods*, Stanford Univ Ca Information Systems Lab, 1984.
- [13] S. Valaee, B. Champagne, and P. Kabal, "Localization of wideband signals using least-squares and total least-squares approaches," *IEEE Transactions on Signal Processing*, vol. 47, no. 5, pp. 1213–1222, 1999.
- [14] S. Valaee and P. Kabal, "Wideband array processing using a two-sided correlation transformation," *IEEE Transactions on Signal Processing*, vol. 43, no. 1, pp. 160–172, 1995.

- [15] S. Valaee and P. Kabal, "The optimal focusing subspace for coherent signal subspace processing," *IEEE Transactions on Signal Processing*, vol. 44, no. 3, pp. 752–756, 1996.
- [16] M. Allam and A. Moghaddamjoo, "Two-dimensional DFT projection for wideband direction-of-arrival estimation," *IEEE Transactions on Signal Processing*, vol. 43, no. 7, pp. 1728–1732, 1995.
- [17] M. A. Doron and A. J. Weiss, "On focusing matrices for wideband array processing," *IEEE Transactions on Signal Processing*, vol. 40, no. 6, pp. 1295–1302, 1992.
- [18] S. G. Mallat and Z. Zhang, "Matching pursuits with time-frequency dictionaries," *IEEE Transactions on Signal Processing*, vol. 41, no. 12, pp. 3397–3415, 1993.
- [19] S. Mallat and Z. Zhang, "Adaptive time-frequency decomposition with matching pursuits," in *Proceedings of the IEEE-SP International Symposium Time-Frequency and Time-Scale Analysis*, pp. 7–10, Victoria, Canada, October 1992.
- [20] H. Hung and M. Kaveh, "Focussing matrices for coherent signal-subspace processing," *IEEE Transactions on Acoustics, Speech, and Signal Processing*, vol. 36, no. 8, pp. 1272–1281, 1988.
- [21] J. A. Cadzow, Y.-S. Kim, and D.-C. Shiue, "General direction-of-arrival estimation: a signal subspace approach," *IEEE Transactions on Aerospace & Electronic Systems*, vol. 25, no. 1, pp. 31–47, 1989.
- [22] Q. Xie, J. Tao, Y. Wang, J. Geng, S. Cheng, and F. Lü, "Use of ultrasonic array method for positioning multiple partial discharge sources in transformer oil," *Review of Scientific Instruments*, vol. 85, no. 8, Article ID 084705, 2014.
- [23] Q. Xie, Y.-Q. Li, F.-C. Lü, C.-R. Li, N. Wang, and Y.-J. Ding, "Method for PD location in oil combining ultrasonic phased array with wideband array signal processing," *Proceedings of the Chinese Society of Electrical Engineering*, vol. 29, no. 28, pp. 13–17, 2009.
- [24] Y. Q. Xu, H. W. Zhang, T. Li, Y. Yang, J. Tao, and Q. Xie, "Application of chaotic monkey algorithm in partial discharge location with ultrasonic array signals," *Insulating Materials*, vol. 47, no. 5, pp. 92–95, 2014.
- [25] T. Wang, G. Cheng, and S. Wan, "Fourier-wavelet regularized deconvolution in medical ultrasound imaging," *Technical Acoustics*, vol. 30, no. 6, pp. 501–504, 2011.
- [26] Z. Tan, D. Feng, G. Chen et al., "Pre-processing in medical ultrasonic lesions images," *Foreign Electronic Measurement Technology*, vol. 33, no. 3, pp. 89–91, 2014.

Research Article

DOA Estimation of Cylindrical Conformal Array Based on Geometric Algebra

Minjie Wu, Xiaofa Zhang, Jingjian Huang, and Naichang Yuan

Department of Electronic Science and Engineering, National University of Defense Technology, Deya Road 109, Changsha 410073, China

Correspondence should be addressed to Minjie Wu; wmj601@nuaa.edu.cn

Received 7 July 2016; Revised 18 October 2016; Accepted 2 November 2016

Academic Editor: Youssef Nasser

Copyright © 2016 Minjie Wu et al. This is an open access article distributed under the Creative Commons Attribution License, which permits unrestricted use, distribution, and reproduction in any medium, provided the original work is properly cited.

Due to the variable curvature of the conformal carrier, the pattern of each element has a different direction. The traditional method of analyzing the conformal array is to use the Euler rotation angle and its matrix representation. However, it is computationally demanding especially for irregular array structures. In this paper, we present a novel algorithm by combining the geometric algebra with Multiple Signal Classification (MUSIC), termed as GA-MUSIC, to solve the direction of arrival (DOA) for cylindrical conformal array. And on this basis, we derive the pattern and array manifold. Compared with the existing algorithms, our proposed one avoids the cumbersome matrix transformations and largely decreases the computational complexity. The simulation results verify the effectiveness of the proposed method.

1. Introduction

A conformal antenna is an antenna that conforms to a prescribed shape. The shape can be some part of an airplane, high-speed missile, or other vehicle [1]. Their benefits include reduction of aerodynamic drag, wide angle coverage, and space-saving [2]. Nevertheless, due to the complex curved surface structure, the pattern of each antenna is inconsistent. Thus, the conformal array can no longer be regarded as a simple isotropic one. The pattern multiplication theorem is not available as well. Most classical DOA estimation algorithms cannot be directly transplanted to such scene.

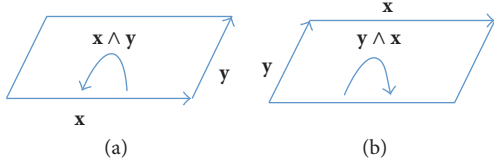
In recent years, there has been a considerable interest in estimating DOAs for conformal array. Milligan used Euler rotation angles to find the patterns with elements in a conformal array that requires one to rotate not only the direction but also the polarization [3]. In [2], Wang et al. proposed a uniform method for the element polarized pattern transformation of arbitrary 3D conformal arrays based on Euler rotation. Yang et al. introduced a conformal array DOA algorithm with an unknown source number; the method was realized by virtue of the pseudo expected signal [4]. However, the root mean square error (RMSE) deteriorated severely

when the number of snapshots was small. Up to the present, we have observed that most of DOA estimation algorithms for conformal array are based on the Euler rotation transformation which converts the local coordinate system to the global coordinate system. Though the Euler rotation angle is a useful tool for spatial rotation transformation [5], a huge amount of computation is incurred.

Geometric algebra is the largest possible associative algebra that integrates all algebraic systems (algebra of complex numbers, matrix algebra, quaternion algebra, etc.) into a coherent mathematical language [6]. Three-dimensional pattern analysis of arbitrary conformal arrays using the mathematical framework of the geometric algebra was introduced [7]. Nevertheless, this mathematical language was not transplanted to the DOA estimation. In [8], Zou et al. took several elements as a new one and transformed the original array into another regular array to estimate the DOA. However, this method was only suitable for some particular array structures. Combining the MUSIC with geometric algebra to solve the DOA estimation has not been addressed in the literature. In this paper, we fill this gap and study the problem based on the cylindrical conformal array. Compared with the existing methods, the proposed one has three main

TABLE 1: Properties of the outer product.

Property	Meaning
Antisymmetry	$(\mathbf{x} \wedge \mathbf{y}) = -(\mathbf{y} \wedge \mathbf{x})$
Scaling	$\mathbf{x} \wedge (\gamma \mathbf{y}) = \gamma(\mathbf{x} \wedge \mathbf{y})$
Distributivity	$\mathbf{x} \wedge (\mathbf{y} + \mathbf{z}) = (\mathbf{x} \wedge \mathbf{y}) + (\mathbf{x} \wedge \mathbf{z})$
Associativity	$\mathbf{x} \wedge (\mathbf{y} \wedge \mathbf{z}) = (\mathbf{x} \wedge \mathbf{y}) \wedge \mathbf{z}$

FIGURE 1: The geometry of outer product (a) $\mathbf{x} \wedge \mathbf{y}$ and (b) $\mathbf{y} \wedge \mathbf{x}$.

advantages. Firstly, it does not need to calculate the rotation matrices and therefore has a much lower computational complexity. Subsequently, it is not limited to the cylindrical conformal array due to its strong commonality. Finally, it can still work effectively even when the number of polarized signals is larger than that of the array elements.

The structure of this paper is as follows. In Section 2, the rotors in geometric algebra which establishes the mathematical knowledge of transformation is briefly introduced. In Section 3, we derive the cylindrical conformal array manifold using rotors and present the GA-MUSIC algorithm. In addition, to better explain the superiority of GA-MUSIC in reducing the computational complexity, we briefly introduce the Euler angle and compare it with the proposed algorithm. Simulations using the proposed method for cylindrical conformal array are given in Section 4. Finally, the conclusions are drawn.

2. Rotors in Geometric Algebra

Geometric algebra was first introduced by the British mathematician, named Clifford, in the nineteenth century. He constructed the geometric product by combining the inner product with the outer product. The main advantage of the geometric algebra is embodied in processing the rotation transformation [9]. Various rotations can be described by an element called the rotor. A rotor is more general than an Euler rotation angle because a rotor can be used in an arbitrary dimensional space.

We begin by introducing a new product between vectors that we call the outer product. Let us use the wedge symbol “ \wedge ” to denote outer product with the properties listed in Table 1.

The outer product is regarded as the “addition operator” of subspaces, in that the outer product $\mathbf{x} \wedge \mathbf{y}$ spans the subspace that \mathbf{x} and \mathbf{y} span together, as long as \mathbf{x} and \mathbf{y} are independent. The geometry is illustrated in Figure 1.

Next, we will introduce the fundamental product of the geometric algebra, namely, geometric product. It is simply the sum of the outer and inner product:

$$\mathbf{xy} = \mathbf{x} \cdot \mathbf{y} + \mathbf{x} \wedge \mathbf{y}. \quad (1)$$

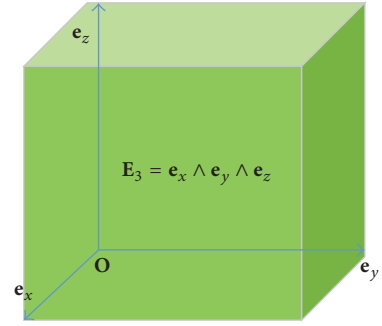


FIGURE 2: The geometry of 3-blade.

Reversing the order of \mathbf{x} and \mathbf{y} in (1), by means of the symmetry of the inner product and the antisymmetry of the outer product, it follows that

$$\mathbf{yx} = \mathbf{x} \cdot \mathbf{y} - \mathbf{x} \wedge \mathbf{y}. \quad (2)$$

Thus, combining (1) with (2), the inner product and the outer product can be uniformly represented by the geometric product:

$$\begin{aligned} \mathbf{x} \cdot \mathbf{y} &= \frac{\mathbf{xy} + \mathbf{yx}}{2} \\ \mathbf{x} \wedge \mathbf{y} &= \frac{\mathbf{xy} - \mathbf{yx}}{2}. \end{aligned} \quad (3)$$

Generally, we call an outer product of k vectors a k -blade. The value of k is called the grade of the blade. Specifically, the top-grade blades \mathbf{E}_n in an n -dimensional space are called pseudoscalars. In principle, blades are just elements of the geometric algebra. To be useful for doing geometry, blades can be interpreted as subspaces. $\mathbf{x} \wedge \mathbf{y}$ is a 2-blade as shown in Figure 1(a). By introducing vector \mathbf{z} , we can construct the 3-blade $\mathbf{x} \wedge \mathbf{y} \wedge \mathbf{z}$, which coincides with the Cartesian coordinate system. As shown in Figure 2, the unit vectors \mathbf{e}_x , \mathbf{e}_y , and \mathbf{e}_z , in that order, form a right-handed Cartesian coordinate system. \mathbf{E}_3 is the pseudoscalar, relative to the origin denoted by \mathbf{O} . The 3-blade is drawn as a parallelepiped. The volume depicts the weight of the 3-blade, but, in principle, blades have no specific shape.

As shown in Figure 3, vector \mathbf{y} is obtained by rotating vector \mathbf{x} with θ . We can regard the rotation as two consecutive reflections, first in \mathbf{a} and then in \mathbf{b} . The expression that reflects \mathbf{x} in the line with direction \mathbf{a} is

$$\mathbf{x}' = \mathbf{axa} = 2(\mathbf{a} \cdot \mathbf{x})\mathbf{a} - \mathbf{x}. \quad (4)$$

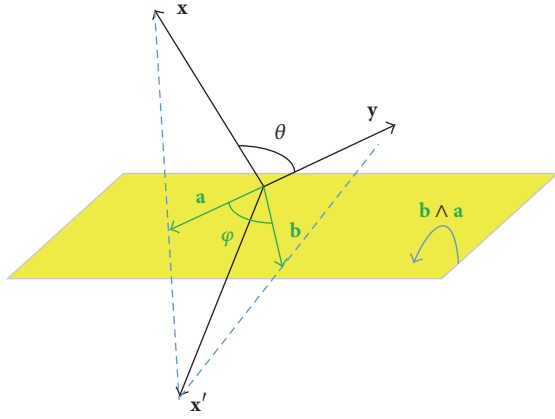
In (4), \mathbf{a} must be unit length. We give the detailed derivation process in Appendix. The regularity condition can be dropped by using an inverse geometric product, as in

$$\mathbf{x}' = \mathbf{axa}^{-1} = 2(\mathbf{a} \cdot \mathbf{x})\mathbf{a}^{-1} - \mathbf{x}, \quad (5)$$

where

$$\mathbf{a}^{-1} = \frac{\mathbf{a}}{\mathbf{a} \cdot \mathbf{a}} \quad (6)$$

with $(\cdot)^{-1}$ representing the inverse operator.

FIGURE 3: Rotation of vector \mathbf{x} .

Then, \mathbf{y} can be obtained by reflecting \mathbf{x}' in the line with direction \mathbf{b} :

$$\mathbf{y} = \mathbf{b}\mathbf{x}'\mathbf{b}^{-1} = \mathbf{b}\mathbf{a}\mathbf{x}\mathbf{a}^{-1}\mathbf{b}^{-1} = (\mathbf{b}\mathbf{a})\mathbf{x}(\mathbf{b}\mathbf{a})^{-1} = \mathbf{R}\mathbf{x}\mathbf{R}^{-1}. \quad (7)$$

Thus, we can identify \mathbf{R} as the rotor. To proceed further, we rewrite \mathbf{R} according to the definition of the geometric product:

$$\mathbf{R} = \mathbf{b}\mathbf{a} = \mathbf{b} \cdot \mathbf{a} + \mathbf{b} \wedge \mathbf{a}. \quad (8)$$

Here, we consider the case that the vectors are unit length. This assumption is reasonable, because the basic vectors of the Cartesian coordinate system satisfy it as well. The geometric product of $\mathbf{b} \wedge \mathbf{a}$ itself is

$$\begin{aligned} (\mathbf{b} \wedge \mathbf{a})(\mathbf{b} \wedge \mathbf{a}) &= (\mathbf{b}\mathbf{a} - \mathbf{b} \cdot \mathbf{a})(\mathbf{b} \cdot \mathbf{a} - \mathbf{a}\mathbf{b}) \\ &= \mathbf{b} \cdot \mathbf{a}(\mathbf{b}\mathbf{a} + \mathbf{a}\mathbf{b}) - (\mathbf{b} \cdot \mathbf{a})^2 - \mathbf{b}\mathbf{a}\mathbf{b} \\ &= \mathbf{b} \cdot \mathbf{a}(2\mathbf{b} \cdot \mathbf{a}) - (\mathbf{b} \cdot \mathbf{a})^2 - \mathbf{b}(\mathbf{a}\mathbf{a})\mathbf{b} \\ &= (\mathbf{b} \cdot \mathbf{a})^2 - \mathbf{b}\mathbf{b} = \cos^2\theta - 1 = -\sin^2\theta. \end{aligned} \quad (9)$$

Thus, we define the 2-blade \mathbf{E}_2 :

$$\mathbf{E}_2 = \frac{\mathbf{b} \wedge \mathbf{a}}{\sin\theta}. \quad (10)$$

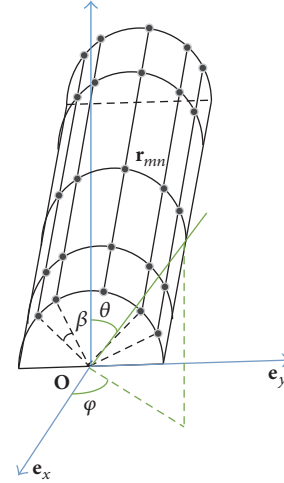
\mathbf{R} can be further simplified by substituting (10) into (8):

$$\mathbf{R} = \cos\theta - \mathbf{E}_2 \sin\theta. \quad (11)$$

The expression is similar to the polar decomposition of a complex number with the unit imaginary replaced by the 2-blade \mathbf{E}_2 . It can also be written as the exponentials of \mathbf{E}_2 :

$$\mathbf{R} = e^{-\mathbf{E}_2\theta}. \quad (12)$$

This formalism is more useful for the log-space of rotors is linear. Up to this point, the angle of rotation in the $\mathbf{b} \wedge \mathbf{a}$ -plane remains to be determined. We split \mathbf{x} into part (\mathbf{x}_p) parallel to $\mathbf{b} \wedge \mathbf{a}$ -plane and part (\mathbf{x}_o) orthogonal to $\mathbf{b} \wedge \mathbf{a}$ -plane. Then, \mathbf{x}_o is not affected by application \mathbf{R} . And we infer that the

FIGURE 4: The cylindrical conformal array consisting of $M \times N$ short dipoles.

rotation must be in $\mathbf{b} \wedge \mathbf{a}$ -plane. As stated above, the rotation consists of two successive reflections which are orthogonal (angle-preserving) transformations. Thus, it allows us to pick any vector in $\mathbf{b} \wedge \mathbf{a}$ -plane to determine the angle. Without loss of generality, we choose vector \mathbf{a} and construct the “sandwich product” $\mathbf{R}\mathbf{a}\mathbf{R}^{-1}$ as shown in (7):

$$\mathbf{R}\mathbf{a}\mathbf{R}^{-1} = \mathbf{b}\mathbf{a}\mathbf{a}^{-1}\mathbf{b}^{-1} = \mathbf{b}\mathbf{a}\mathbf{b}^{-1}, \quad (13)$$

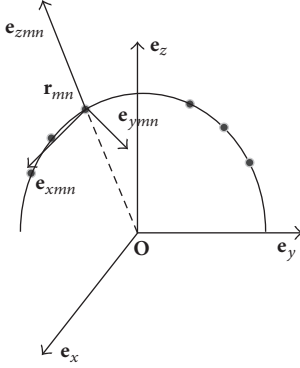
where $\mathbf{b}\mathbf{a}\mathbf{b}^{-1}$ is the reflection of \mathbf{a} in \mathbf{b} . From this, it is clear that the rotation must be over twice the angle between \mathbf{a} and \mathbf{b} , since the angle between \mathbf{a} and $\mathbf{b}\mathbf{a}\mathbf{b}^{-1}$ is twice the angle between \mathbf{a} and \mathbf{b} . The negative signature in (12) represents the rotation direction.

Consequently, if we want to rotate a vector counterclockwise by a specific angle, we only need to apply the rotor to the vector.

3. GA-MUSIC Algorithm

3.1. Array Manifold Modeling Based on GA-MUSIC. In this subsection, we will combine the geometric algebra with MUSIC to estimate the DOA. To illustrate the versatility of this algorithm, we consider $M \times N$ cylindrical conformal array as shown in Figure 4. The array contains N uniformly spaced rings on the surface. In addition, there are M dipoles distributed on each ring. We assume that each dipole is a short dipole whose output voltage is proportional to the electric field along the dipole. The angle between two consecutive elements on the same ring is β .

Assume that there are P far-field narrow band polarization sources. θ_p represents p th signal elevation angle which is measured down from \mathbf{e}_z -axis. φ_p indicates p th signal azimuth angle and is measured counterclockwise from \mathbf{e}_x -axis. The polarization ellipse of p th signal is depicted by constants γ_p and η_p , representing the auxiliary polarization angle and the polarization phase difference [10], respectively.

FIGURE 5: The local coordinate of (m, n) th element.

The array element spatial phase matrix of the p th signal can be described as follows:

$$\mathbf{Y}_p = \mathbf{Y}_{\theta_p, \phi_p} = \begin{bmatrix} u_{p,1} & & \\ & \ddots & \\ & & u_{p,P} \end{bmatrix}, \quad (14)$$

where \mathbf{Y}_p is the diagonal matrix depicting the output signal spatial coherent structures. k th diagonal element, $u_{p,k} = e^{-j2\pi(\boldsymbol{\epsilon}_s^T(\theta_p, \phi_p)\mathbf{r}_k)/\lambda_p}$, represents the space phase factor about p th array element. Among which, $\boldsymbol{\epsilon}_s(\theta_p, \phi_p) = -[\sin\theta_p \cos\phi_p, \sin\theta_p \sin\phi_p, \cos\theta_p]^T$ and λ_p are p th signal propagation vector and the wavelength, respectively. Symbol \mathbf{r}_k is the element location vector and $(\cdot)^T$ denotes the transpose operator.

It is worthwhile to note that the aforementioned element spatial phase matrix, \mathbf{Y}_p , is derived under the global coordinate system. The azimuth and elevation are defined in Figure 4 as well. However, due to the effects of the curvature of conformal carriers, the local coordinate system is distinct from the global one. As stated above, the rotor can be used to realize the rotation between the two coordinate systems. Thus, we define the local coordinate system of (m, n) th element as shown in Figure 5.

\mathbf{e}_{xmm} -axis is the same as \mathbf{e}_x -axis in the global coordinate system, \mathbf{e}_{zmm} is normal to the element surface, and \mathbf{e}_{yym} is tangent to the surface so as to form a right-handed coordinate system. Naturally, transforming the global coordinate into the local one is equivalent to rotating the global coordinate around \mathbf{e}_x -axis. From the last section, we have known that (12) denotes the rotation in $\mathbf{b} \wedge \mathbf{a}$ -plane with twice the value of θ . The rotation angle is

$$\xi = (m-1)\beta - \frac{M-1}{2}\beta = \left(m - \frac{M+1}{2}\right)\beta. \quad (15)$$

Substituting \mathbf{e}_z and \mathbf{e}_y for \mathbf{b} and \mathbf{a} , respectively, then the rotor is

$$\mathbf{R}_{mn} = e^{-(\mathbf{e}_z \wedge \mathbf{e}_y)(\xi/2)}. \quad (16)$$

In addition, \mathbf{e}_x , \mathbf{e}_y , and \mathbf{e}_z are orthogonal to each other and the inner products between them are zero. So,

$$\mathbf{e}_z \wedge \mathbf{e}_y = \mathbf{e}_z \mathbf{e}_y. \quad (17)$$

According to the antisymmetry property of the outer product,

$$\mathbf{e}_z \mathbf{e}_y = \mathbf{e}_z \wedge \mathbf{e}_y = -\mathbf{e}_y \wedge \mathbf{e}_z = -\mathbf{e}_y \mathbf{e}_z. \quad (18)$$

Adopting $\mathbf{E}_3 = \mathbf{e}_x \mathbf{e}_y \mathbf{e}_z$ as the pseudoscalar in the three-dimensional space, (16) can be further simplified:

$$\mathbf{R}_{mn} = e^{\mathbf{E}_3 \mathbf{e}_x (\xi/2)}. \quad (19)$$

Through (7), we obtain the standard orthogonal basis in the local coordinate, and the specific calculation process can refer to [11]. Here, the results are given directly:

$$\mathbf{e}_{xmm} = \mathbf{R}_{mn} \mathbf{e}_x \mathbf{R}_{mn}^{-1} = \mathbf{e}_x \quad (20)$$

$$\begin{aligned} \mathbf{e}_{yym} &= \mathbf{R}_{mn} \mathbf{e}_y \mathbf{R}_{mn}^{-1} \\ &= \cos \left[\left(m - \frac{M+1}{2} \right) \beta \right] \mathbf{e}_y \\ &\quad - \sin \left[\left(m - \frac{M+1}{2} \right) \beta \right] \mathbf{e}_z \end{aligned} \quad (21)$$

$$\begin{aligned} \mathbf{e}_{zmm} &= \mathbf{R}_{mn} \mathbf{e}_z \mathbf{R}_{mn}^{-1} \\ &= \sin \left[\left(m - \frac{M+1}{2} \right) \beta \right] \mathbf{e}_y \\ &\quad + \cos \left[\left(m - \frac{M+1}{2} \right) \beta \right] \mathbf{e}_z. \end{aligned} \quad (22)$$

Referring back to (14), the remaining unknown variable is \mathbf{r}_k . The position vector of (m, n) th element in the global frame is

$$\begin{aligned} \mathbf{r}_{mn} &= (-n\delta) \mathbf{e}_x + \left(R \sin \left(m - \frac{M+1}{2} \right) \beta \right) \mathbf{e}_y \\ &\quad + \left(R \cos \left(m - \frac{M+1}{2} \right) \beta \right) \mathbf{e}_z \end{aligned} \quad (23)$$

$m = 1, \dots, M; n = 1, \dots, N,$

where δ means the spacing between adjacent rings. Thus, \mathbf{Y}_p can be obtained. If g is the gain when the signal perfectly matched the antenna polarization, then the element of generalized polarization sensitive matrix \mathbf{Q} can be represented as

$$q = g \left[\cos(\varphi') \sin(\theta') \quad \sin(\varphi') \sin(\theta') \quad \cos(\theta') \right]^T, \quad (24)$$

where θ' and φ' indicate the elevation and azimuth pointing directions of the short dipole.

According to this, we can get the array manifold:

$$\mathbf{a}_p = \mathbf{a}_{\theta_p, \phi_p, \gamma_p, \eta_p} = \mathbf{Y}_p \mathbf{Q} \Psi_p \mathbf{h}_p, \quad (25)$$

where \mathbf{h}_p is p th signal polarization vector [12] and can be described by γ_p and η_p , that is, $\mathbf{h}_p = [\cos\gamma_p \quad \sin\gamma_p e^{j\eta_p}]^T \cdot \Psi_p$

is the steering vector of the angle field [13] and is independent of the space location:

$$\Psi_p = \begin{bmatrix} -\sin \varphi_p & \cos \theta_p \cos \varphi_p \\ \cos \varphi_p & \cos \theta_p \sin \varphi_p \\ 0 & -\sin \theta_p \end{bmatrix}. \quad (26)$$

The received signals of the array are a superposition of the response of each signal, and the output can be expressed as

$$\mathbf{x}(t) = \sum_{p=1}^P \mathbf{a}_p s_p(t) + \mathbf{n}(t), \quad (27)$$

where $s_p(t)$ is p th signal and $\mathbf{n}(t)$ is assumed to be zero mean, complex Gaussian processes statistically independent of each other, with covariance σ_n^2 .

Up to the present, we have perfectly applied the geometric algebra to the derivation of the steering vector of the conformal array and acquired the GA-MUSIC algorithm. This is also the focus of our work. As for the content of constructing the spatial spectrum and searching the peak, the readers can refer to literature [14]. As the spatial location of the short dipole is arbitrary when introducing the ‘‘rotors,’’ the GA-MUSIC is not limited to any specific array geometry.

3.2. Comparing with the Conventional Modeling Using Euler Angle. For better understanding of the superiority of the geometric algebra in modeling the conformal array, we will briefly introduce the conventional methods of analysis based on Euler angle. In general, the transformations from the element local coordinates to the array global coordinates can be realized by three successive Euler rotations [2]. The corresponding rotation matrix can be written as

$$\begin{aligned} \mathbf{R}(C, D, F) &= \mathbf{R}_x(C) \mathbf{R}_y(D) \mathbf{R}_z(F) = \begin{bmatrix} 1 & 0 & 0 \\ 0 & \cos C & -\sin C \\ 0 & \sin C & \cos C \end{bmatrix} \begin{bmatrix} \cos D & 0 & -\sin D \\ 0 & 1 & 0 \\ \sin D & 0 & \cos D \end{bmatrix} \begin{bmatrix} \cos F & -\sin F & 0 \\ \sin F & \cos F & 0 \\ 0 & 0 & 1 \end{bmatrix} \\ &= \begin{bmatrix} \cos D \cos F & -\cos D \sin F & -\sin D \\ \cos C \sin F - \cos F \sin C \sin D & \cos C \cos F + \sin C \sin D \sin F & -\cos D \sin C \\ \sin C \sin F + \cos C \cos F \sin D & \cos F \sin C - \cos C \sin D \sin F & \cos C \cos D \end{bmatrix}, \end{aligned} \quad (28)$$

where C, D, F are three successive Euler rotation angles about \mathbf{e}_x -axis, \mathbf{e}_y -axis, and \mathbf{e}_z -axis, respectively. $\mathbf{R}_x(C)$, $\mathbf{R}_y(D)$, and $\mathbf{R}_z(F)$ are the corresponding Euler rotation matrices. Note that, for cylindrical conformal array, two successive Euler rotations are usually sufficient [2]. The third Euler rotation

matrix is added here to account for some irregular or complex conformal arrays. Moreover, as shown in (28), the rotation matrix is invertible. Thus, the inversion is taken with respect to $\mathbf{R}(C, D, F)$, resulting in

$$\begin{aligned} \mathbf{R}(C, D, F)^{-1} &= \mathbf{R}_z^{-1}(F) \mathbf{R}_y^{-1}(D) \mathbf{R}_x^{-1}(C) = \begin{bmatrix} \cos F & \sin F & 0 \\ -\sin F & \cos F & 0 \\ 0 & 0 & 1 \end{bmatrix} \begin{bmatrix} \cos D & 0 & \sin D \\ 0 & 1 & 0 \\ -\sin D & 0 & \cos D \end{bmatrix} \begin{bmatrix} 1 & 0 & 0 \\ 0 & \cos C & \sin C \\ 0 & -\sin C & \cos C \end{bmatrix} \\ &= \begin{bmatrix} \cos D \cos F & \cos C \sin F - \cos F \sin C \sin D & \sin C \sin F + \cos C \cos F \sin D \\ -\cos D \sin F & \cos C \cos F + \sin C \sin D \sin F & \cos F \sin C - \cos C \sin D \sin F \\ -\sin D & -\cos D \sin C & \cos C \cos D \end{bmatrix}. \end{aligned} \quad (29)$$

From (28) and (29), it is not hard to find that

$$\mathbf{R}(C, D, F)^{-1} = \mathbf{R}(C, D, F)^T. \quad (30)$$

So, $\mathbf{R}(C, D, F)$ is the orthogonal matrix. Then, taking the transformation from the element local coordinates to the array global coordinates is equivalent to taking the transposition/inversion with respect to the aforementioned rotation matrix. If we model the conformal array adopting the Euler angle, three matrix multiplications and one matrix transposition are involved for each element.

In practical applications, the matrix operations are essentially the multiplication and addition operations between elements. To quantify what we mean by this, the amounts of multiplication and addition operations of the two algorithms (i.e., GA-MUSIC and Euler angle) are computed, respectively, as shown in Table 2. Suppose that one matrix transposition is regarded as one multiplication or addition operation. As is known to all, the multiplication between two 3×3 matrices requires 9×3 multiplications and 9×2 additions. For convenience, the multiplication operation and the addition operation are collectively referred to as the operation. Then,

TABLE 2: The computational complexity of GA-MUSIC and Euler angle.

	Multiplications	Additions	Transpositions	Operations
Euler angle	$2 \times 9 \times 3 \times MN$	$2 \times 9 \times 2 \times MN$	MN	$91 \times MN$
GA-MUSIC	$4 \times MN$	$2 \times MN$	0	$6 \times MN$

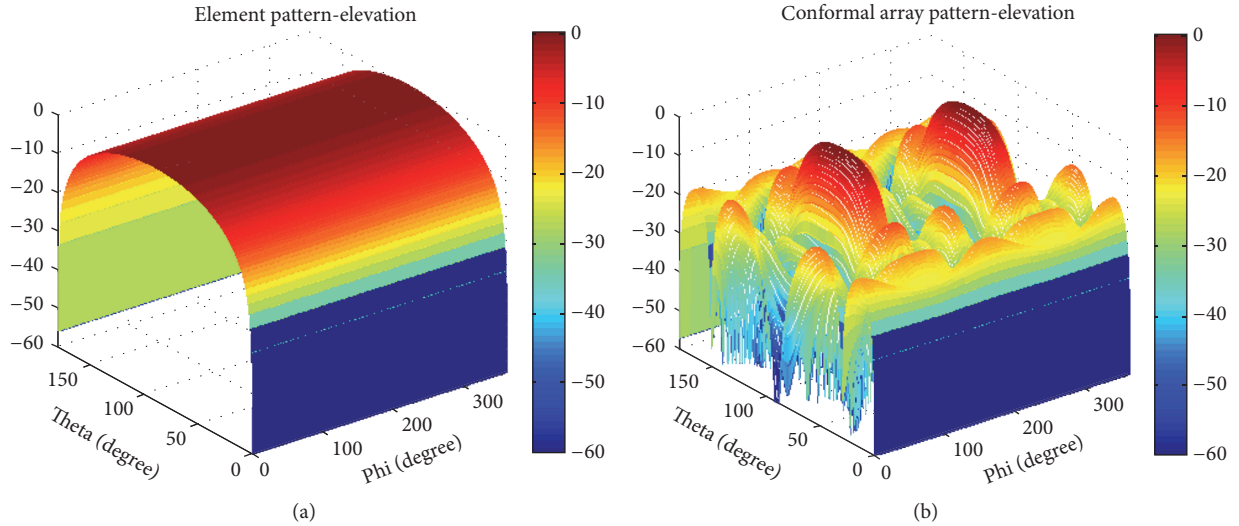


FIGURE 6: Pattern analysis: (a) pattern of single short dipole and (b) pattern of cylindrical conformal array.

the calculation of (28) contains $2 \times 9 \times 3 + 2 \times 9 \times 2$ operations. For the conformal array consisting of $M \times N$ elements, the transformation between different coordinates involves $91 \times MN$ operations. In contrast to the Euler angle, GA-MUSIC avoids the cumbersome matrix transformations.

From (20)–(22), we know that \mathbf{e}_{ymn} and \mathbf{e}_{zmn} are independent of \mathbf{e}_x . Moreover, \mathbf{e}_{xmn} can be obtained directly from (20) without extra computations. Thus, (21)–(22) can be rewritten in 2×2 matrix. While applying the rotor to construct the array manifold, the computational process is equivalent to 2×2 matrix multiplied by 2×1 vector. Then, the operations for each element involve 4 multiplications and 2 additions. The total amount of operations is $6 \times MN$. Thus, the latter method largely decreases the computational complexity.

To sum up, the Euler rotation and its matrix representation cannot intuitively display the whole procedure. Moreover, as the configuration of the conformal array becomes more irregular and complex, the level of complexity involved in the transformations and the number of calculations required increase significantly.

4. Simulation Results

In this section, Monte-Carlo simulation experiments are employed to verify the effectiveness of the GA-MUSIC algorithm. The array structure is shown in Figure 4. We select M and N as 4 and 2, respectively, for the validations. The pattern of single short dipole is shown in Figure 6(a), while the cylindrical conformal array pattern is displayed in Figure 6(b). Compared with the existing methods, adopting

the geometric algebra will be more simple and intuitive. For the solved array pattern or manifold is the superposition of various elements, the proposed method can be applied to arbitrary array structures. This also proves the superiority of the rotor in solving conformal problems.

Next, the performance of the GA-MUSIC algorithm is to be verified. We make some notations. Firstly, the absolute value of the differences between the estimated mean and the true value is regarded as the deviation. Secondly, the RMSE is utilized as the performance measure. Under these premises, 100 independent simulation experiments are carried out. The RMSE is defined as

$$\text{RMSE} = \sqrt{\frac{1}{100} \sum_{i=1}^{100} [(\hat{\theta}_i - \theta_i)^2 + (\hat{\varphi}_i - \varphi_i)^2]}, \quad (31)$$

where $\{\hat{\theta}_i, \hat{\varphi}_i\}$ are the estimates of elevation angles and azimuth angles, respectively, at i th run. Wang's method [2] and Qun's method [4] are included for comparison.

Provided that there are three signals that can be received, the incident angles are $(15^\circ, 40^\circ)$, $(35^\circ, 10^\circ)$, and $(60^\circ, 65^\circ)$, respectively. The corresponding polarization auxiliary angle and the polarization phase difference are $(20^\circ, 25^\circ)$, $(50^\circ, 45^\circ)$, and $(65^\circ, 65^\circ)$. The snapshot, K , is selected as 100. Figure 7(a) shows the simulation results of the GA-MUSIC algorithm. The position of the spectrum peak represents the corresponding signal DOA. Intuitively, the estimation accuracy of the GA-MUSIC algorithm is high.

We assume that there are nine distinct signals impinging on the cylindrical conformal array at the same time. The

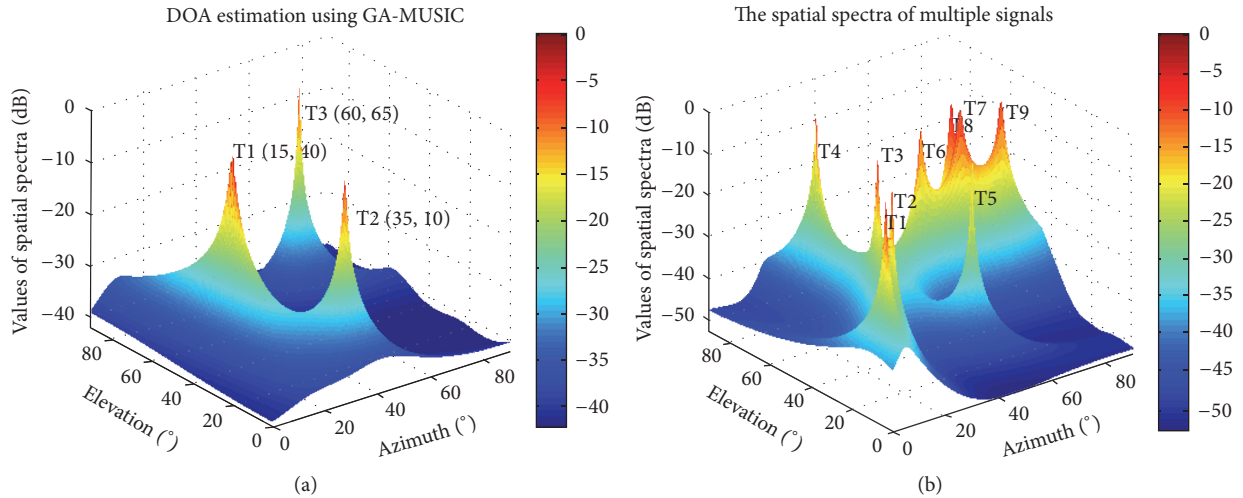


FIGURE 7: The performance of GA-MUSIC algorithm: (a) DOA estimation using GA-MUSIC and (b) the spatial spectra of multiple signals.

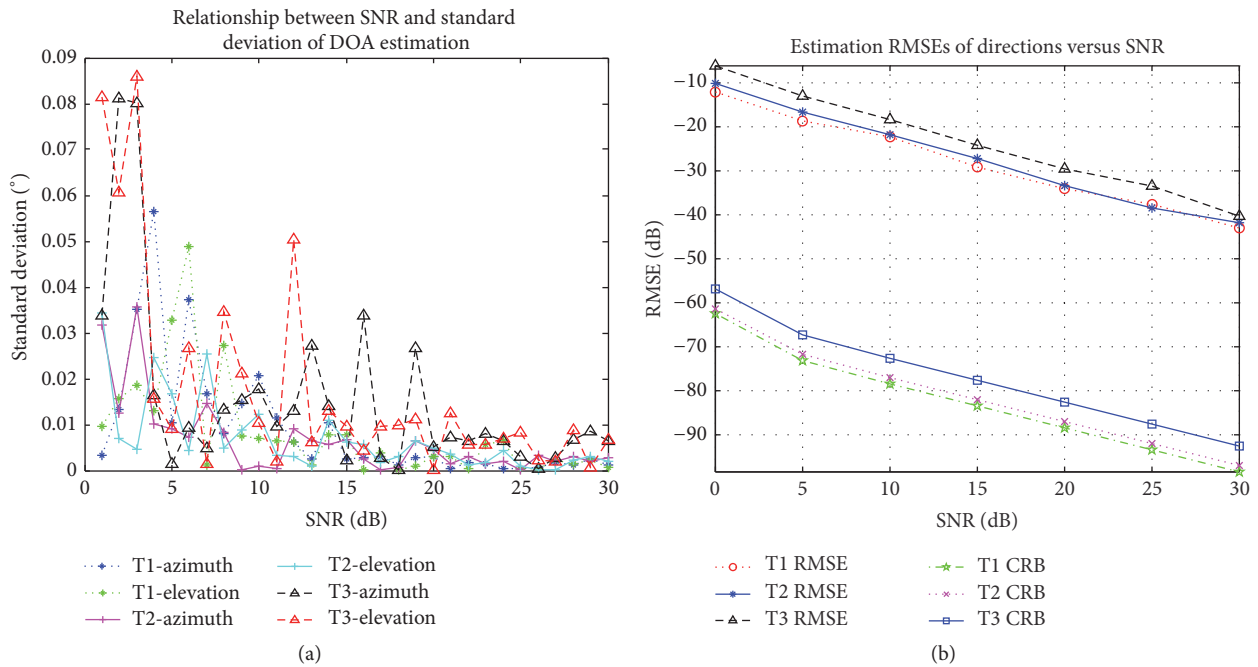


FIGURE 8: The DOA estimation accuracy with $K = 100$: (a) deviation of estimates versus SNR and (b) the RMSE and CRB versus SNR.

spatial spectra are shown in Figure 7(b). It is obvious that the method still works effectively when the number of incident signals is larger than that of the array elements.

Figure 8 displays the performance with a varying SNR from 0 dB to 30 dB. Among them, Figure 8(a) displays the relationship between SNR and deviation of DOA estimation, while Figure 8(b) reveals the Cramer-Rao Lower Bound (CRLB) and the RMSE versus the SNR, respectively. It is clear that the deviation varies inversely with SNR. The higher the SNR, the lower the deviation. The trend of the variance of the CRLB with SNRs is the same as the RMSE, which is expected. Obviously, in the engineering design, the higher the SNR, the better the estimation performance that we can obtain.

Note that, since statistical data have some randomness, the simulation curves in Figure 8(a) are not smooth and do not decline monotonically.

To proceed further, we increase the number of snapshots to 200 and leave the other conditions unchanged. The respective results are shown in Figure 9. Compared with Figure 8, both the deviation and CRB were improved. If we choose the point at some SNR, we can find that the CRB of Figure 8 is nearly twice as much as of Figure 9. For example, the CRB of Target 1 is -82.58 dB when the SNR is 20 dB as shown in Figure 8(b), while, in Figure 9(b), the value is -86.08 dB. In fact, these improvements can be predicted from the derivation of CRLB. For details on the specific

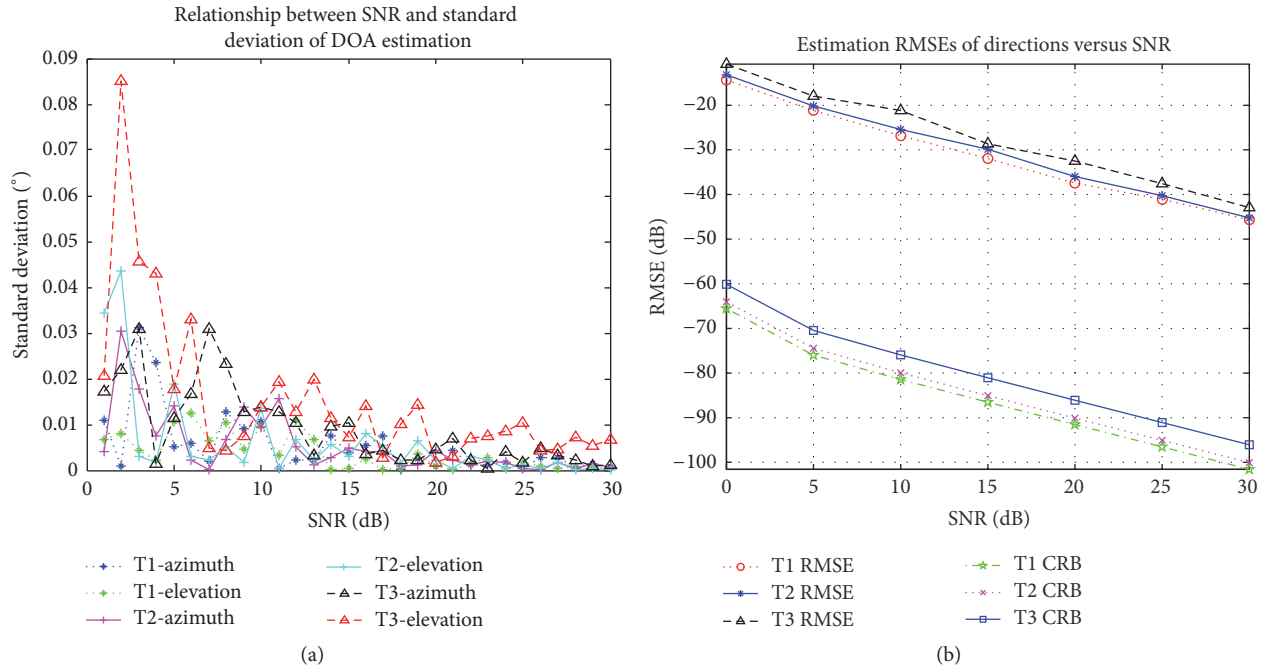


FIGURE 9: The DOA estimation accuracy with $K = 200$: (a) deviation of estimates versus SNR and (b) the RMSE and CRB versus SNR.

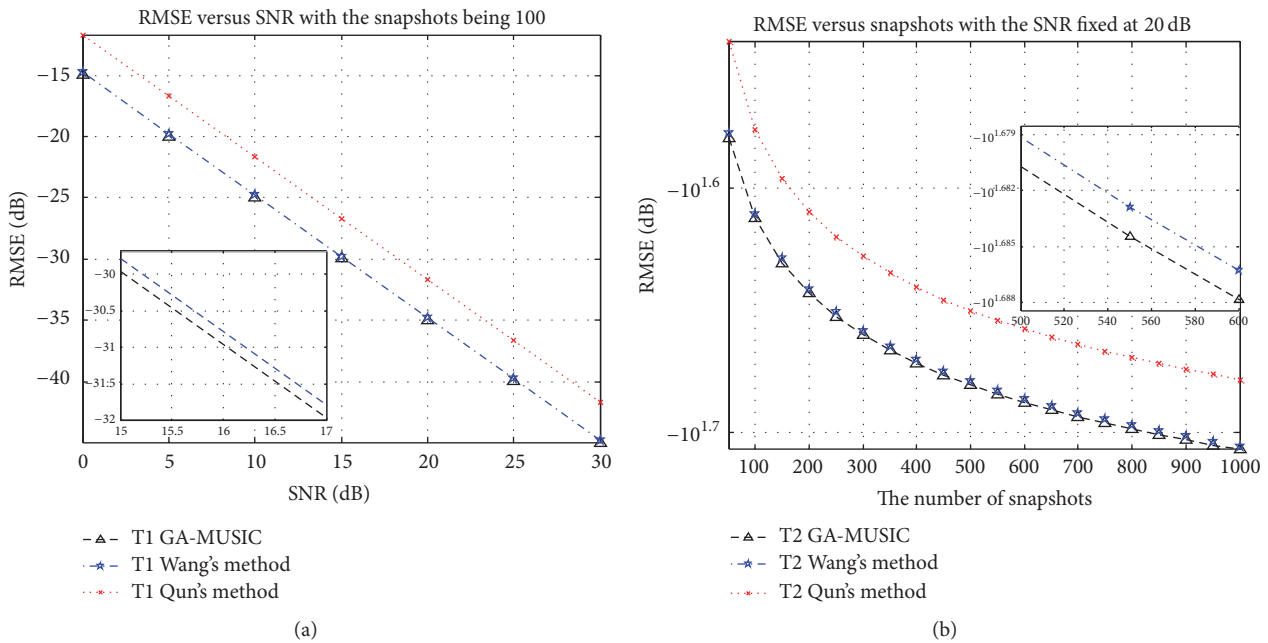


FIGURE 10: Improvements of GA-MUSIC: (a) RMSE versus SNR with the snapshots being 100 and (b) RMSE versus the snapshots with the SNR fixed at 20 dB.

derivation process, see the work of Stoica and Nehorai [15, 16]. The number of snapshots can be extracted from the Fisher information matrix. Moreover, the CRLB is found as the element of the inverse of that matrix. So, we can conclude that CRLB is inversely proportional to K . Thus, the estimation precision will be higher.

Figure 10 shows the improvements of GA-MUSIC over existing algorithms, such as Qun's method [4] and Wang's

method [2]. We study the performance with a varying SNR from 0 dB to 30 dB and the performance with the number of snapshots varying from 100 to 1000, respectively. Without loss of generality, we select the first source (T1) and the second source (T2), respectively, to verify it. As shown in Figure 10(a), the proposed method outperforms Qun's method by exploiting the polarization information of the received data. Moreover, the elliptic covariance matrix of

the GA-MUSIC is nonzero which increases the information utilization rates as well.

The RMSE of the GA-MUSIC is close to that of the Wang's method. The reason is that the estimation accuracy mainly depends on the steering vector. Both the Euler rotation angle and the geometric algebra can be used to derive the steering vector. As previously mentioned, the array manifold was obtained by using the rotor in this paper. However, in [2], Wang derived the array manifold by means of the Euler rotation angle. Therefore, in this case, both methods exhibit the same performance. From Section 3.2, we clearly know the GA-MUSIC is superior to the Euler rotation angle in computational complexity.

Figure 10(b) illustrates the RMSE versus the number of snapshots with the SNR fixed at 20 dB. Compared with Figure 10(a), we can draw similar conclusions.

5. Conclusion

In this paper, we proposed a novel algorithm named GA-MUSIC to estimate the DOA for cylindrical conformal array, which combines the geometric algebra with MUSIC. Compared with existing methods based on Euler rotation angle, it avoids complex matrix transformations and largely decreases the computational complexity. In contrast to the method introduced in the literature [8], our presented method has a strong commonality which can be used for arbitrary array structure. In addition, it can also be suited for the case that the number of polarized signals is larger than that of the array elements. At last, the simulated results verify the effectiveness of the GA-MUSIC algorithm.

Appendix

Here, we derive the calculation process of (4).

From (1)–(3), we get

$$\begin{aligned} \mathbf{xyx} &= (\mathbf{x} \cdot \mathbf{y} + \mathbf{x} \wedge \mathbf{y}) \mathbf{x} = (\mathbf{x} \cdot \mathbf{y}) \mathbf{x} + (\mathbf{x} \wedge \mathbf{y}) \mathbf{x} \\ &= (\mathbf{x} \cdot \mathbf{y}) \mathbf{x} + \frac{\mathbf{xy} - \mathbf{yx}}{2} \mathbf{x} = (\mathbf{x} \cdot \mathbf{y}) \mathbf{x} + \frac{\mathbf{xy}}{2} \mathbf{x} - \frac{\mathbf{yx}}{2} \mathbf{x} \quad (\text{A.1}) \\ &= (\mathbf{x} \cdot \mathbf{y}) \mathbf{x} + \frac{\mathbf{xy}}{2} \mathbf{x} - \frac{\mathbf{y}}{2}. \end{aligned}$$

Thus,

$$\frac{\mathbf{xyx}}{2} = (\mathbf{x} \cdot \mathbf{y}) \mathbf{x} - \frac{\mathbf{y}}{2}. \quad (\text{A.2})$$

Up to the present, (4) has been obtained.

Competing Interests

The authors declare that they have no competing interests.

Acknowledgments

This project was supported by the National Natural Science Foundation of China (Grant no. 61302017).

References

- [1] L. Josefsson and P. Persson, *Conformal Array Antenna Theory and Design*, IEEE Press Series on Electromagnetic Wave Theory, 2006.
- [2] B.-H. Wang, Y. Guo, Y.-L. Wang, and Y.-Z. Lin, "Frequency-invariant pattern synthesis of conformal array antenna with low cross-polarisation," *IET Microwaves, Antennas and Propagation*, vol. 2, no. 5, pp. 442–450, 2008.
- [3] T. Milligan, "More applications of euler rotation angles," *IEEE Antennas and Propagation Magazine*, vol. 41, no. 4, pp. 78–83, 1999.
- [4] Q. Yang, X.-Y. Cao, J. Gao, and W.-Q. Li, "An algorithm of conformal array DOA estimation with unknown source number," in *Proceedings of the 3rd Asia-Pacific Conference on Antennas and Propagation (APCAP '14)*, pp. 502–505, Harbin, China, July 2014.
- [5] H. A. Burger, "Use of euler-rotation angles for generating antenna patterns," *IEEE Antennas and Propagation Magazine*, vol. 37, no. 2, pp. 56–63, 1995.
- [6] V. de Sabbata and B. K. Datta, *Geometric Algebra and Applications to Physics*, CRC Press, Boca Raton, Fla, USA, 2007.
- [7] L. Zou, J. Lasenby, and Z. He, "Pattern analysis of conformal array based on geometric algebra," *IET Microwaves, Antennas & Propagation*, vol. 5, no. 10, pp. 1210–1218, 2011.
- [8] L. Zou, J. Lasenby, and Z. He, "Direction and polarisation estimation using polarised cylindrical conformal arrays," *IET Signal Processing*, vol. 6, no. 5, pp. 395–403, 2012.
- [9] L. Dorst, D. Fontijne, and S. Mann, *Geometric Algebra for Computer Science*, Morgan Kaufmann, Boston, Mass, USA, 2007.
- [10] J. Li and R. T. Compton Jr., "Angle estimation using a polarization sensitive array," *IEEE Transactions on Antennas and Propagation*, vol. 39, no. 10, pp. 1539–1543, 1991.
- [11] D. Hildenbrand, *Foundations of Geometric Algebra Computing*, Springer, Berlin, Germany, 2013.
- [12] G. A. Deschamps, "Techniques for handling elliptically polarized waves with special reference to antennas: part II-geometrical representation of the polarization of a plane electromagnetic wave," *Proceedings of the IRE*, vol. 39, no. 5, pp. 540–544, 1951.
- [13] A. Nehorai and E. Paldi, "Vector-sensor array processing for electromagnetic source localization," *IEEE Transactions on Signal Processing*, vol. 42, no. 2, pp. 376–398, 1994.
- [14] R. Schmidt, "Multiple emitter location and signal parameter estimation," *IEEE Transactions on Antennas and Propagation*, vol. 34, no. 3, pp. 276–280, 1986.
- [15] P. Stoica and A. Nehorai, "MUSIC, maximum likelihood, and cramer-rao bound," *IEEE Transactions on Acoustics, Speech, and Signal Processing*, vol. 37, no. 5, pp. 720–741, 1989.
- [16] P. Stoica and A. Nehorai, "MUSIC, maximum likelihood, and Cramer-Rao bound: further results and comparisons," *IEEE Transactions on Acoustics, Speech, and Signal Processing*, vol. 38, no. 12, pp. 2140–2150, 1990.

Research Article

Efficient AM Algorithms for Stochastic ML Estimation of DOA

Haihua Chen,¹ Shibao Li,¹ Jianhang Liu,¹ Yiqing Zhou,² and Masakiyo Suzuki³

¹College of Computer and Communication Engineering, China University of Petroleum, Qingdao, Shandong 266580, China

²Beijing Key Lab. of Mobile Computing and Pervasive Devices Wireless Research Center, Institute of Computing Technology, Chinese Academy of Sciences, Beijing, China

³Graduate School of Engineering, Kitami Institute of Technology, 165 Koencho, Kitami, Hokkaido 090-8507, Japan

Correspondence should be addressed to Haihua Chen; chenhaihua@upc.edu.cn

Received 19 April 2016; Revised 17 September 2016; Accepted 11 October 2016

Academic Editor: Elias Aboutanios

Copyright © 2016 Haihua Chen et al. This is an open access article distributed under the Creative Commons Attribution License, which permits unrestricted use, distribution, and reproduction in any medium, provided the original work is properly cited.

The estimation of direction-of-arrival (DOA) of signals is a basic and important problem in sensor array signal processing. To solve this problem, many algorithms have been proposed, among which the Stochastic Maximum Likelihood (SML) is one of the most concerned algorithms because of its high accuracy of DOA. However, the estimation of SML generally involves the multidimensional nonlinear optimization problem. As a result, its computational complexity is rather high. This paper addresses the issue of reducing computational complexity of SML estimation of DOA based on the Alternating Minimization (AM) algorithm. We have the following two contributions. First using transformation of matrix and properties of spatial projection, we propose an efficient AM (EAM) algorithm by dividing the SML criterion into two components. One depends on a single variable parameter while the other does not. Second when the array is a uniform linear array, we get the irreducible form of the EAM criterion (IAM) using polynomial forms. Simulation results show that both EAM and IAM can reduce the computational complexity of SML estimation greatly, while IAM is the best. Another advantage of IAM is that this algorithm can avoid the numerical instability problem which may happen in AM and EAM algorithms when more than one parameter converges to an identical value.

1. Introduction

The localization of multiple signal sources by a passive sensor array is of great importance in a wide variety of fields, such as radar, geophysics, radio-astronomy, biomedical engineering, communications, and underwater acoustics. The basic problem in this context is to estimate direction-of-arrival (DOA) of narrow-band signal sources located in the far field of the array.

A number of super-resolution techniques have been introduced, such as the Maximum Likelihood (ML) method [1–7], MUSIC [8, 9], ESPRIT [10], Weighted Subspace Fitting (WSF) [11], and the Bayesian method [12].

Among these techniques, the ML technique is well known for its high accuracy of DOA. There are two famous ML criterions, that is, Deterministic or Conditional Maximum Likelihood (DML) [1, 3–5, 7] and Stochastic or Unconditional ML (SML) [2, 5–7]. The difference between them lies in their signal models. In particular, the SML shows much higher

resolution than other techniques. Furthermore, the SML technique can solve coherent signals without any preprocessing, such as the spatial smoothing [9]. However, the SML technique does not become popular in practice because the estimation of SML generally involves the multidimensional nonlinear optimization problem, and it requires high computational complexity.

To solve the multidimensional nonlinear optimization problem, the Alternating Minimization (AM) algorithm is one of the most classic techniques. It is an iterative technique and usually needs one-dimensional global search in the updating process. There are also some other efficient techniques, such as Alternating Projection (AP) [3], Expectation Maximization (EM) [13], Space Alternating Generalized EM (SAGE) [14], genetic algorithm [15], ant colony algorithm [16], and Particle Swarm Optimization (PSO) [17, 18]. Generally, they are all iterative techniques and usually are formulated for explicit criterions (e.g., these algorithms formulated for the criterions of DML and WSF). As for the SML

criterion, the AM algorithm is still the most commonly used algorithm although its computational complexity is a little high [6].

Therefore, this paper addresses the issue of reducing computational complexity of SML estimation of DOA based on the conventional AM algorithm.

Firstly we show a brief description of SML estimation of DOA and the conventional solving method, AM algorithm. Then using transformation of matrix and properties of spatial projection, we propose an efficient AM (EAM) algorithm by dividing the AM criterion of SML into two components. One depends on a single variable parameter while the other does not. The computational complexity of EAM can be greatly reduced compared to AM algorithm. However, numerical instability may happen in calculation of EAM criterion when more than one parameter converges to an identical value. As a result, oscillation may happen in the convergence phase and extra calculation is needed. To solve this problem and reduce computational complexity further, based on the EAM criterion we get the irreducible form of the EAM criterion (IAM) using a uniform linear array. In this way, the EAM criterion can be written into polynomial forms. The common zeros can be easily canceled in numerator and denominator of the EAM criterion. Furthermore, the computational complexity is also reduced. Finally, simulation results are also shown to demonstrate the validity of the proposed EAM and IAM algorithms.

The rest of this paper is organized as follows. In Section 2 we introduce the problem formulation of DOA. A brief introduction of exact definition of SML estimation for incoherent signals is shown in Section 3. In Section 4, we introduce the conventional AM algorithm and our proposed two efficient algorithms, that is, EAM and IAM algorithms. Simulation results are shown in Section 5 and conclusion is drawn in Section 6.

2. Problem Formulation

Without loss of generality, consider that there are p sensors and q narrow-band sources far from the array, centered around a known frequency, impinging on the sensor array from distinct directions $\theta_1, \theta_2, \dots, \theta_q$, with respect to a reference point, respectively.

Note that the received signals may be coherent because of multipath propagation. In the case where there are signals coherent, the independent signal number is less than q . The task of DOA estimation is to detect all q directions. Also note that here we assume that the signals are narrow-band. For wideband signals, the CSM algorithms [19] can be used as a preprocessing technique to change them into the narrow-band.

Furthermore, the sensor configuration can be arbitrary and we assume that all the sensors are omnidirectional and not coupled [6, 7].

Using complex envelope representation, the p -dimensional vector received by the array can be expressed as

$$\mathbf{x}(t) = \sum_{k=1}^q \mathbf{a}(\theta_k) s_k(t) + \mathbf{n}(t), \quad (1)$$

where $s_k(t)$ is the k th signal received at a certain reference point. $\mathbf{n}(t)$ is a p -dimensional noise vector. $\mathbf{a}(\theta)$ is the "steering vector" of the array towards direction θ , which is represented as

$$\mathbf{a}(\theta) = [a_1(\theta) e^{-j\omega_0 \tau_1(\theta)}, \dots, a_p(\theta) e^{-j\omega_0 \tau_p(\theta)}]^T, \quad (2)$$

where $a_i(\theta)$ is the amplitude response of the i th sensor to a wave-front impinging from the direction θ . $\tau_i(\theta)$ is the propagation delay between the i th sensor and the reference point. The superscript T denotes the transpose of a matrix.

In the matrix notation, (1) can be rewritten as

$$\begin{aligned} \mathbf{x}(t) &= \mathbf{A}(\Theta) \mathbf{s}(t) + \mathbf{n}(t), \\ \mathbf{A}(\Theta) &= [\mathbf{a}(\theta_1) \ \mathbf{a}(\theta_2) \ \cdots \ \mathbf{a}(\theta_q)], \\ \mathbf{s}(t) &= [s_1(t) \ s_2(t) \ \cdots \ s_q(t)]^T, \\ \Theta &= \{\theta_1 \ \theta_2 \ \cdots \ \theta_q\}. \end{aligned} \quad (3)$$

Suppose that the received vector $\mathbf{x}(t)$ is sampled at M time instants t_1, t_2, \dots, t_M and define the matrix of the sampled data as

$$\begin{aligned} \mathbf{X} &= [\mathbf{x}(t_1) \ \mathbf{x}(t_2) \ \cdots \ \mathbf{x}(t_M)] \\ &= \mathbf{A}(\Theta) \mathbf{S} + \mathbf{N}, \end{aligned} \quad (4)$$

where

$$\begin{aligned} \mathbf{S} &= [\mathbf{s}(t_1), \mathbf{s}(t_2), \dots, \mathbf{s}(t_M)], \\ \mathbf{N} &= [\mathbf{n}(t_1), \mathbf{n}(t_2), \dots, \mathbf{n}(t_M)]. \end{aligned} \quad (5)$$

The problem of DOA finding is to be stated as follows. Given the sampled data \mathbf{X} , obtain a set of estimated directions

$$\widehat{\Theta} = \{\widehat{\theta}_1 \ \widehat{\theta}_2 \ \cdots \ \widehat{\theta}_q\} \quad (6)$$

of $\theta_1, \theta_2, \dots, \theta_q$.

3. SML Estimation

In this section, brief descriptions of the exact SML criterion are shown [6, 7].

To solve the problem of ML estimation of DOA, we make the following assumptions.

- (A1) The array configuration is known and any p steering vectors for different q directions are linearly independent; that is, the matrix $\mathbf{A}(\Theta)$ has full rank.
- (A2) p , q , and M satisfy the condition that a unique solution of DOA exists in the noise-free case. As for a uniform linear array, $q \leq 2\eta p / (2\eta + 1)$ and $M \geq \eta$ are the necessary conditions of the uniqueness [20], where η is the rank of \mathbf{S} .
- (A3) p and q are known.
- (A4) The noise samples $\mathbf{n}(t_i)$ are statistically independent Gaussian random vectors with zero mean and the covariance matrix $\sigma^2 \mathbf{I}_p$, where \mathbf{I}_p is a $p \times p$ identity matrix.

(A5) $\mathbf{s}(t_i)$ are independent samples from a complex Gaussian random vector which has zero mean and signal covariance matrix with rank η and is independent of the noise.

According to [6], the SML criterion can be derived based on the process of the array covariance matrix \mathbf{R} defined as

$$\mathbf{R} = E\{\mathbf{X}\mathbf{X}^H\} = \mathbf{A}(\Theta)\mathbf{S}_R\mathbf{A}(\Theta)^H + \sigma^2\mathbf{I}, \quad (7)$$

where $\mathbf{S}_R = E\{\mathbf{S}\mathbf{S}^H\}$ is the signal covariance matrix.

The SML criterion is shown as follows [6, 7].

$$\hat{\Theta}_{\text{SML}} = \arg \min_{\Theta} L_{\text{SML}}(\Theta), \quad (8)$$

$$L_{\text{SML}}(\Theta) = \det \mathbf{R}_{\text{SS}} \times \left(\frac{1}{p-q} \text{tr}\{\mathbf{R}_{\text{NN}}\} \right)^{p-q}, \quad (9)$$

$$\mathbf{R}_{\text{NN}} = \mathbf{V}_N^H(\Theta)\hat{\mathbf{R}}\mathbf{V}_N(\Theta), \quad (10)$$

$$\mathbf{R}_{\text{SS}} = \mathbf{V}_S^H(\Theta)\hat{\mathbf{R}}\mathbf{V}_S(\Theta), \quad (11)$$

where

$$\hat{\mathbf{R}} = \frac{1}{M}\mathbf{X}\mathbf{X}^H \quad (12)$$

is the sample covariance matrix of the sampled data. $\mathbf{V}_S(\Theta)$ is a $p \times q$ matrix composed of an orthonormal system of the signal subspace spanned by $\mathbf{A}(\Theta)$. $\mathbf{V}_N(\Theta)$ is a $p \times (p-q)$ matrix composed of an orthonormal system of the noise subspace, which is an orthogonal complement of the signal subspace. The $q \times q$ matrix, \mathbf{R}_{SS} , corresponds to the covariance matrix of the components for $\mathbf{x}(t)$ in the signal subspace. \mathbf{R}_{NN} is the covariance matrix of the components for $\mathbf{x}(t)$ in the noise subspace.

From (8) and (9), we can see that the estimation of SML is to find a set of Θ which minimizes L_{SML} in (9). This is a multidimensional nonlinear optimization problem.

Note that there are literatures [21, 22] discussing the preciseness of SML criterion derived above. This paper focuses on the problem of reducing the computational complexity of SML estimation. Our efficient algorithms are derived based on (9).

4. Efficient AM Algorithms for SML Estimation

The AM algorithm is the most classic estimation algorithm for multidimensional nonlinear optimization problem in DOA estimation. In this section, we will introduce the conventional AM algorithm firstly, and then we will introduce our proposed efficient AM algorithms.

4.1. Conventional AM Algorithm. The AM method is a popular iterative technique for solving a nonlinear multivariate minimization problem with a multimodal criterion [6]. It can be applied to the SML criterion of DOA in the following manner.

Let $L_k(\hat{\Theta}^{(k)})$ be a cost function of (9) for which the signal number is assumed to be k instead of q , where $\hat{\Theta}^{(k)} = \{\hat{\theta}_1, \hat{\theta}_2, \dots, \hat{\theta}_k\}$.

Initialization Phase. For a certain value of SNR, first assuming a single signal, $k = 1$, find $\hat{\theta}_1$ minimizing $L_1(\hat{\Theta}^{(1)})$ by one-dimensional global search with respect to $\hat{\theta}_1$. Next, assuming two signals, $k = 2$, and fixing $\hat{\theta}_1$ at the value obtained for a single signal, find $\hat{\theta}_2$ minimizing $L_2(\hat{\Theta}^{(2)})$ by one-dimensional global search with respect to $\hat{\theta}_2$. Continue in this fashion until all the initial values for $\hat{\theta}_k$, $k = 1, 2, \dots, q$ are computed.

Convergence Phase. Repeat the following updating process until all parameters are converged. At each updating process, let one parameter, say $\hat{\theta}_k$, be variable and let all other parameters be held fixed. Find $\hat{\theta}_k$ minimizing the criterion $L_q(\hat{\Theta}^{(q)})$ by one-dimensional global search with respect to $\hat{\theta}_k$. Change the index k of the parameter to be updated into $(k \bmod q) + 1$.

Although a global minimum is not guaranteed in the AM algorithm, global solutions can be obtained in most cases because of one-dimensional global searches performed in each update process.

4.2. Efficient AM (EAM) Algorithm for SML Estimation. In this section, we propose an efficient version of the AM algorithm. We call it the EAM algorithm. Using transformation of matrix and properties of spatial projection, the EAM algorithm divides the SML criterion into two components. One depends on a variable parameter and the other one is independent of the variable parameter. In order to simplify expressions, parameters to be estimated are represented without the accent hat, and the argument Θ or $\hat{\Theta}$ is omitted.

In each updating process, let θ_l be a variable parameter and define

$$\Theta_l = \{\theta_1, \theta_2, \dots, \theta_{l-1}, \theta_{l+1}, \dots, \theta_q\}, \quad (13)$$

$$\mathbf{A}_l = [\mathbf{a}(\theta_1), \dots, \mathbf{a}(\theta_{l-1}), \mathbf{a}(\theta_{l+1}), \dots, \mathbf{a}(\theta_q)].$$

\mathbf{V}_{S_l} is an orthonormal system of the subspace spanned by $\{\mathbf{A}_l\}$.

\mathbf{V}_{N_l} is an orthonormal system of the orthogonal complement of the subspace spanned by $\{\mathbf{A}_l\}$.

$$\mathbf{P}_{A_l} = \mathbf{A}_l \{\mathbf{A}_l^H \mathbf{A}_l\}^{-1} \mathbf{A}_l^H = \mathbf{V}_{S_l} \mathbf{V}_{S_l}^H, \quad (14)$$

$$\mathbf{P}_{A_l}^\perp = \mathbf{I} - \mathbf{P}_{A_l} = \mathbf{V}_{N_l} \mathbf{V}_{N_l}^H, \quad (15)$$

$$\mathbf{R}_{S_l} = \mathbf{V}_{S_l}^H \mathbf{R} \mathbf{V}_{S_l}, \quad (16)$$

$$\mathbf{R}_{N_l} = \mathbf{V}_{N_l}^H \mathbf{R} \mathbf{V}_{N_l}, \quad (17)$$

$$\mathbf{v}_l(\theta_l) = \frac{\mathbf{P}_{A_l}^\perp \mathbf{a}(\theta_l)}{\|\mathbf{P}_{A_l}^\perp \mathbf{a}(\theta_l)\|}. \quad (18)$$

Note that when the value of θ_l changes, only $\mathbf{v}_l(\theta_l)$ varies and all others above are fixed. From these definitions, we have

$$\begin{aligned} \text{span}\{\mathbf{V}_{N_l}\} &= \text{span}\{\mathbf{v}_l(\theta_l)\} \oplus \text{span}\{\mathbf{V}_N\}, \\ \text{span}\{\mathbf{V}_S\} &= \text{span}\{\mathbf{v}_l(\theta_l)\} \oplus \text{span}\{\mathbf{V}_{S_l}\}, \end{aligned} \quad (19)$$

where \oplus represents the direct sum of subspaces. It follows from (19) that there exist a $(p - q + 1) \times (p - q + 1)$ unitary matrix \mathbf{T}_1 and a $q \times q$ unitary matrix \mathbf{T}_2 which satisfy

$$\mathbf{V}_{N_l} = [\mathbf{v}_l(\theta_l) \mathbf{V}_N] \mathbf{T}_1, \quad (20)$$

$$\mathbf{V}_S = [\mathbf{v}_l(\theta_l) \mathbf{V}_{S_l}] \mathbf{T}_2. \quad (21)$$

Substituting (20) into (17), we have

$$\begin{aligned} \mathbf{R}_{N_l} &= \mathbf{T}_1^H \begin{bmatrix} \mathbf{v}_l^H(\theta_l) \mathbf{R} \mathbf{v}_l(\theta_l) & \mathbf{v}_l^H(\theta_l) \mathbf{R} \mathbf{V}_N \\ \mathbf{V}_N^H \mathbf{R} \mathbf{v}_l(\theta_l) & \mathbf{V}_N^H \mathbf{R} \mathbf{V}_N \end{bmatrix} \mathbf{T}_1 \\ &= \mathbf{T}_1^H \begin{bmatrix} \mathbf{v}_l^H(\theta_l) \mathbf{R} \mathbf{v}_l(\theta_l) & \mathbf{v}_l^H(\theta_l) \mathbf{R} \mathbf{V}_N \\ \mathbf{V}_N^H \mathbf{R} \mathbf{v}_l(\theta_l) & \mathbf{R}_{NN} \end{bmatrix} \mathbf{T}_1. \end{aligned} \quad (22)$$

Taking the trace of both sides in (22), we have

$$\text{tr}\{\mathbf{R}_{N_l}\} = \text{tr}\{\mathbf{R}_{NN}\} + \mathbf{v}_l^H(\theta_l) \mathbf{R} \mathbf{v}_l(\theta_l). \quad (23)$$

Substituting the definition of $\mathbf{P}_{A_l}^\perp$ and $\mathbf{v}_l(\theta_l)$ into (23), we have

$$\text{tr}\{\mathbf{R}_{N_l}\} = \text{tr}\{\mathbf{R}_{NN}\} + \frac{\mathbf{a}^H(\theta_l) \mathbf{V}_{N_l} \mathbf{R}_{N_l} \mathbf{V}_{N_l}^H \mathbf{a}(\theta_l)}{\mathbf{a}^H(\theta_l) \mathbf{V}_{N_l} \mathbf{V}_{N_l}^H \mathbf{a}(\theta_l)}. \quad (24)$$

Substituting (21) into (11), we have

$$\begin{aligned} \mathbf{R}_{SS} &= \mathbf{T}_2^H \begin{bmatrix} \mathbf{v}_l^H(\theta_l) \mathbf{R} \mathbf{v}_l(\theta_l) & \mathbf{v}_l^H(\theta_l) \mathbf{R} \mathbf{V}_{S_l} \\ \mathbf{V}_{S_l}^H \mathbf{R} \mathbf{v}_l(\theta_l) & \mathbf{V}_{S_l}^H \mathbf{R} \mathbf{V}_{S_l} \end{bmatrix} \mathbf{T}_2 \\ &= \mathbf{T}_2^H \begin{bmatrix} \mathbf{v}_l^H(\theta_l) \mathbf{R} \mathbf{v}_l(\theta_l) & \mathbf{v}_l^H(\theta_l) \mathbf{R} \mathbf{V}_{S_l} \\ \mathbf{V}_{S_l}^H \mathbf{R} \mathbf{v}_l(\theta_l) & \mathbf{R}_{S_l} \end{bmatrix} \mathbf{T}_2. \end{aligned} \quad (25)$$

Taking the determinant of both sides in (25) and using the definition of (16), we have

$$\begin{aligned} \det\{\mathbf{R}_{SS}\} &= \det\{\mathbf{R}_{S_l}\} \times (\mathbf{v}_l^H(\theta_l) \mathbf{R} \mathbf{v}_l(\theta_l) \\ &\quad - \mathbf{v}_l^H(\theta_l) \mathbf{R} \mathbf{V}_{S_l} \mathbf{R}_{S_l}^{-1} \mathbf{V}_{S_l}^H \mathbf{R} \mathbf{v}_l(\theta_l)). \end{aligned} \quad (26)$$

Substitute the definition of $\mathbf{P}_{A_l}^\perp$ and $\mathbf{v}_l(\theta_l)$ into (26), and define

$$\mathbf{W} = \mathbf{R}_{N_l} - \mathbf{V}_{N_l}^H \mathbf{R} \mathbf{V}_{S_l} \mathbf{R}_{S_l}^{-1} \mathbf{V}_{S_l}^H \mathbf{R} \mathbf{V}_{N_l}, \quad (27)$$

and then we have

$$\det\{\mathbf{R}_{SS}\} = \det\{\mathbf{R}_{S_l}\} \frac{\mathbf{a}^H(\theta_l) \mathbf{V}_{N_l} \mathbf{W} \mathbf{V}_{N_l}^H \mathbf{a}(\theta_l)}{\mathbf{a}^H(\theta_l) \mathbf{V}_{N_l} \mathbf{V}_{N_l}^H \mathbf{a}(\theta_l)}. \quad (28)$$

Define

$$\mathbf{u}(\theta_l) = \mathbf{V}_{N_l}^H \mathbf{a}(\theta_l) \quad (29)$$

and then the final form of the proposed algorithm, EAM algorithm, can be derived from (24) and (28) as follows:

$$\text{tr}\{\mathbf{R}_{NN}(\Theta)\} = \text{tr}\{\mathbf{R}_{N_l}\} - \frac{\mathbf{u}^H(\theta_l) \mathbf{R}_{N_l} \mathbf{u}(\theta_l)}{\|\mathbf{u}(\theta_l)\|^2}, \quad (30)$$

$$\det\{\mathbf{R}_{SS}(\Theta)\} = \det\{\mathbf{R}_{S_l}\} \frac{\mathbf{u}^H(\theta_l) \mathbf{W} \mathbf{u}(\theta_l)}{\|\mathbf{u}(\theta_l)\|^2}. \quad (31)$$

In (29), (30), and (31), all quantities except for $\mathbf{u}(\theta_l)$ are fixed and can be computed before starting the one-dimensional search with respect to θ_l . Therefore main computations of each step in the one-dimensional search are a product of the matrix $\mathbf{V}_{N_l}^H$ and the vector $\mathbf{a}(\theta_l)$ in (29) and evaluation of two Hermitian forms in (30) and (31). Evaluation of $\mathbf{u}(\theta_l)$ requires $O(p \times (p - q + 1))$ multiplications. Then evaluation of $\|\mathbf{u}(\theta_l)\|^2$ requires $O((p - q + 1)^2)$ multiplications. Therefore, at each step of one-dimensional search with respect to the variable parameter, θ_l , $O(p \times (p - q + 1))$ multiplications are required. Therefore, computational complexity can be greatly reduced since, in the conventional AM algorithm, we need to calculate the whole SML criterion in each step of one-dimensional search.

(1) *Oscillation Problem in EAM Algorithm.* Define the subspace

$$\mathbf{U}(\Theta) = \text{span}\{\mathbf{a}(\theta_1) \ \mathbf{a}(\theta_2) \ \cdots \ \mathbf{a}(\theta_q)\}. \quad (32)$$

The linear combination

$$\frac{\mathbf{a}(\theta_j) - \mathbf{a}(\theta_i)}{\theta_j - \theta_i} \quad (33)$$

always belongs to $\mathbf{U}(\Theta)$. Even when $\theta_j \rightarrow \theta_i$, we have $\dim\{\mathbf{U}(\Theta)|_{\theta_i \rightarrow \theta_j}\} = q$, where $\dim\{\}$ represents the dimension of the subspace.

On the other hand, when $\theta_j = \theta_i$, we have $\dim\{\mathbf{U}(\Theta)|_{\theta_i = \theta_j}\} < q$. This implies that the criterion has discontinuous points in the parameter space.

Next, we consider calculation of the EAM criterion $\mathbf{v}_l(\theta_l)$ in (18). When the variable parameter θ_l approaches the value of a fixed parameter θ_i , $\mathbf{v}_l(\theta_l)$ vanishes and both the numerator and denominator in (18) become zero. Then $\mathbf{v}_l(\theta_l)$ becomes indefinite. Therefore the calculation of $\mathbf{v}_l(\theta_l)$ becomes numerically instable. This can be verified in Section 5.

In the case that the DOA can be solved, the numerical instability does not occur, since each parameter in the convergence phase of the EAM criterion comes apart from others. However, at the threshold region, when more than one signal approaches an identical value, the numerical instability becomes significant. In practice, when this case happens, the sequence of DOA obtained in the convergence phase of the EAM criterion shows oscillation that is because the estimated directions can not converge well due to the numerical instability and would oscillate around that identical value.

Let us give an example. In the simulation there are two sources located in 0 and 8 degrees (the true DOAs). When

SNR = 0 dB and with specific noise samples, the solutions of SML criterion are 3.999 and 4.001 degrees (the solutions of SML). However, in this case, when calculating $\theta_1 = \theta_2 = 4$ degrees, the oscillation happens. As a result, the estimated DOAs may be 4 and 4 degrees (the estimated DOAs). In this case, because of oscillation, extra computation is required. Furthermore, the estimated DOAs are wrong (because they are not the solutions of SML criterion) although they are very close to the solutions of SML criterion. As a result, the estimation accuracy is also affected. These explanations will be shown in Section 5.

To solve these problems, the key point is to cancel the common zeros in the numerator and denominator of the EAM criterion. Next we try to establish the irreducible form of the EAM criterion using a uniform linear array.

4.3. Irreducible Form of Efficient AM Criterion (IAM). In this section, we derive the irreducible form of the EAM criterion using a uniform linear array. With a uniform linear array, the EAM criterion can be written into polynomial forms. Then we can easily cancel the common zero in both numerator and denominator. Thus numerical instability never happens in IAM criterion. Furthermore, we can find that the IAM algorithm can reduce the computational order of EAM criterion from square to one in each updating process.

The array configuration is uniform linear array composed of omnidirectional sensors, of which steering vector is represented as

$$\mathbf{a}(\theta) = [1 \ e^{-j\phi(\theta)} \ \dots \ e^{-j(p-1)\phi(\theta)}]^T, \quad (34)$$

$$\phi(\theta) = \frac{2\pi\Delta}{\lambda} \sin\theta, \quad (35)$$

where λ is the wavelength of signals impinging on the array and Δ is the sensor spacing between two adjacent sensors. As a necessary condition that a unique direction θ is determined by the phase parameter ϕ , $\Delta \leq \lambda/2$ is imposed on the array configuration. In this paper, $\Delta = \lambda/2$.

Using the uniform linear array, we derive the irreducible form of (30) and (31). Define

$$f_l(\theta) = \frac{\mathbf{u}^H(\theta_l) \mathbf{R}_{N_l} \mathbf{u}(\theta_l)}{\|\mathbf{u}(\theta_l)\|^2}, \quad (36)$$

$$\tilde{f}_l(\theta) = \frac{\mathbf{u}^H(\theta_l) \mathbf{W} \mathbf{u}(\theta_l)}{\|\mathbf{u}(\theta_l)\|^2}$$

which are the varying parts in (30) and (31).

First we derive the irreducible form of (30). Substituting (15) and (29) into $f_l(\theta)$, we get

$$f_l(\theta) = \frac{\mathbf{a}^H(\theta_l) \mathbf{P}_{A_l}^\perp \mathbf{R} \mathbf{P}_{A_l}^\perp \mathbf{a}(\theta_l)}{\mathbf{a}^H(\theta_l) \mathbf{P}_{A_l}^\perp \mathbf{a}(\theta_l)}. \quad (37)$$

Using the uniform linear array defined above, the steering vector $\mathbf{a}(\theta)$ in (34) can be represented as follows:

$$\mathbf{a}^H(\theta) = \boldsymbol{\zeta}_p(z) = [1 \ z \ \dots \ z^{p-1}] \Big|_{z=e^{-j\phi(\theta)}}. \quad (38)$$

Then $f_l(\theta)$ can be rewritten into the form of a rational function

$$f_l(\theta) = \frac{\boldsymbol{\zeta}_p(z) \mathbf{P}_{A_l}^\perp \mathbf{R} \mathbf{P}_{A_l}^\perp \boldsymbol{\zeta}_{p^*}(z)}{\boldsymbol{\zeta}_p(z) \mathbf{P}_{A_l}^\perp \boldsymbol{\zeta}_{p^*}(z)} = \frac{N(z)}{D(z)} \Big|_{z=e^{-j\phi(\theta)}}, \quad (39)$$

where $\boldsymbol{\zeta}_{p^*}(z)$ is the paraconjugate of $\boldsymbol{\zeta}_p(z)$ defined as

$$\boldsymbol{\zeta}_{p^*}(z) = \boldsymbol{\zeta}_p^H\left(\frac{1}{z^*}\right) = [1 \ z^{-1} \ \dots \ z^{-(p-1)}]^T \quad (40)$$

and the superscript $*$ is the complex conjugate of a complex number.

Let θ_l be variable and all other parameters are held fixed as well as in last subsection. As we have discussed in the problem of EAM, when θ_l becomes equal to θ_i , both the polynomials $N(z)$ and $D(z)$ have double zeros at $z = e^{-j\phi(\theta_i)}$ in the complex z -plane, since it holds $\boldsymbol{\zeta}_p(e^{-j\phi(\theta_i)}) \mathbf{P}_{A_l}^\perp = 0$. Without canceling these common zeros, $f_l(\theta)$ is indefinite at $\theta = \theta_i$.

The irreducible form of the EAM criterion of $f_l(\theta)$ can be derived by canceling these common zeros. First, we define the polynomial $W_l(z)$ having zeros at $z = e^{-j\phi(\theta_i)}$, $i = 1, 2, \dots, l-1, l+1, \dots, q$,

$$W_l(z) = \prod_{i=1, i \neq l}^q (z - e^{-j\phi(\theta_i)}) \quad (41)$$

$$= w_0 + w_1 z + \dots + w_{q-1} z^{q-1}.$$

Using the coefficients of $W_l(z)$, define the following $p \times (p - q + 1)$ matrix as

$$\mathbf{W}_l = \begin{bmatrix} w_0 & 0 & \dots & 0 \\ w_1 & w_0 & \dots & 0 \\ \vdots & \vdots & \ddots & 0 \\ w_{q-1} & w_{q-2} & \dots & w_0 \\ 0 & w_{q-1} & \dots & w_1 \\ \vdots & \vdots & \ddots & \vdots \\ 0 & 0 & \dots & w_{q-1} \end{bmatrix}. \quad (42)$$

Then we have $\mathbf{a}^H(\theta_i) \mathbf{W}_l = 0$ for $i = 1, \dots, l-1, l+1, \dots, q$. Since the column vectors in \mathbf{W}_l are all orthogonal to $\mathbf{a}(\theta_i)$, the projection matrix $\mathbf{P}_{A_l}^\perp$ can be written as

$$\mathbf{P}_{A_l}^\perp = \mathbf{W}_l \mathbf{G}_l^{-1} \mathbf{W}_l^H, \quad (43)$$

$$\mathbf{G}_l = \mathbf{W}_l^H \mathbf{W}_l.$$

Here, note that $W_l(z)$ represents a polynomial, while \mathbf{W}_l represents a matrix.

Using the expressions

$$\boldsymbol{\zeta}_{p-q+1}(z) \mathbf{W}_l(z) = [W_l(z) \ z W_l(z) \ \dots \ z^{p-q} W_l(z)]$$

$$= W_l(z) \boldsymbol{\zeta}_{p-q+1}(z), \quad (44)$$

$$\boldsymbol{\zeta}_{p-q+1}(z) = [1 \ z \ \dots \ z^{p-q}],$$

the irreducible form of $f_l(\theta)$ is derived as

$$\begin{aligned} f_l(\theta) &= \frac{W_l(z) \zeta_{p-q}(z) \mathbf{N}_l \zeta_{(p-q)^*}(z) W_l(z)}{W_l(z) \zeta_{p-q}(z) \mathbf{D}_l \zeta_{(p-q)^*}(z) W_l(z)} \Bigg|_{z=e^{-j\phi(\theta)}} \\ &= \frac{\zeta_{p-q}(z) \mathbf{N}_l \zeta_{(p-q)^*}(z)}{\zeta_{p-q}(z) \mathbf{D}_l \zeta_{(p-q)^*}(z)} \Bigg|_{z=e^{-j\phi(\theta)}}, \end{aligned} \quad (45)$$

where $W_l(z)$ is the common zero factor at $z = e^{-j\phi(\theta)}$, $i \leq q$, $i \neq l$, and

$$\begin{aligned} \mathbf{N}_l &= \mathbf{G}_l^{-1} \mathbf{W}_l^H \mathbf{R} \mathbf{W}_l \mathbf{G}_l^{-1} = \{n_{i,j}\}_{i,j=0}^{p-q}, \\ \mathbf{D}_l &= \mathbf{G}_l^{-1} = \{d_{i,j}\}_{i,j=0}^{p-q}. \end{aligned} \quad (46)$$

As for the irreducible form of $\tilde{f}_l(\theta)$, it can be derived like this form similarly,

$$\tilde{f}_l(\theta) = \frac{\zeta_{p-q}(z) \tilde{\mathbf{N}}_l \zeta_{(p-q)^*}(z)}{\zeta_{p-q}(z) \mathbf{D}_l \zeta_{(p-q)^*}(z)} \Bigg|_{z=e^{-j\phi(\theta)}}, \quad (47)$$

where

$$\tilde{\mathbf{N}}_l = \mathbf{N}_l - \mathbf{G}_l^{-1} \mathbf{W}_l^H \mathbf{R} \mathbf{V}_{s_1} \mathbf{R}_{s_1}^{-1} \mathbf{V}_{s_1}^H \mathbf{R} \mathbf{W}_l \mathbf{G}_l^{-1} = \{\tilde{n}_{i,j}\}_{i,j=0}^{p-q}. \quad (48)$$

Define the following polynomials

$$\begin{aligned} n_l(z) &= n_0 + n_1 z + \dots + n_{p-q} z^{p-q}, \\ d_l(z) &= d_0 + d_1 z + \dots + d_{p-q} z^{p-q}, \end{aligned} \quad (49)$$

where

$$\begin{aligned} n_0 &= \sum_{i=0}^{p-q} n_{i,i}, \\ n_m &= 2 \sum_{i=m}^{p-q} n_{i,i-m}, \\ d_0 &= \sum_{i=0}^{p-q} d_{i,i}, \\ d_m &= 2 \sum_{i=m}^{p-q} d_{i,i-m}, \quad m = 1, 2, \dots, p-q, \end{aligned} \quad (50)$$

and similarly define $\tilde{n}_l(z)$ to calculate the matrix $\tilde{\mathbf{N}}_l$ which realizes the same function as $n_l(z)$.

Then we have the final form of $f_l(\theta)$ and $\tilde{f}_l(\theta)$ shown as follows:

$$\begin{aligned} f_l(\theta) &= \frac{\text{Re}\{n_l(e^{j\theta})\}}{\text{Re}\{d_l(e^{j\theta})\}}, \\ \tilde{f}_l(\theta) &= \frac{\text{Re}\{\tilde{n}_l(e^{j\theta})\}}{\text{Re}\{d_l(e^{j\theta})\}}, \end{aligned} \quad (51)$$

where $\text{Re}\{\}$ represents the real part of the complex value.

Therefore the irreducible form of efficient AM criterion (IAM) is shown like this.

$$\begin{aligned} \text{tr}\{\mathbf{R}_{\text{NN}}\} &= \text{tr}\{\mathbf{R}_{\text{N}_l}\} - \frac{\text{Re}\{n_l(e^{j\theta})\}}{\text{Re}\{d_l(e^{j\theta})\}}, \\ \det\{\mathbf{R}_{\text{SS}}\} &= \det\{\mathbf{R}_{s_1}\} \frac{\text{Re}\{\tilde{n}_l(e^{j\theta})\}}{\text{Re}\{d_l(e^{j\theta})\}}. \end{aligned} \quad (52)$$

Furthermore, we can find that \mathbf{R}_{N_l} , \mathbf{R}_{s_1} , \mathbf{N}_l , $\tilde{\mathbf{N}}_l$, and \mathbf{D}_l can be calculated before each updating process. Therefore, at each updating process we only need to evaluate $\text{Re}\{n_l(e^{j\theta})\}$, $\text{Re}\{\tilde{n}_l(e^{j\theta})\}$, and $\text{Re}\{d_l(e^{j\theta})\}$. Evaluation of them only needs $O(p-q)$ multiplications. Compared to $O(p(p-q))$ multiplications in each updating process of EAM algorithm, the computational complexity can be reduced further.

Here we should note that the IAM algorithm is only applicable to the ULA that is because the IAM algorithm is formulated based on (34) and (35). The steering vector can only be written into this form when the array is uniform linear array (ULA). Based on (34) and (35), the EAM criterion can be written into polynomial form. And then the irreducible form of EAM can be derived by canceling the common zero in both numerator and denominator. Therefore, the IAM is only applicable to the ULA.

5. Simulations

In this section, we show some simulation results to demonstrate the validity of the EAM and IAM algorithms. In simulation, the array configuration is a uniform linear array as discussed above.

The SNR is defined as

$$\text{SNR}_k = 10 \log_{10} \frac{E[|s_k(t)|^2]}{\sigma^2}. \quad (53)$$

The Root-Mean-Square-Error (RMSE) is defined as

$$\text{RMSE} = \sqrt{\frac{1}{qN} \sum_{k=1}^q \sum_{n=1}^N |\hat{\theta}_{k,n} - \theta_k|^2}, \quad (54)$$

where $\hat{\theta}_{k,n}$ is the estimation of θ_k at the n th trial. The number of trails in our simulation is 100.

In Figure 1, the scenario is $p = 3$, $q = 2$, $\eta = 2$, $\text{SNR} = 10$, $M = 100$. Two true sources are independently located at 0 and 8 degrees. The estimated bearing θ_2 is fixed at 10 degrees, while θ_1 varies from 9.99999 to 10.00001. The dashed line represents the value of SML with EAM criterion, while the solid line represents the IAM criterion. It shows clearly that numerical instability occurs when the EAM criterion is used. In particular, the value changes violently around the point $\theta_2 = \theta_1 = 10$ degrees because it is indefinite. As for the IAM criterion, we can find that the value becomes monotonic and it is numerically stable.

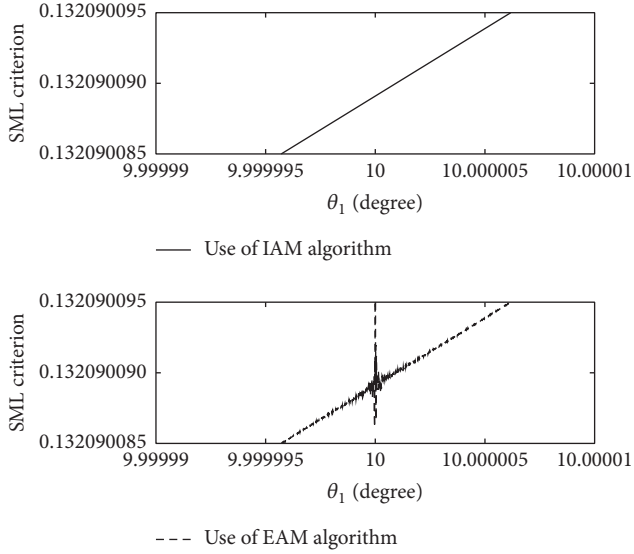


FIGURE 1: Numerical instability in EAM and stability in IAM criterion.

Due to the numerical instability, oscillation may happen as Figure 2 shows. The scenario is the same as Figure 1. In Figures 2(a) and 2(b), the estimated two bearings θ_1 and θ_2 converge to an identical value represented by the solid line and the dashed line. The convergence condition is that when the variation of each bearing is less than 10^{-5} or when the iteration reaches the maximum number, 800. When the EAM criterion is used, the iteration does not stop until it reaches the maximum number because of oscillation. As for the IAM criterion, it converges well for less than 100 iterations. Figure 2(c) shows the oscillation rate of the two criterions in 100 independent trials. We can find that there is no oscillation when the IAM criterion is used. Note that the oscillation rate of EAM decreases when SNR increases as shown in Figure 2(c) that is because the oscillation happens when more than one parameter converges to an identical value. In simulations, two sources are independently located in 0 and 8 degrees. When SNR is relatively low, the case that the estimated two bearings are extremely close (e.g., 3.990 and 4.010) or even equal exists. In this case, oscillation happens. When SNR increases, the estimated two bearings will significantly separate each other. As a result, the oscillation rate will decrease.

Figure 3 shows the comparison of RMSE between SML, MUSIC, and ESPRIT. The scenario is the same as Figure 2 except for SNR. In simulation we use the original AM and our proposed EAM and IAM algorithms for SML estimation of DOA. We find that the RMSE of all the three algorithms are completely the same. The reason is that the proposed IAM and EAM algorithms are just transformations for SML criterion and there is no any modification. All these algorithms can find the solution of SML successfully (of course we have to delete the oscillation cases for AM and EAM criterions. Obviously, oscillation affects the estimation accuracy because the bearings do not converge to their optimal value). Also

TABLE 1: Comparison of computational complexity of AM, EAM, and IAM. The scenario is the same as Figure 5 when SNR = 5 dB.

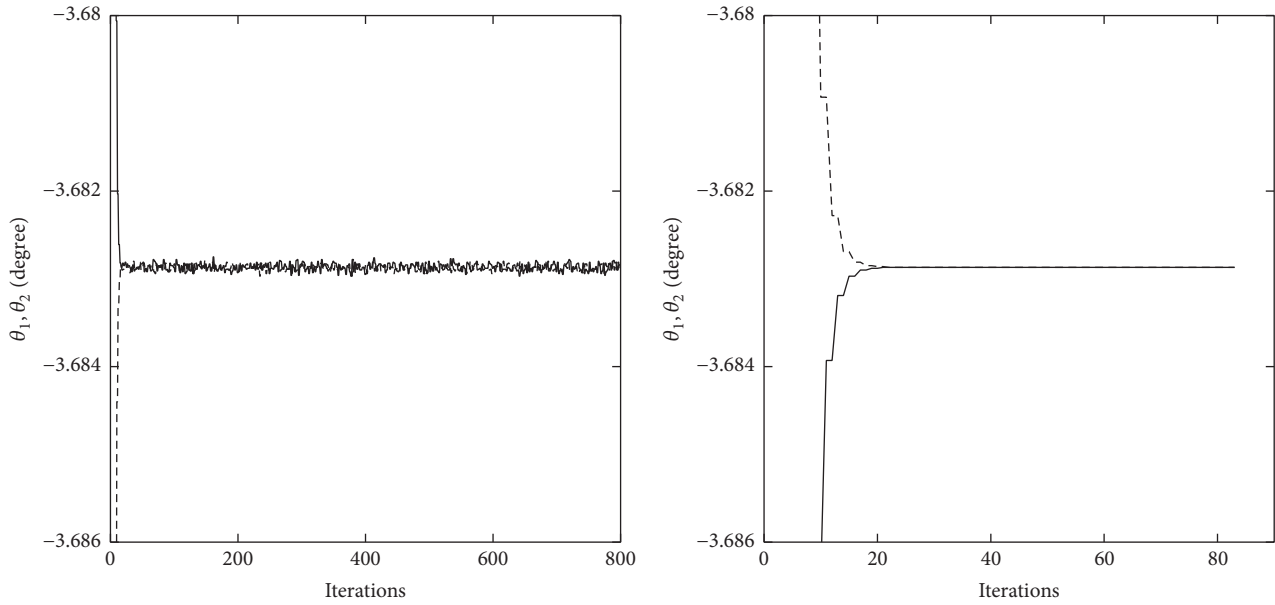
	Average iteration times	Main computational process
AM	127	$127 * (180/0.5 + 0.5 * 2/0.001 + 0.001 * 2/0.00001) = 83,820$ times of calculation of L_{SML} ($\det\{\mathbf{R}_{\text{SS}}\}$ and $\text{tr}\{\mathbf{R}_{\text{NN}}\}$)
EAM	127	127 times of calculation of $\det\{\mathbf{R}_{\text{S}_i}\}$, $\text{tr}\{\mathbf{R}_{\text{N}_i}\}$ and $W + 83,820$ times of calculation of $\mathbf{u}(\theta_i)$
IAM	127	127 times of calculation of $\det\{\mathbf{R}_{\text{S}_i}\}$, $\text{tr}\{\mathbf{R}_{\text{N}_i}\}$, \mathbf{N}_i , $\tilde{\mathbf{N}}_i$ and $\mathbf{D}_i + 83,820$ times of calculation of $\text{Re}\{n_i(e^{j\theta})\}$, $\text{Re}\{\tilde{n}_i(e^{j\theta})\}$, and $\text{Re}\{d_i(e^{j\theta})\}$

Figure 3 shows that the solution of SML is much better than that of MUSIC and ESPRIT.

Figures 4 and 5 and Table 1 show the comparison of computational complexity of AM, EAM, and IAM. Figures 4 and 5 show the average amount of operations of each algorithm. In Figure 4, $p = 3$, $q = 2$, $\eta = 2$, $M = 100$. The true DOA is 0 and 8 degrees. In Figure 5 $p = 8$, $q = 5$, $\eta = 3$, $M = 100$. The true DOA is 0, 8, 16, 24, and 32 degrees. Note that in Figure 5 $\eta < q$, which means that there are correlated signals (coherent case).

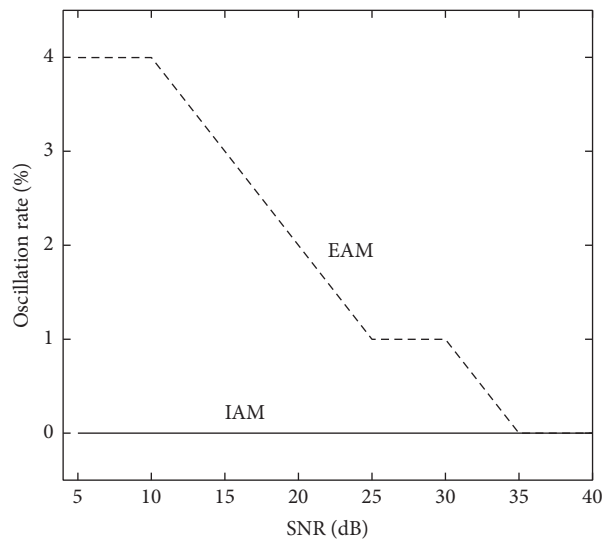
In Figures 4 and 5, “amount of arithmetic operations” represents the summation of all the complex addition, subtraction, multiplication, and division. These two figures show clearly that both EAM and IAM can reduce the computational complexity of SML estimation greatly, while IAM is the best.

Table 1 shows the detailed comparison of computational complexity including average iteration times and main calculation process of Figure 5 when SNR = 5 dB for 30 independent trials. For all these three algorithms, in the one-dimensional global search of each updating process, we use different step-sizes for searching. At first, we have a relatively large step-size (0.5 degrees) for rough search (note that this step-size should not be too large; otherwise the one-dimensional global minimum may be missed) and then much smaller step-sizes (0.001 and 0.00001 degrees) for fine search. For example, for the AM algorithm in the one-dimensional global search of an updating process, the searching range for the variable parameter (θ_i) is from -90° to 90° . As a result, the rough search needs $180/(0.5)$ times of calculation of L_{SML} . And then the fine search needs $(0.5 * 2/(0.001) + 0.001 * 2/(0.00001))$ times of calculation of L_{SML} . Since the number of iterations is 127, the main computational complexity of AM algorithm is 83,820 times of calculation of L_{SML} . For the EAM and IAM algorithms, the main computational complexity is also shown in Table 1 in the same manner. As we have discussed above, for the EAM and IAM algorithm, before each updating process, we can calculate many components in advance (the detailed components are shown in Table 1). We do not need to calculate the whole cost function L_{SML} every time. As a result, the computational complexity of EAM and IAM is much smaller than that of AM algorithm.



(a) The iteration does not stop until it reaches the maximum number, 800, using EAM criterion

(b) The iteration stops at about 85 using IAM criterion



(c) Oscillation rate of EAM and IAM algorithms

FIGURE 2: Oscillation in EAM algorithm while not in IAM.

Furthermore, from Figures 4 and 5, we can find two phenomena. First, the efficiency of EAM and IAM is more obvious than that of AM when the number of parameters increases. Here the number of parameters represents the number of incident signals, that is, q . The task of DOA is to find the directions of all the incident signals. When there are more parameters, the AM algorithm needs more iterations to solve the multidimensional nonlinear optimization problem of SML. For our proposed algorithms (EAM and IAM), in each updating process the computational complexity is greatly reduced. As a result, the efficiency is more obvious when the number of parameters increases (in Figure 5 there are 5 parameters to be estimated, and in Figure 4

there are 2). Second, the computational complexity of all these three methods changes with SNR that is because the computational complexity of all these methods mainly depends on the iteration times for the initial value converges to the estimated value. As we show in Section 4.1, the initial value is determined by the [Initialization Phase]. Obviously, the initial value will change according to different SNRs. Therefore, the total iteration times will change with SNR. As a result, computational complexity also changes with SNR.

In a huge number of simulations, we have confirmed the efficiency of our proposed EAM and IAM algorithms, while IAM is the best.

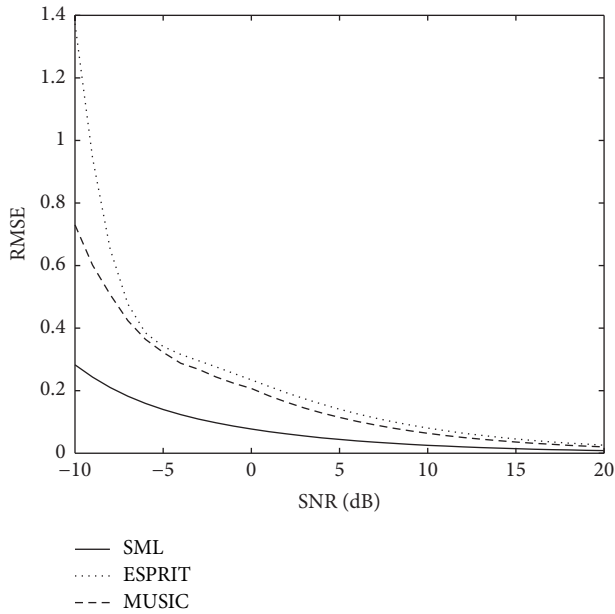


FIGURE 3: Comparison of RMSE between SML, MUSIC, and ESPRIT.

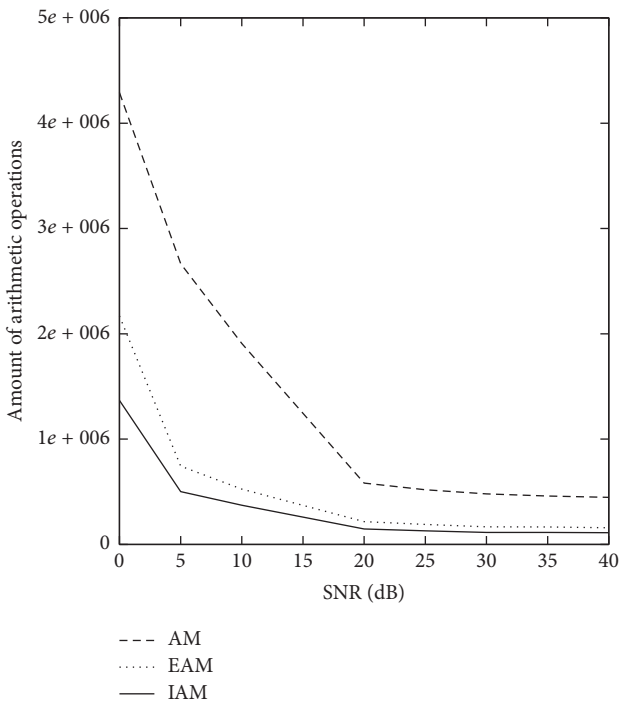


FIGURE 4: Average amount of operations for AM, EAM, and IAM algorithms. $p = 3, q = 2, \eta = 2$.

6. Conclusions

In this paper, to reduce the computational complexity of SML estimation, based on the AM algorithm, we propose two more efficient algorithms, that is, EAM and IAM algorithms. The EAM algorithm mainly uses transformation of matrix and properties of spatial projection to divide the SML criterion

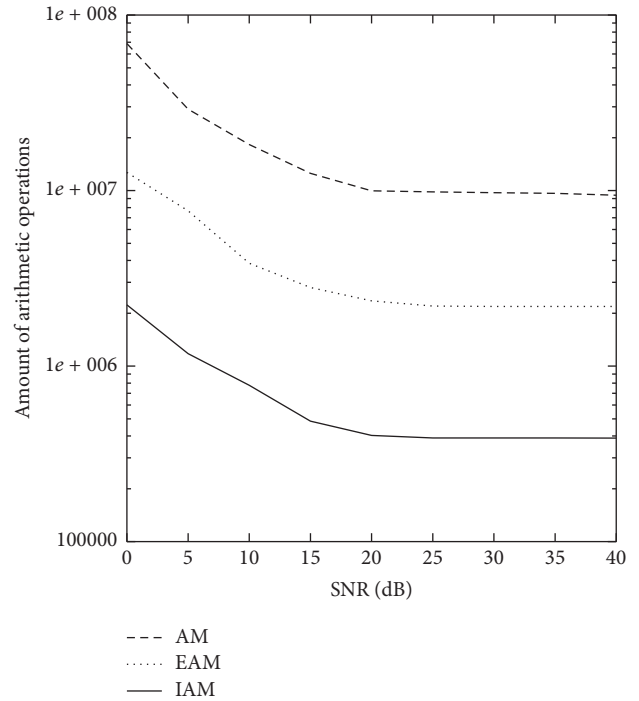


FIGURE 5: Average amount of operations for AM, EAM, and IAM algorithms. $p = 8, q = 5, \eta = 3$.

into two components. One is variable, while the other is fixed. Computational complexity can be greatly reduced since the fixed part can be calculated once in advance and only the varying part should be calculated in each one-dimensional updating process. To avoid numerical instability of EAM (note that because of the numerical instability, wrong estimation of DOA may be got) and to reduce computational complexity further, we derive the irreducible form of EAM, that is, IAM algorithm. The main idea of IAM is to use a uniform linear array and rewrite the EAM criterion into polynomial forms. Then the irreducible form can be got by canceling the common zero factor of the polynomial form. Simulation results show that the IAM algorithm can avoid the numerical instable problem of EAM and reduce computational complexity further.

Competing Interests

The authors declare that they have no competing interests.

Acknowledgments

This paper is supported by the following funds: The National Natural Science Funds, China, with no. 61601519; Fundamental Research Funds for the Central University, China, with nos. 15CX02047A and 15CX05025A; Shandong Provincial Natural Science Foundation, China, with no. ZR2014FM017; Science and Technology Development Plan of Qingdao with no. 15-9-1-80-jch.

References

- [1] Y. Bresler and A. Macovski, "Exact maximum likelihood parameter estimation of superimposed exponential signals in noise," *IEEE Transactions on Acoustics, Speech, and Signal Processing*, vol. 34, no. 5, pp. 1081–1089, 1986.
- [2] A. G. Jaffer, "Maximum likelihood direction finding of stochastic sources: a separable solution," in *Proceedings of the IEEE International Conference in Acoustics, Speech, and Signal Processing (ICASSP '88)*, pp. 2893–2896, New York, NY, USA, April 1988.
- [3] I. Ziskind and M. Wax, "Maximum likelihood localization of multiple sources by alternating projection," *IEEE Transactions on Acoustics, Speech, and Signal Processing*, vol. 36, no. 10, pp. 1553–1560, 1988.
- [4] P. Stoica and K. C. Sharman, "Maximum likelihood methods for direction-of-arrival estimation," *IEEE Transactions on Acoustics, Speech, and Signal Processing*, vol. 38, no. 7, pp. 1132–1143, 1990.
- [5] P. Stoica and A. Nehorai, "Performance study of conditional and unconditional direction-of-arrival estimation," *IEEE Transactions on Acoustics, Speech, and Signal Processing*, vol. 38, no. 10, pp. 1783–1795, 1990.
- [6] M. Wax, "Detection and localization of multiple sources via the stochastic signals model," *IEEE Transactions on Signal Processing*, vol. 39, no. 11, pp. 2450–2456, 1991.
- [7] H. L. van Trees, *Optimum Array Processing: Part IV of Detection, Estimation, and Modulation Theory*, John Wiley and Sons, New York, NY, USA, 2002.
- [8] R. O. Schmidt, "Multiple emitter location and signal parameter estimation," *IEEE Transactions on Antennas and Propagation*, vol. AP-34, no. 3, pp. 276–280, 1986.
- [9] R. T. Williams, S. Prasad, A. K. Mahalanabis, and L. H. Sibul, "An improved spatial smoothing technique for bearing estimation in a multipath environment," *IEEE Transactions on Acoustics, Speech, and Signal Processing*, vol. 36, no. 4, pp. 425–432, 1988.
- [10] R. Roy and T. Kailath, "ESPRIT-estimation of signal parameters via rotational invariance techniques," *IEEE Transactions on Acoustics, Speech, and Signal Processing*, vol. 37, no. 7, pp. 984–995, 1989.
- [11] M. Viberg, B. Ottersten, and T. Kailath, "Detection and estimation in sensor array using weighted subspace fitting," *IEEE Transactions on Acoustics, Speech, and Signal Processing*, vol. 39, no. 11, pp. 2436–2449, 1991.
- [12] B. M. Radich and K. M. Buckley, "Single-snapshot DOA estimation and source number detection," *IEEE Signal Processing Letters*, vol. 4, no. 4, pp. 109–111, 1997.
- [13] T. Li and A. Nehorai, "Maximum likelihood direction finding in spatially colored noise fields using sparse sensor arrays," *IEEE Transactions on Signal Processing*, vol. 59, no. 3, pp. 1048–1062, 2011.
- [14] P.-J. Chung and J. F. Bohme, "Recursive EM and SAGE-inspired algorithms with application to DOA estimation," *IEEE Transactions on Signal Processing*, vol. 53, no. 8, pp. 2664–2677, 2005.
- [15] M.-H. Li and Y.-L. Lu, "Improving the performance of GA-ML DOA estimator with a resampling scheme," *Signal Processing*, vol. 84, no. 10, pp. 1813–1822, 2004.
- [16] W. Shi, J. Huang, and Y. Hou, "Fast DOA estimation algorithm for MIMO sonar based on ant colony optimization," *Journal of Systems Engineering and Electronics*, vol. 23, no. 2, pp. 173–178, 2012.
- [17] J. Wang, Y. Zhao, and Z. Wang, "Low complexity subspace fitting method for wideband signal location," in *Proceedings of the 5th IFIP International Conference on Wireless and Optical Communications Networks*, pp. 1–4, May 2008.
- [18] L. Boccato, R. Krummenauer, R. Attux, and A. Lopes, "Application of natural computing algorithms to maximum likelihood estimation of direction of arrival," *Signal Processing*, vol. 92, no. 5, pp. 1338–1352, 2012.
- [19] H. Wang and M. Kaveh, "Coherent signal-subspace processing for the detection and estimation of angles of arrival of multiple wide-band sources," *IEEE Transactions on Acoustics, Speech, and Signal Processing*, vol. 33, no. 4, pp. 823–831, 1985.
- [20] M. Wax and I. Ziskind, "On unique localization of multiple sources by passive sensor arrays," *IEEE Transactions on Acoustics, Speech, and Signal Processing*, vol. 37, no. 7, pp. 996–1000, 1989.
- [21] P. Stoica, B. Ottersten, M. Viberg, and R. L. Moses, "Maximum likelihood array processing for stochastic coherent sources," *IEEE Transactions on Signal Processing*, vol. 44, no. 1, pp. 96–105, 1996.
- [22] H. Chen and M. Suzuki, "Exact formulation for stochastic ML estimation of DOA," *IEICE Transactions on Fundamentals of Electronics, Communications and Computer Sciences*, vol. 93, no. 11, pp. 2141–2152, 2010.